Vortex Sound Generation in the presence of Porous Materials with an Application to Dissipative Silencers and Lined Ducts

LAU, Chi Kin

A thesis submitted in fulfilment of the requirements for the

Degree of Doctor of Philosophy

at The Hong Kong Polytechnic University

Department of Building Services Engineering

April 2006

Declaration

I hereby declare that this thesis is my own work and that, to the best of my knowledge and belief, it reproduces no material previously published or written, nor material that has been accepted for the award of any other degree or diploma, except where due acknowledgement has been made in the text.

Signature : ______________________

Name : LAU CHI KIN

Acknowledgements

I would like to express my gratitude to my chief supervisor Prof. Shiu-Keung Tang for his guidance throughout the research project and co-supervisor Prof. Kai-Ming Li for his contribution and enlightenment.

I would like to acknowledge all the staff in the laboratories and offices for their support.

I would like to thank my family.

Abstract of Thesis

The main objective of this thesis is to study in details the vortex sound generation under the influence of porous materials. The effects of vortex strengths, separation distance and initial position are examined. The effects of effective fluid density and flow resistance inside the lattice of the porous material on sound generation are also explored.

Acoustic analogy is employed in the present study in order to derive the flow potential, and the matched asymptotic expansion method is used to evaluate the far-field sound pressure.

The present study is relevant to the problem of self-generated noise as the major function of the porous material is to attenuate the noise inside the ductwork system, but additional noise can be generated in the presence of the porous material at the same time. Vortex sound generation under the influence of a porous half cylinder mounted on an otherwise rigid plane, a porous wedge, a piece-wise porous material on an otherwise rigid plane and a lined duct are investigated.

In general, the far-field sound pressure is higher when the effective fluid density or the flow resistance is small. A smaller separation of the vortex from the porous material also increases the far-field sound pressure. The acoustical energy radiated can be higher than that in the rigid surface case when the flow resistance is very small, the separation distance of the vortices is large or the difference of the vortex strengths is large. The far-field sound pressure increases as the length or the thickness of the porous material increases. The far-field sound pressure does not decrease monotonically with increasing flow resistance when the length of the porous material increases due to the substantially large rate of change of the vortex velocity.

Contents

Glossary of Terms

English letters

a	Radius of the cylinder
A_j	$= -\frac{\Gamma_j \omega}{2c_o}\left[\left(r_j - \frac{1}{r_j}\right)\sin(\theta_j)\right]^t$
A_n	Mode magnitude
b	$= \pi/(2\pi - \alpha)$
B	Enthalpy
B_n	Mode magnitude
ci	Cosine integral
c_o	Ambient speed of sound
C	Integration constant
d	Duct width
d_i	Initial perpendicular distance of the vortex from the rigid surface
D_j	$= (\zeta + \zeta_j) - i(\xi_j - \xi)$
E	Overall acoustical energy radiated
f_{1j}	$= \frac{2\beta_j}{1+\eta}\mathrm{Re}\left[\exp(i\gamma_j\beta_j)G(0, i\gamma_j\beta_j) + \exp(-i\gamma_j\beta_j)G(0, -i\gamma_j\beta_j)\right]$
f_{2j}	$= \frac{4\beta_j}{1+\eta}\mathrm{Im}\left[ci(\gamma_j\beta_j)\cos(\gamma_j\beta_j) + si(\gamma_j\beta_j)\sin(\gamma_j\beta_j)\right]$
F	Force acting on unit length of the cylinder
$g_j(k)$	$= \frac{R_f + ikV_{wj}(1+\eta)}{-R_f + ikV_{wj}(1-\eta)}$
$G(0, \chi)$	Incomplete gamma function

G_n	Function of wavenumber, $n = 1, 2$
h	Depth of the porous material
H_n	Function of wavenumber, $n = 1, 2$
$H_{\sigma_j}^{(1)}$	Hankel function of the first kind of order σ_j
i	$\sqrt{-1}$
($\mathbf{i}$, $\mathbf{j}$, $\mathbf{k}$)	Unit vector in the longitudinal, transverse and spanwsie directions respectively
k	Wavenumber
L	Length of porous material
m	Positive integers = 1, 2, 3…
n	Positive integers = 1, 2, 3…
p	Far-field sound pressure
$p - p_o$	Perturbation pressure
p_o	Mean pressure
p_p	Fluid pressure inside the porous material
P_x	Longitudinal dipole
P_y	Transverse dipole
(r, θ)	Polar coordinates
R	Far-field distance
R_f	Flow resistance of the porous material
si	Sine integral
S	Solid boundary
t	Generation time
t_a	Time at which the vortex passes across the y-axis
t_b	Instant when the vorticity centroid passes over $x = 0$

t_c	Time at which the vortex passes across the axis of symmetry of the wedge
t_o	Far-field observer time
T_{ij}	Lighthill stress tensor, $\rho v_i v_j + \left[(p - p_o) - c_o^2(\rho - \rho_o)\right]\delta_{ij} - \sigma_{ij}$
$\mathbf{u_p}$	Fluid velocity inside the porous material
(u, v)	Longitudinal and transverse velocities of the vortex in z-plane
V	Occupied volume
V_{wj}	Velocity of the jth vortex in w-plane
w	Transformed Cartesian coordinates, (ξ, ζ)
W	Complex potential
$\mathbf{x}$	Position vector, (x_1, x_2, x_3)
$\mathbf{y}$	A point lies in the source region
z	Original Cartesian coordinates, (x, y)

Greek letters

α	Wedge angle
β_j	$= R_f \big/ [\lvert V_{wj} \rvert (1+\eta)]$
δ_{ij}	Kronecker delta
ε	Distance between vortices $z_2 = z_1 - \varepsilon$
ϕ	Flow potential
γ_j	$= 1 + \dfrac{r_j e^{i\theta_j} + 1}{r_j e^{i\theta_j} - 1}$
Γ	Vortex strength

η	Ratio of effective fluid density to the fluid density in the medium (ρ_e/ρ_o)
μ	$= (1 + \zeta_j) - i\xi_j$
$\rho v_i v_j$	Reynolds stress tensor
$\rho - \rho_o$	Perturbation density
ρ_e	Effective density of the porous material
ρ_o	Density of the ambient fluid
σ	$= \frac{1}{2\pi}\left\{\frac{1}{2}(1-y_1)+\sum_{n=1,3,5...}^{\infty}\left[B_n e^{\alpha_n(1+h)} - A_n e^{\alpha_n h}\right]\frac{\sinh(\alpha_n h)}{\alpha_n}\right\}$
σ_{ij}	Viscous stress tensor
ϖ	Vorticity
ω	Frequency
ψ	Streamfunction
∇	Differential operator
∇^2	Laplacian operator

Superscript

$\overline{}$	Complex conjugate
$\cdot$	Differentiation with respect to time t
$'$	Differentiation with respect to w

Subscript

1i	Initial condition for vortex located at z_1
2i	Initial condition for vortex located at z_2

c	Contribution from vorticity centroid
ci	Initial condition for the vorticity centroid of the vortex
j	*j*th vortex
k	*k*th vortex
l	Lower porous material
m	Contribution from the mutual induction between vortices
p	Porous material
u	Upper porous material
w	*w*-plane
x	Longitudinal direction
y	Transverse direction
z	*z*-plane
zi	Far-field Inner Potential
zo	Far-field outer potential

Abbreviation

$[]^t$	Fourier transform with respect to time
CFD	Computational Fluid Dynamics
DNS	Direct Numerical Simulation

List of Figures

Chapter 1: Introduction and Literature Review

1.1 Thesis Objective and Background

Ventilation and air conditioning systems are indispensable nowadays, especially in high-rise buildings within congested cities. Their principal function is to provide a better thermal comfort condition in terms of air temperature, air speed, humidity, etc to the occupants [Fanger, 1972; Gallo *et al*., 1988]. However, noise is produced unavoidably. There are three major noise sources inside a ventilation system. The primary noise source is the unbalanced force in the rotating part of the fan unit and is negligible if the machinery is properly installed. Noise is also produced as an unwanted by-product from the fluid flow as a result of instability containing regular fluctuations or turbulence at low Mach number [Lighthill, 1952, 1954]. The noise generated by turbulence alone is an acoustic quadrupole. In addition, the turbulence will interact with the solid surfaces such as bends, edges and cross-sectional area changes inside the ductwork to radiate noise [Curle, 1955]. This noise is an acoustic dipole. This turbulence surface interaction (dipole) is more important than that produced within the turbulent flow (quadrupole) in the air conditioning system where the flow Mach number is low and the flow Reynolds number is high. Noise from the related building services equipment, such as the air handling unit and fan, then propagates into the interior of the building through the air conveying ductworks and affects directly the indoor built environment.

First, the treated air with low temperature will be distributed by means of the air handling unit. Noise and turbulence are generated from the interaction between fan blades and the air flow [Ffowcs Williams and Hawkings, 1969; Peake and Kerschen, 1997; Quinlan and Bent, 1998; Fehse and Neise, 1999; Woodley and

Peake, 1999a, 1999b]. The turbulence further interacts with duct elements to produce noise. Nelson and Morfey [1981] measured the noise radiated from a flat plate placed normal to a low Mach number flow in a duct, and Hourigan *et al.* [1990] examined the acoustic resonance in a flow duct with baffles experimentally. Flow-induced noise due to fluid-structure interactions is also a problem in the ventilation ductwork [Howe, 1998]. Prediction methods for the aerodynamic noise produced in air ducts were also studied [Waddington and Oldham, 1999; Mak and Yang, 2000; Oldham and Waddington, 2001; Mak, 2002]. In the existing literature, there exists a large volume of analytical results on the flow-induced noise. Though they are not directly related to the noise inside the ventilation ductwork [for instance, Howe, 1975, 2003; Dowling and Ffowcs Williams, 1983; Crighton *et al.*, 1992], they do provide useful information on the sound generation mechanisms inside the ductwork.

In the current practice, there are two kinds of control method to alleviate the noise nuisance to the building occupants, namely, the active [Nelson and Elliott, 1993; Hansen and Snyder, 1997; Bies and Hansen, 2003] and the passive methods [Munjal, 1987a; Harries, 1991; Beranek and Vér, 1992; Barron, 2003]. The passive control method can be further categorized into the reactive and dissipative types.

Active control method utilizes electronic feedforward and feedback techniques to cancel the noise. An inverse pressure wave is generated to attenuate an unwanted noise by using the principle of destructive interference of waves. In order to achieve substantial sound cancellation, the cancelling source must produce, with great precision, an equal amplitude but inverted replica of the signal to be cancelled. Only with the advancement of adaptive digital signal-processing theory and hardware has it become possible to maintain these relationships automatically to the desired precision without continuous intervention by a human operator. The advantages of active control are small equipment size, low pressure drop (and associated energy savings in large air handing systems) and good low frequency performance. One can find some examples on controlling the ductwork noise in Swinbanks [1973], Trinder and Nelson [1983] and Tang and Cheng [1998].

Reactive control method consists of a number of elements with different transverse dimensions joined together so as to cause, at every junction, impedance mismatch and hence reflection of a substantial part of the incident acoustical energy back to the source. Some examples of reactive components are the side-branches [Ingard, 1953; Redmore and Mulholland, 1982; Radavich *et al.*, 2001; Tang and Li, 2003; Tang, 2004], the flexible panels [Huang, 1999; Huang *et al.*, 2000, Ramamoorthy *et al.*, 2003] and the expansion chambers [Cummings, 1975; El-Sharkawy and Nayfeh, 1978; Denia *et al.*, 2001; Sadamoto and Murakami, 2002].

The side-branch muffler consists of a Helmholtz resonator [Diskey and Selamet, 1996; Selamet *et* al., 1997; Chen *et al.*, 1998; Griffin, *et al.*, 2001; Selamet and Lee, 2003; Tang, 2005] connected to the main pipe through which the noise is transmitted. It reduces the noise transmission primarily by reflecting the acoustic energy back to the source, and some energy is partly dissipated by the air friction in the neck of the Helmholtz resonator. The effective frequency range of a side-branch muffler is narrow but the transmission loss within this range is large. For the expansion chamber, the maximum transmission loss is obtained when the length of the chamber is equal to an odd multiple of a quarter wavelength of the sound while the minimum transmission loss occurs when the length of the chamber is a multiple of a half wavelength [Munjal, 1987b; Selamet and Radavich, 1997]. Unfortunately, the cross-sectional area changes or cavity along the main duct causes high static pressure loss in the flow system.

The last method is to dissipate sound energy by the air friction (viscous effects) in the porous material lining (usually made of fibreglass or rockwool) inside dissipative silencers [Cummings, 1976; Mechel, 1990a, 1990b; Kirby and Lawrie, 2005]. Effective range of noise control is limited to the middle to high frequencies. Owing to its broadband performance and cost effectiveness, the dissipative silencers are widely adopted in the ventilation systems. For high frequency noise, the dissipative silencers are generally less expensive and have better performance over the active control system. This is because high frequency noise is usually associated with the propagation of higher order modes in addition to plane waves in a duct. Active systems for the control of higher order mode propagation are much more complicated than those for controlling plane waves.

There are many studies that deal with the attenuation performance of a dissipative silencer. Cummings [1976] studied the sound attenuation performance of acoustically lined flow ducts and of the parallel baffle type dissipative silencers having an arbitrary number of central splitters. Cummings and Sormaz [1993] sought an eigensoluton that satisfied the governing differential equation. However, the end effects are not included in their study. Cummings and Chang [1988] studied the transmission loss across a finite length dissipative flow duct silencer with internal mean flow in the absorbent by the mode matching technique followed by experimental validation. Peat and Rathi [1995] used the finite element method to study the sound field in a dissipative flow duct silencer and Glav [2000] derived a transfer matrix to study the characteristics of a dissipative silencer of arbitrary cross-section without mean flow. A closed-form analytical solution for the transmission loss of a dissipative silencer with a circular cross-section is derived using the low frequency approximation by Kirby [2001]. This low frequency approximation is suitable for designing relatively small circular dissipative silencers as a fast and accurate tool provided that the investigation is not extended to the middle to high frequencies. Kirby [2003] studied the transmission loss of an arbitrary cross-section duct with porous material theoretically and experimentally. Selamet *et al.* [2004, 2005] studied analytically the sound attenuation performance of perforated dissipative silencers with and without inlet/outlet extension by applying the pressure and velocity matching technique.

However, the flow inside a ventilation ductwork is in general turbulent and is of low Mach number. From the theory of Lighthill [1952] and the work of Curle [1955], flow turbulence is expected to generate noise even in the presence of acoustically absorptive materials. The self-noise from a dissipative silencer is also a typical problem of aerodynamic sound generation.

Ffowcs Williams [1972] showed that noise could be generated by the turbulence over a sound absorbent lining, implying that the dissipative silencer is also a source of noise. The self-noise generation over perforated duct liners was also studied by Tsui and Flandro [1977] and Nelson [1982]. They provided further theoretical support to the self-noise generation. Quinn and Howe [1984] investigated the production and absorption of acoustic energy when a sound wave impinges on the edges of the acoustic lossless liner theoretically. Self-noise generation from a ducted fan was also studied by Glegg *et al.* [1998]. However, a detailed study on this self-noise generation is rarely found in the existing literature.

Researchers usually deal with the interaction between turbulence and rigid boundaries theoretically, for instance, Ffowcs Williams and Hawkings [1969], Ffowcs Williams and Hall [1970] and Howe [1975]. There are also studies using numerical methods to investigate the sound generation. The sound generated by a circular cylinder at low Mach number flow was investigated by the method of direct numerical simulation (DNS) [Inoue and Hatakeyama, 2002]. Casalino *et al.* [2003] investigated the noise generated by an airfoil in the wake of a rod by the method of computational fluid dynamics (CFD). Many experimental works have been carried out as well [For instance, Nelson and Morfey, 1981; Hourigan *et al.*, 1990; Neise *et al.*, 1993; Quinlan and Bent, 1998; Fehse and Neise, 1999]. The generation of edge-tones and Aeolian tones were studied by Curle [1953] and Phillips [1956] respectively. Bies *et al.* [1997] analyzed the aerodynamic noise generated by a stationary body in a turbulent air stream and Nash *et al.* [1999] studied the tonal noise generation mechanism of the flow over an aerofoil experimentally and compared the results with the theoretical prediction.

In the author's opinion, the research topic on aerodynamic sound generation is complicated as turbulence is hard to model so that many problems cannot be easily studied by using analytical methods. However, the situation becomes much simpler when the low Mach number turbulence is treated as discrete vortices because the dynamics of the latter can be obtained using the potential theory [Crighton, 1972; Dunne and Howe, 1997; Howe, 2003; Tang and Ffowcs Williams, 1998]. The application of vortex sound theory [Powell, 1964] or matched asymptotic expansion method [Crighton, 1972, Obermeier, 1979a, 1979b, and 1980] then enables the estimation of the noise radiation. The far-field inner potential and the near-field outer potential are matched in the first leading order term at large distance which is $1/r$, where r is the radial distance from the origin. Though the vortices are a drastic simplification of a real turbulent flow, they can still provide useful insights to the topics, at least to the leading order of magnitude.

For the application of the vortex sound theory, the characteristics of aerodynamic noise scattered and radiated by a semi-infinite plate were also conducted [Crighton, 1972; Crighton and Leppington, 1970, 1974]. Crighton [1972] estimated the noise radiation from a line vortex around the edge of a rigid half plane by the method of matched asymptotic expansion and Obermeier [1979b, 1980] used similar method to investigate the sound generated by the interaction of vortices with a circular cylinder in the presence of a mean flow. Cannell and Ffowcs Williams [1972] investigated the noise generation when a vortex pair exhausts from a two-dimensional ductwork while Möhring [1978] derived an alternative form of sound generation using the Green's function representation. The aerodynamic noise generation from a vortex ring in the presence a sharp wedge was studied by Chang and Chen [1994]. The vortex interaction with a wall barrier, circular cylinder, wall mounted cylinder and thin-wall aperture and this sound radiation were discussed using the Lighthill acoustic analogy in Abou-Hussein *et al.* [2002]. Tang and Ffowcs Williams [1998] studied the noise radiation when an inviscid vortex approaches a circular cylinder with surface suction. The noise production by an inviscid vortex-nozzle interaction was investigated together with the use of the Lighthill acoustic analogy and the vortex-blob method by Hulshoff *et al*. [2001]. The recent study of Tang [2001] investigated the dynamics of an inviscid vortex upon the influence of the porous material and suggested that the change in the vortex speed gives rise to fluctuating force acting on the porous material and enhances self-noise radiation.

There are also studies investigating vortex-surface noise experimentally. Bearman [1967] measured the velocity of the vortices and the longitudinal spacing between vortices in the wake with splitter plates and base bleed. Kambe *et al.* [1985] studied the sound from a vortex ring passing near the edge of a half-plane while Minota and Kambe [1987] studied the sound generation when a vortex ring interacts with a circular cylinder. Minota *et al.* [1988] also investigated the sound radiation from the interaction of a vortex ring passing near a wedge-like plate.

As discussed earlier, the use of porous material in a dissipative silencer is widely adopted. However, the self-noise generation under the influence of the porous material cannot be neglected as it lowers the overall performance of the silencer and if it is within the worst frequency range of the silencer, noise amplification within some frequency bands may be possible. Despite this problem, the conventional dissipative silencer is used extensively because of cost-effectiveness, broadband performance and stability. Therefore, it is worthable to study the mechanisms of self-noise generation in the dissipative silencer. In addition, a detailed study of the self-noise generation of the porous material is rarely found in the existing literature.

In the present study, two-dimensional self-noise generation upon the influence of the porous material in the low Mach number and high Reynolds number flow condition is investigated. The investigation is based on theoretical modelling. The turbulence is simplified as discrete vortices, and the vortex-surface interaction is investigated. In the present study, the theoretical model derived by Tang [2001] is adopted. It excludes the effects of mean flow. The presence of a mean flow will probably create a stronger sound field. In order to simplify the present theoretical study, the mean flow effect is again ignored. The present study shows how the porous material affects the dynamics of the vortex motion and the possibility of noise amplification. It is hoped that the present study can enhance the understanding of the self-noise generation due to porous materials and reveal the basic mechanisms of self-noise generation in a dissipative silencer.

1.2 Theory of Aerodynamic Sound

The present study is focused on the aerodynamic sound generation, and an introduction to its theory will be outlined in this section. The sound generated by turbulence in an unbounded medium is called aerodynamic sound and is a very small component of the whole fluid motion. Lighthill [1952] transformed the Navier-Stokes and continuity equations into an exact inhomogeneous wave equation whose source terms are important only within the turbulent region. Lighthill's equation states that

$$\left(\frac{1}{c_o^2}\frac{\partial^2}{\partial t^2} - \nabla^2\right)\left[c_o^2\left(\rho - \rho_o\right)\right] = \frac{\partial^2 T_{ij}}{\partial x_i \partial x_j}\,, \tag{1.1}$$

where T_{ij}, t, ρ_o, $\rho - \rho_o$, c_o and ∇^2 are the Lighthill stress tensor, time, mean fluid density, perturbation density, sound speed and Laplacian operator respectively. $\mathbf{x} = (x_1, x_2, x_3)$ is the position, i and j are the suffices over 1, 2 and 3. The Lighthill stress tensor is represented by

$$T_{ij} = \rho v_i v_j + \left[\left(p - p_o\right) - c_o^2\left(\rho - \rho_o\right)\right]\delta_{ij} - \sigma_{ij}\,, \tag{1.2}$$

where p_o and $p - p_o$ are the mean and perturbation pressure, δ_{ij} is the Kronecker delta (= 1 for $i = j$, and 0 for $i \neq j$), σ_{ij} is the viscous stress tensor and $\rho v_i v_j$ is the Reynolds stress. The terms in the Lighthill stress tensor account for the generation of sound, govern the acoustic self-modulation caused by acoustic nonlinearity, the convection of sound waves by the turbulent velocity, refraction caused by sound speed variations, and attenuation due to thermal and viscous actions. When the mean fluid density and sound speed are uniform, $\rho v_i v_j$ and $p - p_o$ can be approximated as $\rho_o v_i v_j$ and $c_o^2(\rho - \rho_o)$ respectively. The Lighthill stress tensor in Equation (1.2) reduces to $T_{ij} = \rho_o v_i v_j$ when the viscous stresses are neglected.

To calculate the sound generated by turbulence in an unbounded medium, we need to solve Equation (1.1) for the radiation into a stationary, ideal fluid produced by a distribution of quadrupole sources whose strength per unit volume is the Lighthill stress tensor T_{ij}. The solution of Equation (1.1) with outgoing wave behaviour is

$$p(\mathbf{x},t) \approx \frac{x_i x_j}{4\pi c_o^2 |\mathbf{x}|^3} \frac{\partial^2}{\partial t^2} \int T_{ij}\left(\mathbf{y}, t - \frac{|\mathbf{x}-\mathbf{y}|}{c_o}\right) d^3\mathbf{y} \,, \tag{1.3}$$

where $\mathbf{y}$ lies within the source region and $|\mathbf{x}| >> |\mathbf{y}|$. However, turbulence is frequently generated in the boundary layers and the wakes of flow past solid boundaries. The unsteady surface forces on these boundaries have significant contribution to the production of sound. It is necessary to generalize the solution of Equation (1.3) to account for the presence of solid boundaries in the flow. Curle [1955] extended the theory of Lighthill [1952] to include the influence of solid boundaries:

$$p(\mathbf{x},t) = \frac{x_i x_j}{4\pi c_o^2 |\mathbf{x}|^3} \frac{\partial^2}{\partial t^2} \int_V T_{ij}\left(\mathbf{y}, t - \frac{|\mathbf{x}-\mathbf{y}|}{c_o}\right) d^3\mathbf{y}$$

$$+ \frac{x_i}{4\pi c_o |\mathbf{x}|^2} \frac{\partial}{\partial t} \oint_S \left(\rho v_i v_j + p_{ij}^{'}\right)\left(\mathbf{y}, t - \frac{|\mathbf{x}-\mathbf{y}|}{c_o}\right) dS_j(\mathbf{y}), \tag{1.4}$$

$$+ \frac{1}{4\pi|\mathbf{x}|} \oint_s \left(\rho v_j\right)\left(\mathbf{y}, t - \frac{|\mathbf{x}-\mathbf{y}|}{c_o}\right) dS_j(\mathbf{y})$$

where S is the solid boundary, V is the occupied volume and $p_{ij}^{'} = (p - p_o)\delta_{ij} - \sigma_{ij}$. The first term on right hand side of Equation (1.4) represents the quadrupole source term distributed over V, while the second and the third terms represent the dipole and monopole source distributed over S. The dipole describes the production of sound by the unsteady surface force that the body exerts on the exterior fluid, whereas the monopole is the sound produced by volume pulsations of the boundary.

In the present study, the turbulence is treated as discrete vortices, and the component div($\rho_o \varpi \wedge \mathbf{v}$) of the Lighthill quadrupole is the principal source of sound at low Mach number (ϖ is the vorticity). Lighthill's equation [Equation (1.1)] can be recast into a form to emphasize the prominent role of vorticity in the production of sound by taking total enthalpy $B = \int \frac{dp}{\rho} + \frac{1}{2}\mathbf{v}^2$ as the independent acoustic variable [Howe, 2003]. The production of sound is governed by the vortex sound equation

$$\left(\frac{1}{c_o^2}\frac{\partial^2}{\partial t^2} - \nabla^2\right) B = \operatorname{div}(\varpi \wedge \mathbf{v}). \tag{1.5}$$

If the mean flow is at rest in the far-field, the acoustic pressure is given by the linearized approximation

$$p(\mathbf{x},t) \approx \rho_o B(\mathbf{x},t). \tag{1.6}$$

In an irrotational flow, Crocco's equation states that $\frac{\partial \mathbf{v}}{\partial t} = -\nabla B$. Therefore

$$B(\mathbf{x},t) = -\frac{\partial \phi(\mathbf{x},t)}{\partial t}, \tag{1.7}$$

in region where $\varpi = 0$ and $\phi(\mathbf{x}, t)$ is the velocity potential that determines the whole motion in the irrotational regions of the fluid. From Equations (1.6) and (1.7), the far-field acoustic pressure is

$$p(\mathbf{x},t) = -\rho_o \frac{\partial \phi(\mathbf{x},t)}{\partial t}. \tag{1.8}$$

1.3 Properties of Porous Material

In the present study, the vortex sound generation under the influence of the porous material is investigated. The characteristics of the porous material have crucial effects on the sound production. There are three approaches to characterize the properties of a porous material: (i) the phenomenological formulae of Morse and Ingard [1968], (ii) empirical curve fitting methods such as that of Delany and Bazley [1970], and (iii) rigid-frame models for more complicated pore microstructures such as parallel tubes or fibres by Attenborough [1982]. The first approach is adopted in the present investigation since the ineffective range for design purposes in silencers is towards the lower frequency region, and the model of Morse and Ingard [1968], based on a real, quasi-steady, effective flow resistivity of the porous material is adequate at lower frequency.

Basically, there are two types of porous materials. The first one is called locally reacting and the other one is called non-locally reacting [Ingard, 1994]. The former states that the surface impedance of a locally reacting boundary is independent of the angle of an oblique incident wave and the latter states that the fluid velocity within the porous material no longer is forced to be perpendicular to the boundary axis. We will focus on the locally reacting one as the porous material in a dissipative silencer usually consists of fibreglass or rockwool which is locally reacting, and the porous material is densely packed.

The flow inside the porous material is governed by the effective fluid density ρ_e and the flow resistance R_f [Morse and Ingard, 1968]. The former describes the inertial properties of the fluid in the pores of the porous material, and the latter the frictional retardation to flow through the pores. For the flow resistance, R_f is adopted by Morse and Ingard [1968] for the description of the viscous effect inside the porous material. The flow inside the porous material is very slow and thus the Reynolds number will not be so meaningful in this case. For a real porous material, ρ_e is between 1.5 and 5. However, ρ_e can be large when the porous material is replaced by a heavy liquid. In the study of the transmission loss across dissipative silencers, the data in Cummings and Sormaz [1993], Peat and Rathi [1995] and Kirby [2001] give $\rho_e \approx 3$. Unless the fluid is perfectly inviscid, one should note that owing to the very tiny fluid passages inside the porous material, the effect of viscosity on the fluid motion inside this material cannot be neglected though the external flow outside it can be satisfactorily represented by the inviscid model [Tang, 2001]. Also, the introduction of the porous material results in finite impedance, which may lower the ability of this boundary to support fluid pressure and produce a pressure-releasing effect. The flow equation within the porous material is, according to Morse and Ingard [1968],

$$\rho_e \frac{\partial \mathbf{u_p}}{\partial t} + R_f \mathbf{u_p} + \nabla p_p = 0\,, \tag{1.9}$$

where ∇ is the differential operator, and $\mathbf{u_p}$ and p_p are the fluid velocity and fluid pressure inside the porous material respectively. Porosity is included implicitly in both ρ_e and R_f. One can notice from the flow equation depicted in Morse and Ingard [1968] as well as in Tang [2001] that ρ_e and R_f produce pressure-releasing and pressure-supporting effects respectively. In addition, a streamfunction ψ_p exists for the flow inside the porous material such that [Bear, 1972]:

$$\nabla^2 \psi_p = 0\,. \tag{1.10}$$

1.4 Thesis Structure

To investigate the self-noise generation mechanisms, the behaviour of two vortices in the proximity of a rigid circular cylinder is investigated in Chapter 2 first. It provides an understanding on how the vortices interacting with a solid body as a reference study for further investigation into the influence of the porous material. Then, Chapter 3 describes the sound generation when the vortices interact with a porous half cylinder mounted on an otherwise rigid plane, and the configuration in this chapter is similar to the situation near the wall boundaries of a dissipative silencer. The vortex sound in the presence of a porous wedge is studied in Chapter 4. It is the case at some flow junctions in ductwork which involve edges or are wedge-like. Chapter 5 analyzes the noise generated when the vortex is under the influence of a finite length porous material on an otherwise rigid plane, and this flow configuration is similar to the situation when the vortex is located near the boundary of a lined duct. Chapter 6 extends the study of Chapter 5 to analyze the self-noise by a vortex in a lined duct and is the last chapter for theoretical study of self-noise generation.

Chapter 2: Sound Generated by a Pair of Vortices in the Proximity of a Rigid Circular Cylinder

2.1 Introduction

There is a general belief that turbulence is made up of vertical eddies or vortices. These vortices will interact with themselves as well as with any solid body embedded in the flow. In this chapter, the far-field sound radiation resulted from the motions of a pair of vortices engaging a rigid circular cylinder without the presence of a mean flow is investigated. The effects of vortex circulations, initial position and separation distance are discussed. In addition, it is valuable to study the influence of a rigid boundary [Howe, 2003] and the wavelength of coherent structures [Becker and Massaro, 1968] on the aerodynamic sound generation as a reference for further investigation into the influence of the porous material.

2.2 Theoretical Model

The formula of Curle [1955] suggests that the sound generated by the interaction between vortices and a submerged solid body can be estimated once the fluctuating forces acting on the latter are known. The potential theory enables the estimation of the flight paths of the vortices and thus these forces. The analysis commences by estimating the vortex paths.

Figure 2.1 shows the schematics of the present numerical investigation. Two rectilinear vortices are situated at $z_1 = (x_1, y_1)$ with vortex strength Γ_1 and $z_2 = (x_2, y_2)$ with vortex strength Γ_2 in the proximity of a rigid circular cylinder centred at the origin in the absence of a mean flow. The vorticity centroid of the two vortices z_c is defined as $(\Gamma_1 z_1 + \Gamma_2 z_2)/\Gamma$, where $\Gamma = \Gamma_1 + \Gamma_2$ is the total vortex strength. In the foregoing analysis, the vortex circulations are normalized by Γ. All length and time scales are normalized by a and a^2/Γ respectively where a is the radius of the cylinder. From the potential theory, the normalized equation of the complex potential is

$$W = \sum_{j=1}^{2}\left[-\frac{i\Gamma_j}{2\pi}\ln\left(z - z_j\right) + \frac{i\Gamma_j}{2\pi}\ln\left(z - \frac{1}{\bar{z}_j}\right) - \frac{i\Gamma_j}{2\pi}\ln z\right], \tag{2.1}$$

where $\bar{z}_j$ denotes the complex conjugate of z_j and $i = \sqrt{-1}$.

The velocity of the jth vortex (u_{zj} and v_{zj}) can be obtained from the derivative of W with respect to z at the position z_j after subtracting the "self-potential", $-i\Gamma_j \ln(z - z_j)/2\pi$, :

$$u_{zj} - iv_{zj} = \left(\dot{r}_j - ir_j\dot{\theta}_j\right)e^{-i\theta_j} = \frac{d}{dz}\left(W + \frac{i\Gamma_j}{2\pi}\ln(z - z_j)\right)\Bigg|_{z=z_j}, \tag{2.2}$$

where (r_j, θ_j) is the polar coordinates of the jth vortex and $\cdot$ denotes differentiation with respect to time.

The radial and angular velocities of the jth vortex ($\dot{r}_j$ and $\dot{\theta}_j$) can be analytically determined:

$$\dot{r}_j = \frac{\Gamma_k}{2\pi} r_k \sin(\theta_j - \theta_k)\left[-\frac{1}{r_j^2 + r_k^2 - 2r_j r_k \cos(\theta_j - \theta_k)} + \frac{1}{r_j^2 r_k^2 - 2r_j r_k \cos(\theta_j - \theta_k) + 1}\right],$$

$$\begin{aligned} r_j \dot{\theta}_j = -\frac{1}{2\pi}\Bigg[& \frac{\Gamma_j r_j}{r_j^2 - 1} - \frac{\Gamma_j}{r_j} - \frac{\Gamma_k}{r_j} - \Gamma_k \frac{r_j - r_k \cos(\theta_j - \theta_k)}{r_j^2 + r_k^2 - 2r_j r_k \cos(\theta_j - \theta_k)} \\ & + \Gamma_k \frac{r_j r_k^2 - r_k \cos(\theta_j - \theta_k)}{r_j^2 r_k^2 - 2r_j r_k \cos(\theta_j - \theta_k) + 1}\Bigg] \end{aligned}, \qquad (2.3)$$

where $j \neq k = 1, 2$. Thus, the paths of the vortices can be obtained by the standard fourth order Runge-Kutta Method. The velocity of the vorticity centroid (u_{zc} and v_{zc}) is

$$\begin{aligned} u_{zc} - iv_{zc} &= \frac{1}{2\pi}\left[\frac{\Gamma_1}{\Gamma}(u_{z1} - iv_{z1}) + \frac{\Gamma_2}{\Gamma}(u_{z2} - iv_{z2})\right] \\ &= \frac{1}{2\pi}\left[\frac{1}{\Gamma}\frac{i\Gamma_1^2 \bar{z}_1}{|z_1|^2 - 1} - \frac{i\Gamma_1}{z_1} + \frac{\Gamma_1}{\Gamma}\frac{i\Gamma_2 \bar{z}_2}{z_1\bar{z}_2 - 1} + \frac{\Gamma_2}{\Gamma}\frac{i\Gamma_1 \bar{z}_1}{z_2\bar{z}_1 - 1} - \frac{i\Gamma_2}{z_2} + \frac{1}{\Gamma}\frac{i\Gamma_2^2 \bar{z}_2}{|z_2|^2 - 1}\right] \end{aligned}. \qquad (2.4)$$

The flight paths of the vortices can be explicitly determined when the separation distance between the vortices is small. This happens when the vortices are either really close to each other or are reasonably far away from the cylinder surface. This is the case where a solid body interacts with an initial shear layer on the low speed side [Ko and Tang, 1990]. Under this circumstance and let $z_2 = z_1 - \varepsilon$, where $|\varepsilon| \to 0$, Equation (2.4) becomes

$$u_{zc} - iv_{zc} = \frac{1}{2\pi}\left[-\frac{i\Gamma}{z_1} + \frac{i\Gamma\bar{z}_1}{|z_1|^2 - 1} - \frac{i\Gamma_2}{z_1^2}\varepsilon + \frac{i\Gamma_2(\bar{z}_1^2\varepsilon + \bar{\varepsilon})}{(|z_1|^2 - 1)^2} - \frac{i\Gamma_2\varepsilon^2}{z_1^3} - \frac{i\Gamma_2^2}{\Gamma}\frac{\bar{z}_1|\varepsilon|^2}{(|z_1|^2 - 1)^2} \right. \\ \left. + \frac{i\Gamma_2^2}{\Gamma}\frac{\bar{z}_1(z_1\bar{\varepsilon} + \bar{z}_1\varepsilon)^2}{(|z_1|^2 - 1)^3} + \frac{i\Gamma_2\Gamma_1}{\Gamma}\frac{(\bar{z}_1^3\varepsilon^2 + z_1\bar{\varepsilon}^2)}{(|z_1|^2 - 1)^3} + O(|\varepsilon|^3) \right]. \tag{2.5}$$

Assuming the two vortices can be viewed as a single vortex of strength Γ located at the centroid z_c, this single vortex will then perform a circular motion round the cylinder with a velocity given by

$$u_{zc} - iv_{zc} = \frac{1}{2\pi}\left[-\frac{i\Gamma}{z_c} + \frac{i\Gamma\bar{z}_c}{z_c\bar{z}_c - 1} \right]$$

$$\approx \frac{1}{2\pi}\left[-\frac{i\Gamma}{z_1} + \frac{i\Gamma\bar{z}_1}{|z_1|^2 - 1} - \frac{i\Gamma_2}{z_1^2}\varepsilon + \frac{i\Gamma_2(\bar{\varepsilon} + \bar{z}_1^2\varepsilon)}{(|z_1|^2 - 1)^2} - \frac{i\Gamma_2^2}{\Gamma z_1^3}\varepsilon^2 - \frac{i\Gamma_2^2\bar{z}_1|\varepsilon|^2}{\Gamma(|z_1|^2 - 1)^2} \right. \\ \left. + \frac{i\bar{z}_1\Gamma_2^2(z_1\bar{\varepsilon} + \bar{z}_1\varepsilon)^2}{\Gamma(|z_1|^2 - 1)^3} + O(|\varepsilon|^3) \right]. \tag{2.6}$$

One can observe immediately that Equations (2.5) and (2.6) are equivalent up to $O(|\varepsilon|^2)$. The velocity of *j*th vortex relative to the centroid is then

$$u_{zj} - iv_{zj} - (u_{zc} - iv_{zc}) = \frac{1}{2\pi}\left[-\frac{i\Gamma_k}{\varepsilon} + \frac{i\Gamma_k\varepsilon}{z_j^2} - \frac{i\Gamma_k\bar{z}_j^2\varepsilon}{(|z_j|^2 - 1)^2} + O(|\varepsilon|^2) \right]. \tag{2.7}$$

For small $|\varepsilon|$, the only important velocity components are $-i\Gamma_2/2\pi\varepsilon$ and $i\Gamma_1/2\pi\varepsilon$, which are the velocities of the isolated rectilinear vortices. The motion therefore consists of a large circular movement of the centroid around the cylinder together with more rapid circular movements of the vortices about the centroid. It will be demonstrated later that the above approximated paths can predict reasonably well the forces and sound generated by closely packed vortices. When a single vortex moves around the rigid circular cylinder, the vortex will move in circular motion. Equation (2.6) describes the circular motion of a single vortex about a rigid circular cylinder, and Equation (2.5) describes the motion of the vorticity centroid of the two vortices about the rigid circular cylinder which is equivalent up to $O(|\varepsilon^2|)$, so one can conclude that two vorticity centroid of the two vortices describes circular motion when ε is small.

The force per unit length, F, acting on the cylinder is obtained by calculating the force needed to keep the image vortices moving along the assumed paths as in Tang and Ffowcs Williams [1998]:

$$F = \sum (u_j \mathbf{i} + v_j \mathbf{j}) \times \Gamma_j \mathbf{k} , \qquad (2.8)$$

under the conservation of vortex impulse, where **i**, **j** and **k** are the unit vectors in the longitudinal, transverse and spanwise directions respectively. In the present situation, the position of the image vortex with strength $-\Gamma_j$ is $e^{i\theta_j} \big/ r_j$, and its velocity is $(-\dot{r}_j + r_j \dot{\theta}_j) e^{i\theta_j} \big/ r_j^2$. The force acting on unit length of the cylinder, F, in the present study is normalized by $\rho_o \Gamma^2/a$ and $F = F_x\mathbf{i} + F_y\mathbf{j}$ where

$$F_x = -\sum_{j=1}^{2} \Gamma_j \left[\dot{r}_j \left(1 + \frac{1}{r_j^2} \right) \sin\theta_j + r_j \dot{\theta}_j \cos\theta_j \left(1 - \frac{1}{r_j^2} \right) \right],$$

$$F_y = \sum_{j=1}^{2} \Gamma_j \left[\dot{r}_j \left(1 + \frac{1}{r_j^2} \right) \cos\theta_j - r_j \dot{\theta}_j \sin\theta_j \left(1 - \frac{1}{r_j^2} \right) \right]. \qquad (2.9)$$

where subscripts x and y denote the longitudinal and transverse directions respectively.

The far-field sound radiation by the influence of solid boundaries can be estimated from Equation (1.4). In the present and subsequent chapters, the quadrupole source term in Equation (1.4) is ignored as the contribution from it is not important in the low Mach number and high Reynolds number flows in the presence of solid surfaces. The contribution from the monopole source term is equal to zero in the case of a rigid circular cylinder. In the two-dimensional sense, the surface integral becomes a line integral in the spanwise direction, and this line integral can be transformed into a time integral as in Ffowcs Williams and Hawkings [1968]. The time integral can then be solved numerically [Tang and Ko, 1997]. The acoustical contribution from each element of a line source arrives at the far-field location at different time. Integration over the length of the line source is equivalent to integration over time [Ffowcs Williams, 1968]. The far-field acoustic pressure is:

$$p = -\frac{1}{2\pi\sqrt{2\mathrm{R}c_o}}\left[\int_{-\infty}^{t_o-\mathrm{R}/c_o}\frac{\partial}{\partial\tau}\left(F_x\cos\theta + F_y\sin\theta\right)\frac{d\tau}{\sqrt{t_o-\tau-\mathrm{R}/c_o}}\right], \tag{2.10}$$

where R, c_o and t_o are the far-field distance, speed of sound in the undisturbed medium and far-field observer time respectively. The far-field sound pressure is normalized by $\rho_o\Gamma^2/a^2$.

2.3 Vortex Paths, Forces and Sound

The present study is focused on the fluctuating force created and the sound radiated from the unsteady motions of two vortices in the proximity of a rigid circular cylinder. Owing to the symmetry of the vortices about the x and y axes in the present investigation [Figure 2.1], the initial positions of the vortices are chosen to be on the x-axis. Since there is only phase difference between the drag and the lift forces created on the cylinder, only results related to the drag force, F_x, and the drag dipole strength in the x-direction, P_x, will be presented. The drag dipole P_x is defined as

$$P_x = -\int_{-\infty}^{t_o - R/c_o} \frac{\partial}{\partial \tau} F_x \frac{d\tau}{\sqrt{t_o - \tau - c_o}} \tag{2.11}$$

Figure 2.2 shows the paths of the vortices located at z_{1i} = (–2.1, 0) and z_{2i} = (–1.9, 0) with $\Gamma_1 = \Gamma_2 = 0.5$. Thus, $\varepsilon = 0.2$. As suggested by Equations (2.5) to (2.7), one can observe from Figure 2.2 that the vortices are in circular movement relative to the vorticity centroid and so is the vorticity centroid relative to the centre of the circular cylinder. The period of the vorticity centroid of the vortices around the cylinder is approximately equal to $4\pi^2 r_c^2 \left(r_c^2 - 1\right)/\Gamma$, which is the period of the circular motion of a single vortex with strength Γ located at a distance r_c from the cylinder centre [Howe, 2003]. Those of the vortices about the vorticity centroid are roughly $4\pi^2\varepsilon^2/\Gamma$, which is consistent with the prediction by Equation (2.7). It can also be shown that $r_1^2 + r_2^2$ is fairly time-invariant.

The resultant force acting on the cylinder consists of components resulted from the interaction between mean vortex motion (z_c) and the cylinder, and the mutual induction between the vortices. The former, F_{xc}, results in a low frequency fluctuation, while the latter, F_{xm}, produces a high frequency component [Figure 2.3(a)]. Small magnitude high frequency fluctuations are found in the low frequency force, which are the results of the small effects from the mutually induced vortex motions. The magnitude of the low frequency force compares well with the single vortex prediction, which is $\Gamma^2 \big/ 2\pi r_c^3$ [Howe, 2003]. While the period of F_{xc} equals that for the vorticity centroid to cover one revolution around the cylinder centre, that of F_{xm} is half that of the mutually induced nominal vortex circular motion, and the corresponding lift forces are just 180^{o} out-of-phase with those presented.

Obviously, both the drag and lift dipole strength time fluctuations are composed of low frequency and high frequency components as in the case of the forces [Figure 2.3(b)]. The amplitude of the P_{xc} compared well with that resulted from a single vortex with circulation Γ rotating around a circular cylinder, which is $\Gamma^{2.5} \Big/ \left(4\sqrt{2}\pi r_c^4 \sqrt{r_c^2 - 1}\right)$ [Howe, 2003]. The characteristics of the time fluctuations of these dipole strengths resemble very much that of the forces. However, the magnitude of the high frequency component in the dipole strength is much higher than that of the low frequency one, suggesting that the mutually induced vortex motions are more dominant in the sound radiation process. One should note that the high frequency component in a sound is more significant than the low frequency one as it contributes much more to the overall sound power radiation.

When the vortices are located closer to the cylinder surface with ε fixed, the motions of the vortices relative to z_c are no longer circular due to the effect of the rigid cylinder. Figure 2.4(a) is an example of the vortex motion with $z_{1\mathrm{i}}$ = (–1.3,0) and $z_{2\mathrm{i}}$ = (–1.1,0). Under this condition, the vorticity centroid is still describing a circular motion around the cylinder. The motions of the vortices relative to it look similar to those in the vortex leapfrogging [Tang and Ko, 2000]. The orbits of the vortices relative to the centroid are oval-like [Figure 2.4(b)]. However, one can observe that the principal axes of these oval orbits are rotating clockwisely. These unsteady motions appear to be very important in affecting the forces on the cylinder and the dipole strengths [Figures 2.5(a) and 2.5(b)]. The effects of increasing ε at a fixed initial vorticity centroid location to the vortex motions are very similar to those shown in Figure 2.4, but one can observe from Figures 2.6(a) and 2.6(b) that the increasing cylinder effect relative to the mutual induction strength between vortices can result in a wrangling vorticity centroid flight path while the oval-like vortex orbits relative to this centroid remain. Certainly, one can expect that there will be a drop in the force and dipole strength magnitudes upon the increase of ε. At large ε, the frequencies of the fluctuations in F_{xc} and F_{xm} (and thus P_{xc} and P_{xm}) are very similar.

The combined effects of variations in z_c and ε on the drag forces are summarized in Figure 2.7. One can note that F_{xc}, which is more related to vorticity centroid motion, reduces in magnitude as z_c increases at a fixed ε. The magnitude of F_{xc} increases as ε increases at a fixed z_c. F_{xm}, which is primarily related to the relative motions of the vortices about z_c, deviates considerably from the prediction using the approximated vortex paths [Equations (2.5) – (2.7)] when ε is large compared with z_c. The under-estimation of the magnitude of F_{xm} increases with ε. One can also find that the magnitude of F_{xc} is always higher than that of the corresponding F_{xm}.

While the variations of the magnitude of P_{xc} with z_c and ε resemble very much those of F_{xc}, those of P_{xm} show complicated dependence on ε [Figure 2.8]. The approximated vortex paths under-estimate the magnitude of P_{xm} at large ε, but give over-estimations at small ε. At small ε, one can observe that the magnitude of

P_{xm} decreases approximately linearly with ε, but this amplitude reaches a minimum at a critical ε for a fixed z_c. For $\varepsilon > 1$, the presence of the rigid circular cylinder affects the motion of the vortices. A substantial rate of change of vortex velocity is observed such that the dipole strength increases. Results shown in Figures 2.7 and 2.8 suggest that a substantial reduction of sound power is possible without a significant change in the drag/lift force by carefully adjusting the vortex spacing (wavelength of coherent structures in a shear layer).

When one of the vortices is considerably stronger than the other, the forces created on the cylinder and sound generated are different from those discussed above. Figures 2.9(a) and 2.9(b) illustrate the vortex paths when $\Gamma_1 = 0.1$, $\Gamma_2 = 0.9$, $z_{1i} = (-2.1,0)$, $z_{2i} = (-1.9,0)$. The path of the stronger vortex is approximately circular around the cylinder with a very small fluctuating amplitude of around 0.02 [Figure 2.9(b)]. The circular motion of the weaker vortex about the vorticity centroid is also observed. The stronger vortex dominates the fluid mechanics and also the aeroacoustics. Low frequency and high frequency components are again observed in the drag force and dipole strength time fluctuations as in the corresponding $\Gamma_1 = \Gamma_2 = 0.5$ case [Figure 2.3]. However, the circular motion of the weaker vortex here results in an amplitude modulation pattern in the high frequency fluctuations [Figure 2.10].

The combined effects of z_c and ε for $\Gamma_1 \neq \Gamma_2$ on F_{xm} are illustrated in Figure 2.11(a). It can be observed that for vortices of comparable strengths, the results are similar to those shown before in Figure 2.7. When one of the vortices is considerably stronger than the other, the magnitude of F_{xm} is not really sensitive to the change in ε unless the latter is really large. The prediction from the approximated vortex paths [Equations (2.5) – (2.7)] appears satisfactory for relatively large ε of even up to more than 1. Similar observations can be found for F_{xc}. Again, the maximum $|F_{xc}|$ remains larger than that of $|F_{xm}|$ for small z_c.

Figure 2.11(b) shows the effects of z_c and ε on P_{xm} for $\Gamma_1 \neq \Gamma_2$. Similar to Figure 2.8, the magnitude of P_{xm} decreases linearly with ε at a fixed z_c when ε is small. The prediction from the approximated vortex paths works well at $\Gamma_1 = 0.99$, $\Gamma_2 = 0.01$, $z_{ci} = (-1.8,0)$. These observations, together with those shown previously in Figures 2.7 and 2.8, tend to suggest that, apart from the fact that the forces and aeroacoustics generation can again be modified by the separation of vortices, breaking vortical flow structures will increase the forces acting on a submerged object and the sound power radiated if the total circulation and the coherence of the broken up structures inside the near flow field are not reduced.

2.4 Summary

The fluctuating force and far-field sound generated by the motions of two vortices in the proximity of a rigid circular cylinder using the potential theory and the acoustic analogy have been investigated. Effects of circulation ratio, initial vortex position and separation distance on the force and sound generated are examined in detail.

Results obtained in the present study demonstrate how the separation between vortical structures in a flow, that is, the wavelength of coherent structures, has affected the flow induced force on submerged bodies and the eventual aeroacoustics. They also suggest that breaking up large scale flow structures into smaller ones enhances the fluid force on submerged bodies and increases the acoustic radiation if the total circulation within the flow and the coherence of the broken up flow structures are not reduced. The results also act as a reference to those in later chapters where the effects of the porous material on the vortex sound are studied.

Chapter 3: Sound Generated by Vortices in the presence of a Porous Half Cylinder Mounted on a Rigid Plane

3.1 Introduction

An introduction on vortex sound radiation due to the interaction of two vortices with a rigid circular cylinder has been given in Chapter 2. The force acting on the cylinder is also discussed. In this chapter, the investigation proceeds to study the influence of the porous material. The unsteady motions of two vortices in the proximity of a porous half cylinder on an otherwise rigid horizontal plane are investigated, and the present configuration is similar to the situation near to the boundary of a dissipative silencer. The effects of vortex circulations, initial vortex height and separation distance are discussed. In addition, the effects of effective fluid density and flow resistance of the porous material are also studied. Since the normal velocity at the boundaries of the porous material does not vanish, the calculation becomes complicated. In this chapter, the complex potential and the velocity of the inviscid vortex are evaluated through the use of conformal mapping as in Tang [2001], while the far-field potential is derived with the use of the matched asymptotic expansion method as in Crighton [1972] and Obermeier [1979a, 1980]. The far-field acoustic pressure is evaluated using Equation (1.8).

3.2 Theoretical Development

Two rectilinear vortices with circulations Γ_1 and Γ_2 initially located at the complex locations z_{1i} and z_{2i} respectively interact with a half cylinder composed of a porous material as shown in Figure 3.1. The present configuration is intended to represent one flow boundary inside a dissipative silencer. The horizontal separation between the vortices is denoted by ε. The properties of the porous material are characterized by the effective fluid density, ρ_e, and the flow resistance, R_f, inside its lattice [Morse and Ingard, 1968] as mentioned in Chapter 1.

With the help of the conformal mapping [Churchill and Brown, 1990], the original z-plane ($z = x + iy$) is transformed into the w-plane ($w = \xi + i\zeta$) as shown in Figure 3.2, and the mapping function is

$$z = f(w) = -\frac{i+w}{i-w} \Rightarrow w = f^{-1}(z) = i\frac{z+1}{z-1}. \tag{3.1}$$

It has been shown by Tang [2001] that the surface flow impedance is unaltered upon any conformal transformation. In the present study, all the length scales are normalized by the cylinder radius a, and the strengths of the vortices are normalized by the total vortex strength Γ (= $\Gamma_1 + \Gamma_2$). Here, time is normalized by a^2/Γ. V_{wj} and R_f are normalized by Γ/a and $\rho_o\Gamma/a^2$ respectively. The streamfunction, ψ_{wj}, and the velocity, V_{wj}, of the jth vortex in the w-plane can then be obtained by matching the fluid pressure and normal fluid velocity along the impedance boundary [Tang, 2001]:

$$\psi_{wj} = \frac{\Gamma_j}{4\pi}\int_{-\infty}^{\infty}\frac{1}{|k|}\left(e^{-|k|\zeta_j} + g_j e^{|k|\zeta_j}\right)\frac{e^{-|k|\zeta}}{g_j}e^{ik(\xi_j-\xi)}dk \tag{3.2}$$

where

$$g_j(k) = \frac{R_f + ikV_{wj}(1+\eta)}{-R_f + ikV_{wj}(1-\eta)}, \tag{3.3}$$

and η is the ratio of effective fluid density to the fluid density in the medium (ρ_e/ρ_o) such that η is always greater than 1. Equation (3.2) is derived from matching the flow potential in the fluid region in a channel bounded by the porous region. Details of the derivation of Equations (3.2) and (3.3) can be found in Tang [2001]. The corresponding vortex velocity in the w-plane, V_{wj}, is evaluated by differentiating Equation (3.2) with respect to ζ:

$$V_{wj} = \frac{\Gamma_j}{4\pi}\int_{-\infty}^{\infty} \frac{-e^{-2|k|\zeta_j}}{g_j} e^{ik(\xi_j-\xi)} dk \,. \tag{3.4}$$

It is parallel to the ξ-axis and is a sole function of ζ_j.

The overall stream function, ψ_w, in the presence of other vortices is therefore

$$\psi_w = \sum_{j=1}^{4} \frac{\Gamma_j}{4\pi}\int_{-\infty}^{\infty} \frac{1}{|k|}\left(e^{-|k|\zeta_j} + g_j e^{|k|\zeta_j}\right)\frac{e^{-|k|\zeta}}{g_j} e^{ik(\xi_j-\xi)} dk \tag{3.5}$$

and the velocity of the jth vortex, u_{wj} and v_{wj}, in the w-plane are

$$u_{wj} = V_{wj} + \sum_{k=1\neq j}^{4} \left.\frac{\partial \psi_{wk}}{\partial \zeta}\right|_{\xi=\xi_j,\zeta=\zeta_j}, v_{wj} = -\sum_{k=1\neq j}^{4} \left.\frac{\partial \psi_{wk}}{\partial \xi}\right|_{\xi=\xi_j,\zeta=\zeta_j} . \tag{3.6}$$

Also, $\Gamma_3 = -\Gamma_1$, $u_{w3} = u_{w1}$, $v_{w3} = -v_{w1}$ and $\Gamma_4 = -\Gamma_2$, $u_{w4} = u_{w2}$, $v_{w4} = -v_{w2}$. The paths of the vortices in z-plane are calculated by integrating Equation (3.6) numerically using the standard fourth order Runge-Kutta method together with the Routh's correction [Routh, 1881]:

$$u_{zj} - iv_{zj} = \frac{1}{f'(w)}\left[u_{wj} - iv_{wj} + \frac{i}{4\pi}\frac{f''(w)}{f'(w)}\right], \tag{3.7}$$

where $'$ represents differentiation with respect to w. Routh's correction details the motion of a particle transformed from an original z-plane to a w-plane and the correlation between the particle motions in these planes.

With the Cauchy-Rieman principle, the flow potential in w-plane is

$$\phi_w = \sum_{j=1}^{4} \frac{1}{2\pi}\int_0^\infty \frac{\Gamma_j}{k}\left(e^{-k\zeta_j} + g_j e^{k\zeta_j}\right)\frac{e^{-k\zeta}}{g_j}\sin(k(\xi_j - \xi))dk + C \quad , \tag{3.8}$$

where C is the integration constant that can be evaluated by observing that the flow potential vanishes as $|z| \to \infty$. For the Cauchy-Rieman principle, it states that For a flow is irrotational, the streamlines and potential lines are everywhere mutually perpendicular except at a stagnation point. The incompressible flow potential in the z-plane, ϕ_z, can then be found by substituting w by $f^{-1}(z)$ [Equation (3.1)] in Equation (3.8). The far-field potential, ϕ_{zo}, can then be obtained using the matched asymptotic expansion method [Crighton, 1972; Obermeier, 1979a, 1980], and the far-field sound pressure is evaluated through the use of Equation (1.8).

3.2.1 Acoustically Hard Surface

When the effective fluid density or the flow resistance is so large that the fluid can hardly enter the wall mounted half cylinder, $g_j \to -1$ [Equation (3.3)]. The flow potential in Equation (3.8) becomes

$$\phi_w = -\sum_{j=1}^{4} \frac{1}{2\pi} \int_0^{\infty} \frac{\Gamma_j}{k} \left(e^{-k(\zeta+\zeta_j)} - e^{-k(\zeta-\zeta_j)} \right) \sin(k(\xi_j - \xi)) dk + C \,, \tag{3.9}$$

and by observing the flow potential vanishes as $|z| \to \infty$ ($\xi \to 0$ and $\zeta \to 1$), the constant C [Gradshteyn and Ryzhik, 1980] is

$$C = \sum_{j=1}^{4} \frac{\Gamma_j}{2\pi} \left(\tan^{-1} \frac{\xi_j}{1+\zeta_j} - \tan^{-1} \frac{\xi_j}{1-\zeta_j} \right). \tag{3.10}$$

By substituting $w = f^{-1}(z)$ into Equation (3.9), the flow potential in the z-plane is thus

$$\phi_z = -\sum_{j=1}^{4} \frac{\Gamma_j}{2\pi} \mathrm{Im}\left\{ \ln\left(1 - \frac{1}{z\bar{z}_j} \right) - \ln\left(1 - \frac{z_j}{z} \right) \right\}, \tag{3.11}$$

which is the flow potential of two vortices interacting with a rigid half cylinder mounted on a rigid plane [Howe, 2003]. The far-field inner potential produced by the two vortices is, for large $|z|$,

$$\phi_{zi} \approx -\sum_{j=1}^{2} \frac{\Gamma_j}{\pi r}\left(r_j - \frac{1}{r_j}\right)\sin(\theta_j)\cos\theta . \tag{3.12}$$

The far-field so produced in the frequency domain is the solution of the Helmholthz equation $\nabla^2\phi + k^2\phi = 0$, which is $\phi = \sum_{j=1}^{4} A_j H^{(1)}_{\sigma_j}(kr)e^{i\sigma_j\theta}$, where $H^{(1)}_{\sigma_j}$ is the Hankel function of the first kind of order σ_j and k is the wavenumber. The matched asymptotic expansion method [Obermeier, 1979b] suggests that for low frequency sound radiation, $\sigma_j = 1$ and

$$A_j = -\frac{\Gamma_j \omega}{2c_o}\left[\left(r_j - \frac{1}{r_j}\right)\sin(\theta_j)\right]^t , \tag{3.13}$$

where $k = \omega/c_o$, c_o is the ambient speed of sound and $[\ ]^t$ represents the Fourier transform with respect to time. The far-field inner potential at $z \rightarrow \infty$ must match the far-field outer potential at $z \rightarrow 0$, and σ must set equal to one to match the condition. At a large distance R, one obtains with the property of the Hankel function [Abramowitz and Stegun, 1972] that for positive ω,

$$\phi = -\sum_{j=1}^{2} \frac{\Gamma_j \omega}{2c_o}\left[\left(r_j - \frac{1}{r_j}\right)\sin(\theta_j)\right]^t \sqrt{\frac{2c_o}{\pi\omega \mathrm{R}}}\, e^{i(\omega \mathrm{R}/c_o - 3\pi/4)} . \tag{3.14}$$

The far-field outer potential ϕ_{zo} can be obtained by using the inverse Fourier transform :

$$\phi_{zo} = -\frac{1}{2\pi}\sum_{j=1}^{2}\int_{-\infty}^{\infty}\frac{\omega\Gamma_j}{2c_o}\left[\left(r_j - \frac{1}{r_j}\right)\sin(\theta_j)\right]^t\sqrt{\frac{2c_o}{\pi\omega\mathrm{R}}}e^{i(\omega\mathrm{R}/c_o - 3\pi/4)}e^{-i\omega t}d\omega\,. \tag{3.15}$$

It is straight-forward to observe that the integrand in Equation (3.15) comes from a convolution and the far-field pressure [Equation (1.8)] is, with the help of Gradshteyn and Ryzhik [1980]:

$$p = \frac{1}{\pi}\sqrt{\frac{1}{2c_o\mathrm{R}}}\sum_{j=1}^{2}\frac{\partial}{\partial t}\int_{-\infty}^{t_o-\mathrm{R}/c_o}\frac{\partial}{\partial\tau}\left[\left(r_j - \frac{1}{r_j}\right)\sin(\theta_j)\right]\frac{\Gamma_j d\tau}{\sqrt{t_o - \tau - \mathrm{R}/c_o}}\cos\theta\,, \tag{3.16}$$

where the far-field sound pressure p is normalized by $\rho_0\Gamma^2/a^2$. The far-field sound pressure is a longitudinal dipole (P_x). Equation (3.16) is exactly the same as that depicted in Abou-Hussein et al. [2002] and agrees with the deduction of Curle [1955].

3.2.2 Perfectly Inviscid Fluid

When the flow resistance R_f inside the lattice of the half cylinder vanishes, it can be shown using Gradshteyn and Ryzhik [1980] that $g_j = \dfrac{1+\eta}{1-\eta}$ from Equation (3.3) and $C = -\sum_{j=1}^{4}\dfrac{\Gamma_j}{2\pi}\left(\dfrac{1}{g_j}\tan^{-1}\dfrac{\xi_j}{1+\zeta_j} + \tan^{-1}\dfrac{\xi_j}{1-\zeta_j}\right)$ since $\eta \neq 1$. From Equation (3.8), the flow potential in z-plane becomes

$$\phi_z = \sum_{j=1}^{4}\frac{\Gamma_j}{2\pi}\mathrm{Im}\left\{\frac{1}{g_j}\left[\ln\left(1-\frac{1}{z\bar{z}_j}\right) - \ln\left(1-\frac{1}{z}\right)\right] + \left[\ln\left(1-\frac{z_j}{z}\right) - \ln\left(1-\frac{1}{z}\right)\right]\right\}. \tag{3.17}$$

The far-field inner potential produced by the vortices in a perfectly inviscid fluid is, for large $|z|$,

$$\phi_{zi} \approx -\sum_{j=1}^{2} \frac{\Gamma_j}{\pi r}\left(r_j + \frac{1}{g_j r_j}\right)\sin(\theta_j)\cos\theta \tag{3.18}$$

Thus, the far-field sound pressure is

$$p = \frac{1}{\pi}\sqrt{\frac{1}{2c_o \mathrm{R}}}\sum_{j=1}^{2}\frac{\partial}{\partial t}\int_{-\infty}^{t_o-\mathrm{R}/c_o}\frac{\partial}{\partial \tau}\left[\left(r_j + \frac{1}{g_j r_j}\right)\sin(\theta_j)\right]\frac{\Gamma_j\, d\tau}{\sqrt{t_o - \tau - \mathrm{R}/c_o}}\cos\theta\,. \tag{3.19}$$

Equation (3.19) shows that the pressure generated in a perfectly inviscid fluid is again a longitudinal dipole and it converges to Equation (3.16) for large η ($g_j \to -1$).

3.2.3 Combined Effects of η and R_f

With a finite flow resistance R_f, the effects from the porous material become complicated. The flow potential in the *w*-plane is

$$\begin{aligned}\phi_w = \sum_{j=1}^{4}\frac{\Gamma_j}{2\pi}\Bigg\{&-\tan^{-1}\frac{\xi_j-\xi}{\zeta+\zeta_j} + \tan^{-1}\frac{\xi_j-\xi}{\zeta-\zeta_j} + \frac{2}{1+\eta}\int_0^\infty \frac{ke^{-k(\zeta+\zeta_j)}\sin(k(\xi_j-\xi))}{\left(\beta_j^2+k^2\right)}dk \\ &+ \frac{2R_f}{|V_{wj}|(1+\eta)^2}\int_0^\infty \frac{e^{-k(\zeta+\zeta_j)}\cos(k(\xi_j-\xi))}{\beta_j^2+k^2}dk + C\Bigg\}\end{aligned}, \tag{3.20}$$

where

$$C = \sum_{j=1}^{4} \frac{i\Gamma_j}{2\pi} \Big\{ -\mathrm{Re}\big[\ln(1+i\overline{w}_j)\big] + \mathrm{Re}\big[\ln(1+iw_j)\big]$$
$$-\frac{2}{1+\eta}\mathrm{Im}\big[-ci(\beta_j\mu_j)\cos(\beta_j\mu_j) - si(\beta_j\mu_j)\sin(\beta_j\mu_j)\big],$$
$$-\frac{2}{1+\eta}\mathrm{Re}\big[ci(\beta_j\mu_j)\sin(\beta_j\mu_j) - si(\beta_j\mu_j)\cos(\beta_j\mu_j)\big]\Big\}$$

$\overline{w}_j$ = conjugate of w_j, $\mu_j = (1+\zeta_j) - i\xi_j$ and $\beta_j = R_f \big/ [|V_{wj}|(1+\eta)]$, and *si* and *ci* are the sine and cosine integrals respectively. The velocity of each vortex has to be estimated by iteration as in Tang [2001]. The corresponding flow potential ϕ_z is

$$\phi_z = \sum_{j=1}^{4} \frac{\Gamma_j}{2\pi} \left[\begin{array}{l} -\mathrm{Im}\left\{ \ln\left(1-\dfrac{1}{z\overline{z}_j}\right) - \ln\left(1-\dfrac{z_j}{z}\right)\right\} \\ +\dfrac{2}{1+\eta}\mathrm{Im}\left\{ \begin{array}{l} \big[-ci(\beta_j D_j)\cos(\beta_j D_j) - si(\beta_j D_j)\sin(\beta_j D_j)\big] \\ -\big[-ci(\beta_j\mu_j)\cos(\beta_j\mu_j) - si(\beta_j\mu_j)\sin(\beta_j\mu_j)\big] \end{array} \right\} \\ +\dfrac{2}{1+\eta}\mathrm{Re}\left\{ \begin{array}{l} \big[ci(\beta_j D_j)\sin(\beta_j D_j) - si(\beta_j D_j)\cos(\beta_j D_j)\big] \\ -\big[ci(\beta_j\mu_j)\sin(\beta_j\mu_j) - si(\beta_j\mu_j)\cos(\beta_j\mu_j)\big] \end{array} \right\} \end{array} \right], \qquad (3.21)$$

where $D_j = (\zeta+\zeta_j) - i(\xi_j - \xi)$. The flow potential ϕ_{zi} at large $|z|$ becomes

$$\phi_{zi} \approx \sum_{j=1}^{4} \frac{\Gamma_j}{2\pi r} \left[\left(r_j - \frac{1}{r_j}\right)\sin(\theta-\theta_j) - f_{1j}\cos\theta - f_{2j}\sin\theta \right], \qquad (3.22)$$

where

$$f_{1j} = \frac{2\beta_j}{1+\eta}\mathrm{Re}\big[\exp(i\gamma_j\beta_j)G(0, i\gamma_j\beta_j) + \exp(-i\gamma_j\beta_j)G(0, -i\gamma_j\beta_j)\big],$$

$$f_{2j} = \frac{4\beta_j}{1+\eta}\mathrm{Im}\big[ci(\gamma_j\beta_j)\cos(\gamma_j\beta_j) + si(\gamma_j\beta_j)\sin(\gamma_j\beta_j)\big],$$

$\gamma_j = 1 + \dfrac{r_j e^{i\theta_j} + 1}{r_j e^{i\theta_j} - 1}$, and $G(0,\chi)$ is the incomplete gamma function [Abramowitz and Stegun, 1972]. The far-field outer potential, ϕ_{zo}, can be obtained in the same way as in the two previous cases. Equation (3.22) indicates that a transverse dipole (P_y) of magnitude f_{2j} exists when the flow resistance is finite. A longitudinal dipole (P_x) of magnitude f_{1j} adds to the half cylinder dipole.

One should note that R_f in the present chapter is normalized by $\rho_o\Gamma/a^2$. Therefore, this parameter can vary over a very wide range. For weak vortex strength, R_f can be very large and it decreases as the vortex strength increases. It vanishes in the case of a perfectly inviscid fluid. In the foregoing analysis, R_f ranges from 0 to 100. One can notice from later discussions that the acoustic radiation with R_f = 100 are already close to those of the rigid half cylinder.

In the foregoing discussions, the far-field sound pressure is evaluated at a radial distance R of 100. The acoustical energy (E) radiated by the unsteady vortex motions is equal to

$$E = \int_0^t \int_0^{2\pi} \left(P_x^2 + P_y^2\right) r\, d\theta\, dt \tag{3.23}$$

3.3 Single Vortex

For a single vortex translating past a rigid wall mounted half cylinder, Abou-Hussein *et al*. [2002] studied the effects of mean flow on its path and the sound generation. The magnitude of sound pressure increases as y_{1i} decreases. Active sound generation is observed during the period when the vortex undergoes a substantial large rate of change of velocity when it is close to the rigid half cylinder. A single vortex moving over a rigid flat plane generates no sound.

For a perfectly inviscid fluid, the flow resistance vanishes (R_f = 0). Figure 3.3(a) shows the corresponding effect of η on the vortex path with $x_{1i} = -10$ and y_{1i} = 0.5. The path of a vortex engaging a rigid wall mounted half cylinder is also shown for comparison. The theory in the previous section (Section 3.2.2) indicates that the vortex path converges to that under rigid wall condition at very large η. The vortex path bends towards the porous half cylinder surface because of the pressure-releasing effect. The smaller the value of η, the greater the degree of bending towards the porous half cylinder surface. It will be shown later in Chapter 4 that such situation also appears when a vortex moves in the vicinity of a wedge with inhomogeneous surface flow impedance. The vortex resumes its original height as it gradually goes away from the porous half cylinder (at $x > 2$). Figures 3.3(b) to 3.3(e) show the corresponding time variation of the vortex velocities and accelerations. The time t_a denotes the time at which the vortex passes across the y-axis ($x = 0$). The magnitude of the vortex longitudinal velocity u_{z1} increases as η decreases while the magnitude of the vortex transverse velocity v_{z1} is fairly constant for a perfectly inviscid fluid. One can also notice that the magnitudes of the vortex accelerations increase with decreasing η. When y_{1i} increases, less severe vortex path bending can be observed at a fixed η.

Equations (3.16) and (3.19) suggest that the far-field sound pressure is a longitudinal dipole (P_x) for the case of a rigid half cylinder ($g_j \to -1$) or a perfectly inviscid fluid ($g_j = (1 + \eta)/(1 - \eta)$). The sound pressure increases [Figure 3.3(f)] as the vortex comes closer to the porous half cylinder surface and undergoes substantial large longitudinal and transverse accelerations [Figures 3.3(d) and 3.3(e)]. The pressure fluctuation patterns for various η are pulse-like and are similar to that for the case of a hard cylinder, except that the duration of active sound production is reduced as η decreases. Amplifications of the first peak and trough are found upon the introduction of the porous material and the extent of such amplification increases with decreasing η. It is found that a decrease in either y_{1i} or η will lead to an increase in the strength of the far-field sound pressure fluctuation.

For non-vanishing flow resistance ($R_f \neq 0$), Morse and Ingard [1968] and Tang [2001] suggested that η and R_f produce pressure-releasing and pressure-supporting effects respectively (Chapter 1). Figure 3.4(a) shows such effects on the vortex path at a fixed η with the vortex located at $x_{1i} = -10$ and $y_{1i} = 0.5$. The vortex paths for $R_f > 10$ are close to that of the rigid half cylinder case. The vortex bends away from the porous half cylinder surface at $x < 0$ and the extent of the bending increases as R_f decreases towards 0.1. Further away from the porous half cylinder at $x > 2$, it is observed that for $0.5 \leq R_f < 10$, the vortex path first gets closer to the x-axis at small R_f but gradually rises back to $y = 0.5$ after reaching a minimum separation distance at $R_f \approx 1$. At $R_f = 0.1$, the earlier movement of the vortex away from the porous half cylinder surface at $x < 0$ is so serious that the vortex height y_1 is greater than 0.5 after the vortex moves over the porous half cylinder. However, the vortex path collapses gradually with that for $\eta = 5$, $R_f = 0$ [Figure 3.3(a)] as R_f is further reduced. When R_f is reduced further towards zero, the pressure-releasing effect becomes more important such that the vortex path bends towards the porous half cylinder again and converges to that of the perfectly inviscid fluid case. One can also notice from Figure 3.4(a) that the vortex paths with non-vanishing R_f are not symmetrical about the y-axis.

Figure 3.4(b) illustrates the effects of η on the vortex path with R_f fixed at 5. The vortex bends away from the porous half cylinder surface as in Figure 3.4(a). The degree of the initial path bending increases with η for $\eta \leq 1000$. The vortex height y_1 after the vortex passes over the porous half cylinder first drops below 0.5 as η increases from 3, but rises up above 0.5 as η further increases from 100. One is expecting that y_1 will resume the value of 0.5 as $\eta \rightarrow \infty$. When η tends to one, the pressure-releasing effect is very strong. The vortex comes closer to the porous half cylinder surface for small R_f as it decelerates after passing across the vertical centerline of the porous half cylinder as shown in Figure 3.4(c). The path becomes similar to that under the hard wall condition for $R_f > 1$.

Figure 3.5 shows the effect of flow resistance on vortex velocity at a fixed $\eta = 5$. The amplitude of v_{z1} decreases for all R_f compared with the rigid wall condition. However, one can notice that u_{z1} increases when R_f is very small and decreases with increasing R_f. When the flow resistance inside the porous material is finite, the transverse and longitudinal vortex velocities decrease with increasing flow resistance. However, when the flow resistance is small, the longitudinal velocity of the vortex increases because of the relatively weaker frictional force inside the porous material. Figure 3.6 shows the corresponding time variations of vortex accelerations. The amplitude of the longitudinal acceleration of the vortex decreases from $R_f = 10$ to $R_f = 0.1$ and then increases again by further reducing R_f to 0. However, the vortex undergoes longer duration of longitudinal acceleration for $0.1 < R_f < 10$. The same is true for the transverse acceleration of the vortex.

Unlike the situation in an inviscid flow, the present far-field sound pressure consists of a longitudinal dipole, P_x, and a transverse dipole, P_y [Equation (3.22)]. Figures 3.7(a) and 3.7(b) show some examples of the time variations of P_x and P_y for

$\eta = 5$ at various R_f respectively. It is observed that the decrease of R_f reduces the magnitudes of the peak and trough of P_x, but prolongs the duration of active sound radiation for $0.001 \leq R_f \leq 0.1$. This also results in earlier radiation of sound. However, the amplitude of P_x is higher than that under the rigid half cylinder condition for $10 > R_f > 0.1$ and $R_f < 0.001$. The time variation of P_x converges to those for the rigid half cylinder and perfectly inviscid fluid cases as $R_f \to \infty$ and 0 respectively. On the other hand, the increase of the flow resistance enhances the radiation of P_y, though their magnitudes are small compared to those of P_x. The duration of the transverse dipole radiation appears longer than that of the longitudinal one. In addition, the magnitude of P_y is higher at small R_f. At very large R_f, the results converge to those in the rigid half cylinder case.

Figures 3.8(a) to 3.8(c) summarize the effects of η and R_f on the amplitudes of P_x and P_y at $x_{1i} = -10$, $y_{1\mathrm{i}} = 0.3$, 0.5 and 0.8 respectively for $10^{-5} < R_f \leq 100$. Those of P_x for the cases of a rigid half cylinder and an inviscid fluid are included for the sake of referencing. For $y_{1\mathrm{i}} = 0.3$ [Figure 3.8(a)], the vortex is likely to hit the porous half cylinder at $\eta = 1.5$ and $R_f < 0.009$. This violates the assumption of the theory and thus no data in this R_f range can be presented. For all η studied, the amplitude of P_x is approximately equal to that of the rigid half cylinder case for $R_f > 1$. At $R_f < 1$, the amplitude of P_x fluctuates about its ‘rigid half cylinder’ value, but increases as $R_f \to 0$ and finally converges to the corresponding values for the perfectly inviscid fluid. The amplitude of P_y peaks at around $R_f \sim 0.5$. As $R_f \to 0$ or ∞, P_y drops towards its theoretical value for a perfectly inviscid fluid and a rigid half cylinder respectively (that is, $P_y = 0$). The decrease of η increases the amplitude of P_y for the whole range of R_f, while the increase of P_x is only observed at $R_f < 0.5$.

Again, the increase of η leads to a reduction of the transverse dipole amplitude for the other two values of $y_{1\mathrm{i}}$ [Figures 3.8(b) and 3.8(c)]. The amplitude of the transverse dipole becomes weaker when the porous half cylinder is less pressure-releasing as anticipated by the theory (larger η and/or higher R_f). As can be expected, the increase in $y_{1\mathrm{i}}$ reduces the effects of the porous half cylinder on the sound radiation. Results in Figure 3.8 suggest that certain combinations of η and R_f will lead to louder sound radiation than the rigid half cylinder case, especially for small $y_{1\mathrm{i}}$ with small η and very small R_f. Also, it is noted that the amplitude of P_y is always below those of P_x, but their difference decreases with increasing $y_{1\mathrm{i}}$.

Figure 3.9 illustrates the overall acoustical energy (E) radiated by the unsteady vortex motions under the influence of η and R_f. At a small $y_{1\mathrm{i}}$ [Figure 3.9(a)], the introduction of the porous material enhances the radiation of acoustical energy at $\eta = 5$ and small R_f ($<10^{-4}$). This radiation becomes less important as η decreases from 5 to 1.5 for $R_f > 0.5$, while this trend is reversed for $R_f < 0.5$. As R_f increases from 0.5 to 100, the strength of the radiation eventually falls below that of the rigid half cylinder case for a fixed η. However, all the curves in Figure 3.9(a) converge to $E = 0.1769$, which is the energy radiated in the rigid half cylinder case for large R_f.

The situations at $y_{1\mathrm{i}} = 0.5$, presented in Figure 3.9(b), follow closely those shown in Figure 3.9(a), except that the results at $0.001 \le R_f \le 0.01$ are very close to each other. The increase in $y_{1\mathrm{i}}$ reduces the induction effect of the porous half cylinder on the vortex, resulting in a less significant sound radiation even at small η and R_f. Further increase $y_{1\mathrm{i}}$ to 0.8 does not affect much the trend of E with R_f and η for $R_f > 0.1$, but E decreases with decreasing η otherwise [Figure 3.9(c)]. In this case, less acoustical energy than in the rigid half cylinder case is radiated for $R_f <$ 0.1.

Figures 3.10(a) to 3.10(d) show the change in the directivity patterns of the sound radiations. One can notice that the dipole axis does change with time as in Minota and Kambe [1987] but it should be noted that the longitudinal dipole dominates the sound field as the magnitude of P_x is nearly always much higher than that of P_y [Figure 3.8]. The rotation of the dipole axis can only be observed when P_x is sufficiently small, which is also the instant of less significant sound radiation.

3.4 Two Interacting Vortices with Identical strengths

The sound generation by two identical vortices will be examined in this section. The initial vertical height of the vortices $y_{1i} = y_{2i}$ is set at 0.5 and $x_{1i} = -10$ and the strengths of the two vortices are set equal at $\Gamma_1 = \Gamma_2 = 0.5$. It is well known that two vortices of thin cores will undergo leapfrogging and such motion is periodic in the absence of the cylinder [Tang and Ko, 2000]. The present investigation is focused on how this motion and the corresponding sound generation are affected by the porous half cylinder. In the foregoing discussions, the vorticity centroid of the two vortices is defined as in Chapter 2. That is $z_c = (\Gamma_1 z_1 + \Gamma_2 z_2)/\Gamma$, where $\Gamma = \Gamma_1 + \Gamma_2$. Similar to Section 3.3, the results associated with the combinations of η and R_f under which the vortices come very close to the porous half cylinder surface are excluded.

Figure 3.11 illustrates some examples of the vortex paths at different ε in the presence of a rigid half cylinder. The paths of the individual vortices relative to z_c are also given at the bottom of the figure. For $\varepsilon \leq 0.4$, the path of the vorticity centroid collapses with that of a single vortex of strength Γ located at $x_{1i} = -10$ with $y_{1i} = 0.5$. The relative paths of the vortices are in circular motion about the vorticity centroid [Figure 3.11(a)]. The presence of the rigid half cylinder does not affect much the mutual induction between the two vortices at this ε.

At increased ε, the path of z_c deviates from that shown in Figure 3.11(a) and the paths of the two vortices relative to the vorticity centroid become chaotic and not circular. The leapfrogging vortex motions become more disturbed as ε increases from 0.8 to 1.6 [Figures 3.11(b) to 3.11(d)]. The larger vortex separation weakens the mutual induction strengths between the vortices.

Figures 3.12 to 3.14 show the time variation of vortex velocities and accelerations at different separation distance in the presence of a rigid half cylinder. Here, t_b represents the instant when the vorticity centroid passes over $x = 0$. The vortex velocities and accelerations are not affected much in the presence of a rigid half cylinder when ε is small [Figure 3.12]. The strengths of these components are very strong and fluctuate seriously due to the mutual induction between the two vortices. At increased ε, the magnitudes of the vortex velocities and accelerations decrease, and the mutual induction strengths between the vortex are weakened [Figures 3.13 and 3.14].

Figures 3.15(a) to 3.15(c) show the far-field sound pressure time fluctuations at different ε. It is expected that the sound radiation is more significant when the vortices are in the proximity of the half cylinder. The periodic leapfrogging vortex motions at small ε results in a higher frequency sound radiation [Figure 3.15(a)], which carries most of the sound energy. There is a lower frequency sound fluctuation embedded inside the result shown in Figure 3.15(a), which is similar to that produced by a single vortex of strength $\Gamma = 1$ located at $z_{1i} = (-10, 0.5)$. The increase in ε leads to less ordered leapfrogging vortex motions. The pulses in

Figures 3.15(b) and 3.15(c) are created at the instants when the vortex slip-through occurs as in the case without the cylinder [Tang and Ko, 2003].

As discussed in Section 3.3 [Figure 3.3(a)], a finite effective fluid density inside the porous material lattice will create a pressure-releasing effect, reducing the effect of the porous half cylinder relative to the mutual induction between the vortices. At $\varepsilon = 0.4$, ordered periodic vortex leapfrogging motions can be observed when $\eta = 5$ and $R_f = 0$ [Figure 3.16(a)]. The reduction of η to 3 does not disturb much the leapfrogging vortex motions though the vortex paths are much closer to the porous half cylinder surface. The same is also true for $\eta = 2$ [Figure 3.16(b)]. The stronger effect from the porous half cylinder due to the shorter separation between it and the vortices does result in a slight deviation of the vortex paths relative to z_c from circular motion. The path of z_c resembles those shown in Figure 3.3(a). Similar observation can be made at increased ε [for instance, Figure 3.16(c)] provided that the vortices do not hit the porous half cylinder.

When the flow resistance inside the porous half cylinder is finite, the vortices tend to bend away from the porous half cylinder surface as they propagate across the porous half cylinder [Figure 3.17] as in the single vortex case [Figure 3.4]. However, unlike the cases of a rigid half cylinder or a perfectly inviscid fluid [Figures 3.11 and 3.16 respectively], an increase in the pairing period is observed in the present two interacting vortices case upon the introduction of R_f. The separation of the vortices eventually increases due to the combined effects of η and R_f [Figure 3.17]. Further decreasing η at a fixed R_f brings the vortices further away from the x-axis after they pass over the porous half cylinder into the region $x > 2$ [Figures 3.17(c) and 3.17(d)] and thus reduces the frequency of sound. Such reduction in sound frequency is more pronounced at small ε. However, one should note that the acoustical energy radiated when the vortices are at $|x| > 2$ is insignificant. The vortex dynamics at increased ε are similar to those presented in Figure 3.17, though one expects that the two vortices will move closer to the porous half cylinder provided that no impingement occurs.

Figures 3.18 to 3.20 show some examples of the time variation of vortex velocities and accelerations at $\varepsilon = 0.4$ and $\eta = 5$ with different R_f. It is observed that the magnitudes of the vortex velocities and accelerations decrease at $t - t_b > 0$. Figures 3.21(a) and 3.21(b) illustrate the time variations of P_x and P_y at different R_f respectively at $\varepsilon = 0.4$ and $\eta = 5$. One can observe that there are high and low frequency components in the time variation of P_x [Figure 3.21(a)]. The former is due to the nominally circular motion of the vortices relative to z_c, whose frequency decreases after the vortices pass over the porous half cylinder. The strength of this component relative to the low frequency one first decreases with increasing R_f but the trend reverses when R_f increases beyond ~0.1. The smaller the value of ε, the higher the frequency of the radiated sound and thus less supportive the porous material to the sound radiation can be expected at small R_f. Similar high frequency time fluctuations are also found in P_y but the amplitudes are very small when compared to those in P_x [Figure 3.21(b)]. The amplitudes of these frequency components first increases with R_f but they decrease as R_f increases away beyond unity. P_y vanishes when $R_f = 0$ or $R_f \rightarrow \infty$.

The increase in the separation ε to 0.8 reduces the mutual induction strength between the vortices, resulting in much less regular leapfrogging motions. The corresponding time variations of P_x and P_y with finite R_f are given in Figures 3.21(c) and 3.21(d) respectively. The results for the rigid half cylinder at $\varepsilon = 0.8$ have been shown in Figure 3.15(b). One can notice that the amplitudes of the two dipoles for ε

= 0.4 and 0.8 do not differ much, but the higher frequency fluctuation at ε = 0.4 implies more significant radiation of acoustical energy.

Figure 3.22 illustrates the dependence of the amplitudes of P_x and P_y on R_f, η and ε. Again the amplitude of P_y is about a half or a full order below that of P_x. It is found that the introduction of the porous half cylinder reduces in general the amplitude of the longitudinal dipole P_x for small ε [Figure 3.22(a)] for $\eta \geq 3$. Certainly, one can anticipate that there will be some amplifications of P_x close to R_f = 0 for small η, provided that the vortices do not hit the porous half cylinder. However, the vortices can be very close to the porous half cylinder or even hit the porous half cylinder when η drops below 3, making the whole vortex approach invalid.

The increase in ε appears to have amplified P_x and it is not surprising to find the rapid increase of P_x when $R_f \to 0$ [Figures 3.22(b) and 3.22(c)]. When ε = 1.6, the amplitude of P_x is always above that of the rigid half cylinder case. The trend of P_x variation with ε shown in Figure 3.22 suggests that louder noise will occur upon an increase of ε. This implies that the presence of a porous material near to a jet shear layer can be noisier than the case where the porous material is replaced by a rigid one, if the material is not located at a position where the dominant flow structures have a short wavelength (the initial shear layer mode) [Hussain and Zaman, 1985]. Figure 3.23(a) further suggests that the porous material can reduce the overall acoustical energy radiation when ε is small. It can also be noted that E decreases with decreasing η. However, this trend is reversed at ε = 0.8 and 1.6 at R_f < 0.1 [Figures 3.23(b) and 3.23(c) respectively]. The sound produced by the mutual interaction of the vortices depends very much on the unsteady leapfrogging motions.

The smaller the value of ε, the higher the frequency of the sound radiated and thus less supportive the porous material to the sound radiation can be expected. The effect of $y_{1i} = y_{2i}$ in this two interacting vortices case is similar to those observed in the single vortex case.

3.5 Two Interacting Vortices with Different Strengths

The sound generation by two vortices with different strengths in the presence of a porous half cylinder will be investigated in this section. Without loss of generality, the initial vertical heights of the vortices $y_{1i} = y_{2i}$ are set at 0.5 as in Section 3.4. Figure 3.24 shows the vortex paths with different Γ_1 and Γ_2 in the presence of a rigid half cylinder. When the difference of Γ_1 and Γ_2 is small and $\varepsilon = 0.4$, the path of z_c collapses with that of a single vortex with $\Gamma = \Gamma_1 + \Gamma_2$ located at $x_{1i} = -10$ and $y_{1i} = 0.5$. The vortices are in circular motion about z_c but the stronger vortex is in a more rapid motion than the weaker one [Figure 3.24(a)]. This situation becomes more acute if the difference of vortex strengths increases at a fixed ε [Figure 3.24(b)]. The path of the stronger vortex is circular relative to z_c with very small fluctuating amplitude, and the path of z_c collapses with that of a single vortex located at z_{ci} with vortex strength Γ while the weaker vortex moves in a larger circle relative to the vorticity centroid. The stronger vortex dominates the fluid mechanics and also the aeroacoustics as in the case where the vortices are located in the proximity of a rigid circular cylinder (Chapter 2). The presence of a circular cylinder does not affect much the mutual induction between the two vortices with $\Gamma_1 \neq \Gamma_2$ at small ε. At increased ε, the path of z_c deviates from that shown in Figure 3.24(a) and the paths of the vortices relative to z_c become chaotic and not circular [Figure 3.24(c)]. The stronger vortex follows closely the path of z_c but the weaker one does not.

The velocity and acceleration of the vortex with $\Gamma_1 \neq \Gamma_2$ are shown in Figures 3.25 to 3.27. Large fluctuations of these components are observed with $\Gamma_1 = 0.6$ and $\Gamma_2 = 0.4$ when $\varepsilon = 0.4$[Figure 3.25]. The amplitudes of the velocities and accelerations of the weaker vortex are higher than those of the stronger one. Such difference in amplitude is more pronounced by further increasing the difference of the vortex strengths [Figure 3.26]. At $\varepsilon = 0.8$ with $\Gamma_1 = 0.6$ and $\Gamma_2 = 0.4$, the mutual induction between the vortices is weakened and the magnitudes of the velocities and accelerations decrease [Figure 3.27].

When $\varepsilon = 0.4$, the far-field sound pressure time fluctuation with $\Gamma_1 = 0.6$ and $\Gamma_2 = 0.4$ resembles very much those presented in Figure 3.15(a) [Figure 3.28(a)]. The sound radiation is more significant when the two vortices propagate across the rigid half cylinder at small ε except that an amplitude modulation pattern [Figure 2.10] is observed due to the motion of the weaker vortex. Figures 3.28(b) and 3.28(c) show the sound pressure when the difference of the vortex strengths increases at a fixed ε and ε increases at a fixed $\Gamma_1 \neq \Gamma_2$ respectively. One can observe that when the difference of the vortex strengths increases, the sound pressure fluctuation is modulated by the weaker vortex [Figure 3.28(b)]. The sound pressure fluctuation becomes more irregular when the separation distance between the two vortices increases.

For a perfectly invisvid fluid, $R_f = 0$, the vortices move in a closer path towards the surface of the porous half cylinder due to the pressure-releasing effect [Figure 3.29]. For $\varepsilon = 0.4$, $\Gamma_1 = 0.6$ and $\Gamma_2 = 0.4$ at a finite $\eta = 5$, ordered periodic vortex leapfrogging motions can be observed [Figure 3.29(a)]. When the difference of vortex strengths increases at a fixed η, the paths of the vortices are similar to those shown in Figure 3.29(a) except that the stronger vortex follows closely the path of z_c and the weaker vortex moves in a larger circular path relative to z_c [Figure 3.29(b)]. The reduction of η to 3 does not disturb much the leapfrogging vortex motions though the vortices are much closer to the porous half cylinder surface [Figure 3.29(c)]. The increase in the separation distance ε results in a less distinctive leapfrogging vortex motions close to the porous half cylinder surface at η = 5 provided that the weaker vortex does not hit the porous half cylinder [Figure 3.29(d)].

The dynamics of equal strength vortices at a finite flow resistance inside the porous half cylinder have been discussed in Section 3.4. When the vortex strengths are different at a finite R_f, the vortices also bend away from the porous half cylinder surface as they propagate over the half cylinder, and an increase in the pairing period is observed as in Figure 3.17 [Figure 3.30]. When $\Gamma_1 = 0.6$ and $\Gamma_2 = 0.4$, the vortex paths are similar to the case in rigid half cylinder condition at $\varepsilon = 0.4$, $\eta = 5$ and $R_f = 10$ [Figure 3.30(a)]. The vortices bend away from the x-axis as they pass over the porous half cylinder when R_f is further reduced from 0.1 at a fixed ε and η [Figure 3.30(b)]. The stronger vortex propagates more rapidly than the weaker one. An increase in the pairing period is observed as in Figure 3.17. Unlike the situation in Figure 3.17, the vortices bend away from the x-axis before they pass over the porous half cylinder at $x > -2$. At a fixed R_f with decreased η, an increase in the vortex pairing period is more pronounced when the vortices are at $x > 2$ but not at $-2 < x < 2$ [Figure 3.30(c)]. When the difference of the vortex strengths increases, the vortices bend away from the porous half cylinder at $x > -2$, and the period of vortex pairing increases as shown in Figure 3.30(d). The path of the stronger vortex deviates slightly from the path of z_c while the weaker vortex moves in a larger circular path relative to z_c. At increased ε, the vortex dynamics are similar to those presented in Figure 3.30 provided that no impingement occurs. The vortices move closer to the porous half cylinder surface, and the paths of the vortices relative to z_c become chaotic and not circular.

Figure 3.31 shows the sound pressure time fluctuation at a fixed $\varepsilon = 0.4$ with $\Gamma_1 = 0.8$, $\Gamma_2 = 0.2$ and $\eta = 5$ at various R_f. High and low frequency components are found in the time variation of P_x [Figure 3.31(a)], and the strengths of these frequency components decrease when R_f decreases from 0.01 but the trend reverses when R_f increases beyond 0.01. An amplitude modulation pattern is also observed in the high frequency component. The magnitude of P_x converges to that under the rigid wall condition at large $R_f \sim 10$. Figures 3.32 to 3.34 shows the time variations of vortex velocities and accelerations at a fixed $\varepsilon = 0.4$ with $\Gamma_1 = 0.8$, $\Gamma_2 = 0.2$ at various R_f. The velocities and accelerations of the weaker vortex are higher than the stronger one at various R_f. The presence of a finite R_f inside the porous half cylinder does not affect the velocities and accelerations of the vortex compare with the rigid half cylinder case [Figure 3.26]. From the vortex paths shown in Figures 3.30(b) and 3.30(d) and the time variation of the vortex velocities and accelerations [Figures 3.32 to 3.34], one can predict that the modulation becomes less influential when the difference of the vortex strengths decreases. Similar high and low frequency components are found in the transverse dipole P_y but the amplitude of P_y is always lower than that of P_x [Figure 3.31(b)]. The maximum amplitude of P_y increases with R_f for $R_f < 1$ but the opposite occurs for $R_f > 1$, and the dynamics of the weaker vortex also has an amplitude modulation effect on P_y. At an increased ε with different Γ_1 and Γ_2, the longitudinal and transverse dipoles do not differ much from those shown in Figures 3.13(c) and 3.13(d).

Figure 3.35 summaries the combined effects of η, R_f, ε and the vortex strengths on the amplitudes of P_x and P_y. For $\varepsilon = 0.4$, $\Gamma_1 = 0.6$ and $\Gamma_2 = 0.4$, the magnitudes of P_x and P_y converge to those under the rigid half cylinder condition for large $R_f \sim 10$ and those for the perfectly inviscid fluid case when $R_f \to 0$ [Figure 3.35(a)]. The introduction of the porous half cylinder reduces the magnitude of P_x generally for $\eta = 5$ but there are some amplifications of P_x when $R_f \to 0$ for $\eta = 3$. The amplitude of P_x decreases with increasing R_f for $R_f < 0.01$ and then it increases with R_f for $R_f > 0.01$. The magnitude of P_y is about half or a full order below that of P_x, and the magnitude of P_y at $\eta = 3$ is always greater than that at $\eta = 5$. Similar findings are reported in Figure 3.22. When the difference of the vortex strengths increases ($\Gamma_1 = 0.8$ and $\Gamma_2 = 0.2$), the results are similar to those presented in Figure 3.35(a) [Figure 3.35(b)] except that the weaker vortex hits the porous half cylinder when $\eta = 3$ and $R_f \to 0$.

When ε increases to 0.8 with $\Gamma_1 = 0.6$ and $\Gamma_2 = 0.4$ [Figure 3.35(c)], the fluctuation of P_x around the " rigid half cylinder" value is more serious at $R_f > 10^{-3}$ as the sound produced by the mutual induction between the vortices depends very much on the unsteady leapfrogging motions. Generally, the magnitude of P_x is amplified, and there is a rapid increase of P_x when $R_f \to 0$, especially when η is small. The magnitude of P_x at small η is higher than that in the case for $\Gamma_1 = \Gamma_2$ [Figure 3.22(b)]. The weaker vortex moves towards the porous half cylinder surface under the strong pressure-releasing effect and undergoes substantial large vortex accelerations, resulting in a higher value of P_x. The amplitude of P_y follows similar trend when $\varepsilon = 0.4$ [Figure 3.35(a) and 3.35(b)]. At increased ε, the combined effects of η and R_f suggest louder noise generation, and the trend is similar to those presented in the case with equal vortex strengths [Figure 3.22]. In addition, the amplitude of P_x increases by further increasing the difference of vortex strengths [Figure 3.35(d)].

From Figure 3.35(a), one can anticipate that the overall acoustical energy radiation can be lowered upon the introduction of the porous material when the difference of the vortex strengths is small for small ε [Figure 3.36(a)]. When Γ_1 = 0.8 and Γ_2 = 0.2 at a fixed ε = 0.4, the overall acoustical energy radiation is lower than that under the rigid wall condition [Figure 3.36(b)]. At increased ε = 0.8 with η = 5, Γ_1 = 0.6 and Γ_2 = 0.4, the energy is lower than that under the rigid half cylinder condition but such reduction of acoustical energy is not found at small η with R_f < 0.001 [Figure 3.36(c)]. The substantial large rate of change of vortex velocity due to the chaotic motion of a weaker one under the strong pressure-releasing effect increases the total amount of energy radiation at increased ε. Further increasing the difference of Γ_1 and Γ_2 results in a stronger acoustical energy radiation for R_f < 0.001 [Figure 3.36(d)]. The smaller the value of η, the stronger the acoustical energy radiation .

3.6 Remarks

The low Mach number condition in the present study results in the radiation of low frequency sound whose peak value depends substantially on the vortex circulation. At R = 100 with an ambient speed of sound c = 343 (normalized by Γ/a), y_{1i} = 0.3 and η = 1.5, the maximum peak normalized sound pressure radiated at R_f = 1 by a single vortex is 1.3×10^{-4} [Fig. 3.8(a)]. With a Γ = 0.14m^2/s, the maximum sound pressure level is around 23.5dB, but this pressure level goes up to ~78.9dB when Γ = 3.4m^2/s. For a rigid half cylinder, the corresponding maximum sound pressure levels are 21dB and 72dB respectively.

In the case of two vortices with $y_{1i} = y_{2i} = 0.5$, $\varepsilon = 0.8$, $\eta = 5$ and $R_f = 1$, the sound pressure levels with $\Gamma = 0.14\text{m}^2/\text{s}$ and $3.4\text{m}^2/\text{s}$ are approximately 19.8dB and 75.2dB respectively [Fig. 3.22(b)]. The corresponding values for rigid half cylinder are 19.3dB and 74.7dB respectively.

The above dimensional examples illustrate that the aeroacoustics studied in the present study can be significant and the introduction of porous material can enhance the sound radiation at certain combinations of parameters.

3.7 Summary

In the present investigation, the sound generation by the unsteady vortex motions in the presence of a porous half cylinder on an otherwise rigid horizontal plane is studied theoretically. The far-field sound pressure so produced is evaluated through the use of the conformal mapping and the matched asymptotic expansion method. The effects of the effective fluid density and flow resistance inside the porous material on the vortex motions and the far-field sound radiation are discussed.

In the presence of a porous material with a finite flow resistance, longitudinal and transverse dipoles co-exist in the far-field but the latter is significantly weaker than the former in general. When a single vortex engages the porous half cylinder, the time variation of the strength of each dipole is pulse-like. The amplitude of the longitudinal dipole converges to that for the rigid half cylinder case when the flow resistance is large for all effective fluid density studied, but is larger than the latter at small flow resistance. The rate of increase of the dipole amplitude becomes rapid at vanishing flow resistance. The larger vortex height above the rigid plane reduces the amplitudes of the dipoles. However, the overall acoustical energy radiated remains higher than that for the rigid half cylinder case at some combinations of the effective fluid density and flow resistance.

When two identical vortices exist in the proximity of the porous half cylinder, both the longitudinal and transverse dipoles consists of a low and a high frequency components. The former is due to the macroscopic vortex centroid motions and the latter to the leapfrogging motions of the vortices. When the two vortices are close to each other, the corresponding dipoles are dominated by the high frequency fluctuations. The overall acoustical energy so radiated is less than that for the rigid half cylinder case. The opposite is found at larger vortices separation for all combinations of flow resistance and effective fluid density studied. When the vortex strengths are different, the results are similar to those for the two identical vortices case except that the acoustical energy radiated is higher than that for the rigid half cylinder case when the difference of vortex strengths increases.

The present results show that suitable combinations of the effective fluid density and the flow resistance within a porous material will enhance the radiation of sound in the presence of a turbulent shear flow, especially when the flow structures involved are of lower frequency.

Chapter 4: Vortex Sound in the presence of a Wedge with Inhomogeneous Surface Flow Impedance

4.1 Introduction

As mentioned in chapter 1, the problem of self-generated noise upon the influence of the porous material is not well known. In chapters 2 and 3, the forces and sound generated by the interaction of the vortices with a rigid or porous circular cylinder are discussed, and the effect of the wavelength of coherent structure on the sound generation is also addressed. In this chapter, the sound generated by the unsteady motion of an inviscid vortex in the presence of a wedge with inhomogeneous surface flow impedance is studied as some flow junctions in ductwork involve edges or are wedge-like, which tend to scatter aerodynamic sound. The important effects of the porous material properties and the wedge angle are discussed.

4.2 Theoretical Development

Figure 4.1 shows the nomenclature used and the flow configuration for the present investigation. The wedge consists of two materials. One of the materials is assumed porous while the other is rigid for simplicity. Here the noise radiated when an inviscid vortex with circulation Γ originally moving close to the rigid surface turns around the edge of the sharp wedge is considered. The wedge angle α varies between 0 and π. All the length scales in the present study are normalized by d_i, which is the initial perpendicular distance of the vortex from the rigid surface and the time scale is normalized by d_i^2/Γ.

The Bernoulli's equation suggests that the vortex moves around the edge as the vortex is experiencing a force resulting from the fluid pressure difference between the edge and the boundary at infinity. The analysis is started by transforming the present vortex system [Figure 4.1], which is hereinafter referred to as the z-plane ($z = x + iy$, $y \geq 0$), to a w-plane ($w = \xi + i\zeta$), which is a parallel passage with $0 \leq \zeta \leq 1$ as shown in Figure 4.2. The conformal mapping [Kober, 1952] required is

$$z = f(w) = e^{(2\pi-\alpha)w} \Rightarrow w = f^{-1}(z) = \frac{1}{2\pi-\alpha}\ln z\,. \tag{4.1}$$

The branch cut in the z-plane is the positive x-axis.

The streamfunction in the w-plane, ψ_w can be obtained by the integration [Tang, 2001] as in Chapter 3:

$$\psi_w = \frac{1}{4\pi}\int_{-\infty}^{\infty}\frac{1}{|k|}\left(e^{-|k|\zeta_1} + ge^{|k|\zeta_1}\right)\frac{e^{-|k|\zeta} - e^{-2|k|}e^{|k|\zeta}}{g + e^{-2|k|}}e^{ik(\xi_1-\xi)}dk\,, \tag{4.2}$$

where $w_1 = \xi_1 + i\zeta_1$ represents the position of the vortex in the w-plane and

$$g(k) = \frac{ikV_w + (ikV_w\eta + R_f)\coth(|k|h)}{ikV_w - (ikV_w\eta + R_f)\coth(|k|h)}, \tag{4.3}$$

where h is the depth of the porous material in the w-plane. In addition, V_w and R_f are normalized by Γ/d_i and $\rho_o\Gamma/d_i^2$ respectively. The corresponding vortex velocity in the w-plane is evaluated by differentiating Equation (4.2) with respect to ζ:

$$V_{w1} = \frac{1}{4\pi}\int_{-\infty}^{\infty}\left(e^{-|k|\zeta_1} + ge^{|k|\zeta_1}\right)\frac{-e^{-|k|\zeta} - e^{-2|k|}e^{|k|\zeta}}{g + e^{-2|k|}} e^{ik(\xi_1 - \xi)}dk \, . \tag{4.4}$$

The paths of the vortex in the z-plane are calculated by integrating Equation (4.4) numerically with the standard fourth order Runge-Kutta method together with the Routh's correction [Equation (3.7)].

With the use of Cauchy-Rieman principle, the flow potential in the w-plane, ϕ_w, is

$$\phi_w = -\frac{i}{4\pi}\int_{-\infty}^{\infty}\frac{1}{k}\left(ge^{|k|\zeta_1} + e^{-|k|\zeta_1}\right)\frac{e^{-|k|\zeta} + e^{-2|k|}e^{|k|\zeta}}{g + e^{-2|k|}} e^{ik(\xi_1 - \xi)}dk + C \, , \tag{4.5}$$

where C is the integration constant that can be evaluated by observing that the flow potential vanishes as $|\xi| \to \infty$. It can be shown after some algebra that

$$\phi_w = \frac{1}{2\pi}\int_{0}^{\infty}\mathrm{Im}\left[\frac{1}{k}\left(ge^{k\zeta_1} + e^{-k\zeta_1}\right)\frac{e^{-k\zeta} + e^{-2k}e^{k\zeta}}{g + e^{-2k}} e^{ik(\xi_1 - \xi)}\right]dk + C \, . \tag{4.6}$$

The incompressible flow potential in the z-plane, ϕ_z, can then be found by substituting the inverse of Equation (4.1) into Equation (4.6). Expressing $z = re^{i\theta}$, where r and θ are the polar coordinates in the flow field, one obtains from Equation (4.1) that

$$\xi = \frac{\ln r}{2\pi - \gamma}\, , \; \theta = (2\pi - \alpha)\zeta \; \text{ and } \; h = \frac{\alpha/2}{2\pi - \alpha}\, . \tag{4.7}$$

Thus, the far-field outer potential, ϕ_{zo}, can be obtained using matched asymptotic expansion method as in Crighton [1972] and Obermeier [1979a, 1980], and the far-field sound pressure can be obtained from Equation (1.8).

4.3 Acoustically Hard Surface

The case for edges with acoustically hard surfaces has been investigated by several researchers, such as Crighton [1972], Panaras [1985] and Kambe [1986]. However, the case for arbitrary wedge angle has not been explicitly presented. The condition of hard surfaces requires that $\left|-ikV_{w1}\eta + R_f\right| >> \left|kV_{w1}\right|$ for all value of k and $g = -1$ [Equation (4.3)]. The final potential is independent of h. The flow potential in the w-plane is, according to Equation (4.5), given by

$$\begin{aligned}\phi_w &= \frac{1}{2\pi}\int_0^\infty \frac{1}{k}\left(-e^{k\zeta_1} + e^{-k\zeta_1}\right)\frac{e^{-k\zeta} + e^{-2k}e^{k\zeta}}{e^{-2k} - 1}\sin\left[k\left(\xi_1 - \xi\right)\right]dk + C \\ &= -\frac{1}{\pi}\int_0^\infty \sinh\left(k\zeta_1\right)\frac{\cosh\left[k\left(1-\zeta\right)\right]}{k\sinh\left(k\right)}\sin\left[k\left(\xi - \xi_1\right)\right]dk + C\end{aligned}, \qquad (4.8)$$

and by observing the flow potential vanishes when $|\xi| \to \infty$, one finds for non-zero R_f that

$$C = \zeta_1/2. \qquad (4.9)$$

Using the formula tabulated in Gradshteyn and Ryzhik [1980], one obtains

$$\phi_w = -\frac{1}{2\pi}\left\{\tan^{-1}\left[\tan\left(\frac{\pi}{2}(1-\zeta_1+\zeta)\right)\tanh\left(\frac{\pi}{2}(\xi-\xi_1)\right)\right]\right.$$
$$\left.-\tan^{-1}\left[\tan\left(\frac{\pi}{2}(1-\zeta_1-\zeta)\right)\tanh\left(\frac{\pi}{2}(\xi-\xi_1)\right)\right]\right\}+\frac{\zeta_1}{2}. \tag{4.10}$$

Substituting Equation (4.7) into Equation (4.10), the potential in the z-plane, ϕ_z, in the polar form,

$$\phi_z = -\frac{1}{2\pi}\left\{\tan^{-1}\left[\cot\left(\frac{b(\theta-\theta_1)}{2}\right)\frac{r^b-r_1^b}{r^b+r_1^b}\right]-\tan^{-1}\left[\cot\left(\frac{b(\theta_1+\theta)}{2}\right)\frac{r^b-r_1^b}{r^b+r_1^b}\right]\right\}$$
$$+\frac{b\theta_1}{2\pi}, \tag{4.11}$$

where $b = \pi/(2\pi - \alpha)$.

When $\alpha = \pi$, the wedge becomes an infinite flat surface and $b = 1$. It can be shown exactly using sine rule that,

$$\phi_z = \frac{1}{2\pi}\left[\tan^{-1}\left(\frac{r\sin\theta - r_1\sin\theta_1}{r\cos\theta - r_1\cos\theta_1}\right)-\tan^{-1}\left(\frac{r\sin\theta + r_1\sin\theta_1}{r\cos\theta - r_1\cos\theta_1}\right)\right], \tag{4.12}$$

which is consistent with existing literature, for instance Lamb [1993]. For large r, $\phi_z \to 0$. For $0 \le \alpha < \pi$, $b < 1$, one can approximate Equation (4.11) as

$$\phi_z \approx \frac{-1}{2\pi}\left\{\tan^{-1}\left[\cot\left(\frac{b(\theta-\theta_1)}{2}\right)\left(1-2\frac{r_1^b}{r^b}\right)\right]-\tan^{-1}\left[\cot\left(\frac{b(\theta_1+\theta)}{2}\right)\left(1-2\frac{r_1^b}{r^b}\right)\right]\right\}$$
$$+\frac{b\theta_1}{2\pi}$$

$$=\frac{-1}{2\pi}\left\{\tan^{-1}\left[\cot\left(\frac{b(\theta-\theta_1)}{2}\right)\right]-\frac{r_1^b}{r^b}\sin[b(\theta-\theta_1)]-\tan^{-1}\left[\cot\left(\frac{b(\theta_1+\theta)}{2}\right)\right]\right. \quad . \qquad (4.13)$$
$$\left.+\frac{r_1^b}{r^b}\sin(b(\theta+\theta_1))\right\}+\frac{b\theta_1}{2\pi}$$

$$=-\frac{1}{\pi}\frac{r_1^b}{r^b}\cos(b\theta)\sin(b\theta_1)$$

This shows that there is a relatively strong radiation back to the downstream side where the wedge is located. For a rigid half plate occupying the region $x > 0$, $y = 0$ in the z-plane, $\alpha = 0$ and $b = 0.5$, and the far-field outer potential becomes

$$\phi_{zo} \approx -\frac{1}{\pi}\sqrt{\frac{r_1}{r}}\cos\left(\frac{\theta}{2}\right)\sin\left(\frac{\theta_1}{2}\right). \qquad (4.14)$$

For the case investigated by Crighton [1972], the half-plane is located at $x < 0$, $y = 0$. The results of Crighton [1972] can be obtained by rotating the present w-plane 180^o in the anticlockwise direction. That is, by substituting θ and θ_1 in Equation (4.14) by $\theta - \pi$ and $\theta_1 - \pi$ respectively, and the far-field pressure can be estimated by Equation (1.8). For $\alpha = \pi$, $b = 1$ and the far-field pressure in Equation (1.8) vanishes as the vortex is moving parallel to the x-axis in the z-plane. Figure 4.3 illustrates the far-field pressure time variation for different α with the directivity factor ignored. Here, t_c denotes the time at which the vortex passes across the axis of symmetry of the wedge. One can notice that every far-field pressure time variation contains a tail which decays relatively slowly after the vortex passes over the edge of the wedge. This is typical for two-dimensional sound radiation due to the non-compactness of the source field so that sound generated from different parts of the source arrives at the far-field at different instants. The rate of decay is slower at larger α. The larger the wedge angle α, the longer the active sound radiation period. Also, both the tail and the far-field pressure amplitude drops rapidly when α approaches π. One should note that b increases with α so that the ratio $(r_1/r)^b$ actually decreases with increasing α for $r >> r_1$. This implies that the sound generated with a rigid half-plane is more significant at large distance.

4.4 Perfectly Inviscid Fluids

For a perfectly inviscid fluid, the flow resistance $R_f \equiv 0$. Equation (4.3) then reduces to

$$g(k) = \frac{1 + \eta \coth(|k|h)}{1 - \eta \coth(|k|h)}, \qquad (4.15)$$

The potential in the w-plane, according to Equation (4.6), is

$$\phi_w = -\frac{1}{\pi}\int_0^\infty \frac{\cosh(k\zeta_1) + \eta \coth(kh)\sinh(k\zeta_1)}{\cosh(k) + \eta \coth(kh)\sinh(k)} \frac{\cosh[k(1-\zeta)]}{k} \sin[k(\xi - \xi_1)]dk + C. \qquad (4.16)$$

In this case, $C = (\eta\zeta_1 + h)/2(\eta + h)$.

In general, Equation (4.16) is not easy to solve analytically. However, if $|\xi - \xi_1| \rightarrow \infty$, the solution can be approximated by considering the approximation for small k,

$$\cosh(k)\sinh(kh) + \eta\cosh(kh)\sinh(k) \approx \eta\sinh\left[\frac{(\eta + h)k}{\eta}\right]. \tag{4.17}$$

As an approximation to Equation (4.16), one can then write for a finite h, $|\xi - \xi_1| \rightarrow \infty$ and $k' = k(\xi - \xi_1)$:

$$\begin{aligned}
\phi_w &= \frac{-1}{\pi}\int_0^\infty \frac{\cosh(k\zeta_1)\sinh(kh) + \eta\coth(kh)\sinh(k\zeta_1)}{\cosh(k)\sinh(kh) + \eta\cosh(kh)\sinh(k)} \\
&\quad\cdot\frac{\cosh[k(1-\zeta)]}{k}\sin[k(\xi - \xi_1)]dk + C \\
&\approx \frac{-1}{\eta\pi}\int_0^\infty \frac{(\eta+1)\sinh[k(\zeta_1 + h)] + (\eta - 1)\sinh[k(\zeta_1 - h)]}{\sinh\left[k\left(\frac{\eta + h}{\eta}\right)\right]} \\
&\quad\cdot\frac{\cosh[k(1-\zeta)]}{k'}\sin(k')dk' + C
\end{aligned}. \tag{4.18}$$

Equation (4.18) can be solved analytically, even when $\eta \rightarrow 0$, using the formula shown in Gradshteyn and Ryzhik [1980]. For $|\xi - \xi_1| \rightarrow \infty$, one obtains

$$\phi_w = \frac{1}{\pi}\sin\left(\frac{\eta\pi\zeta_1}{\eta + h}\right)\cos\left[\frac{\eta\pi}{\eta + h}(1-\zeta)\right]\exp\left[-\frac{\eta\pi(\xi - \xi_1)}{\eta + h}\right]. \tag{4.19}$$

Figure 4.4 shows that Equation (4.19) agrees well with the results obtained from direct numerical integration of Equation (4.16). The comparison is not extended to the range $\xi - \xi_1 > 4$ as ϕ_w will be too small to be handled accurately in the numerical integration. However, one can note from the conformal mapping adopted that the ratio of r/r_1 is already very large when $\xi - \xi_1 = 4$. After applying the conformal mapping [Equation (4.7)], one obtains

$$\phi_z = \frac{1}{\pi}\sin\left[\frac{\eta\pi\theta_1}{\eta(2\pi-\alpha)+\frac{\alpha}{2}}\right]\cos\left[\frac{\eta\pi}{\eta(2\pi-\alpha)+\frac{\alpha}{2}}(2\pi-\alpha-\theta)\right]\left(\frac{r_1}{r}\right)^{\frac{\eta\pi}{\eta(2\pi-\alpha)+\frac{\alpha}{2}}}$$

$$= -\frac{1}{\pi}\sin\left[\frac{\eta\pi\theta_1}{\eta(2\pi-\alpha)+\frac{\alpha}{2}}\right]\cos\left[\frac{\eta\pi\left(\theta+\frac{\alpha}{2\eta}\right)}{\eta(2\pi-\alpha)+\frac{\alpha}{2}}\right]\left(\frac{r_1}{r}\right)^{\frac{\eta\pi}{\eta(2\pi-\alpha)+\frac{\alpha}{2}}} \quad . \qquad (4.20)$$

Equation (4.20) reduces to Equation (4.13) for large η. For $\eta = 1$, there is no porous surface. The situation then reduces to that of a wedge with wedge angle $\alpha/2$ and rigid surfaces. Equations (4.16) and (4.20) give the same result as that obtained from Equation (4.13), by taking the wedge angle to be $\alpha/2$ instead of α and rotating the far-field anticlockwisely by $\alpha/2$. Though η is not likely to be less than unity, Equation (4.20) tends to suggest that the magnitude of the far-field pressure decreases should such a pressure-releasing surface exists. For $\eta = 0$, there will be no sound radiation. Figure 4.5 summarizes the effect of η on the far-field radiation directivity. It is expected that the introduction of a pressure-releasing surface allows more sound radiation in a direction closer to this surface. The larger the wedge angle or the smaller the value of η, the greater this shift.

The far-field pressure magnitudes for some values of η at $\alpha = \pi$ are shown in Figure 4.6. This case has been investigated by Tang and Li [2001] on the assumption that the frequency of the radiated sound is so low that the impedance surface has no effect on the sound radiation. Thus, only the dipole radiation was considered in Tang and Li [2001]. As expected, the scattered sound field becomes weaker as η increases from unity and the rate of such weakening decreases considerably quickly for small η. The magnitudes of the sound fields are higher than those shown in Tang and Li [2001]. Together with the fact that the present scattered field magnitude varies with (Mach number)^b where b is less than unity, the scattered field is much stronger than the dipole radiation discussed in Tang and Li [2001].

For α less than π, the vortex moves towards the pressure-releasing surface after it passes over the edge of the wedge. Figure 4.7 shows the vortex path at $\eta = 2$, 4 and ∞ for $\alpha = \pi/3$. The initial vortex position is at one unit length perpendicular to the hard surface at $r_1 \approx 100$. It can be noted that the smaller the value of η, the closer the vortex will be to the pressure-releasing surface eventually. Figure 4.8 shows the sound pressure time fluctuations for finite η. These patterns are basically similar to those for the rigid surface case [Figure 4.3]. However, one can note that the peak pressure is higher for smaller η. The tail of the sound pressure fluctuation pattern becomes shorter as η decreases, implying shorter period for active and significant sound production at smaller η. The power associated with the radial radiation term $1/r$ is $\eta\pi$ / $[\eta(2\pi - \alpha)+\alpha/2]$, which increases with η. The far-field sound, therefore, decays more rapidly at increasing η. Similar results are obtained at different α ($< \pi$). The effect of wedge angle on the sound radiation is summarized in Figure 4.9. Again, the magnitude of the sound pulse increases with decreasing α.

4.5 Combined Effects of η and R_f

For a real porous material, R_f is finite, and the effects from the porous material become complicated. The far-field potential ϕ_w can be obtained from Equations (4.5) and (4.6). Again, let $k' = k(\xi - \xi_1)$, one obtains

$$\phi_w = \frac{1}{\pi}\left\{\int_0^\infty \mathrm{Im}[G(k)]\frac{\cos k'}{k'}dk' - \int_0^\infty \mathrm{Re}[G(k)]\frac{\sin k'}{k'}dk'\right\} + \frac{\zeta_1}{2}, \tag{4.21}$$

where

$$G = \frac{ikV_{w1}\cosh(k\zeta_1)\sinh(kh) + (ikV_{w1}\eta + R_f)\cosh(kh)\sinh(k\zeta_1)}{ikV_{w1}\cosh(k)\sinh(kh) + (ikV_{w1}\eta + R_f)\cosh(kh)\sinh(k)}\cosh[k(1-\zeta)]. \tag{4.22}$$

It can be shown that

$$G = \left\{\frac{ikV_{w1}[\coth(k\zeta_1) - \coth(k)]}{ikV_{w1}[\coth(k) + \eta\coth(kh)] + R_f\coth(kh)} + 1\right\}\frac{\sinh(k\zeta_1)\cosh[k(1-\zeta)]}{\sinh(k)}. \tag{4.23}$$

Again, the analytical solution for Equation (4.21) is hard to find without assumption. As we are interested in the far-field where $|\xi - \xi_1| \to \infty$, ϕ_w then depends on the value of G as $k \to 0$, which is unity. One can thus conclude to the leading order of magnitude that

$$\phi_w = -\frac{1}{\pi}\int_0^\infty \mathrm{Re}[G(k)]\frac{\sin k'}{k'}dk' + \frac{\zeta_1}{2} \Rightarrow \phi_{zo} = -\frac{1}{\pi}\frac{r_1^b}{r^b}\cos(b\theta)\sin(b\theta_1). \tag{4.24}$$

The directivity of sound radiation for non-vanishing R_f is the same as that with hard surfaces or at large η.

Figure 4.10 illustrates the combined effects of η and R_f on the vortex path. In general, the vortex propagates towards the porous surface soon after it passes over the edge of the wedge. It is observed that the larger the value of η or R_f, the less serious the bending of the vortex path. The increase in the flow resistance R_f makes the porous surface less pressure-releasing and produces the same effect as increasing η. The far-field sound pressure fluctuations for $\alpha = \pi/3$ and $\eta = 2$ are shown in Figure 4.11. The increase in R_f reduces the magnitude of the pulse. The less severe vortex path bending towards the porous surface at larger R_f and η results in smaller vortex acceleration and thus weaker sound radiation. It is found that the magnitude of the sound pulse increases as η decreases when R_f is fixed. However, the variation becomes insignificant for $R_f \geq 10$. The increase in the wedge angle α again reduces the magnitude of the sound pulse, but the far-field sound fluctuation patterns are very similar to those as shown in Figure 4.9.

Figure 4.12 summarizes the combined effects of α, η and R_f on the sound pulse magnitude. Again, one can observe that the introduction of a porous material results in louder sound radiation. This is the result of the increase in the porous material thickness with wedge angle so that the pressure-supporting interface between the porous and the rigid materials becomes less influential.

4.6 Summary

The sound field produced by a vortex engaging the edge of a wedge with inhomogeneous surface impedance is investigated theoretically in this chapter. The wedge is made up symmetrically of a rigid material and an acoustically softer material, which can be a porous material or a heavy liquid. The initial location of the vortex is on the rigid material side far away from the edge of the wedge. The effects of the wedge angle, the effective fluid density and the flow resistance of the porous material on the directivity and the magnitude of the far-field sound are discussed. A general expression for the leading order approximation of the sound field is derived.

In all cases studied, the far-field sound is a pulse whose magnitude decreases with increasing wedge angle. The time variation of each pulse contains a tail which is typical for two-dimensional sound radiation. The rate of decay of the pulse increases as the wedge angle increases. When the wedge angle is fixed, the magnitude of the far-field sound pulse decreases as the solid surface becomes acoustically harder. The vortex path bends towards the porous material after it passes over the edge of the wedge when the surface impedance is reduced, resulting in higher vortex acceleration and thus stronger sound radiation. The final velocity of the vortex is higher than that in the hard surface case.

In a perfectly inviscid fluid medium, the far-field sound is only affected by the effective fluid density and the wedge angle. It is found that a finite effective fluid density deflects the directivity towards the porous surface. The extent of such deflection increases with increasing effective fluid density. However, the rate of decay of the sound pulse with distance from the edge is lower if the effective fluid density is reduced. The introduction of a porous surface in a perfectly inviscid fluid results in louder and more distant sound radiation.

When the fluid possesses a finite viscosity, the flow resistance inside the lattice of the porous material becomes significant. The higher the flow resistance, the higher the ability of the porous surface to support pressure, resulting in weaker sound pulse in the far-field. However, unlike the effect of the effective fluid density, the directivity and the rate of decay of the sound radiation in the leading order of magnitude are the same as those with hard surfaces, regardless of the magnitude of the flow resistance.

Chapter 5: Vortex Sound Generation due to a Piece-wise Porous Material on an Infinite Rigid Plane

5.1 Introduction

The problem of sound generation by an inviscid vortex translating past a porous half cylinder and a porous wedge are studied in Chapters 3 and 4 respectively. In this chapter, vortex sound in the presence of a piece-wise porous material with finite thickness on an otherwise infinite rigid plane is studied. Apart from the initial vortex height, the effective fluid density and the flow resistance of the porous material, the effects of the length and the thickness of the porous material on the vortex dynamics and the far-field sound radiation are also discussed. The conformal mapping technique applied in Chapters 3 and 4 is not easy to implement in this circumstance. However, the streamfunctions in the flow and in the porous regions and the velocity of the vortex can be evaluated by the continuity of fluid velocity and pressure on the porous boundary together with the use of Fourier transform. The far-field sound pressure is derived using the matched asymptotic expansion method as in the previous chapters.

5.2 Theoretical Development

An inviscid vortex with circulation Γ located at z_{1i} far away from the piece-wise porous material with length L and thickness h is considered [Figure 5.1]. All the length scales in the present study are normalized by the initial vortex height y_{1i} above the x-axis. Also, the time scale, the velocity of the vortex and the flow resistance R_f are normalized by y_{1i}^2/Γ, Γ/y_{1i} and $\rho_o\Gamma/y_{1i}^2$ respectively.

Inside the fluid region ($y \geq 0$),

$$\nabla^2 \psi_z = -\delta(x - x_1)\delta(y - y_1), \tag{5.1}$$

and within the porous material ($-h \leq y \leq 0$, $0 \leq x \leq L$) [Equation (1.10)],

$$\nabla^2 \psi_{pl} = 0, \tag{5.2}$$

where ψ_z and ψ_{pl} are the streamfunctions in the fluid and in the porous regions respectively, and are normalized by Γ. ∇^2 and δ are Laplacian operator and delta function respectively. The boundary conditions at the interface of the porous material and the rigid wall are:

$$\left.\frac{\partial \phi_{pl}}{\partial x}\right|_{x=0} = \left.\frac{\partial \psi_{pl}}{\partial y}\right|_{x=0} = \left.\frac{\partial \phi_{pl}}{\partial x}\right|_{x=L} = \left.\frac{\partial \psi_{pl}}{\partial y}\right|_{x=L} = -\left.\frac{\partial \psi_{pl}}{\partial x}\right|_{y=-h} = 0, \tag{5.3}$$

where ϕ_{pl} is the flow potential in the porous region. Equation (5.3) implies that the normal velocity at the interface between the porous material and the rigid wall vanishes. From Equations (5.2) and (5.3), one can quickly find that the solution of ψ_{pl} is

$$\psi_{pl} = \sum_{n=1}^{\infty} A_n e^{\alpha_n h} \sin(\alpha_n x) \sinh[\alpha_n (h + y)], \tag{5.4}$$

where $\alpha_n = n\pi/L$, $n = 1, 2, 3, \ldots$ and A_n is the mode magnitude.

As in Tang [2001], the x-Fourier transform of Equation (5.1) gives

$$\psi_z^x = \begin{cases} G_1 e^{-|k|y} + G_2 e^{|k|y} & 0 \le y \le y_1 \\ H_1 e^{-|k|y} + H_2 e^{|k|y} & y_1 \le y \le \infty \end{cases}, \tag{5.5}$$

where G_1, G_2, H_1 and H_2 are function of k and $\psi_z^x = \int_{-\infty}^{\infty} \psi_z e^{ikx} dk$. The continuity of ψ_z^x and the vorticity jump $\frac{\partial \psi_z^x}{\partial y}$ at $y = y_1$ lead to

$$H_1 - G_1 = \frac{1}{2|k|} e^{ikx_1 + |k|y_1} \text{ and } G_2 - H_2 = \frac{1}{2|k|} e^{ikx_1 - |k|y_1}. \tag{5.6}$$

$H_2 = 0$ for the outgoing wave condition. And on the porous boundary ($y = 0$, $0 \le x \le L$), the continuity of normal fluid velocity gives

$$-\left.\frac{\partial \psi_z}{\partial x}\right|_{y=0} = -\left.\frac{\partial \psi_{pl}}{\partial x}\right|_{y=0}. \tag{5.7}$$

The relationship between G_1 and A_n can be found by substituting the x-Fourier transforms of Equations (5.4) and (5.5) into Equation (5.7):

$$G_1 = \sum_{n=1}^{\infty} \alpha_n A_n e^{\alpha_n h} \sinh(\alpha_n h) \frac{(-1)^n e^{ikL} - 1}{k^2 - \alpha_n^2} - \frac{1}{2|k|} e^{ikx_1 - |k|y_1}. \tag{5.8}$$

The continuity of pressure on the porous boundary ($y = 0$, $0 \le x \le L$) gives, from Equation (1.9),

$$\frac{\partial}{\partial t}\left(\left.\frac{\partial \psi_z}{\partial y}\right|_{y=0}\right) = \eta\frac{\partial}{\partial t}\left(\left.\frac{\partial \psi_{pl}}{\partial y}\right|_{y=0}\right) + R_f\left.\frac{\partial \psi_{pl}}{\partial y}\right|_{y=0}. \tag{5.9}$$

The application of the inverse Fourier transform to Equation (5.9) suggests that,

$$\frac{1}{2\pi}\int_{-\infty}^{\infty}|k|\left(\dot{G}_2 - \dot{G}_1\right)e^{-ikx}dk = \sum_{n=1}^{\infty}\left(\eta\dot{A}_n + R_f A_n\right)\alpha_n e^{\alpha_n h}\sin(\alpha_n x)\cosh(\alpha_n h), \tag{5.10}$$

where $\cdot$ denotes differentiation with respect to time. After some algebra, Equation (5.10) can be expressed into

$$-\frac{1}{\pi}\sum_{n=1}^{\infty}\alpha_n\dot{A}_n e^{\alpha_n h}\sinh(\alpha_n h)\int_0^L I_n(x)\sin(\alpha_m x)dx - \frac{u_{z1}}{\pi}\int_0^L\frac{2y_1(x_1-x)\sin(\alpha_m x)}{\left[y_1^2+(x_1-x)^2\right]^2}dx + \frac{v_{z1}}{\pi}\int_0^L\frac{(x_1-x)^2-y_1^2}{\left[y_1^2+(x_1-x)^2\right]^2}\sin(\alpha_m x)dx = \frac{1}{2}\left(\eta\dot{A}_m + R_f A_m\right)\alpha_m e^{\alpha_m h}\cosh(\alpha_m h),$$

(5.11)

where m = 1, 2, 3, …,

$I_n = \cos(\alpha_n x)\left[ci(\alpha_n x) - ci(\alpha_n(L-x))\right] + \sin(\alpha_n x)\left[si(\alpha_n x) + si(\alpha_n(L-x)) + \pi\right]$, and

$si(x) = -\int_x^{\infty}\frac{\sin t}{t}dt$ and $ci = -\int_x^{\infty}\frac{\cos t}{t}dt$ represent the sine and cosine integrals respectively,. In addition, the integral I_n in Equation (5.11) can be further reduced to

$$\int_0^L I_n(x)\sin(\alpha_m x)dx = \begin{cases} \dfrac{2\alpha_m}{\alpha_m^2-\alpha_n^2}\left[ci(m\pi)-ci(n\pi)\right] & \text{if } m+n \text{ is even}, m\neq n \\ \\ \dfrac{\pi L}{2}+\int_0^L si(\alpha_n x)dx & \text{if } m=n \\ \\ 0 & \text{otherwise} \end{cases} . \quad (5.12)$$

On the other hand, the longitudinal and transverse velocities of the vortex are [Tang, 2001]:

$$\begin{aligned} u_{z1} &= \left.\frac{\partial\left(\psi_z - G_2 e^{|k|y}\right)}{\partial y}\right|_{x=x_1, y=y_1} \\ &= \frac{1}{\pi}\sum_{n=1}^{\infty}\alpha_n A_n e^{\alpha_n h}\sinh(\alpha_n h)\int_0^L \frac{(x_1-x)\cos(\alpha_n x)}{(x_1-x)^2+y_1^2}dx + \frac{1}{4\pi y_1} \end{aligned} , \quad (5.13)$$

and

$$\begin{aligned} v_{z1} &= -\left.\frac{\partial\left(\psi_z - G_2 e^{|k|y}\right)}{\partial x}\right|_{x=x_1, y=y_1} \\ &= \frac{1}{\pi}\sum_{n=1}^{\infty}\alpha_n A_n e^{\alpha_n h}\sinh(\alpha_n h)\int_0^L \frac{y_1\cos(\alpha_n x)}{(x_1-x)^2+y_1^2}dx \end{aligned} . \quad (5.14)$$

The integrals in Equations (5.13) and (5.14) correspond to the flow field induced by the normal fluid velocity at y = 0, 0 ≤ x ≤ L. Equations (5.13) and (5.14) can be coupled with Equation (5.11) to estimate the vortex position z_1 and the mode magnitude A_n. Initial $A_n \equiv 0$.

The streamfunction ψ_z can be derived by the inverse Fourier transform of Equation (5.5) together with the help of Equation (5.8):

$$\psi_z = \frac{1}{2\pi}\sum_{n=1}^{\infty}\alpha_n A_n e^{\alpha_n h}\sinh(\alpha_n h)\int_{-\infty}^{\infty}\frac{(-1)^n e^{ikL}-1}{k^2-\alpha_n^2}e^{-|k|y}e^{-ikx}dk$$
$$-\frac{1}{4\pi}\int_{-\infty}^{\infty}\frac{1}{|k|}e^{-ik(x-x_1)-|k|(y+y_1)}dk+\frac{1}{4\pi}\int_{-\infty}^{\infty}\frac{1}{|k|}e^{-ik(x-x_1)+|k|(y-y_1)}dk \quad . \qquad (5.15)$$

The flow potential can then be evaluated through the use of the Cauchy-Rieman principle:

$$\phi_z = \frac{1}{2\pi}\sum_{n=1}^{\infty}\alpha_n A_n e^{\alpha_n h}\sinh(\alpha_n h)\int_{-\infty}^{\infty}\frac{1}{ik}\frac{(-1)^n e^{ikL}-1}{k^2-\alpha_n^2}|k|e^{-|k|y}e^{-ikx}dk$$
$$-\frac{1}{4\pi}\int_{-\infty}^{\infty}\frac{1}{ik}e^{-ik(x-x_1)-|k|(y+y_1)}dk-\frac{1}{4\pi}\int_{-\infty}^{\infty}\frac{1}{ik}e^{ik(x-x_1)-|k|(y-y_1)}dk+C \quad , \qquad (5.16)$$

where C is the integration constant. It can be shown that by observing the flow potential vanishes when $|z| \to \infty$, $C = 0$. Using the formula tabulated in Gradshteyn and Ryzhik [1980], the flow potential becomes

$$\phi_z = \frac{1}{2\pi}\sum_{n=1}^{\infty}\alpha_n A_n e^{\alpha_n h}\sinh(\alpha_n h)\int_{-\infty}^{\infty}\frac{1}{ik}\frac{(-1)^n e^{ikL}-1}{k^2-\alpha_n^2}|k|e^{-|k|y}e^{-ikx}dk$$
$$+\frac{1}{2\pi}\tan^{-1}\frac{y-y_1}{x-x_1}-\frac{1}{2\pi}\tan^{-1}\frac{y+y_1}{x-x_1} \quad . \qquad (5.17)$$

The integral term in Equation (5.17) represents the flow potential induced by the porous material while the other is the flow potential induced by an infinite rigid plane. The far-field inner potential at large $|z|$ is

$$\phi_{zi} = \left[-\frac{2}{\pi} \sum_{n=1,3,5,\ldots}^{\infty} \frac{1}{\alpha_n} A_n e^{\alpha_n h} \sinh(\alpha_n h) - \frac{1}{\pi} r_1 \sin\theta_1 \right] \frac{\cos\theta}{r} + O\left(r^{-2}\right), \tag{5.18}$$

where (r_1, θ_1) is the polar coordinates of the inviscid vortex position and (r, θ) is a point in the flow field. Following the steps in Chapter 3, the far-field sound pressure p at large distance R is

$$p = \frac{1}{\pi} \sqrt{\frac{1}{2c_o \mathrm{R}}} \frac{\partial}{\partial t} \int_{-\infty}^{t_o - \mathrm{R}/c_o} \frac{\partial}{\partial \tau} \left[\frac{2}{\pi} \sum_{n=1,3,5,\ldots}^{\infty} \frac{1}{\alpha_n} A_n e^{\alpha_n h} \sinh(\alpha_n h) + \frac{1}{\pi} r_1 \sin\theta_1 \right] \times \frac{d\tau}{\sqrt{t_o - \tau - \mathrm{R}/c_o}} \cos\theta, \tag{5.19}$$

where the far-field sound pressure is normalized by $\rho_0 \Gamma / y_{1i}^2$ and it can be shown from Equation (5.19) that the far-field sound pressure consists of longitudinal dipoles.

5.3 Vortex Paths and Sound

In the present investigation, the far-field sound pressure is obtained at large r, and the directivity of the sound pressure consists of longitudinal dipoles only. The vortex dynamics are obtained from the coupled Equations (5.11), (5.13) and (5.14) with the appropriate number of mode A_n and so is the far-field sound pressure in

Equation (5.19). Ten terms for A_n are enough for a reliable solution as the difference of P_x for 10-terms with that for 20-terms is already in the order of 10^{-6} [Figure 5.2] while the maximum $|P_x|$ for the 20-terms is in the order of 10^{-3} for $L = 2$, $h = 2$ and $\eta = 5$ at different R_f [Figure 5.3]. In the rest of this chapter, only results obtained with 10-terms for A_n are presented.

For the case of an infinite rigid plane, the longitudinal and transverse velocities of the vortex from Equations (5.13) and (5.14) converge to $u_{z1} = \dfrac{1}{4\pi y_0}$ and $v_z = 0$. The inviscid vortex propagates with a constant velocity in the longitudinal direction, and generates no sound. P_x tends to zero when $\eta = 5$ at large R_f or large $\eta = 100$ at various R_f with fixed $L = 2$ and $h = 2$ [Figure 5.4]. The effective fluid density or the flow resistance inside the lattice of the porous material is so large that it has no effect on both the vortex dynamics and the sound pressure. Besides, the mode magnitude A_n for all n ($n = 1$ to 10) tends to zero.

5.3.1 Perfectly Invscid Fluid

For a perfectly inviscid fluid, the flow resistance vanishes ($R_f = 0$). Figure 5.4(a) shows the effects of L and η for $h = 2$ on the vortex path. The vortex is initially located far away from the finite length porous material for $L = 1$, $\eta = 3$. The inviscid vortex experiences the pressure-releasing effect due to the porous material and bends towards the porous material for $-2 < x < 0.5$. It gradually propagates back to its original height for $0.5 < x < 2$ due to the pressure-supporting effect of the rigid plane at $y = 0$, $x \geq 1$. The vortex path is symmetrical about the transverse axis at $x = 0.5$. When the porous material is less pressure-releasing, less severe bending towards the porous material is observed, and the vortex path converges to that under the infinite rigid wall condition for large η. When the length of the porous material is increased to 2 at η = 3, the degree of bending towards the porous material is more serious than that for the case with L = 1 and η = 3. This situation becomes more serious when the length of the porous material is further increased to L = 10/3. It is due to the longer duration of the interaction between the inviscid vortex and the porous material. The vortex undergoes a substantial large rate of change of velocity by such prolonged interaction [Figures 5.4(b) to 5.4(e)]. Here, t_a denotes the time at which the vortex passes across the leading edge of the porous material. The larger the value of η, the smaller the magnitudes of u_{z1} and v_{z1}. The magnitudes of u_{z1} and v_{z1} increase with L [Figures 5.4(b) and 5.4(c)]. One can also observe that the vortex accelerations are increased by either decreasing η or increasing L [Figures 5.4(d) and 5.4(e)]. Figure 5.4(f) shows the time variation of the longitudinal dipole P_x at a fixed h = 2. The magnitude of P_x increases as η decreases for L = 1 [Figure 5.4(f)] due to the amplification of the vortex accelerations [Figures 5.4(d) and 5.4(e)], and P_x approaches zero for η = 100. On the other hand, P_x increases with L, and a longer duration of active sound generation is also observed. It is due to the earlier movement of the inviscid vortex and the longer duration under the influence of the porous material.

At a fixed L and η under various h, the inviscid vortex propagates in a path closer to the porous material because of the stronger pressure-releasing effect of a thicker porous material [Figure 5.5(a)]. The larger the value of h, the more serious bending towards the porous material. The vortex motions are not affected by further increasing h at a fixed L = 1 and η = 3. One can expect that this value of h increases when either L increases or η decreases. The magnitudes of u_{z1}, v_{z1} and the longitudinal and transverse accelerations increase at increased L [Figures 5.5(b) to

5.5(e)], and an amplification of P_x is observed as h increases [Figure 5.5(f)]. However, the amplitude of P_x reaches its maximum at $h \approx 1$.

Figure 5.6 summarizes the effects of L, h and η on the generation of P_x in a perfectly inviscid fluid. In general, the amplitude of P_x increases when L or h increases. When h is small (h = 0.01), the influence of the porous material on the vortex accelerations diminishes [Figures 5.5(d) and 5.5(e)], resulting in a lower amplitude of P_x [Figure 5.5(f)]. Increase in P_x is concentrated from h = 0.1 to 1 [Figures 5.6(a) and 5.6(b)]. The amplitude of P_x is not affected much by further increasing h. It is due to the pressure-supporting effect from the rigid wall at $x > 1$. One can notice that P_x increases for $h > 1$ when L = 2 and L = 10/3 [Figures 5.6(c) and 5.6(d)]. For the effect of η, a higher magnitude of P_x is observed under a strong pressure-releasing effect for small η. The acoustical energy radiated in a perfectly inviscid fluid exhibits similar pattern with the sound pressure presented in Figure 5.6 [Figure 5.7].

5.3.2 Combined Effects of η and R_f

When the flow resistance R_f is finite, the effective fluid density and the flow resistance R_f inside the lattice of the porous material will produce pressure-releasing and pressure-supporting effects respectively as shown in Chapters 3 and 4. Figure 5.8(a) shows their combined effects on the vortex motion for L = 1, h = 1 and η = 3 under various R_f. The situation for the perfectly inviscid fluid (R_f = 0) is also shown for the sake of comparison. For R_f = 0.05, the vortex bends towards the porous material at $-2 < x < 0.5$ because of the pressure-releasing effect, and then surfs up at $0.5 < x < 1.2$ due to the presence of the rigid wall. At $x > 1.2$, the inviscid vortex propagates in a path lower than the cases for the rigid wall condition and the perfectly inviscid fluid. Similar phenomenon was also observed in Chapter 3 that the inviscid vortex will not resume its original height after interacting with the porous half cylinder mounted on an otherwise rigid plane when R_f is small. In addition, the vortex path is not symmetrical about $x = 0.5$. When $R_f = 0.1$, the vortex propagates more closely to its original height at $-2 < x < 1.2$ but at $x > 1.2$, it still bends towards the horizontal axis. This situation of the vortex path at $x > 1.2$ is different once the flow resistance is increased (for instance, $R_f = 1$), the vortex path gradually rises back to its initial height, and soon recovers to that under the rigid wall condition for $R_f = 10$. At large R_f, the pressure-supporting effect is very strong that it overcomes the pressure-releasing effect, A_n tends to zero and becomes less influential to the vortex velocity [Equations (5.13) and (5.14)] such that the path of the inviscid vortex matches that for the rigid wall case.

Figures 5.8(b) to 5.8(e) show the corresponding time variations of vortex velocity and acceleration for $L = 1$, $h = 1$ and $\eta = 3$ with different R_f. The magnitude of u_{z1} increases as R_f increases from 0 to 0.1 [Figure 5.8(b)]. One can also notice that such increase in u_{z1} is from $x > 1.2$ (The instant for $t - t_a > 20$). However, u_{z1} decreases for $0.1 < R_f < 10$ and matches the rigid wall condition when $R_f = 10$. The magnitude of v_{z1} decreases with increasing R_f [Figure 5.8(c)]. The acceleration of the vortex increases with decreasing R_f [Figures 5.4(d) and 5.4(e)] though that of u_{z1} does not. Figure 5.8(f) shows some examples of the time variation of P_x at $L = 1$, $h = 1$ and $\eta = 3$ at various R_f. The amplitude of P_x is maximum for the perfectly inviscid fluid case, and decreases with increasing R_f. The magnitudes of the first crest and trough decrease while the magnitude of the second crest increases as R_f increases from 0 to 0.1. When $R_f > 1$, the magnitude of P_x decreases since the magnitudes of vortex accelerations are lowered [Figures 5.8(d) and 5.8(e)]. The properties of the porous material are dominated by the pressure-supporting effect at increased R_f, and the sound radiation becomes very weak as R_f increases to 10.

Figure 5.9(a) shows the vortex dynamics for various h and η at L = 1 and R_f = 1. The smaller the value of η, the greater the bending towards the porous material. This serious bending in the vortex path is due to the strong pressure-releasing effect at small η. The vortex path converges to that for the infinite rigid plane condition for η = 100. Similar to the perfectly inviscid fluid case, the degree of bending increases with increasing h, and the vortex motion is not affected by further increasing h beyond 1. The effect of increasing h is similar to that of decreasing the value of η (increasing the pressure-releasing effect) but the former one produces no further effect on the vortex dynamics at large h. The effects of varying h and η on the vortex dynamics are similar to those presented in the perfectly inviscid fluid case [Figures 5.4(a) and 5.5(a)]. Figure 5.9(b) shows the time variation of P_x with different h and η. The magnitude of P_x decreases when h decreases or η increases. When h increases, the pulse shape of P_x shifts upwards, and the magnitude of P_x increases.

Figure 5.10(a) shows the effect of L at h = 2 and η = 5 for various R_f on the vortex dynamics. When the flow resistance is fixed at R_f = 2, the vortex propagates in a path closer to the porous material with a longer L. The same is true for a fixed R_f with different L. When L increases to 10/3, the variation of the vortex dynamics [Figure 5.10(a)] and the vortex velocity [Figures 5.10(b) and 5.10(c)] are similar to those presented in Figure 5.8. However the longitudinal acceleration of the vortex increases as R_f increases from 0 to 0.45 and then decreases again upon further increase in R_f, while the transverse acceleration decreases at increased R_f [Figures 5.10(d) and 5.10(e)]. When the length of the porous material is increased to 10/3, the small flow resistance inside the porous material increases the vortex acceleration when the vortex propagates over $x = 1$ and $x = 10/3$. This is due to the bigger impedance mismatch between the junction of the rigid wall and the porous material at small R_f. One can expect that the magnitude of P_x decreases with increasing R_f [Figure 5.10(f)].

The magnitude of P_x at different L, h, η and R_f is summarized in Figure 5.11. For $L = 1$ [Figure 5.11(a)], an increase in the thickness h of the porous material increases the magnitude of P_x, but the magnitude of P_x is not affected by further increasing h beyond 1. The thickness h does not affect very much the vortex dynamics [Figure 5.9(a)] and the vortex accelerations [Figures 5.9(d) and 5.9(e)]. The magnitude of P_x is higher for $\eta = 3$ than that for $\eta = 5$, and it decreases more than two orders as R_f increases from 0 to 100. A more rapid decrease in P_x is observed from $R_f = 0$ to $R_f = 10$ when L is small. The magnitude of P_x increases when L increases from 1 to 2 [Figure 5.11(b)] for a fixed η and R_f [Figure 5.11(a)]. The vortex propagates with substantial large vortex acceleration [Figures 5.2(d) and 5.2(e)] under the pressure-releasing effect of the porous material, resulting in an amplification of P_x. It is the consequence of the longer duration of the interaction between the inviscid vortex and the porous material. Comparing the thickness of the porous material at $L = 1$ and $L = 2$, an increase of the magnitude of P_x is observed for h deeper than 1. One can also expect that the variation of P_x for $L = 10/3$ is similar to those for $L = 1$ and $L = 2$ [Figures 5.11(b) and 5.11(c)], but the magnitude of P_x is not lowered when R_f increases [Figure 5.11(c)]. It may be due to the fluctuation of the vortex acceleration at different R_f [Figures 5.10(d) and 5.10(e)]. The magnitude of P_x decreases as R_f increases from 0 to 0.09 and increases slightly for $0.09 < R_f < 0.45$. It converges to that under the rigid wall condition for $R_f \geq 10$. The corresponding sound energy radiation is shown in Figure 5.12. The energy variation pattern is similar to those presented in Figure 5.11.

5.4 Summary

The vortex sound generation in the presence of a piece-wise porous material on an otherwise infinite rigid plane is studied. The configuration is analogous to the boundary of a dissipative silencer or a lined duct. The streamfunctions inside the fluid medium and the porous material are derived, and the coupled equations of the vortex motions are evaluated by matching the continuity of pressure and normal fluid velocity at the interface of the fluid medium and the porous material. The standard fourth order Runge-Kutta method is used to solve the coupled equations. The far-field sound pressure is evaluated by the method of matched asymptotic expansions.

When an inviscid vortex engages a finite length porous material, the sound pressure radiated consists of longitudinal dipoles, and the time variations of the longitudinal dipoles are pulse-like. The vortex generates no sound when the length or thickness of the porous material is small such that the presence of the porous material does not affect the vortex acceleration. The sound pressure increases as the effective fluid density decreases because of the strong pressure-releasing effect of the porous boundary. It decreases when a finite flow resistance exists inside the porous material. However, the magnitude of the sound pressure does not decrease monotonically with increasing flow resistance when the length of the porous material increases. The value of this sound pressure converges to that for the rigid wall condition when the flow resistance is large. One can also conclude that the magnitude of the sound pressure is higher when the flow resistance vanishes. The effect of thickening the porous material is similar to that of lengthening it except that an increase in the sound pressure with increasing flow resistance is not observed. A thicker porous material produces a stronger sound but the sound magnitude has an upper bound as the vortex motion will not be affected by further increasing the thickness at a specified length of the porous material.

Chapter 6: Vortex Sound Generation in a Lined Duct

6.1 Introduction

We show in Chapter 5 that the sound pressure generated under the influence of a piece-wise porous material on an otherwise infinite rigid plane consists of longitudinal dipoles. The sound pressure increases by either increasing the length or the thickness of the porous material. Also, the sound pressure magnitude increases under the influence of a pressure-releasing surface. The situation in Chapter 5 of an inviscid vortex interacting with a finite length porous material on an otherwise infinite rigid plane is analogous to the case near the boundary of a lined duct. The focus in Chapter 5 is extended to model the vortex sound generation in a lined duct in this chapter. The effects of the length, thickness, effective fluid density and flow resistance of the porous material are examined. The effect of initial vortex height is also discussed.

6.2 Theoretical Development

An inviscid vortex with circulation Γ located at z_{1i} moves inside a lined duct as shown in Figure 6.1. The length and the thickness of the porous material are denoted by L and h respectively, while d denotes the width of the air duct. Also, all the length scales, the time and the flow resistance of the porous material in the present study are normalized by d, d^2/Γ and $\rho_o\Gamma/d^2$ respectively.

The analysis is started by deriving the streamfunction in the flow and porous regions as in Chapter 5. The streamfunction in the fluid region for $0 \le y \le 1$ satisfies Equation (5.1), while the streanfunction ψ_{pl} ($0 \le x \le L$, $-h \le y \le 0$) and ψ_{pu} ($0 \le x \le L$, $1 \le y \le 1 + h$) within the porous materials satisfy Equation (1.10). Thus, one can substitute the boundary condition [Equation (5.3)] of the porous materials into the solution of Equation (1.10). The streamfunction ψ_{pl} ($0 \le x \le L$, $-h \le y \le 0$) is the same as that shown in Equation (5.4), while the streamfunction ψ_{pu} ($0 \le x \le L$, $1 \le y \le 1 + h$) is

$$\psi_{pu} = \sum_{n=1}^{\infty} B_n e^{\alpha_n(1+h)} \sin(\alpha_n x) \sinh[\alpha_n(1+h-y)], \tag{6.1}$$

where $\alpha_n = n\pi/L$ and $n = 1, 2, 3,\ldots$ and B_n is the mode magnitude.

Through the application of continuity of normal fluid velocity at $y = 0$, $0 \le x \le L$ and $y = 1$, $0 \le x \le L$, one obtains from Equation (5.5),

$$G_1 = \sum_{n=1}^{\infty} \alpha_n A_n e^{\alpha_n h} \sinh(\alpha_n h) \frac{(-1)^n e^{ikL} - 1}{k^2 - \alpha_n^2} - G_2, \tag{6.2}$$

and

$$H_1 = \sum_{n=1}^{\infty} \alpha_n B_n e^{\alpha_n(1+h)} \sinh(\alpha_n h) \frac{(-1)^n e^{ikL} - 1}{k^2 - \alpha_n^2} e^{|k|} - H_2 e^{2|k|}. \tag{6.3}$$

In this case, $H_2 \neq 0$. Substitute ψ_{pl} [Equation (5.4)], ψ_{pu} [Equation (6.1)] and ψ_z [Equation (5.5)] into the continuity of pressure at the boundary [Equation (5.9)], $y = 0$, $0 \leq x \leq L$ and $y = 1$, $0 \leq x \leq L$:

$$\frac{1}{2\pi}\int_{-\infty}^{\infty}|k|\left(\dot{G}_2-\dot{G}_1\right)e^{-ikx}dk=\sum_{n=1}^{\infty}\left(\eta\dot{A}_n+R_f A_n\right)\alpha_n e^{\alpha_n h}\sin(\alpha_n x)\cosh(\alpha_n h), \tag{6.4}$$

and

$$\frac{1}{2\pi}\int_{-\infty}^{\infty}|k|\left(\dot{H}_2 e^{|k|}-\dot{H}_1 e^{-|k|}\right)e^{-ikx}dk=-\sum_{n=1}^{\infty}\left(\eta\dot{B}_n+R_f B_n\right)\alpha_n e^{\alpha_n(1+h)}\sin(\alpha_n x)\cosh(\alpha_n h). \tag{6.5}$$

The longitudinal and transverse velocities of the vortex are [Equations (5.13) and (5.14)]:

$$\begin{aligned}u_{z1}&=\frac{1}{4}\cot(y_1\pi)\\&\quad-\frac{1}{\pi}\sum_{n=1}^{\infty}\alpha_n A_n e^{\alpha_n h}\sinh(\alpha_n h)\int_0^{\infty}\frac{(-1)^n\cos[k(L-x_1)]-\cos(kx_1)}{k^2-\alpha_n^2}\frac{k\cosh[k(y_1-1)]}{\sinh k}dk\\&\quad+\frac{1}{\pi}\sum_{n=1}^{\infty}\alpha_n B_n e^{\alpha_n(1+h)}\sinh(\alpha_n h)\int_0^{\infty}\frac{(-1)^n\cos[k(L-x_1)]-\cos(kx_1)}{k^2-\alpha_n^2}\frac{k\cosh(ky_1)}{\sinh k}dk\end{aligned}, \tag{6.6}$$

and

$$\begin{aligned}v_{z1}&=\frac{1}{\pi}\sum_{n=1}^{\infty}\alpha_n A_n e^{\alpha_n h}\sinh(\alpha_n h)\int_0^{\infty}\frac{(-1)^n\sin[k(L-x_1)]+\sin(kx_1)}{k^2-\alpha_n^2}\frac{k\sinh[k(y_1-1)]}{\sinh k}dk\\&\quad-\frac{1}{\pi}\sum_{n=1}^{\infty}\alpha_n B_n e^{\alpha_n(1+h)}\sinh(\alpha_n h)\int_0^{\infty}\frac{(-1)^n\sin[k(L-x_1)]+\sin(kx_1)}{k^2-\alpha_n^2}\frac{k\sinh(ky_1)}{\sinh k}dk\end{aligned}, \tag{6.7}$$

respectively. The first term in Equation (6.6) is equivalent to an inviscid vortex moving inside a rigid air duct with a constant velocity, and the integrals in Equations (6.6) and (6.7) correspond to the flow fields induced by the normal velocity at $y = 0$, $0 \leq x \leq L$ and $y = 1$, $0 \leq x \leq L$ (porous material/fluid interfaces). Thus, the path of the vortex can be obtained by integrating the coupled Equations (6.4) to (6.7) numerically using the standard fourth order Runge-Kutta method.

The flow potential of an inviscid vortex can be evaluated through the use of Cauchy-Rieman principle with Equation (5.5),

$$\phi_z = -\frac{1}{2\pi}\int_{-\infty}^{\infty}\frac{1}{ik}(-|k|G_1 e^{-|k|y} + |k|G_2 e^{|k|y})e^{-ikx}dk + C\ , \tag{6.8}$$

where C is the integration constant. It can be shown by observing the flow potential tends to $(1 - y_1)/2$ when $|x| \rightarrow \infty$ that $C = 0$. Equation (6.8) becomes

$$\begin{aligned}\phi_z &= \frac{1}{2\pi}\tan^{-1}\left[\tan\frac{(1-y_1+y)\pi}{2}\tanh\frac{(x-x_1)\pi}{2}\right] \\ &+ \frac{1}{2\pi}\tan^{-1}\left[\tan\frac{(1-y_1-y)\pi}{2}\tanh\frac{(x-x_1)\pi}{2}\right] \\ &+ \frac{1}{\pi}\sum_{n=1}^{\infty}\alpha_n A_n e^{\alpha_n h}\sinh(\alpha_n h)\int_0^{\infty}\frac{(-1)^{n+1}\sin[k(x-L)]+\sin kx}{k^2-\alpha_n^2}\frac{\cosh[k(1-y)]}{\sinh k}dk \\ &- \frac{1}{\pi}\sum_{n=1}^{\infty}\alpha_n B_n e^{\alpha_n(1+h)}\sinh(\alpha_n h)\int_0^{\infty}\frac{(-1)^{n+1}\sin[k(x-L)]+\sin kx}{k^2-\alpha_n^2}\frac{\cosh ky}{\sinh k}dk\end{aligned}\ . \tag{6.9}$$

The integral terms in Equation (6.9) together represent the flow potential induced by the porous material while the remainder implies the flow potential due to the infinite rigid duct. Using the formula tabulated in Gradshteyn and Ryzhik [1980], the far-field inner potential at large $|x|$ is

$$\phi_{zi} = \frac{1}{2}(1 - y_1) + \sum_{n=1,3,5...}^{\infty}\left[B_n e^{\alpha_n(1+h)} - A_n e^{\alpha_n h}\right]\frac{\sinh(\alpha_n h)}{\alpha_n}, \tag{6.10}$$

and the far-field outer potential can be obtained by the matched asymptotic method as in Chapter 3:

$$\phi_{zo} = \frac{1}{2\pi}\int_{-\infty}^{\infty}\left[\frac{1}{2}(1 - y_1) + \sum_{n=1,3,5...}^{\infty}\left[B_n e^{\alpha_n(1+h)} - A_n e^{\alpha_n h}\right]\frac{\sinh \alpha_n h}{\alpha_n}\right]^t e^{ikx} e^{-i\omega t} d\omega, \tag{6.11}$$

where $[]^t$ denotes the Fourier transform with respect to time. Thus, the far-field pressure is evaluated through the use of Equation (1.8):

$$p = -\frac{\partial}{\partial t_o}\sigma\left(t - \frac{x}{c_o}\right), \tag{6.12}$$

where $\sigma = \frac{1}{2\pi}\left\{\frac{1}{2}(1 - y_1) + \sum_{n=1,3,5...}^{\infty}\left[B_n e^{\alpha_n(1+h)} - A_n e^{\alpha_n h}\right]\frac{\sinh(\alpha_n h)}{\alpha_n}\right\}$ and the far-field sound pressure is normalized by $\rho_0\Gamma^2/d^2$. Equation (6.11) shows that a plane acoustic wave is generated under the influence of the porous material inside the lined duct.

6.3 Vortex Paths and Sound

In Chapter 5, we show that the far-field sound pressure is not affected much by the presence of higher order modes inside the porous material. In this chapter, the mode magnitude A_n and B_n are calculated up to 5-terms each as the difference of p obtained from a 5-terms truncation with 10-terms truncation is in the order of 10^{-5} while the maximum of p for the 10-terms calculation is in the order of 10^{-3} for $y_{1i} = 0.2$, $L = 2$, $h = 0.2$, $\eta = 3$ with various R_f. The vortex is initially located at far away from the porous material, and the vortex height is set to be $y_{1i} = 0.2$ or 0.3 such that the vortex propagates in the positive x-direction. The contribution from the upper part of the porous material is less than that from the lower part. When the vortex is initially located at the centreline of the air duct, it will remain stationary in the original position and generates no sound. When $y_{1i} > 0.5$, the vortex propagates in the negative x-direction with constant velocity so that the porous material does not affect the vortex motion.

6.3.1 Perfectly Invscid Fluid

For a perfectly inviscid fluid, the flow resistance $R_f = 0$. Figure 6.2(a) shows the vortex path with different h and η at for $y_{1i} = 0.2$ and $L = 1$. For $h = 0.2$ and $\eta = 3$, the vortex propagates towards the porous material ($0 \leq x \leq 1$ and $-0.2 \leq y \leq 0$) with a minimum vortex height of $y \approx 0.14$ ($x \approx 0.52$) due to the pressure-releasing effect of the porous material. The vortex moves upwards for $0.52 < x < 1.4$ under the influence of the pressure-supporting effect of the rigid wall beyond $x = 1$. The loss in symmetry is due to the pressure-supporting effect from the rigid wall at the downstream section when the vortex propagates across the porous material. One can notice that the larger the value of η ($\eta = 5$), the less severe the vortex will bend towards the lower porous material. When h increases to 0.4 with η fixed at 3, the vortex experiences a stronger pressure-releasing effect by the lower porous material and propagates closer to its surface. This situation becomes more serious when h is increased further. One can expect from Figure 5.5(a) that the vortex motion becomes independent of h

when h is large. Unlike the vortex paths for a perfectly inviscid fluid in Chapters 3 and 5 [Figures 3.3(a) and 5.4(a)], the vortex paths are not symmetrical about x = $0.5L$ in the present situation, and the vortex will not propagate back to its initial height after interacting with the porous material.

Figures 6.2(b) and 6.2(c) show the corresponding longitudinal and transverse velocities of the vortex. The longitudinal and transverse velocities of the vortex are $1/4\cot(y_1\pi) = 0.34$ and 0 respectively when the vortex is located at $y_{1i} = 0.2$ and is far away from the porous material [Equations (6.6) and (6.7)]. Relatively large change in the vortex velocity is observed when the vortex propagates over the porous material, suggesting significant sound generation [Powell, 1964; Tang and Ffowcs and Williams, 1998]. The magnitude of the vortex velocity increases at a decreased η due to the strong pressure-releasing effect. The increase in h also results in a significant change in the vortex velocity. The time variation of the corresponding vortex acceleration is shown in Figures 6.2(d) and 6.2(e).

The time variation of the sound pressure is shown in Figure 6.2(f). The sound pressure is pulse-like. The first crest and trough of the sound pressure increase with increasing h or decreasing η for $y_{1i} = 0.2$ and $L = 1$. However, the amplitude of p reaches a maximum value at $h \approx 0.8$. Similar observations are also found in Chapter 5 [Figure 5.5(f)].

When the length of the porous material is increased from 1 to 2 with $y_{1i} = 0.2$, $\eta = 3$ and $h = 0.2$, the vortex propagates in a path closer to the porous material [Figure 6.3]. The vortex bends towards the porous material with either increasing h or decreasing η. The velocity and the acceleration of the vortex are similar to those presented in Figures 6.2(b) to 6.2(e) [Figure 6.4] except that more fluctuating peaks are found in their transverse components. The magnitudes of the vortex velocity and acceleration increase with increasing h or decreasing η.

When y_{1i} increases to 0.3 with L = 1, the vortex experiences the effect of the porous material earlier, and the degree of bending of the vortex path towards the porous material is higher than that in the case of y_{1i} = 0.2 [Figure 6.2(a)]. It is also noticed from Figure 6.3 that the vortex paths are not symmetrical about x = 0.5L for L = 1.

Figure 6.5 shows the time variation of sound pressure corresponding to the vortex path shown in Figure 6.3. The duration of active sound generation is prolonged, and the magnitude of p increases as L increases with y_{1i} = 0.2, h = 0.2 and η = 3 compared with the sound pressure p for L = 1 [Figure 6.2(a)]. More crests and troughs are found, and the magnitude of p increases when h is increased to 0.8 with y_{1i} = 0.2, L = 2 and η = 3. The magnitude of p decreases as the porous material is less pressure-releasing (η = 5). The magnitude of p decreases with increasing y_{1i}, but the pulse shape of p is similar to the case of y_{1i} = 0.2 [Figure 6.2(f)]. The magnitude of p increases when h is increased further to 0.4 while it decreases when η increases.

6.3.2 Combined Effects of η and R_f

Figure 6.6(a) shows the vortex path when y_{1i} = 0.2, h = 0.2, η = 3 and L = 1 with various R_f. The vortex path for R_f = 0 is also shown for the sake of comparison. When R_f = 0.5, the vortex bends away from the porous material for $0 < x < 0.6$ because of the pressure-supporting effect and then propagates towards the x-axis for $x > 0.6$. The vortex path for R_f = 0.5 is different from the case in a perfectly inviscid fluid. The degree of bending away from the porous material ($0 < x < 0.6$) and that towards the x-axis ($x > 0.6$) becomes serious when R_f is increased to 3. The minimum vortex height $y_1 \approx 0.1$ at $R_f = 7$. After reaching the minimum vortex height, the vortex bends away from the porous material at increased $R_f = 30$, and the vortex moves in the horizontal direction with constant speed for large R_f (for instance, $R_f = 100$).

Figures 6.6(b) and 6.6(c) show the corresponding time variations of the vortex velocities. One can observe that the longitudinal velocity of the vortex increases as R_f increases from 0 to 7 and then decreases again for $R_f > 7$. The initial longitudinal velocity is different from the final velocity after interacting with the porous material because of the lower vortex height at $x > 2$. The transverse velocity of the vortex decreases at increasing R_f and tends to its theoretical value of zero for $R_f = 100$ [Equation (6.7)]. The flow impedance of the porous material depends on the R_f, m and the speed of the vortex. These three parameters also affect the duration of influence of the porous material on the vortex motion. In addition, the flow impedance seen by the vortex varies as it approaches the porous material. Therefore, the final height and velocity of the vortex do not vary monotonically with R_f even when m is fixed. Figures 6.6(d) and 6.6(e) show the effect of R_f on the time variation of the vortex acceleration. One can observe that the magnitude of the acceleration fluctuates seriously, and the maximum acceleration occur at $t - t_a \approx 2$ for $0.5 < R_f < 7$ during which the vortex is under the influence of the porous material. Louder sound radiation is thus expected [Figure 6.6(f)] at $R_f = 7$.

Figure 6.7 shows some examples of the vortex paths at different R_f. Figure 6.7(a) shows the vortex path for $y_{1i} = 0.2$, $h = 0.4$, $\eta = 3$ and $L = 1$ with various R_f. The vortex propagates towards the porous material more seriously compared with the vortex paths shown in Figure 6.6(a) as a strong pressure-releasing effect is produced by a thicker porous material. The vortex moves away from the porous material for $0 < x < 0.6$ as R_f increases from 0 to 7. For $x > 0.6$, the vortex propagates towards the rigid surface and reaches a constant vertical height after interacting with the porous material. When the flow resistance is greater than 7, the vortex propagates away from the porous material and moves in the horizontal direction with constant speed when R_f is further increased. The vortex dynamics with various R_f are similar to those presented in Figure 6.6(a) when $h = 0.2$. When η increases from 3 to 5 with $y_{1i} = 0.2$, $h = 0.2$ and $L = 1$ [Figure 6.7(b)], the vortex moves away from the porous material due to the presence of a less pressure-releasing surface. One can expect that an increase in y_{1i} or L will cause the vortex to propagate with a higher degree of bending towards the porous material, and the corresponding sound pressure is shown in Figure 6.8.

Figure 6.9(a) illustrates the dependence of the sound pressure magnitude on the flow resistance with $y_{1i} = 0.2$ and $L = 1$ with various h and η. The magnitude of p does not vary much as R_f increases from 0 to 1. An increase in p is observed for $1 < R_f < 10$ due to the substantial large rate of change of the vortex velocity [Figures 6.6(d) and 6.6(e)]. A general decrease of the magnitude of p follows when R_f is increased further. For $h = 0.2$ and $\eta = 5$, the magnitude of p is lower than that for $\eta = 3$ as a less pressure-releasing surface is experienced by the vortex, and the porous material becomes acoustically hard for large η (for instance, $\eta = 100$). At the same time, the sound pressure p also decreases with decreasing h. One can observe that the magnitude of p reaches its maximum value at $h \approx 0.8$ [Figure 6.9(a)], and similar finding is also reported in Chapter 5 [Figure 5.6].

Figure 6.9(b) summarizes the sound pressure magnitude p against the flow resistance R_f when y_{1i} increases to 0.3 for $L = 1$ with various h and η. The variation of p with different R_f is similar to those presented in Figure 6.9(a). The amplitude of the sound pressure p is approximately constant for small $R_f \leq 1$, it then increases with R_f for $1 < R_f < 10$. It will approach its theoretical value ($p = 0$) for large R_f. For $y_{1i} = 0.3$, the effect of increasing h or decreasing η provides a stronger pressure-releasing effect as suggested in Figure 6.9(a) [Figure 6.9(b)]. One can notice that the magnitude of p is lower than that in the case for $y_{1i} = 0.2$. When L increases from 1 to 2 at a fixed y_{1i} [Figure 6.9(c)], the magnitude of p is greater than that in the case for $L = 1$ [Figure 6.9(a)]. Though an increase in y_{1i} with $L = 2$ results in a lower magnitude of p, its magnitude is higher than that in the case for $L = 1$ and $y_{1i} = 0.3$ [Figure 6.9(b)].

Figure 6.10 summaries the acoustical energy radiated with various flow resistance. When $y_{1i} = 0.2$ and $L = 1$, the acoustical energy E radiated increases as η decreases or h increases [Figure 6.10(a)], while it tends to zero when η is large (for instance, $\eta = 100$). The acoustical energy E first decreases when R_f increases from 0 to 1 and then increases for $1 < R_f < 10$. The magnitude of E drops as R_f increases towards 100. When y_{1i} increase to 0.3 at a fixed L, the variation of E is similar to those presented in Figure 6.10(a) [Figure 6.10(b)]. One can notice that the variation of E is not so significant when y_{1i} increases. From Figure 6.9(c), one can expect that the acoustical energy radiated increases as L increases [Figure 6.10(c)].

6.4 Summary

In this chapter, the vortex sound generation inside a lined duct is investigated. The method employed in Chapter 5 is applied. The far-field sound pressure generated is in form of a plane acoustic wave, and the time variation of the sound pressure is pulse-like. The vortex with an anti-clockwise circulation propagates towards the lower porous material in a perfectly inviscid fluid if the vortex is initially located below the centreline of the duct. Active sound generation is observed when the vortex interacts with the porous material due to the substantial large rate of change of the vortex velocity. The sound pressure can be increased by either increasing the length, the thickness or decreasing the effective fluid density of the porous material.

When a finite flow resistance exists inside the porous material, the sound pressure and the acoustical energy radiated first decrease when the flow resistance increases from zero and then increase when the flow resistance increases from one to ten. The sound pressure and the acoustical energy radiated drop rapidly when the flow resistance is large.

Chapter 7: Conclusions and Recommendations for Future Work

7.1 Conclusions

In the present study, the vortex sound generation due to the presence of porous materials is investigated theoretically. Porous materials are commonly used inside the dissipative duct silencers for attenuating noise. The present study deals with the problem of self-noise generation from the porous materials. Chapter 2 describes how two vortices interacting with a rigid circular cylinder to produce sound while the subsequent chapters describe the sound generation under the influence of the porous materials.

In Chapter 2, two vortices in the proximity of a rigid circular cylinder are investigated. When the separation of the vortices is small or when the vortices are far away from the cylinder, the radiated dipoles consist of low and high frequency components. The former is due to the interaction between the vorticity centroid of the two vortices and the cylinder, while the latter one is due to the mutual induction between the vortices. The radiated dipoles are much stronger when the vortices are close to each other or are in a closer proximity of the circular cylinder. However, the amplitude of radiated dipoles reaches a minimum at a critical vortex separation and increases again.

When one of the vortices is considerably stronger than the other, the stronger vortex dominates the fluid mechanics and the acoustics. Low and high frequency components are observed in the dipole time fluctuation. However, the contribution from the weaker vortex results in an amplitude modulation pattern in the high frequency fluctuations. The strength of such modulation becomes weaker when the circulation of the weaker vortex is reduced.

Chapter 3 studies the interaction between vortices and a porous half cylinder mounted on an otherwise rigid plane. Unlike the case of a rigid half cylinder, the presence of a porous one results in the co-existence of the longitudinal and transverse dipoles. When a single vortex engages the porous half cylinder, the time variation of the strength of each dipole is pulse-like. Its amplitude increases as the effective fluid density decreases. The amplitude of the longitudinal dipole converges to that for the rigid half cylinder case when the flow resistance is large, but is larger than the latter at small flow resistances. The larger the initial vortex height above the rigid plane, the lower the amplitude of the dipole. The overall acoustical energy radiated remains higher than that for the rigid half cylinder case at some combinations of the effective fluid density and flow resistance.

When two identical vortices exist in the proximity of the porous half cylinder, both the longitudinal and transverse dipoles contain low and high frequency components. The former is due to the macroscopic vortex centroid motions and the latter to the leapfrogging motions of the vortices as in Chapter 2. When the vortices are close to each other, the overall acoustical energy radiated is less than that in the rigid half cylinder case and the dipoles are dominated by the high frequency fluctuation. The opposite is found at larger vortex separation for all effective fluid density and flow resistance studied. When the vortex strengths are different, the acoustical energy radiated is higher when the difference in the vortex strengths increases.

In Chapter 4, the vortex sound in the presence of a wedge is studied. The wedge consists of two materials. One of the materials is assumed porous while the other is rigid. The far-field sound pressure is a pulse whose magnitude decreases with increasing wedge angle. The rate of decay of the pulse increases as the wedge angle increases. When the wedge angle is fixed, the magnitude of the sound pressure decreases as the solid surface becomes more acoustically hard by either increasing the effective fluid density or the flow resistance of the porous wedge.

In a perfectly invsicd fluid medium, a finite effective fluid density deflects the radiation directivity towards the porous surface. The extent of such deflection increases with increasing effective fluid density but the rate of decay of the sound pressure with distance from the edge is lower if the effective fluid density is reduced. When the fluid possesses non-vanishing viscosity, the directivity and the rate of decay of the sound in the leading order of magnitude are the same as those with hard surfaces, regardless of the magnitude of the flow resistance.

Chapter 5 discusses the vortex sound generation in the presence of a piece-wise porous material on an otherwise rigid plane. The sound radiated consists of a longitudinal dipole, and the time variation of the longitudinal dipole is pulse-like. The amplitude of the dipole increases as the effective fluid density or the flow resistance of the porous material decreases. The opposite is found when the length or the thickness of the porous material is reduced for all effective fluid density and flow resistance studied. When the flow resistance is large, the vortex generates no sound. The amplitude of the longitudinal dipole increases when the length of the porous material increases and does not decrease monotonically with increasing flow resistance. The sound pressure magnitude matches that for the case of a rigid wall for a large flow resistance.

Chapter 6 extends the study of Chapter 5 to investigate the vortex sound generation inside a lined duct. The far-field pressure generated is a plane wave and is pulse-like. The sound pressure increases when the length or the thickness of the porous material increases. On the contrary, the sound pressure decreases as the effective fluid density increases. With a finite flow resistance, the amplitude of the sound pressure converges to that for the case of a perfectly inviscid fluid when the flow resistance is small. The variations of the sound pressure magnitudes at various flow resistance are similar to those presented in Chapter 5. The sound pressure magnitude does not decrease monotonically with increasing flow resistance.

7.2 Recommendations for Future Work

The present study focuses on the vortex sound generation under the influence of a porous material theoretically. There are two folds which can be dealt with in the future (i) theoretically and (ii) experimentally.

7.2.1 Theoretical Development

The mean flow effect is excluded in the present study because it is expected to produce amplification to a sound field. The mean flow effect can be added in the future study as in Tang and Ffowcs Williams [1998]. Other than the mean flow, vortex shedding is found when a fluid flows over an obstacle, an area change, an edge and etc because of flow separation [Davies and Ffowcs Williams, 1968], the effects of the shed vortices from the porous material should be investigated.

The introduction of the porous material will affect the boundary layer and vortex shedding, eventually the sound radiation. Kutta-condition can be imposed when the fluid flow interacts with a porous edge [Howe, 1999]. Instability waves or gust [Glegg and Jochault, 1988; Peake and Kerschen, 1997] can be studied instead of the discrete vortices because the waves may be a better representation of the turbulence than the discrete vortices, especially in the proximity of a solid surface.

The flow geometries in the present study are simple. The effect on sound generation of the elliptical porous cylinder and the half porous cylinders mounted on the two sides of air duct can also be studied. Numerical conformal mapping can be employed to deal with complicated geometry like the dissipative silencer with several splitters. Such investigations can provide practical information on the self-noise generation.

7.2.2 Experimental Investigation

Experimental investigation can be taken to study the self-noise generation. The measurement should be carried out inside a wind tunnel, and the air supply system should provide a steady flow. Hot-wire is recommended to obtain the information of the flow field. It can be used to analyze the free stream turbulence level, which has significant effects on the vortex shedding and boundary layer development on the solid surfaces. The turbulence level should be measured.

The wall pressure spectrum across the porous material can be measured by the wall pressure sensor. It can be used to evaluate the boundary layer development and the force acting on the porous material. The wall pressure sensor should also be mounted on the rigid duct wall in order to study how the wall pressure changes across the porous material.

The transmission loss in the presence of different mean flow conditions with and without the porous material in an air duct should be studied. It can indicate the performance of the porous material in dissipating sound energy under various flow conditions. The transmission loss across the lined duct can be measured by the four-microphone method. The collected data on the self-noise generation can be correlated with the turbulence level, wall pressure spectrum, transmission loss and mean flow. The obtained data will demonstrate how the turbulence interacts with the porous material to radiate noise, and how the turbulence lowers the sound absorption performance of the porous material.

Publications Arising from this Thesis

Lau, C.K. Tang, S.K. "An example for the sound production of the vortex surface sound interaction" *The Tenth International Congress on Sound and Vibration*, Sweden, pp.377 – 384 (2003)

Lau, C.K. and Tang, S.K. "On sound generation due to a vortex pair interacting with a circular cylinder of homogeneous surface impedance" *The Eleventh Congress on Sound and Vibration*, pp.377 – 384 Russia, (2004)

Tang, S.K. and Lau, C.K. "Vortex sound in the presence of a wedge with inhomogeneous surface flow impedance" *Journal of Sound and Vibration*, Vol. 281, pp.1077 – 1091 (2005)

Lau, C.K. and Tang, S.K. "Sound generated by vortices in the presence of a porous half-cylinder mounted on a rigid plane" *Journal of the Acoustical Society of the America*, Vol. 119, pp. 2084 – 2095 (2006)

Lau, C.K. and Tang, S.K. "Force and sound generated by two vortices interacting with a circular cylinder". (Submitted to *American Institute of Aeronautics and Astronautics Journal*)

Lau, C.K. and Tang, S.K. "Vortex sound in the presence of a finite-length porous material on an otherwise rigid plane". (Under preparation)

Abou-Hussein, H., DeBenedictis, A., Harrison, N., Kim, M., Rodrigues, M.A., Zagadou, F. and Howe, M.S. "*Vortex-surface interaction noise: A compendium of worked examples* " *Journal of Sound and Vibration*, Vol. 252, pp.883 – 918 (2002)

Abramowitz, M. and Stegun, I.A. *Handbook of Mathematical Functions with Formulas, Graphs and Mathematical Tables*. John Wiley and Sons, New York (1972)

Attenborough, K. "Acoustical characteristics of porous materials" *Physics Reports*, Vol. 82, pp.179 – 227 (1982)

Barron, R.F. *Industrial Noise Control and Acoustics*. Marcel Dekker, New York (2003)

Bear, J. *Dynamics of Fluids in Porous Media*. Dover, New York (1972)

Bearman, P.W. "On vortex street wakes" *Journal of Fluid Mechanics*, Vol.28, pp.625 – 641 (1967)

Becker, H.A. and Massaro, T.A. "Vortex evolution in a round Jet" *Journal of Fluid Mechanics*, Vol. 31, pp.435 – 448 (1968)

Beranek, L.L. and Vér, I.L. *Noise and Vibration Control Engineering. Principles and Applications*. John Wiley and Sons, New York (1992)

Bies, D.A. and Hansen, C.H. *Engineering Noise Control Theory and Practice*. Spon Press, New York (2003)

Bies, D.A., Pickles, J.M. and Leclercq, D.J.J. "Aerodynamic noise generated by a stationary body in a turbulent air stream" *Journal of Sound and Vibration*, Vol. 204, pp.631 – 632 (1997)

Cannell, P. and Ffowcs Williams, J.E. "Radiation from line vortex filaments exhausting from a two-dimensional semi-infinite duct" *Journal of Fluid Mechanics*, Vol. 51, pp.357 – 362 (1972)

Casalino, D., Jacob, M, and Roger, M. "Prediction of rod-airfoil interaction noise using the Ffowcs-Williams-Hawkings analogy" *American Institute of Aeronautics and Astronautics Journal*, Vol. 41, pp.182 – 191 (2003)

Chang, C.C. and Chen, T.L. "Acoustic emission by a vortex ring passing near a sharp wedge" *Proceedings of Royal Society of London Series A: Mathematical and Physical Sciences*, Vol. 445, pp.141 – 155 (1994)

Chen, K.T., Chen, Y.H., Lin, K.Y. and Weng, C.C. "The improvement on the transmission loss of a duct by adding Helmholtz resonators" *Applied Acoustics*, Vol. 54, pp.71 – 82 (1998)

Churchill, R.V. and Brown, J.W. *Complex Variables and Applications*. McGraw-Hill, New York (1990)

Crighton, D.G. "Radiation from vortex filament motion" *Journal of Fluid Mechanics*. Vol.51, pp.357 – 362 (1972)

Crighton, D.G., Dowling, A.P., Ffowcs Williams, J.E., Heckl, M. and Leppington, F.G. *Modern methods in Analytical Acoustics*. Springer-Verlag, London (1992)

Crighton, D.G. and Leppington, F.G. "Scattering of aerodynamic noise by semi-infinite compliant plate" *Journal of Fluid Mechanics*, Vol. 43, pp.721 – 736 (1970)

Crighton, D.G.. and Leppington, F.G. "Radiation properties of the semi-infinite vortex sheet: the initial-value problem" *Journal of Fluid Mechanics*, Vol. 64, pp.393 – 414 (1974)

Cummings, A. "Sound transmission in a folded annular duct" *Journal of Sound and Vibration*, Vol. 41, pp.375 – 379 (1975)

Cummings, A. "Sound attenuation in ducts lined in two opposite walls with porous material, with some applications to splitters" *Journal of Sound and Vibration*, Vol. 49, pp.9 – 35 (1976)

Cummings, A. and Chang, I.J. "Sound attenuation of a finite length dissipative flow duct silencer with internal mean flow in the absorbent" *Journal of Sound and Vibration*, Vol. 127, pp.1 – 17 (1988)

Cummings, A. and Sormaz, N. "Acoustic attenuation in dissipative splitter silencers containing mean fluid flow" *Journal of Sound and Vibration*, Vol. 168, pp.209 – 227 (1993)

Curle, N. "The mechanics of edge-tones" *Proceedings of Royal Society of London Series A: Mathematical and Physical Sciences*, Vol. 216, pp.412 – 424 (1953)

Curle, N. "The influence of solid boundaries upon aerodynamic sound" *Proceedings of the Royal Society of London Series A: Mathematical and Physical Sciences*, Vol. 231, pp.505 – 514 (1955)

Davies, H.G. and Ffowcs Williams, J.E. "Aerodynamic sound generation in a pipe" *Journal of Fluid Mechanics*, Vol. 32, pp.765 – 778 (1968)

Denia, F.D., Albelda, J. and Fuenmayor, F.J. "Acoustical behaviour of elliptical chamber mufflers" *Journal of Sound and Vibration*, Vol. 241, pp.401 – 421 (2001)

Delany, M.E. and Bazley, E.N. "Acoustical properties of fibrous materials" *Applied Acoustics*, Vol. 3, pp.105 – 116 (1970)

Diskey, N.S. and Selamet, A. "Helmholtz resonators: one-dimensional limit for small cavity length-to-diameter ratios" *Journal of Sound and Vibration*, Vol. 195, pp.512 – 517 (1996)

Dowling, A.P. and Ffowcs Williams, J.E. *Sound and Sources of Sound*. Ellis Horwood, New York (1983)

Dunne, R.C. and Howe, M.S. "Wall-bounded blade-tip vortex interaction noise" *Journal of Sound and Vibration*, Vol. 202, pp.605 – 618 (1997)

EI-Sharkawy, A.I. and Nayfeh, A.H. "Effect of an expansion chamber on the propagation of sound in circular ducts" *Journal of the Acoustical Society of America*, Vol. 63, pp.667 – 674 (1978)

Fanger, P.O. *Thermal Comfort: Analysis and Applications in Environmental Engineering.* McGraw-Hill, New York (1972)

Fehse, K.-R. and Neise, W. "Generation mechanisms of low-frequency centrifugal fan noise" *American Institute of Aeronautics and Astronautics Journal*, Vol. 37, pp.1173 – 1179 (1999)

Ffowcs Williams, J.E. "The acoustics of turbulence near sound-absorbent liners" *Journal of Fluid Mechanics*, Vol. 51, pp.737 – 749 (1972)

Ffowcs Williams, J.E. and Hall, L.H. "Aerodynamic sound generation by the turbulent flow in the vicinity of a scattering half-plane" *Journal of Fluid Mechanics*, Vol/ 40, pp.657 – 670 (1970)

Ffowcs Williams, J.E. and Hawkings, D.L. "Shallow water wave generation by unsteady flow" *Journal of Fluid Mechanics*, Vol. 31, pp.779 – 788 (1968)

Ffowcs Williams, J.E. and Hawkings, D.L. "Sound generation by turbulence and surfaces in arbitrary motion" *Proceedings of Royal Society of London Series A: Mathematical and Physical Sciences*, Vol. 264, pp.321 – 342 (1969)

Gallo, C, Sala, M. and Sayigh, A.M.M. *Architecture: Comfort and Energy.* Elsevier, UK (1988)

Glav, R. "The transfer matrix for a dissipative silencer of arbitrary cross-section" *Journal of Sound and Vibration*, Vol. 236, pp.575 – 594 (2000)

Glegg, S.A.L. and Jochault, C. "Broadband self-noise from a ducted fan" *American Institute of Aeronautics and Astronautics Journal*, Vol. 36, pp.1387 – 1395 (1998)

Gradshteyn, I.S. and Ryzhik, I.M. *Table of Integrals, Series, and Products*. Academic Press, London (1980)

Griffin, S., Lane, S.A. and Huybrechts, S. "Coupled Helmholtz resonators for acoustic attenuation" *Transactions of the American Society of Mechanical Engineers, Journal of Vibration and Acoustics*, Vol. 123, pp.11 – 17 (2001)

Hansen, C.H. and Snyder, S.D. *Active Control of Noise and Vibration*. Spon Press, New York (1997)

Harris, C.M. *Handbook of Acoustical Measurements and Noise Control*. McGraw-Hill, New York (1991)

Hourigan, K., Welsh, M.C., Thompson, M.C. and Stokes, A.N. "Aerodynamic sources of acoustic resonance in a duct with baffles" *Journal of Fluids and Structures*, Vol. 4, pp.345 -370 (1990)

Howe, M.S. "Contributions to the theory of aerodynamic sound, with application to excess jet noise and the theory of flute" *Journal of Fluid Mechanics*, Vol. 71, pp.625 – 673 (1975)

Howe, M.S. *Acoustics of Fluid-Structure Interactions*. Cambridge University Press, Cambridge (1998)

Howe, M.S. "Trailing edge noise at low Mach numbers" *Journal of Sound and Vibration*, Vol. 225, pp.211 – 238 (1999)

Howe, M.S. *Theory of Vortex Sound*. Cambridge University Press, Cambridge (2003)

Huang, L. "A theoretical study of duct noise control by flexible panels" *Journal of the Acoustical Society of America*, Vol. 106, pp.1801 – 1809 (1999)

Huang, L., Choy, Y.S., So. R.M.C. and Chong, L.T. "Experimental study of sound propagation in a flexible duct" *Journal of the Acoustical Society of America*, Vol. 108, pp.624 – 631 (2000)

Hulshoff, S.J., Hirschberg, A. and Hofmans, G.C.J. "Sound production of vortex-nozzle interactions" *Journal of Fluid Mechanics*, Vol. 439, pp.335 – 352 (2001)

Hussain, A.K.M.F. and Zaman, K.B.M.Q. "An experimental study of organized motions un the turbulent plane mixing layer" *Journal of Fluid Mechanics*, Vol. 159, pp.85 – 104 (1985)

Ingard, K.U. "On the theory and design of acoustic resonators" *Journal of the Acoustical Society of America*, Vol. 25, pp.1037 – 1061 (1953)

Ingard, K.U. *Notes on Sound Absorption Technology*. Poughkeepsie, New York (1994)

Inoue, O. and Hatakeyama, N. "Sound generation by a two-dimensional circular cylinder in a uniform flow" *Journal of Fluid Mechanics*, Vol. 471, pp.285 – 314 (2002)

Kambe, T. "Acoustic emissions by vortex motions" *Journal of Fluid Mechanics*, Vol. 173, pp.643 – 666 (1986)

Kambe, T., Minota, T. and Ikushima, Y. "Acoustic wave emitted by a vortex ring passing near the edge of a half-plane" *Journal of Fluid Mechanics*, Vol. 155, pp.77 – 103 (1985)

Kirby, R. "Simplified techniques for predicting the transmission loss of a circular dissipative silencer" *Journal of Sound and Vibration*, Vol. 243, pp.403 – 426 (2001)

Kirby, R. "Transmission loss predictions for dissipative silencers of arbitrary cross section in the presence of mean flow" *Journal of the Acoustical Society of America*, Vol. 114, pp.200 – 209 (2003)

Kirby, R. and Lawrie, J.B. "A point collection approach to modeling large dissipative silencers" *Journal of Sound and Vibration*, Vol. 286, pp.313 – 339 (2005)

Ko, N.W.M. and Tang, S.K. "Effect of external exciter on the far field of an air jet" *Journal of Sound and Vibration*, Vol. 137, pp.154 – 158 (1990)

Kober, H. *Dictionary of Conformal Representations*. Dover Publications, Inc (1952)

Kuchemann, D. "Report on the I.U.T.A.M. Symposium on concentrated vortex motions in fluids" *Journal of Fluid Mechanics*, Vol. 21, pp.1 – 20 (1965)

Lamb, H. *Hydrodynamics*. Cambridge University Press, Cambridge (1993)

Lighthill, M.J. “On sound generated aerodynamically I. General theory” *Proceedings of the Royal Society of London Series A: Mathematical and Physical Sciences,* Vol. 211, pp.564 – 587 (1952)

Lighthill, M.J. “On sound generated aerodynamically II. Turbulence as a source of sound” *Proceedings of the Royal Society of London Series A: Mathematical and Physical Sciences*, Vol. 222, pp.1 – 32 (1954)

Mak, C.M. “Development of a prediction method for flow-generated noise produced by duct elements in ventilation systems” *Applied Acoustics*, Vol. 63, pp.81 – 93 (2002)

Mak, C.M. and Yang, J. “A prediction method for aerodynamic sound produced by closely spaced elements in air ducts” *Journal of Sound and Vibration*, Vol. 229, pp.743 – 753 (2000)

Mechel, F.P. “Theory of baffle-type silencers” *Acustica*, Vol. 70, pp.93 – 111 (1990a)

Mechel, F.P. “Numerical results to the theory of baffle-type silencers” *Acutsica*, Vol. 72, pp.7 – 20 (1990b)

Minota, T. and Kambe, T. “Acoustic waves emitted by a vortex ring passing near a circular cylinder” *Journal of Sound and Vibration*, Vol. 119, pp.509 – 528 (1987)

Minota, T., Murakame, T. and Kambe, T. “Acoustic wave emitted by a vortex ring passing near a wedge-like plate” *Fluid dynamics Research*, Vol. 4, pp.57 – 71 (1988)

Möhring, W. “On vortex sound at low mach number” *Journal of Fluid Mechanics*, Vol. 85, pp.685 – 691 (1978)

Morse, P.M. and Ingard, K.U. *Theoretical Acoustics*. McGraw-Hill, New York (1968)

Munjal, M.L. *Acoustics of Ducts and Mufflers*. John Wiley and Sons, New York (1987a)

Munjal, M.L. “A simple numerical method for three-dimensional analysis of simple expansion chamber mufflers of rectangular as well as circular cross-section with a stationary medium” *Journal of Sound and Vibration*, Vol. 116, pp.71 – 88 (1987b)

Nash, E.C., Lowson, M.V. and McAlpine, A. “Boundary-layer instability noise on aerofoils” *Journal of Fluid Mechanics*, Vol. 382, pp.27 – 61 (1999)

Neise, W., Frommhold, W., Mechel, F.P. and Holste, F. “Sound power determination in rectangular flow ducts” *Journal of Sound and Vibration*, Vol. 174, pp.210 – 237 (1993)

Nelson, P.A. “Noise generated by flow over perforated surfaces” *Journal of Sound and Vibration*, Vol. 83, pp.11 – 26 (1982)

Nelson, P.A. and Elliott, S.J. *Active Control of Sound*. Academic Press, New York (1993)

Nelson, P.A. and Morfey, C.L. “Aerodynamic sound production in low speed flow ducts” *Journal of Sound and Vibration*, Vol. 79, pp.263 – 289 (1981)

Obermerier, F. “New representation of aeroacoustic source distribution I. General theory” *Acustica*, Vol. 42, pp.56 – 61 (1979a)

Obermeier, F. “New representation of aeroacoustic source distribution II. 2-dimenional model flows” *Acustica*, Vol. 42, pp.62 – 71 (1979b)

Obermeier, F. “The influence of solid bodies on low Mach number vortex sound” *Journal of Sound and Vibration*, Vol. 72, pp.39 – 49 (1980)

Oldham, D.J. and Waddington, D.C. “The prediction of airflow-generated noise in ducts from considerations of similarity” *Journal of Sound and Vibration*, Vol. 248, pp.780 – 787 (2001)

Panaras, A.G. “Pressure pulse generated by the interaction of a discrete vortex wit an edge” *Journal of Fluid Mechanics*, Vol. 154, pp.445 – 461 (1985)

Peake, N. and Kerschen, E.J. “Influence of mean loading on noise generated by the interaction of gusts with a flat-plate cascade: upstream radiation” *Journal of Fluid Mechanics*, Vol. 347, pp.315 – 346 (1997)

Peat, K.S. and Rathi, K.L. “A finite element analysis of the convected acoustic wave motion in dissipative silencers” *Journal of Sound and Vibration*, Vol. 184, pp.529 – 545 (1995)

Powell, A. “Vortex sound theory” *Journal of the Acoustical Society of America*, Vol. 36, pp.177 – 195 (1964)

Phillips, O.M. “The intensity of Aeolian tones” *Journal of Fluid Mechanics*, Vol. 1, pp.607 -624 (1956)

Quinlan, D.A. and Bent, P.H. “High frequency noise generation in small axial flow fans” *Journal of Sound and Vibration*, Vol. 218, pp.177 – 204 (1998)

Quinn, M.C. and Howe, M.S. “On the production and absorption of sound by lossless liners in the presence of mean flow” *Journal of Sound and Vibration*, Vol. 97, pp.1 – 9 (1984)

Radavich, P.M., Selamet, A. and Novak, J.M. “A computational approach for flow-acoustic coupling in closed side branches” *Journal of the Acoustical Society of America*, Vol. 109, pp.1343 – 1353 (2001)

Ramamoorthy, S., Grosh, K. and Nawar, T.G. “Structural acoustic silencers – design and experiment” *Journal of the Acoustical Society of America*, Vol. 114, pp.2812 – 2824 (2003)

Redmore, T.C. and Mulholland, K.A. “The application of mode coupling theory to the transmission of sound in sidebranch of a rectangular duct system” *Journal of Sound and Vibration*, Vol. 85, pp.323 – 331 (1982)

Routh, E.J. “Some applications of conjugate functions” *Proceedings of the London mathematical Society*, Vol. 12, pp.73 – 89 (1881)

Sadamoto, A. and Murakami, Y. “Resonant properties of short expansion chambers in a circular duct: including extremely short cases and asymmetric mode wave incidence cases” *Journal of Sound and Vibration*, Vol. 249, pp.165 – 187 (2002)

Selamet, A. and Lee, I.J. “Helmholtz resonator with extended neck” *Journal of the Acoustical Society of America*, Vol. 113, pp.1975 – 1985 (2003)

Selamet, A. and Radavich, P.M. “The effect of length on the acoustic attenuation performance of concentric expansion chambers: an analytical, computational and experimental investigation” *Journal of Sound and Vibration*, Vol. 201, pp.407 – 426 (1997)

Selamet, A., Radavich, P.M., Diskey, N.S. and Novak, J.M. “Circular concentric Helmholtz resonator” *Journal of the Acoustical Society of America*, Vol. 101, pp.41 – 51 (1997)

Selamet, A., Xu, M.B., Lee, I.J. and Huff, N.T. “Analytical approach for sound attenuation in perforated dissipative silencers” *Journal of the Acoustical Society of America*, Vol. 115, pp.2091 – 2099 (2004)

Selamet, A. Xu, M.B., Lee, I.J. and Huff, N.T. “Analytical approach for sound attenuation in perforated dissipative silencers with inlet/outlet extensions” *Journal of the Acoustical Society of America*, Vol. 117, pp.2078 – 2089 (2005)

Swinbanks, M.A. “The active control of sound propagation in long ducts” *Journal of Sound and Vibration*, Vol. 27, pp.411 – 436 (1973)

Tang, S.K. “Effects of porous boundaries on the dynamics of an inviscid vortex filament” *Quarterly Journal of Mechanics and Applied Mathematics*, Vol. 54, pp.65 – 84 (2001)

Tang, S.K. “Sound transmission characteristics of Tee-junctions and the associated length corrections” *Journal of the Acoustical Society of America*, Vol. 115, pp.218 – 227 (2004)

Tang, S.K. “On Helmholtz resonators with tapered necks” *Journal of Sound and Vibration*, Vol. 279, pp.1085 – 1096 (2005)

Tang, S.K. and Cheng, J.S.F. “On the application of active noise control in an open end rectangular duct with and without flow” *Applied Acoustics*, Vol. 53, pp.193 – 210 (1998)

Tang, S.K. and Ffowcs Williams, J.E. “Acoustic radiation from a vortex approaching a circular cylinder with surface suction” *Acustica*, Vol. 84, pp.1007 – 1013 (1998)

Tang, S.K. and Ko, N.W.M. “Sound generation by interaction of two inviscid two-dimensional vortices” *Journal of the Acoustical Society of American*, Vol. 102, pp.1463 – 1473 (1997)

Tang, S.K. and Ko, N.W.M. “Sound sources in the interactions of two inviscid-dimensional vortex pairs” *Journal of Fluid Mechanics*, Vol. 419, pp.177 – 201 (2000)

Tang, S.K. and Ko, N.W.M. “Basic sound generation mechanisms in inviscid vortex interactions at low Mach number” *Journal of Sound and Vibration*, Vol. 262, pp.87 – 115 (2003)

Tang, S.K. and Li. F.Y.C. “On low frequency sound transmission loss of double sidebranches: A comparison between theory and experiment” *Journal of the Acoustical Society of AmericaI*, Vol. 113, pp.3215 – 3225 (2003)

Tang, S.K. and Li, K.M. “Vortex sound generation due to a flow impedance discontinuity on a flat surface” *Journal of the Acoustical Society of American*, Vol. 109, pp.1334 – 1341 (2001)

Trinder, M.C.J. and Nelson, P.A. “Active control in finite length ducts” *Journal of Sound and Vibration*, Vol. 83, pp.95 – 105 (1983)

Tsui, C.Y. and Flandro, G.A. “Self-induced sound generation by flow over perforated duct liners” *Journal of Sound and Vibration*, Vol. 50, pp.315 – 331 (1977)

Waddington, D.C. and Oldham, D.J. “Generalized flow noise prediction curves for air duct elements” *Journal of Sound and Vibration*, Vol. 222, pp.163 – 169 (1999)

Woodley, B.M. and Peake, N. “Resonant acoustic frequencies of a tandem cascade. Part 1. Zero relative motion” *Journal of Fluid Mechanics*, Vol. 393, pp.215 – 240 (1999a)

Woodley, B.M. and Peake, N. “Resonant acoustic frequencies of a tandem cascade. Part 2. Rotating blade rows” *Journal of Fluid Mechanics*¸ Vol. 393, pp.241 – 256 (1999b)

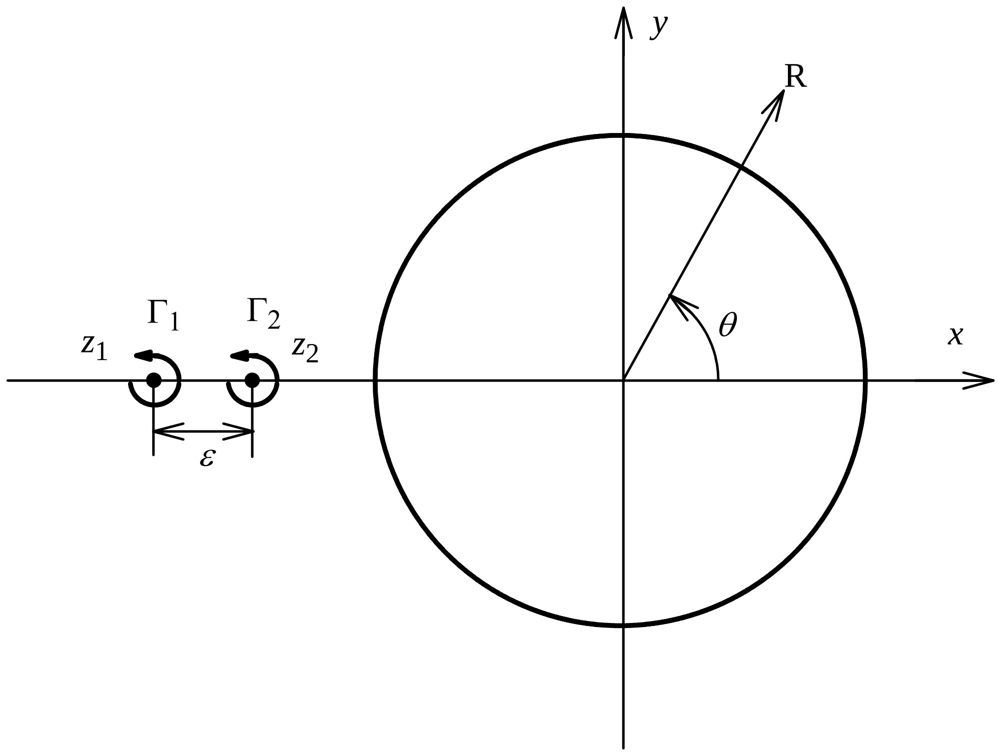

Figure 2.1 Schematics diagram of two rectilinear vortices in the proximity of a rigid circular cylinder.

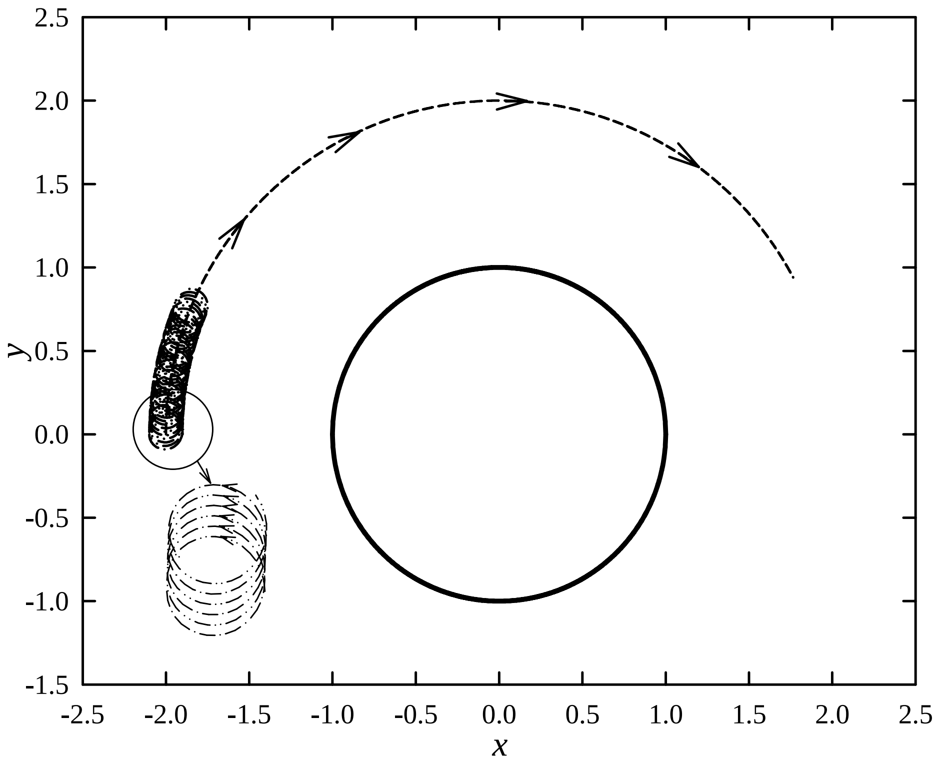

Figure 2.2 Paths of vortices at small ε and large z_c. ——— Cylinder surface; – – – – vorticity centroid; — · — z_1; — ·· — z_2; Arrows direction of motion. $z_{1i} = (-2.1, 0)$, $z_{2i} = (-1.9, 0)$, $\Gamma_1 = \Gamma_2 = 0.5$.

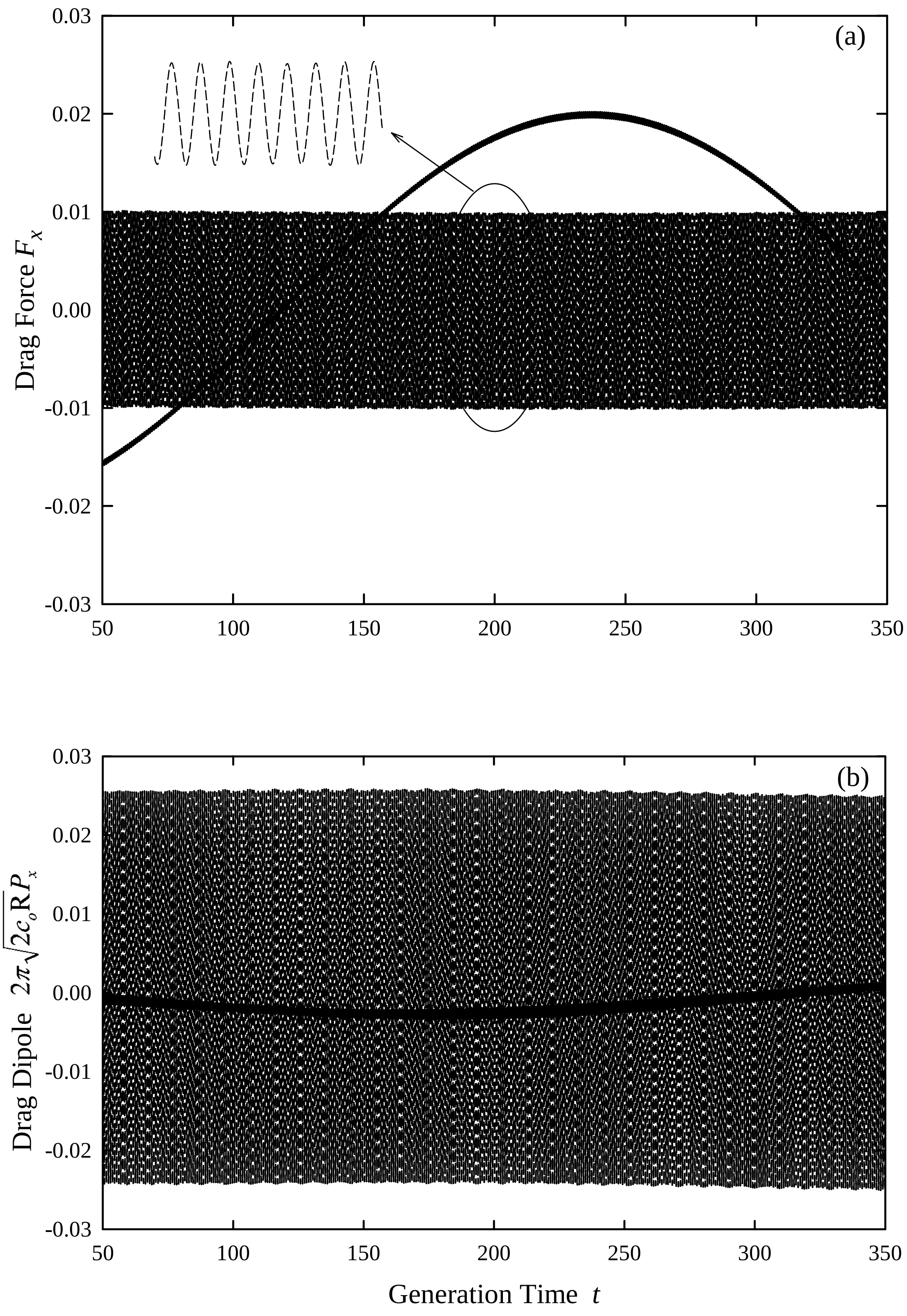

Figure 2.3 *(a) Time variation of the drag force at small ε and large z_c. ——— F_{xc}; – – – – F_{xm}; (b) Time variation of the x - direction dipole strength at small ε and large z_c. ——— P_{xc}; – – – – P_{xm}. z_{1i} = (–2.1, 0), z_{2i} = (–1.9, 0), $\Gamma_1 = \Gamma_2$ = 0.5.*

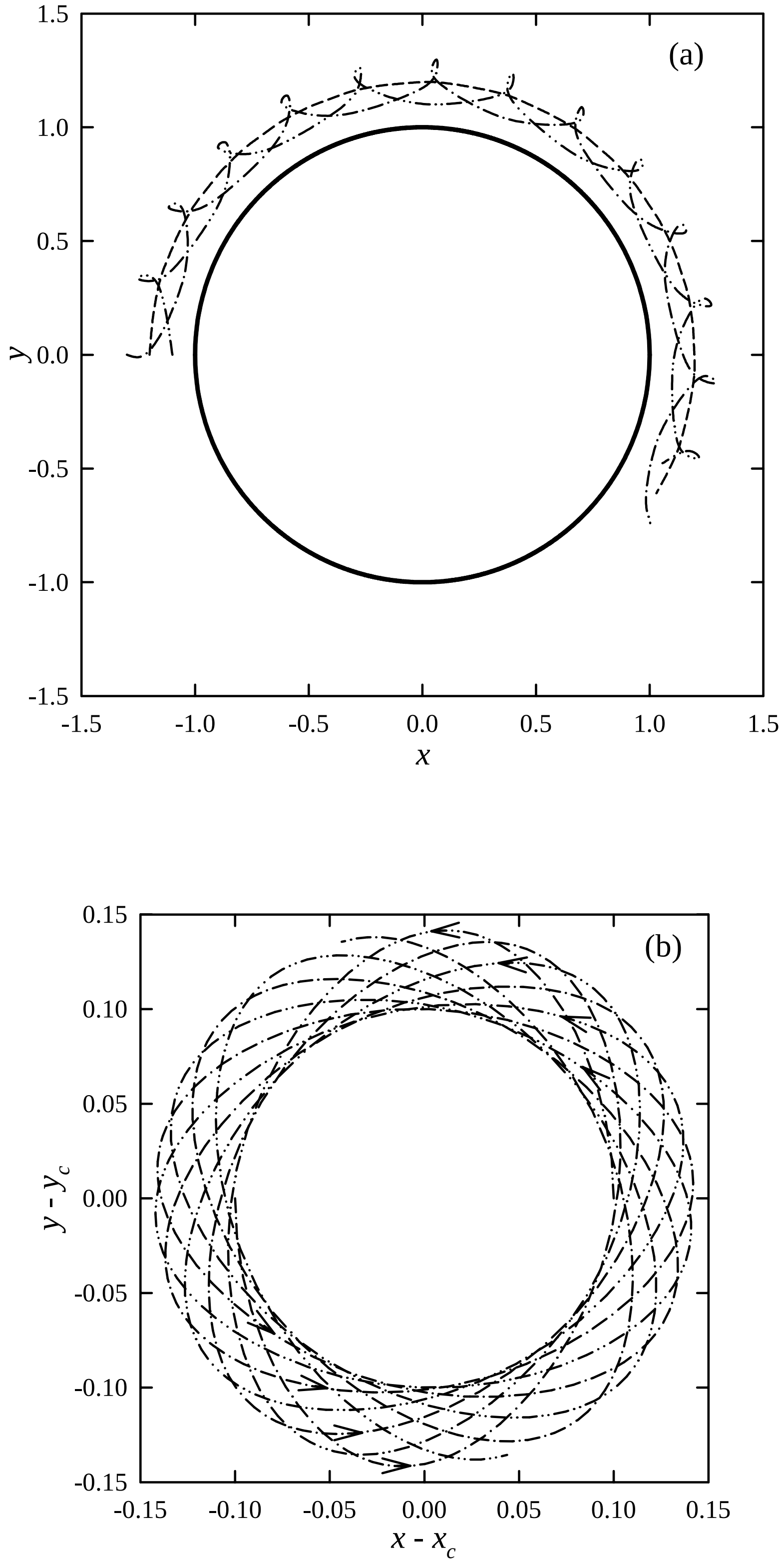

Figure 2.4 Paths of vortices at small ε and small z_c. (a) Vortex paths relative to cylinder centre; (b) Vortex paths relative to vorticity centroid ($0 \le t \le 300$). ——— Cylinder surface; – – – – vorticity centroid; — · — z_1; — ·· — z_2; Arrows direction of motion. $z_{1i} = (-1.3, 0)$, $z_{2i} = (-1.1, 0)$, $\Gamma_1 = \Gamma_2 = 0.5$.

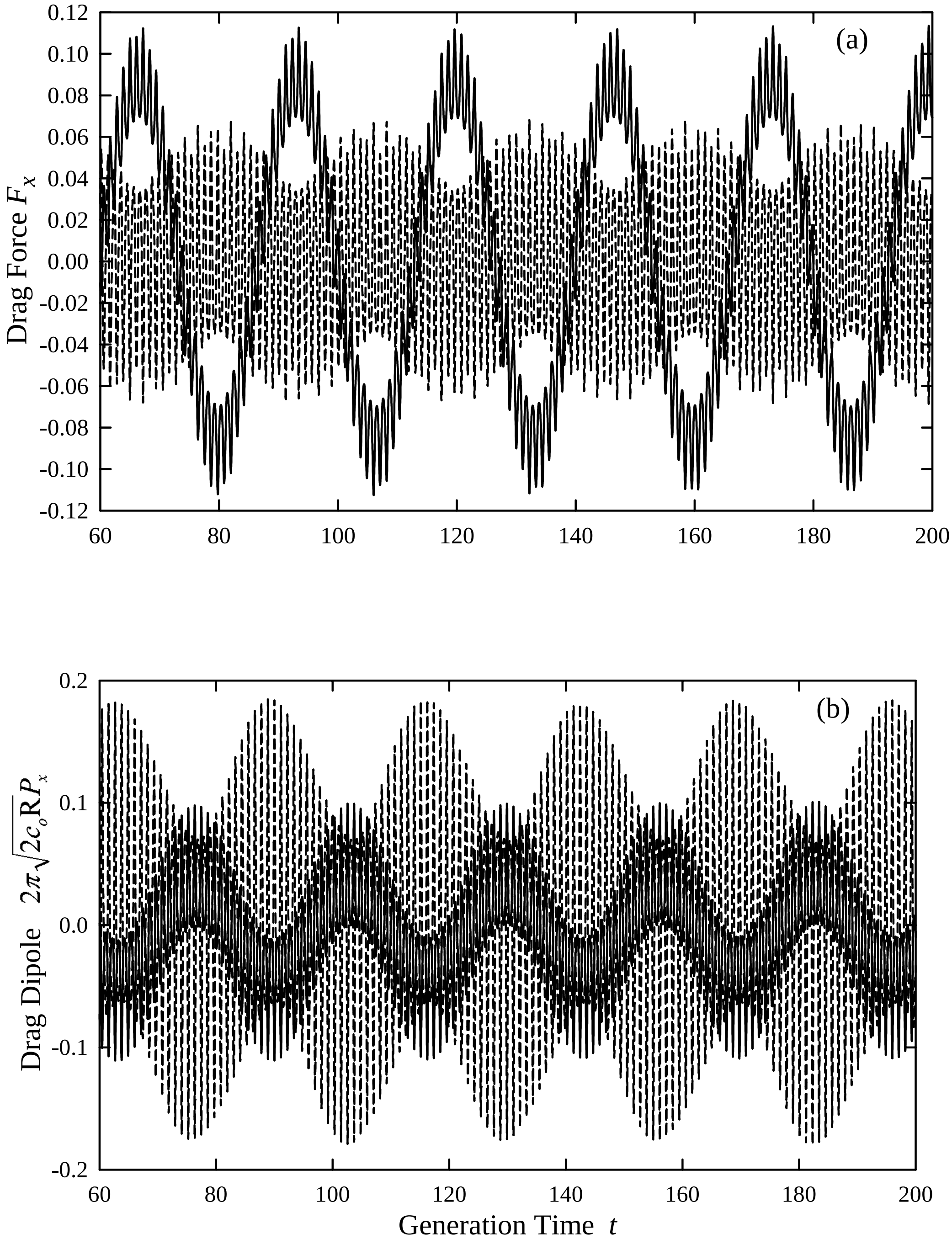

Figure 2.5 *(a) Time variation of the drag force at small ε and small z_c. ——— F_{xc}; – – – – F_{xm}; (b) Time variation of the x - direction dipole strength at small ε and small z_c. ——— P_{xc}; – – – – P_{xm}. z_{1i} = (–1.3, 0), z_{2i} = (–1.1, 0), $\Gamma_1 = \Gamma_2$ = 0.5.*

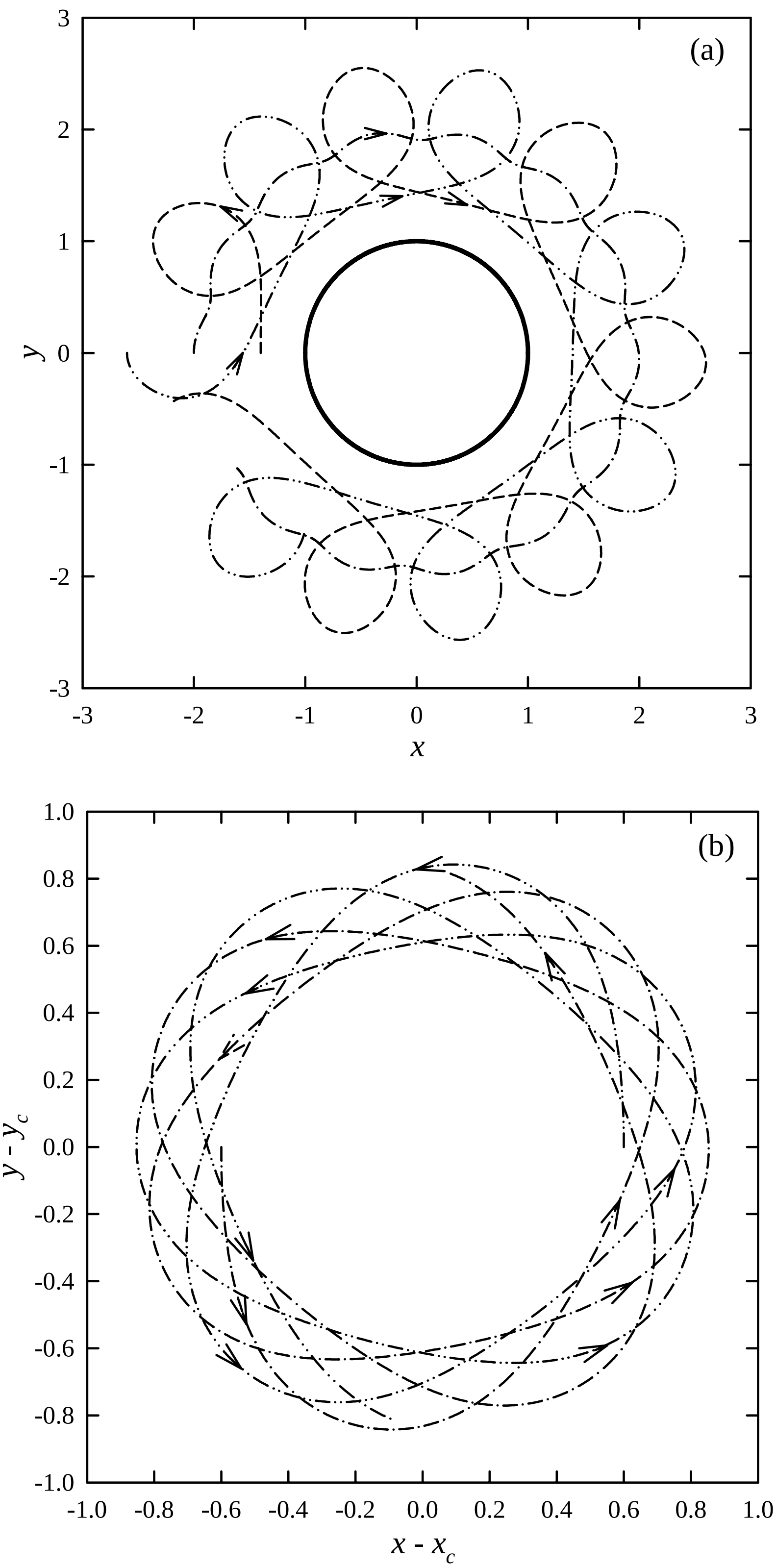

Figure 2.6 *Paths of vortices at large ε and large z_c. (a) Vortex paths relative to cylinder centre; (b) Vortex paths relative to vorticity centroid. ——— Cylinder surface; – – – – vorticity centroid; —·— z_1; —··— z_2; Arrows direction of motion. z_{1i} = (–2.6, 0), z_{2i} = (–1.4, 0), $\Gamma_1 = \Gamma_2 = 0.5$.*

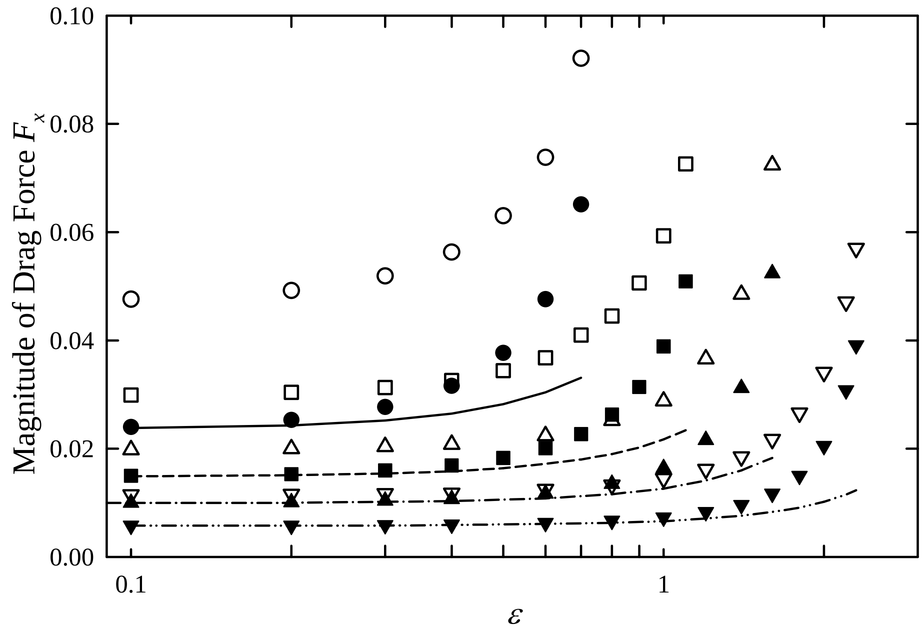

Figure 2.7 Combined effects of z_c and ε on drag force for $\Gamma_1 = \Gamma_2 = 0.5$. Maximum $|F_{xc}|$: ○ $z_{ci} = (-1.5,0)$; □ $z_{ci} = (-1.75,0)$; △ $z_{ci} = (-2,0)$; ▽ $z_{ci} = (-2.4,0)$; Maximum $|F_{xm}|$: ● $z_{ci} = (-1.5,0)$; ■ $z_{ci} = (-1.75,0)$; ▲ $z_{ci} = (-2,0)$; ▼ $z_{ci} = (-2.4,0)$; Approximation from simplified vortex paths for maximum $|F_{xm}|$: ——— $z_{ci} = (-1.5,0)$; – – – – $z_{ci} = (-1.75,0)$; — · — $z_{ci} = (-2,0)$; — ·· — $z_{ci} = (-2.4,0)$.

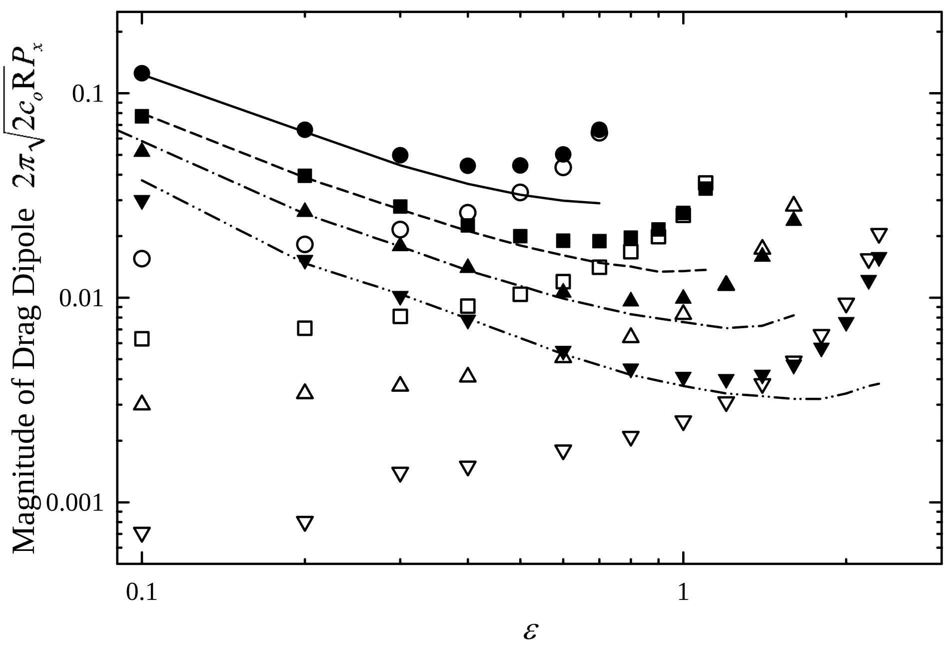

Figure 2.8 Combined effects of z_c and ε on dipole strength for $\Gamma_1 = \Gamma_2 = 0.5$. Maximum $|P_{xc}|$: ○ $z_{ci} = (-1.5,0)$; □ $z_{ci} = (-1.75,0)$; △ $z_{ci} = (-2,0)$; ▽ $z_{ci} = (-2.4,0)$; Maximum $|P_{xm}|$: ● $z_{ci} = (-1.5,0)$; ■ $z_{ci} = (-1.75,0)$; ▲ $z_{ci} = (-2,0)$; ▼ $z_{ci} = (-2.4,0)$; Approximation from simplified vortex paths for maximum $|P_{xm}|$: ——— $z_{ci} = (-1.5,0)$; – – – – $z_{ci} = (-1.75,0)$; — · — $z_{ci} = (-2,0)$; — ·· — $z_{ci} = (-2.4,0)$.

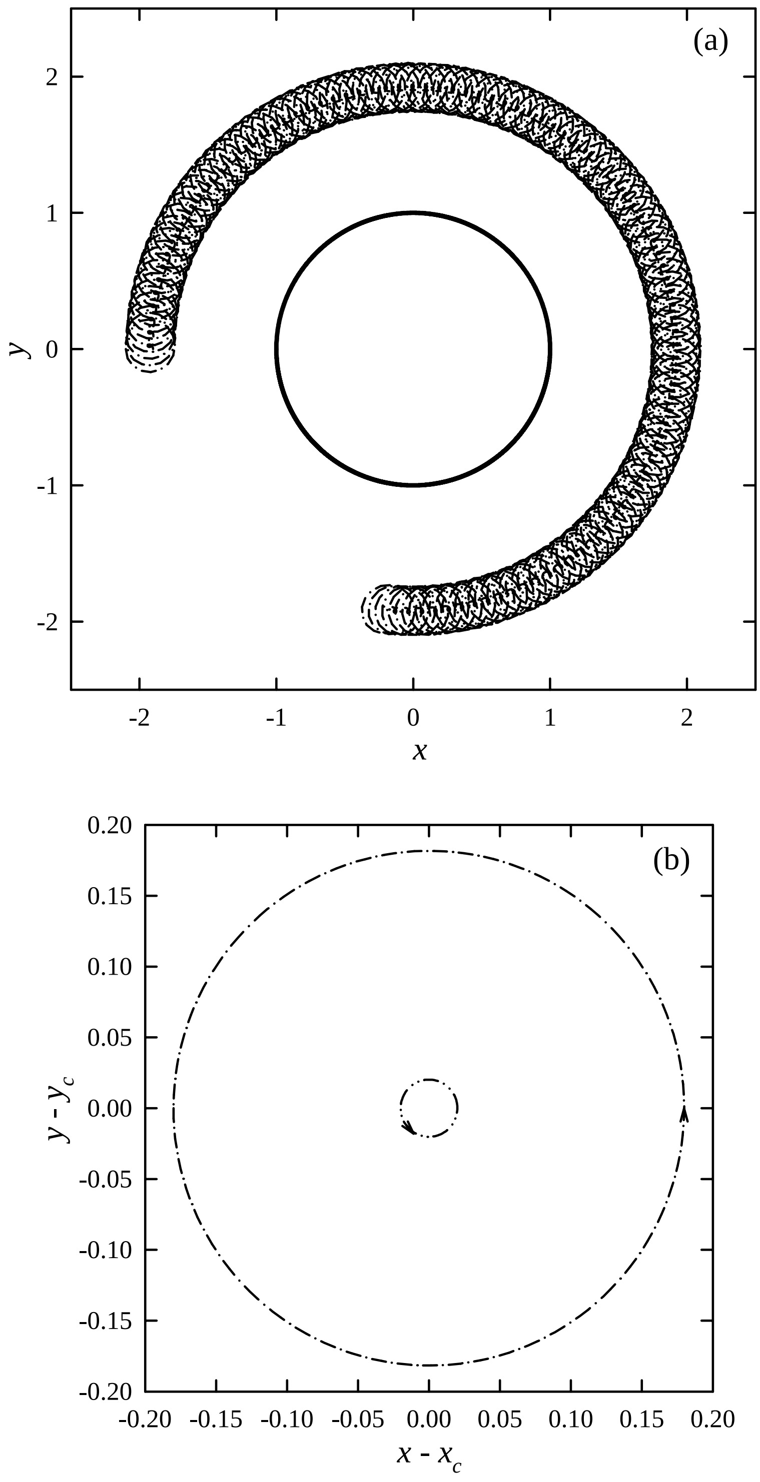

Figure 2.9 Vortex paths when one of the vortices is considerably stronger than the other. (a) Vortex paths relative to cylinder centre; (b) vortex paths relative to vorticity centroid ($0 \leq t \leq 250$). ——— Cylinder surface; – – – – vorticity centroid; — · — z_1; — ·· — z_2; Arrows direction of motion. $z_{1i} = (-2.1, 0)$, $z_{2i} = (-1.9, 0)$, $\Gamma_1 = 0.1$, $\Gamma_2 = 0.9$.

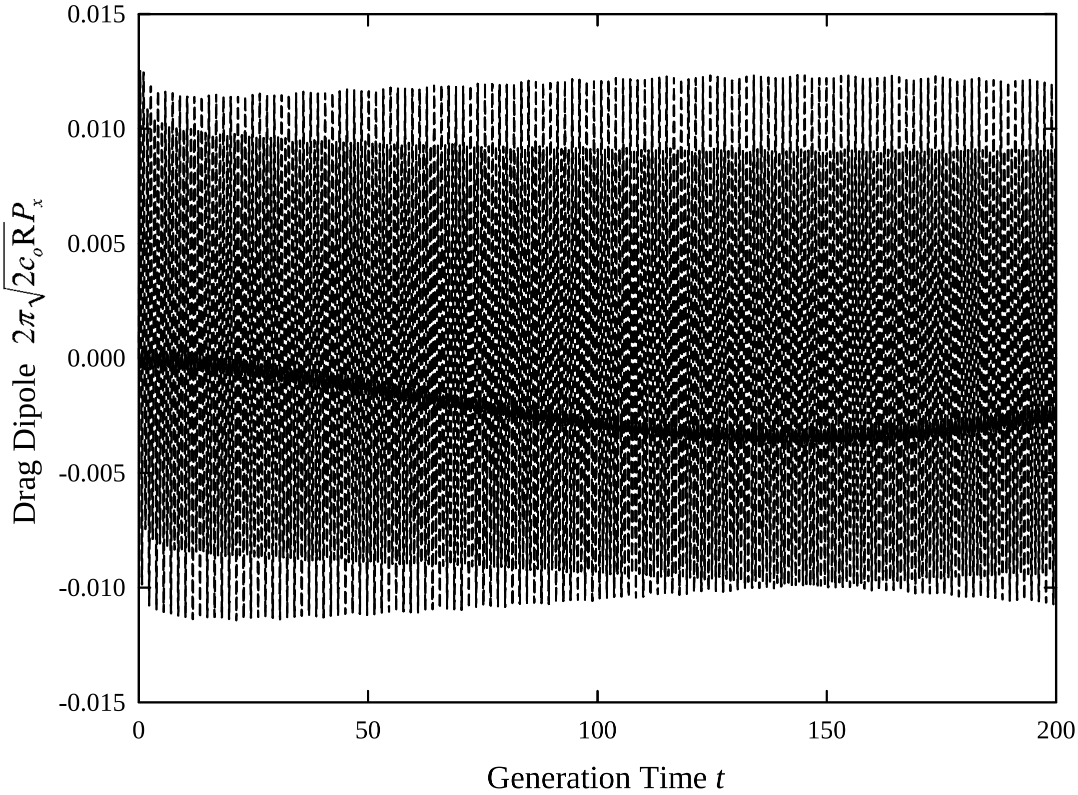

Figure 2.10 Example of time variation of the x - direction dipole strength for $\Gamma_1 \neq \Gamma_2$. ——— P_{xc}; – – – – P_{xm}. z_{1i} = (–2.1, 0), z_{2i} = (–1.9, 0), Γ_1 = 0.1, Γ_2 = 0.9.

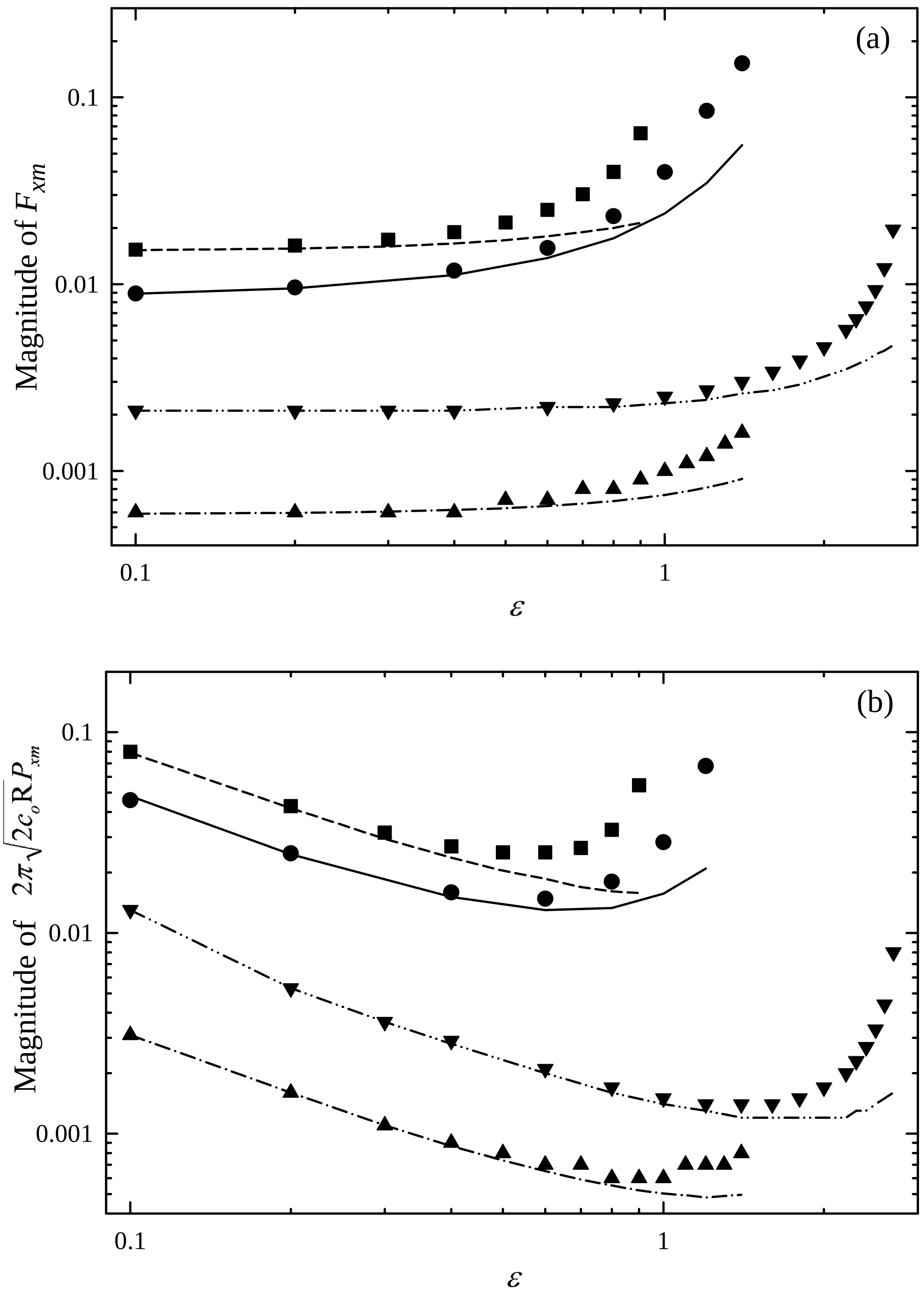

Figure 2.11 Combined effects of z_c and ε on drag force and dipole strength for $\Gamma_1 \neq \Gamma_2$. (a) $|F_{xm}|$; (b) $|P_{xm}|$. ● z_{ci} = (–1.98,0), Γ_1 = 0.3, Γ_2 = 0.7; ■ z_{ci} = (–1.53,0), Γ_1 = 0.8, Γ_2 = 0.2; ▲ z_{ci} = (–1.8,0), Γ_1 = 0.99, Γ_2 = 0.01; ▼ z_{ci} = (–2.44,0), Γ_1 = 0.9, Γ_2 = 0.1; Data from approximated vortex paths: ——— z_{ci} = (–1.98,0), Γ_1 = 0.3, Γ_2 = 0.7; – – – – z_{ci} = (–1.53,0), Γ_1 = 0.8, Γ_2 = 0.2; —· — z_{ci} = (–1.8,0), Γ_1 = 0.99, Γ_2 = 0.01; —·· — z_{ci} = (–2.44,0), Γ_1 = 0.9, Γ_2 = 0.1.

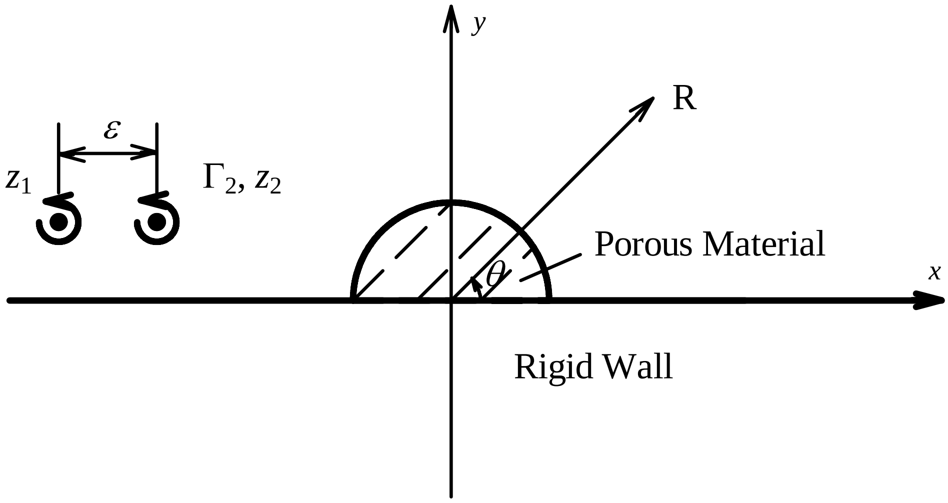

Figure 3.1 Schematics of vortex model and nomenclatures in the original z-plane.

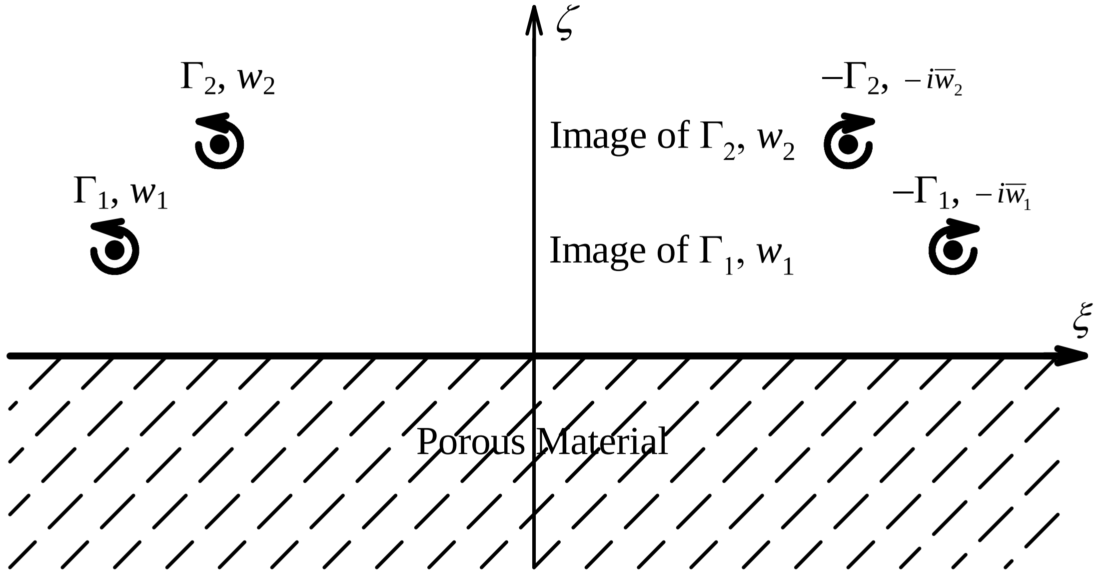

Figure 3.2 Schematics of vortex model and nomenclatures in the transformed w-plane.

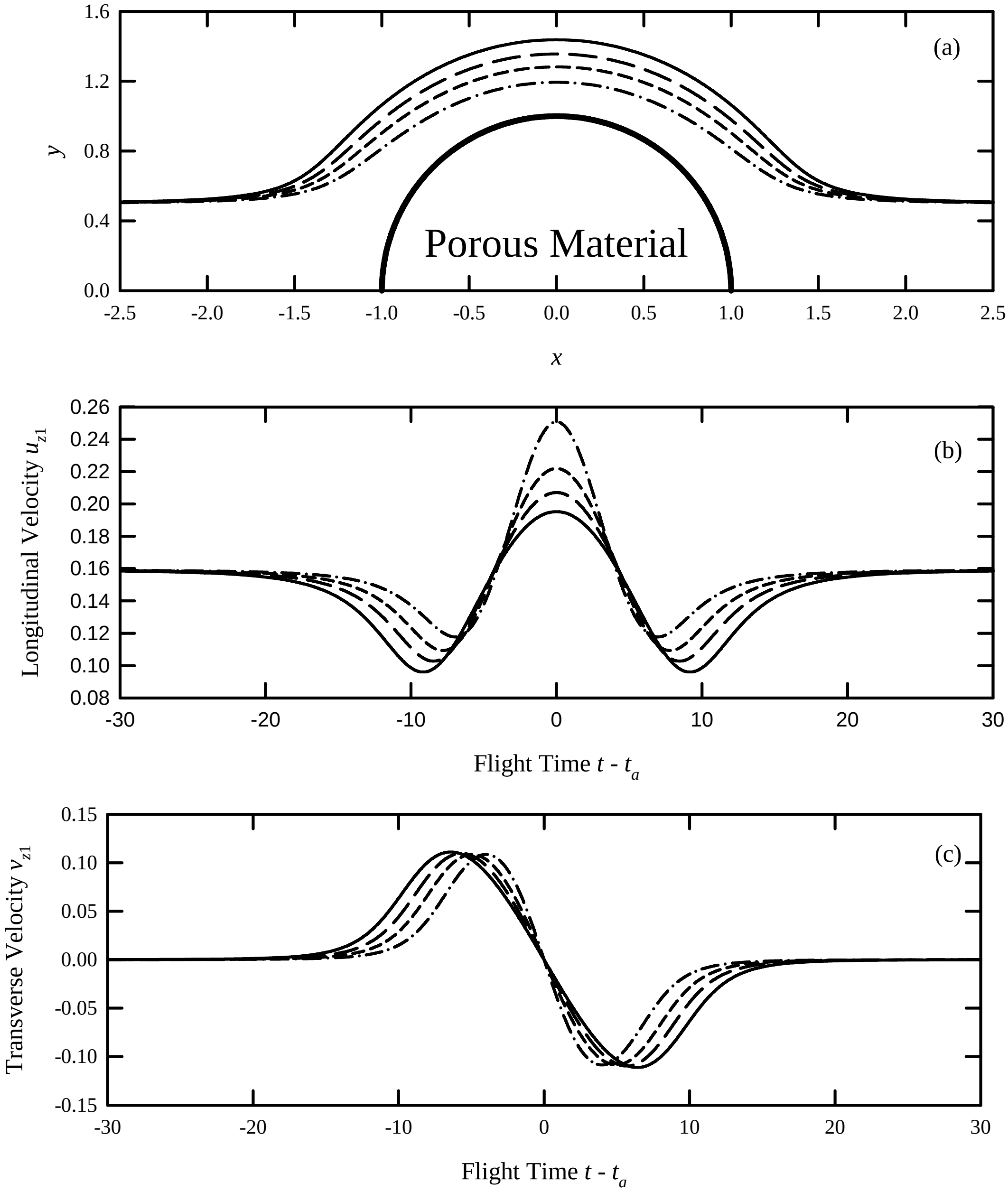

Figure 3.3 Effect of pressure-releasing surface on vortex motion, velocity, acceleration and sound generation. (a) Vortex path; (b) Longitudinal velocity; (c) Transverse velocity; (d) Longitudinal acceleration; (e) Transverse acceleration; (f) Sound pressure.— · — $\eta = 3$; – – – $\eta = 5$; ——— $\eta = 10$; —— rigid half cylinder. Initial $z_{1i} = (-10, 0.5)$.

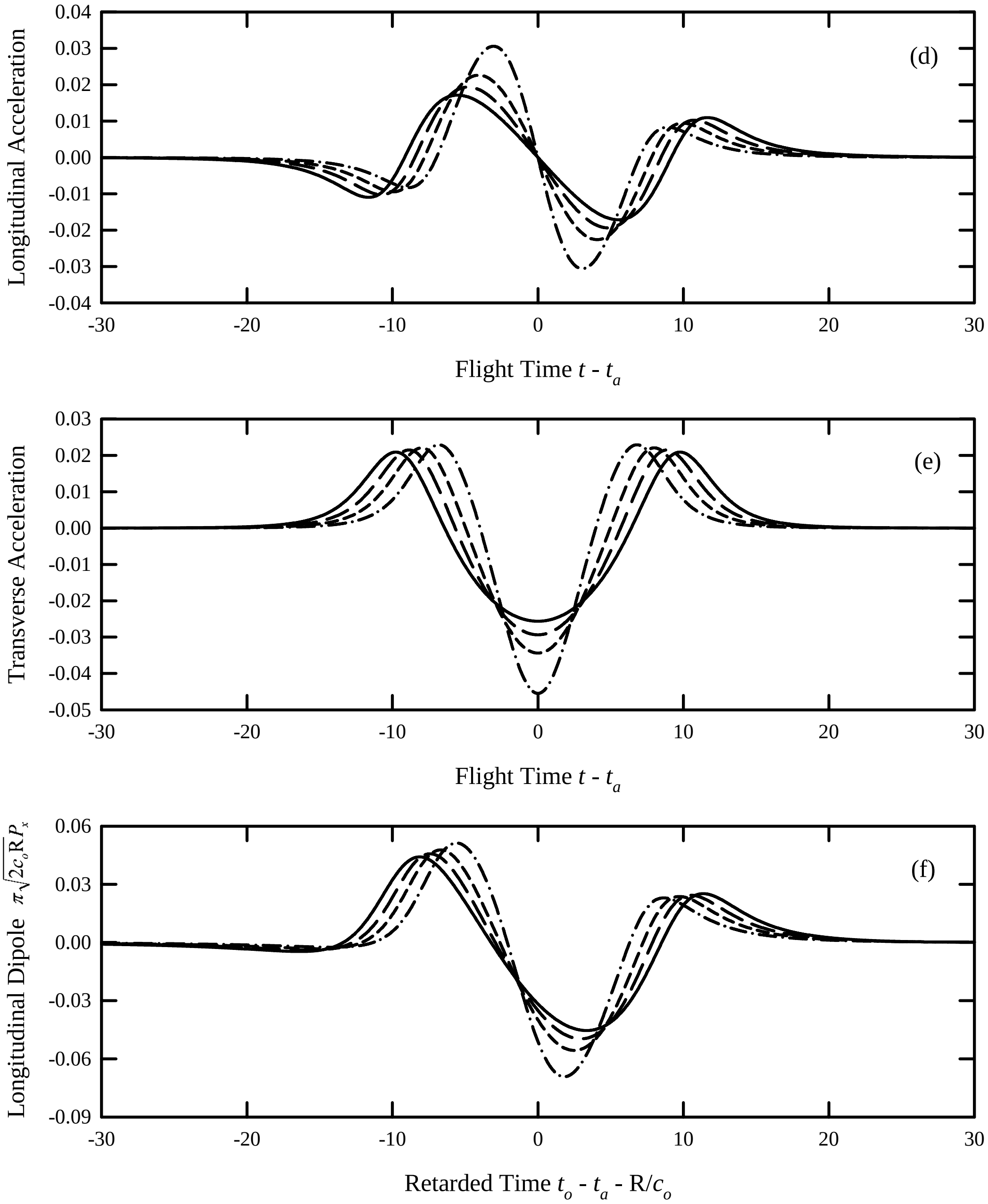

Figure 3.3 Continued

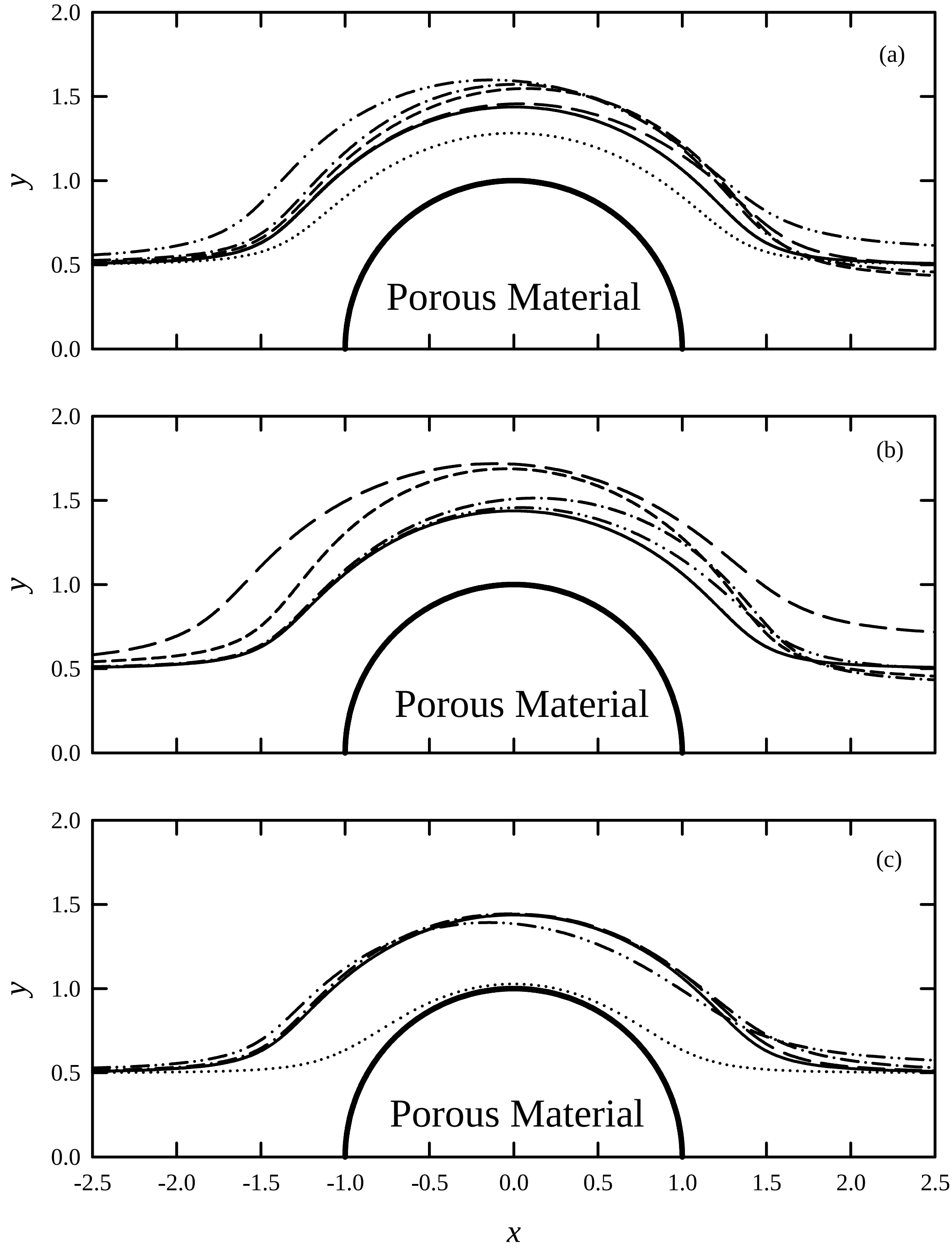

Figure 3.4 Combined effects of effective fluid density and flow resistance on the vortex path. (a) η = 5. ········ R_f = 0; — ·· — R_f = 0.1; — · — R_f = 0.5; – – – R_f = 1; ——— R_f = 10; ——— rigid half cylinder; (b) R_f = 5. — ·· — η = 3; — · — η = 10; – – – η = 100; ——— η = 1000; ——— rigid half cylinder; (c) η = 1.5. ········ R_f = 0; — ·· — R_f = 0.1; — · — R_f = 0.5; ——— R_f = 10; ———: rigid half cylinder. Initial location of the vortex at x_{1i} = –10 and y_{1i} = 0.5.

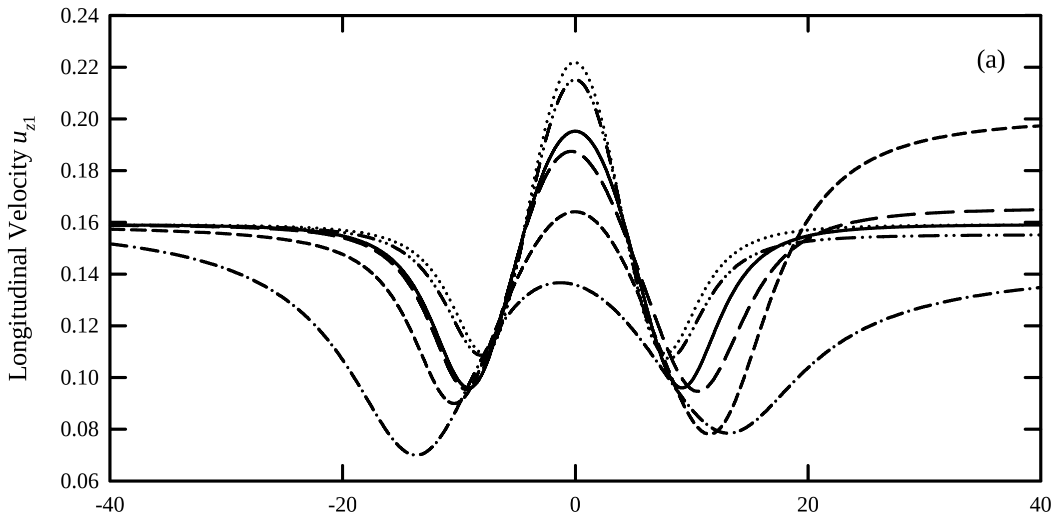

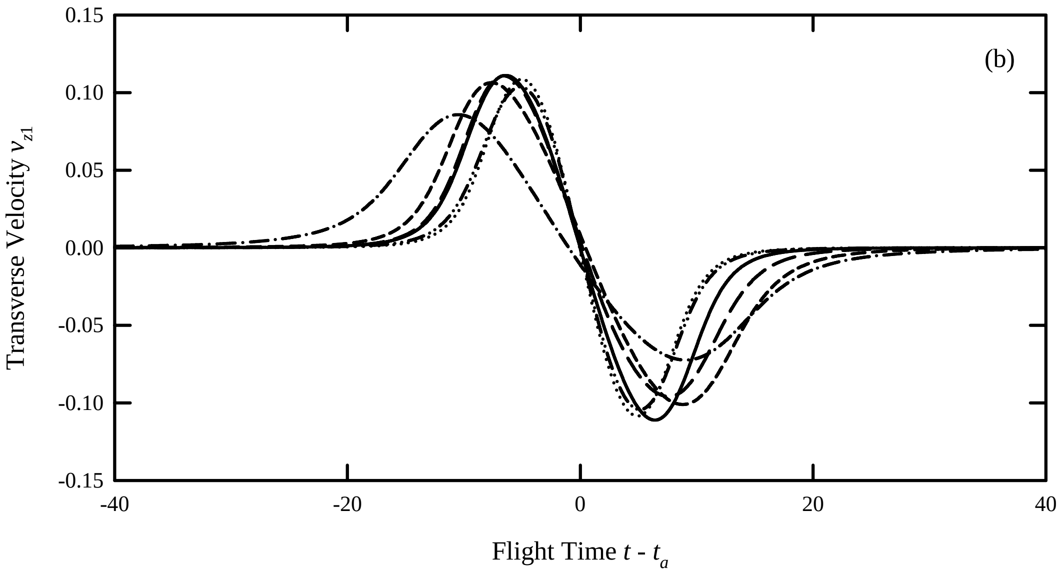

Figure 3.5 Effects of flow resistance on vortex velocity. (a) Longitudinal velocity; (b) Transverse velocity. ········ R_f = 0; — ·· — R_f = 0.001; — · — R_f = 0.1; – – – – R_f = 1; ——— R_f = 10; ——— rigid half cylinder. Initial z_{1i} = (–10, 0.5), η = 5.

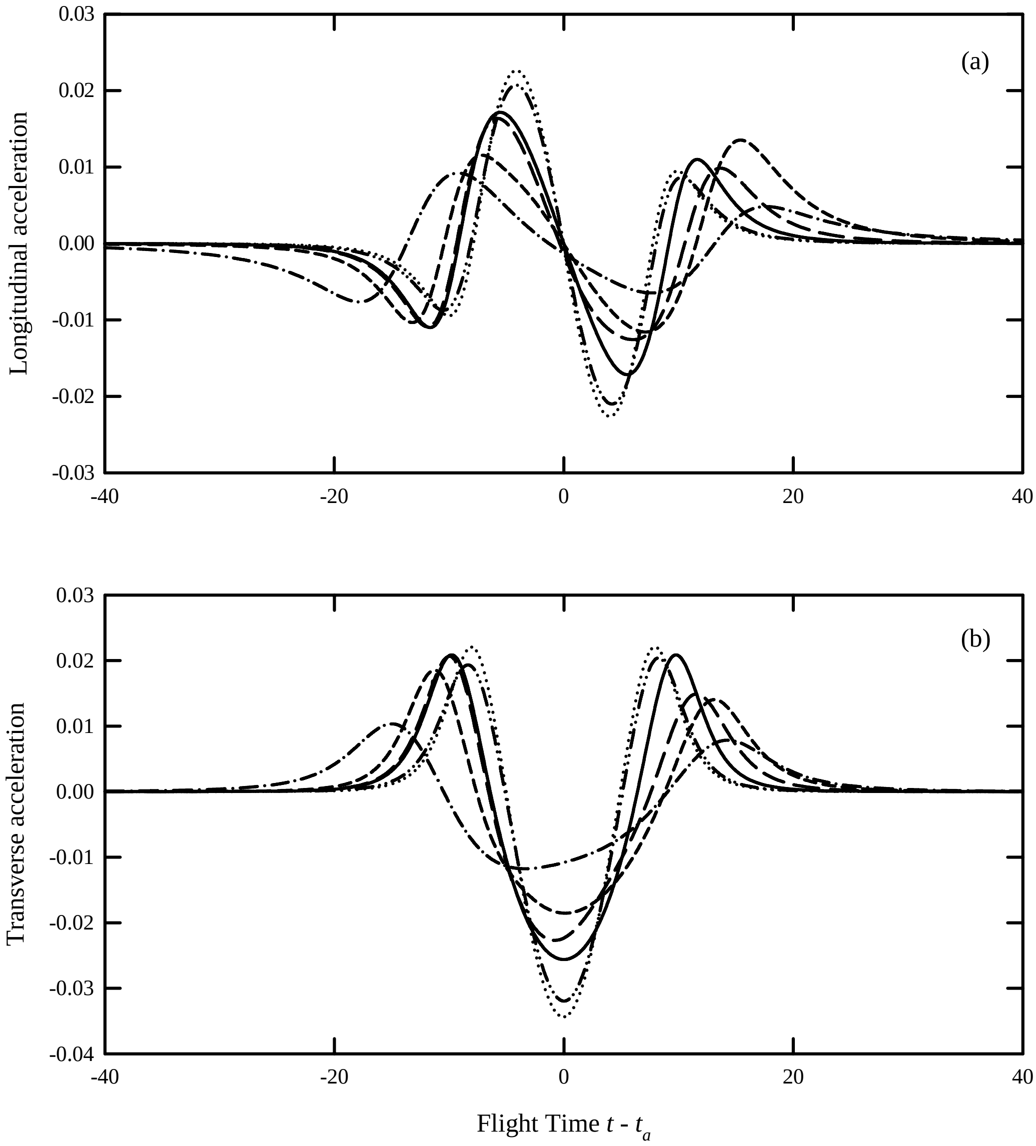

Figure 3.6 Effects of flow resistance on vortex acceleration. (a) Longitudinal acceleration; (b) Transverse acceleration. ········ $R_f = 0$; —— ·· —— $R_f = 0.001$; —— · —— $R_f = 0.1$; – – – – $R_f = 1$; ——— $R_f = 10$; ——— *rigid half cylinder. Initial* $z_{1i} = (-10, 0.5)$, $\eta = 5$.

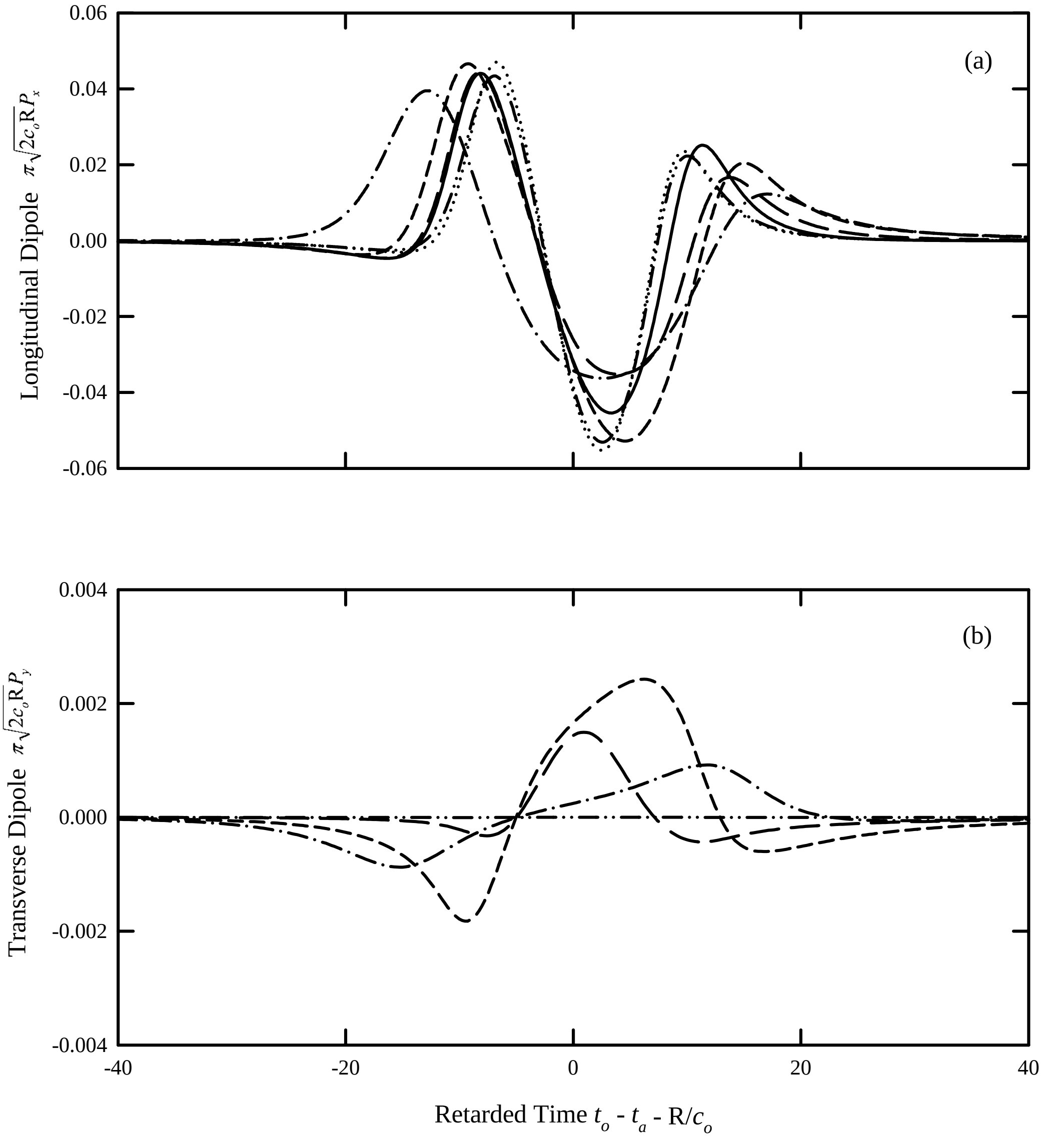

Figure 3.7 Sound pressure time variation for η = 5 at different R_f. (a) Longitudinal dipole; (b) transverse dipole. ········ R_f = 0; —— ·· —— R_f = 0.001; —— · —— R_f = 0.1; – – – – R_f = 1; ——— ——— R_f = 10; ——— rigid half cylinder. Initial z_{1i} = (–10, 0.5).

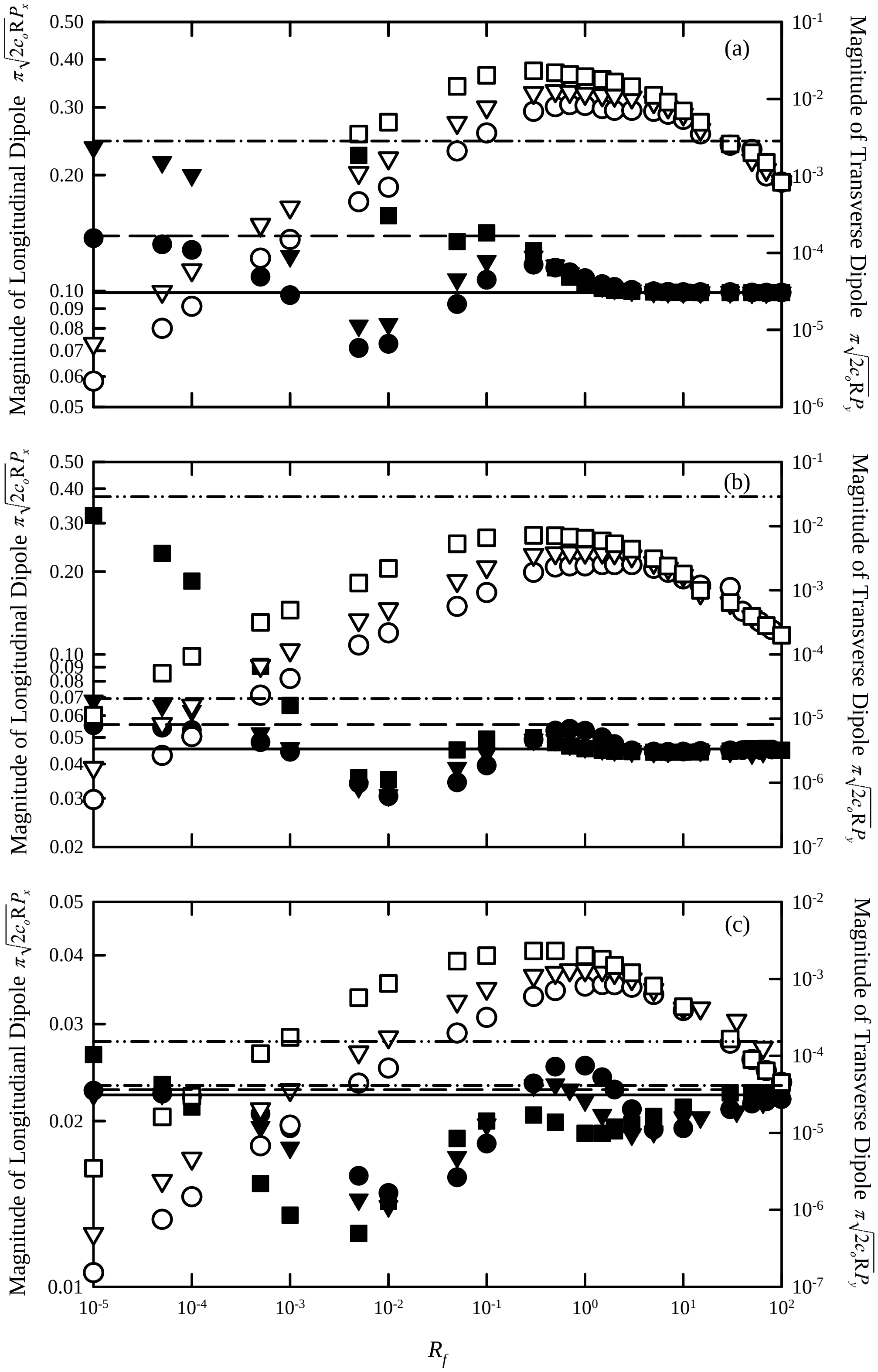

Figure 3.8 Combined effects of effective fluid density, flow resistance and initial vortex height on radiated sound amplitude. (a) y_{1i} = 0.3; (b) y_{1i} = 0.5; (c) y_{1i} = 0.8. —··— P_x for η = 1.5, R_f = 0; —·— P_x for η = 3, R_f = 0; — — — P_x for η = 5, R_f = 0; ——— rigid half cylinder. □ η = 1.5; ▽ η = 3; ○ η = 5. Closed Symbols for P_x, open symbols for P_y.

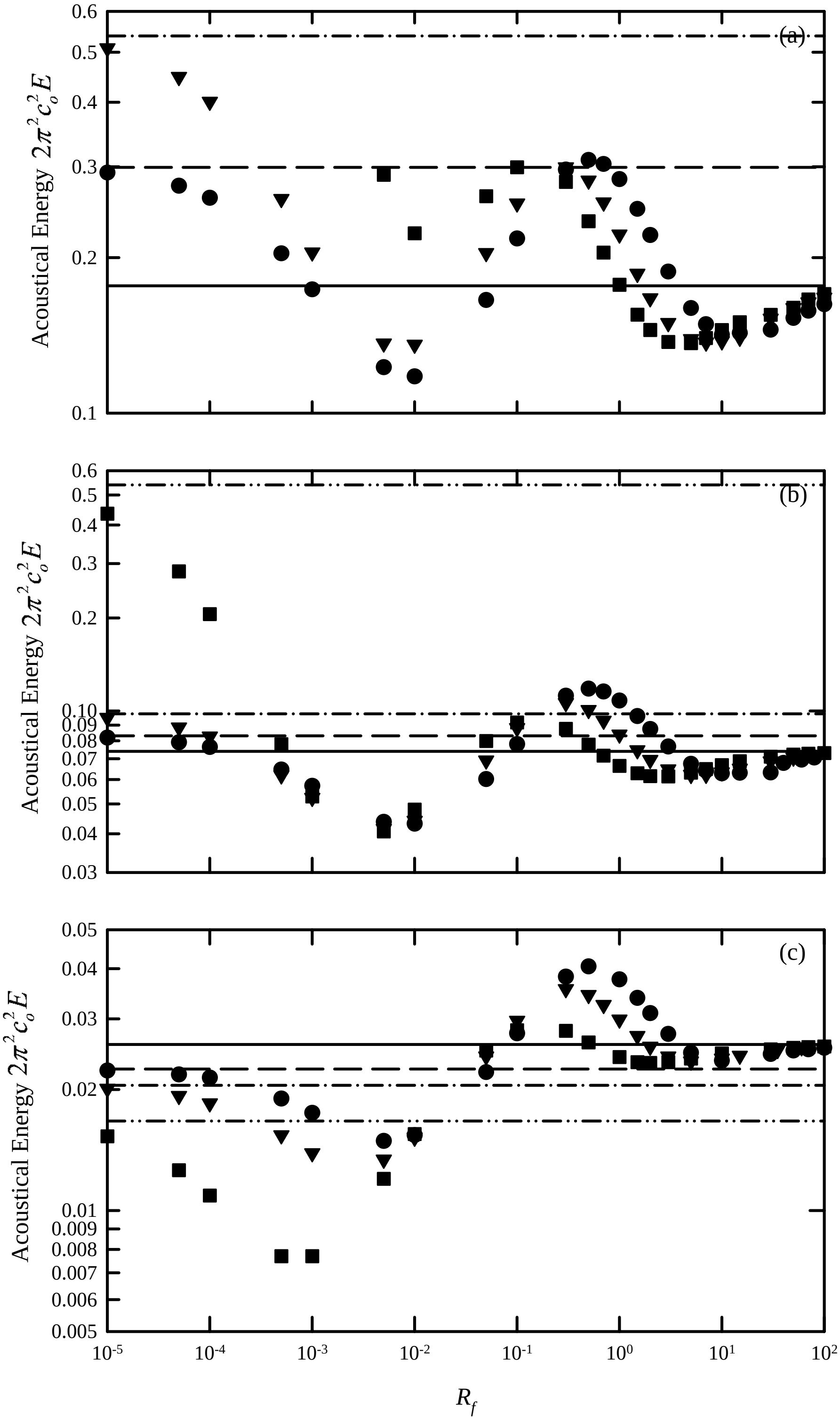

Figure 3.9 Combined effects of effective fluid density, flow resistance and initial vortex height on acoustical energy radiation. (a) y_{1i} = 0.3; (b) y_{1i} = 0.5; (c) y_{1i} = 0.8. —··— P_x for η = 1.5, R_f = 0; —·— P_x for η = 3, R_f = 0; — — — P_x for η = 5, R_f = 0; ——— rigid half cylinder. ■ η = 1.5; ▼ η = 3; ● η = 5.

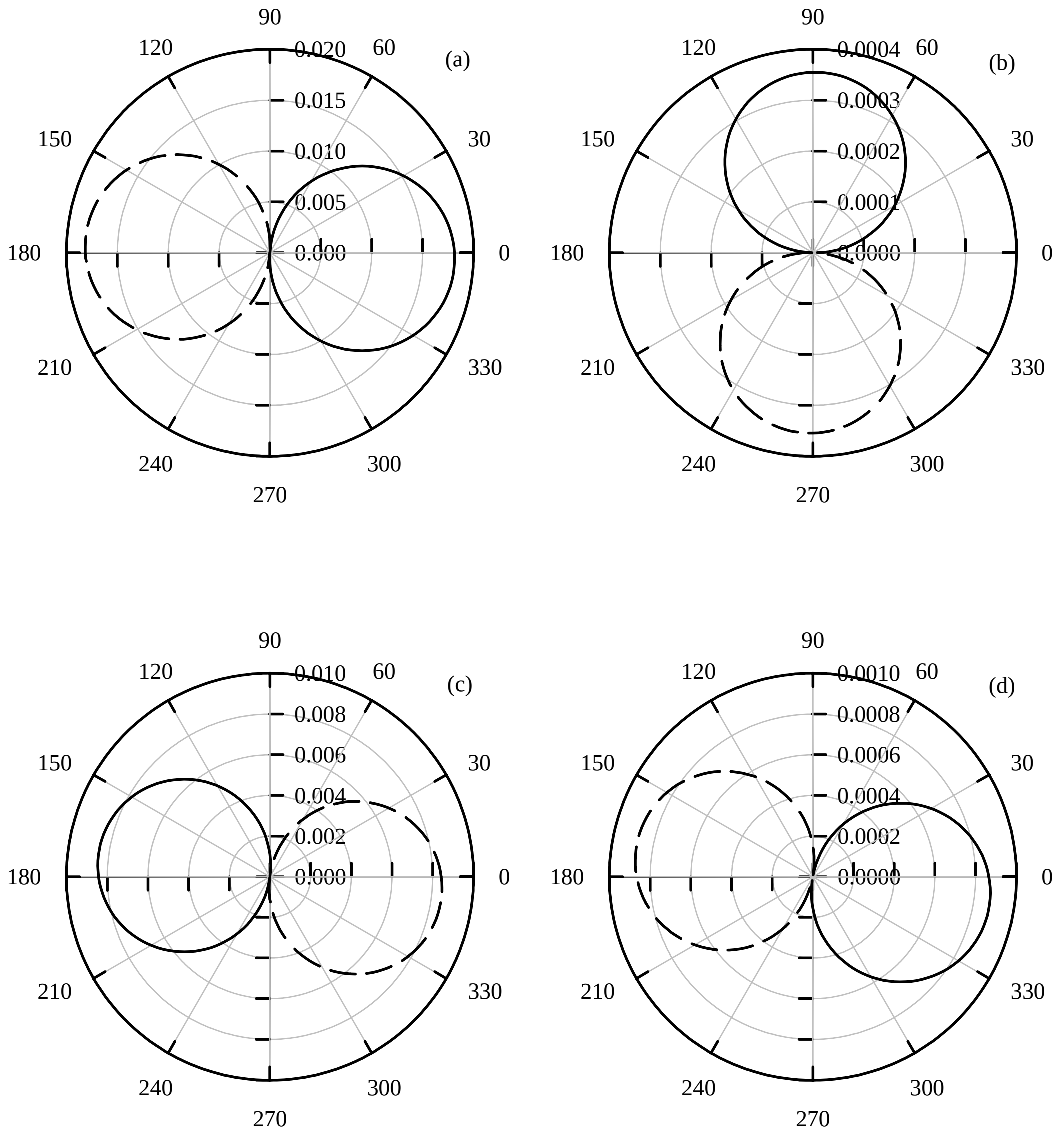

Figure 3.10 Time variation of far-field directivity. (a) $t_o - t_a - R/c_o = -16.14$; (b) $t_o - t_a - R/c_o = -6.76$; (c) $t_o - t_a - R/c_o = 13.86$; (d) $t_o - t_a - R/c_o = 53.86$. — — — negative sound pressure; ——— positive sound pressure. Initial $z_{1i} = (-10, 0.8)$, $\eta = 1.5$ and $R_f = 0.5$.

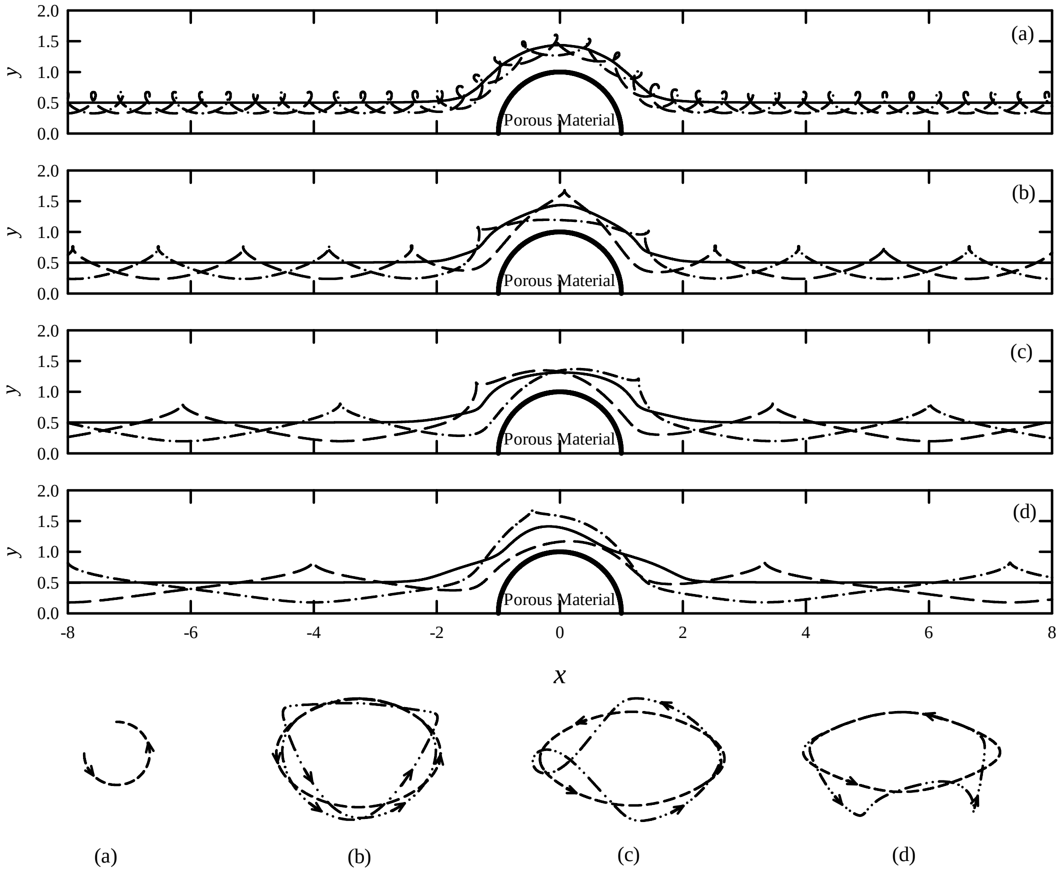

Figure 3.11 Unsteady leapfrogging motions of two identical vortices near a rigid half cylinder. (a) $\varepsilon = 0.4$; (b) $\varepsilon = 0.8$; (c) $\varepsilon = 1.2$; (d) $\varepsilon = 1.6$. ———— z_1; — · — z_2; ——— z_c; – – – – z_1 relative to z_c at $x < -2$ or $x > 2$; — ·· — z_2 relative to z_c at $-2 < x < 2$. Initial $z_{ci} = (-10, 0.5)$, $\Gamma_1 = \Gamma_2 = 0.5$.

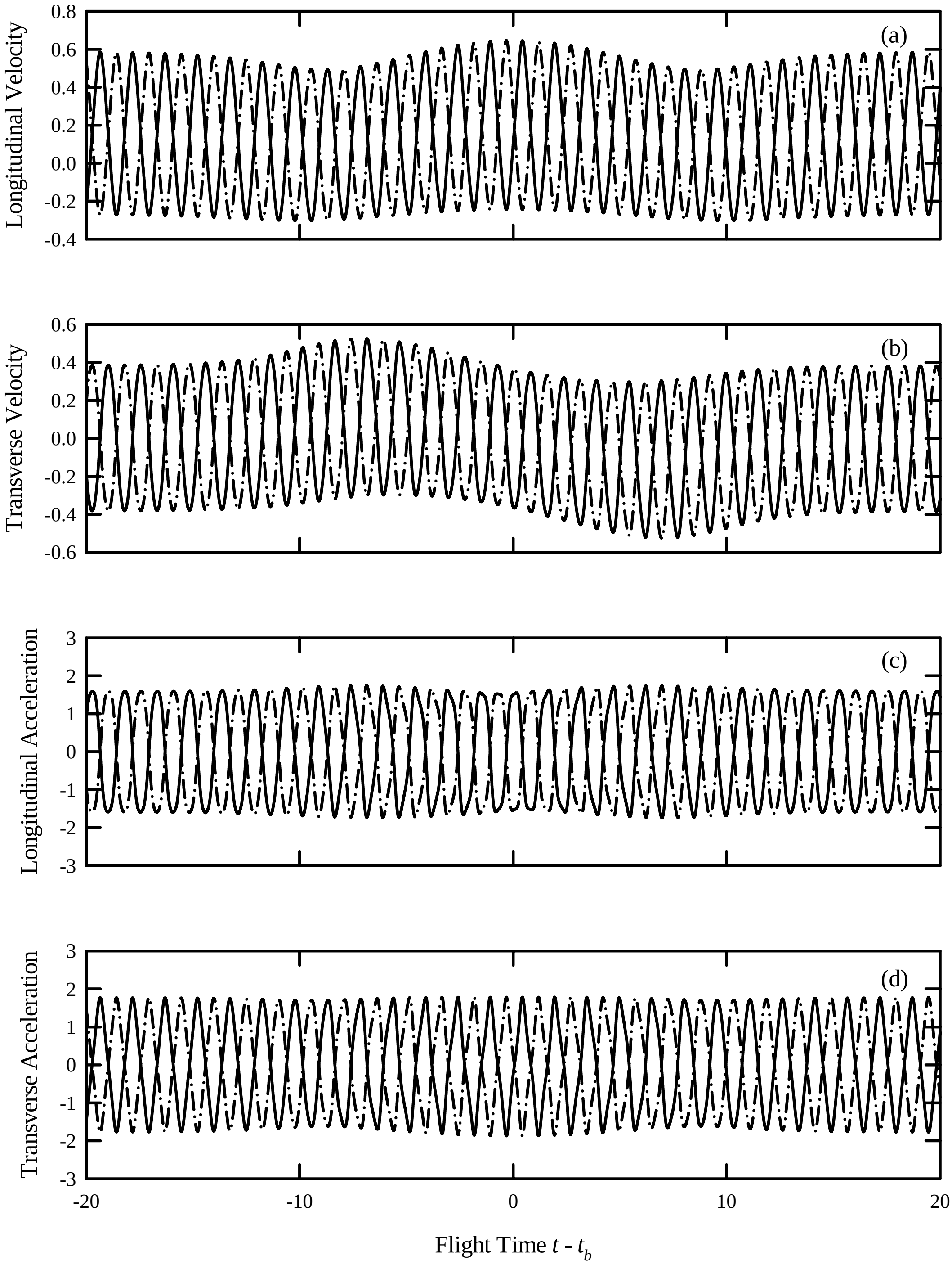

Figure 3.12 Time variation of vortex velocity and acceleration at small ε in the presence of a rigid half cylinder. (a) Longitudinal velocity; (b) Transverse velocity; (c) Longitudinal acceleration; (d) Transverse acceleration. ——— z_1; — · — z_2. z_{ci} initially located at (–10, 0.5), $\Gamma_1 = \Gamma_2 = 0.5$, $\varepsilon = 0.2$.

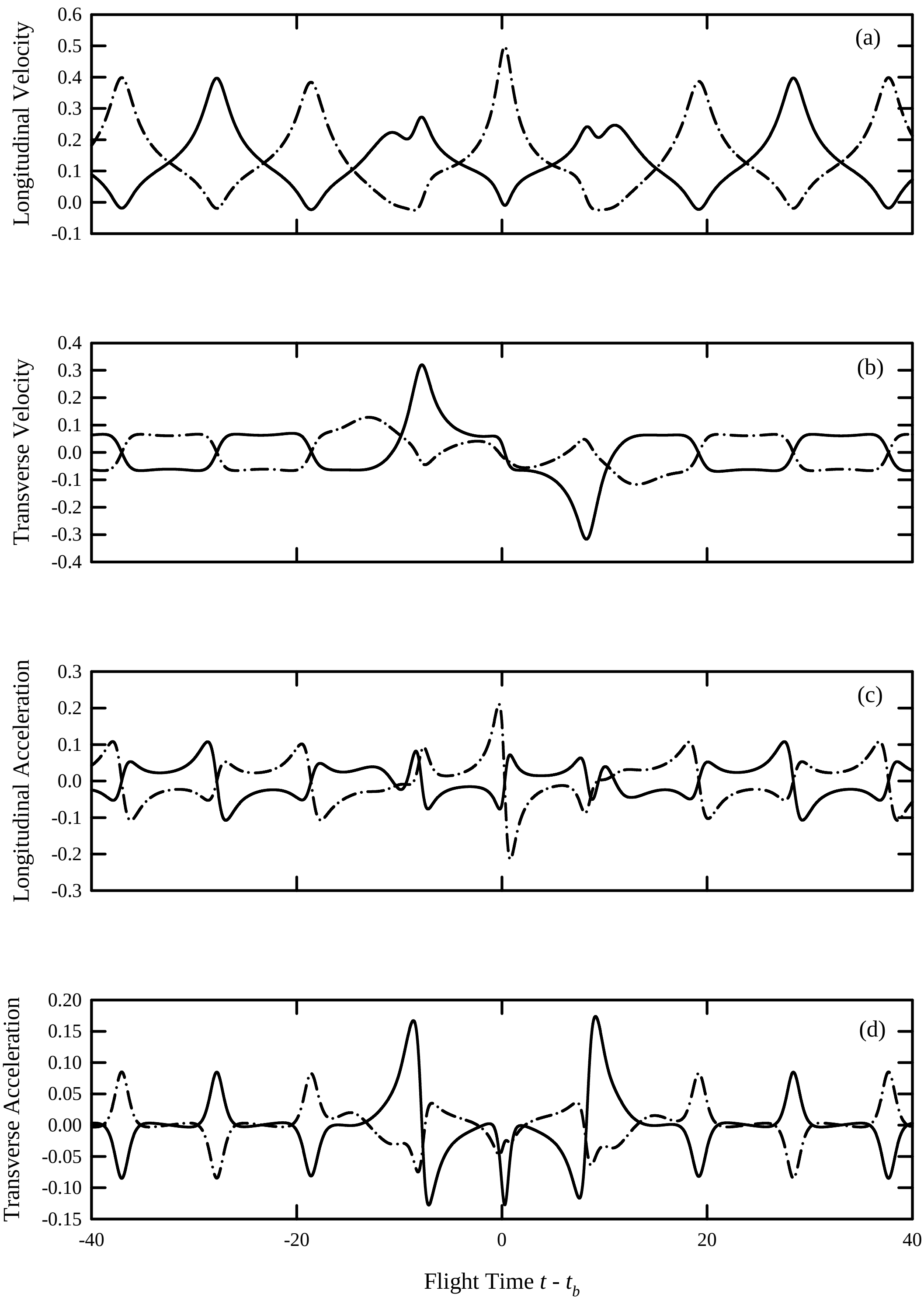

Figure 3.13 Time variation of vortex velocity and acceleration at $\varepsilon = 0.8$ in the presence of a rigid half cylinder. (a) Longitudinal velocity; (b) Transverse velocity; (c) Longitudinal acceleration; (d) Transverse acceleration. ——— z_1; — · — z_2. z_{ci} initially located at (–10, 0.5), $\Gamma_1 = \Gamma_2 = 0.5$.

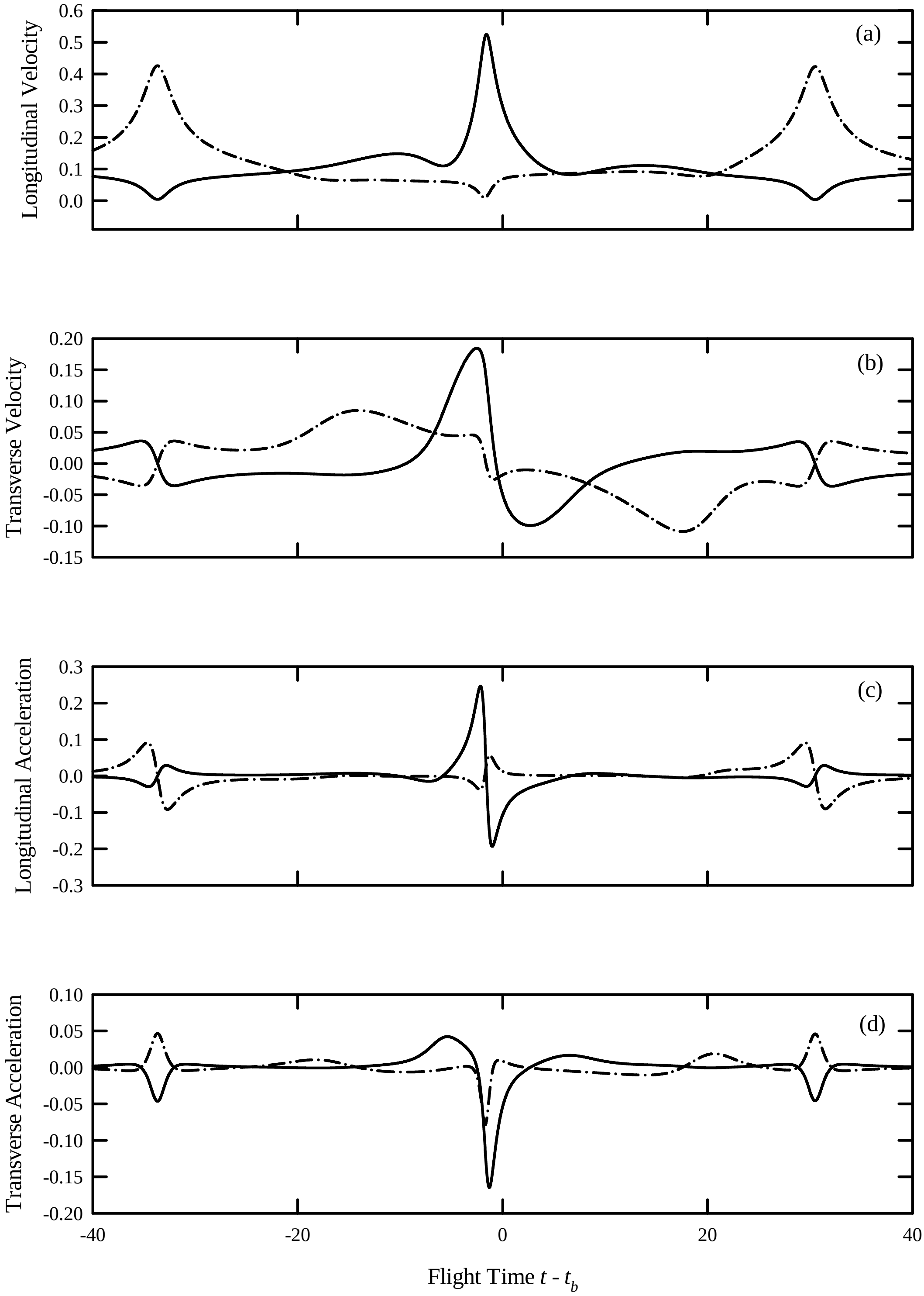

Figure 3.14 Time variation of vortex velocity and acceleration at large ε in the presence of a rigid half cylinder. (a) Longitudinal velocity; (b) Transverse velocity; (c) Longitudinal acceleration; (d) Transverse acceleration. ——— z_1; — · — z_2. z_{ci} initially located at (–10, 0.5), $\Gamma_1 = \Gamma_2 = 0.5$, $\varepsilon = 1.6$.

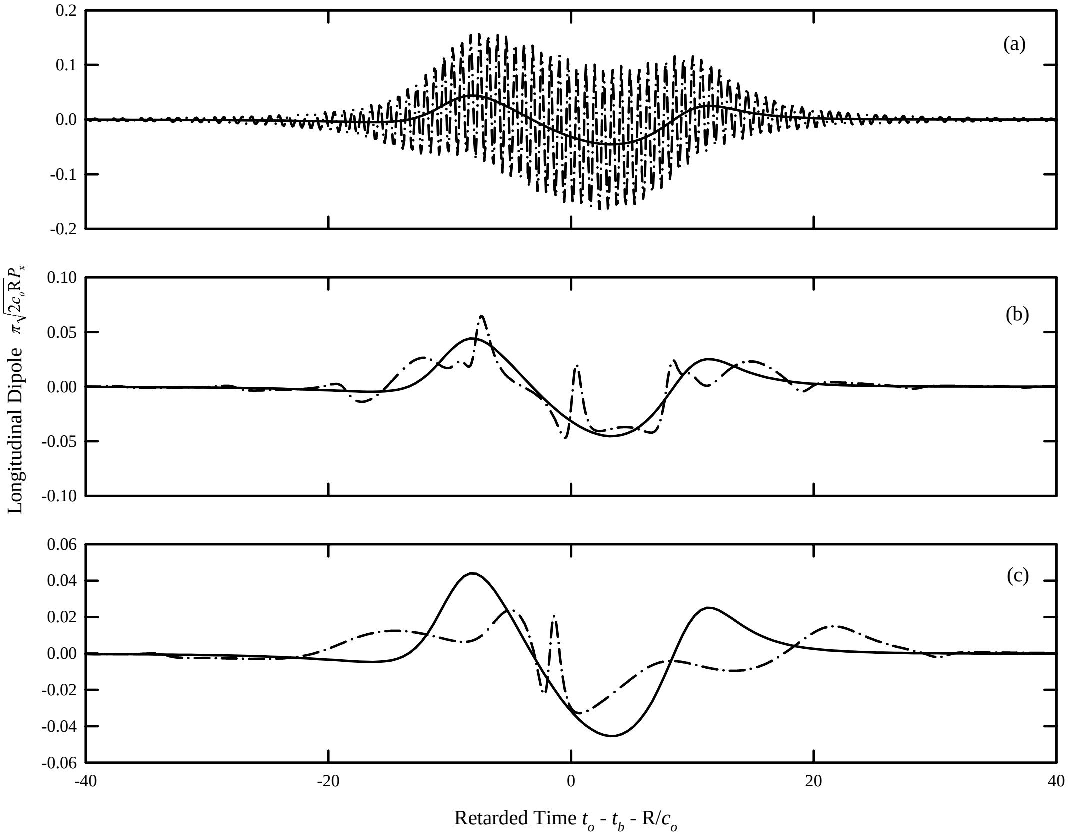

Figure 3.15 Time variation of longitudinal dipole magnitude at different separation distance in the presence of a half rigid cylinder. (a) ε = 0.2; (b) ε = 0.8; (c) ε = 1.6. ——— Equivalent single vortex results; — · — two interacting identical vortices results. z_{ci} initially at (–10, 0.5), Γ_1 = Γ_2 =0.5.

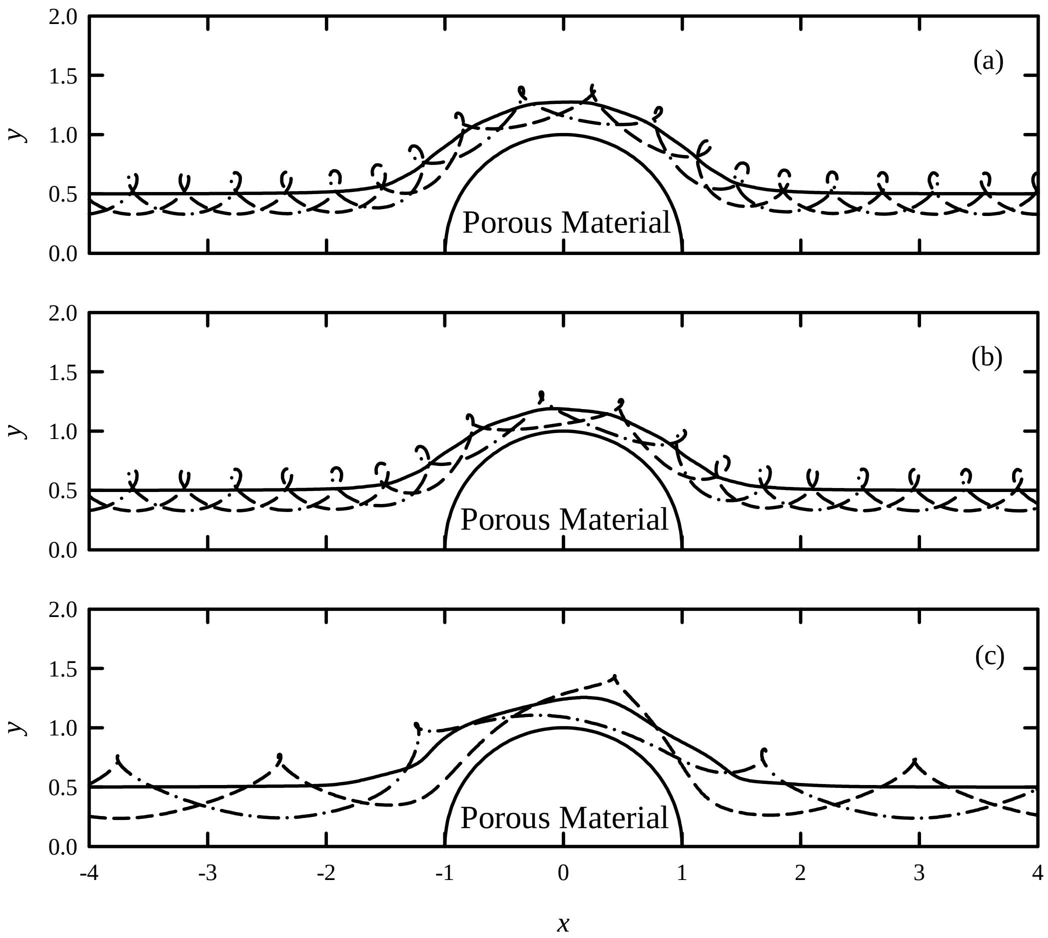

Figure 3.16 Paths of two interacting vortices for perfectly inviscid fluid cases. (a) $\varepsilon = 0.4$, $\eta = 5$; (b) $\varepsilon = 0.4$, $\eta = 2$; (c) $\varepsilon = 0.8$, $\eta = 5$. ——— z_1; — · — z_2; ——— z_c. z_{ci} initially at (–10, 0.5), $\Gamma_1 = \Gamma_2 = 0.5$.

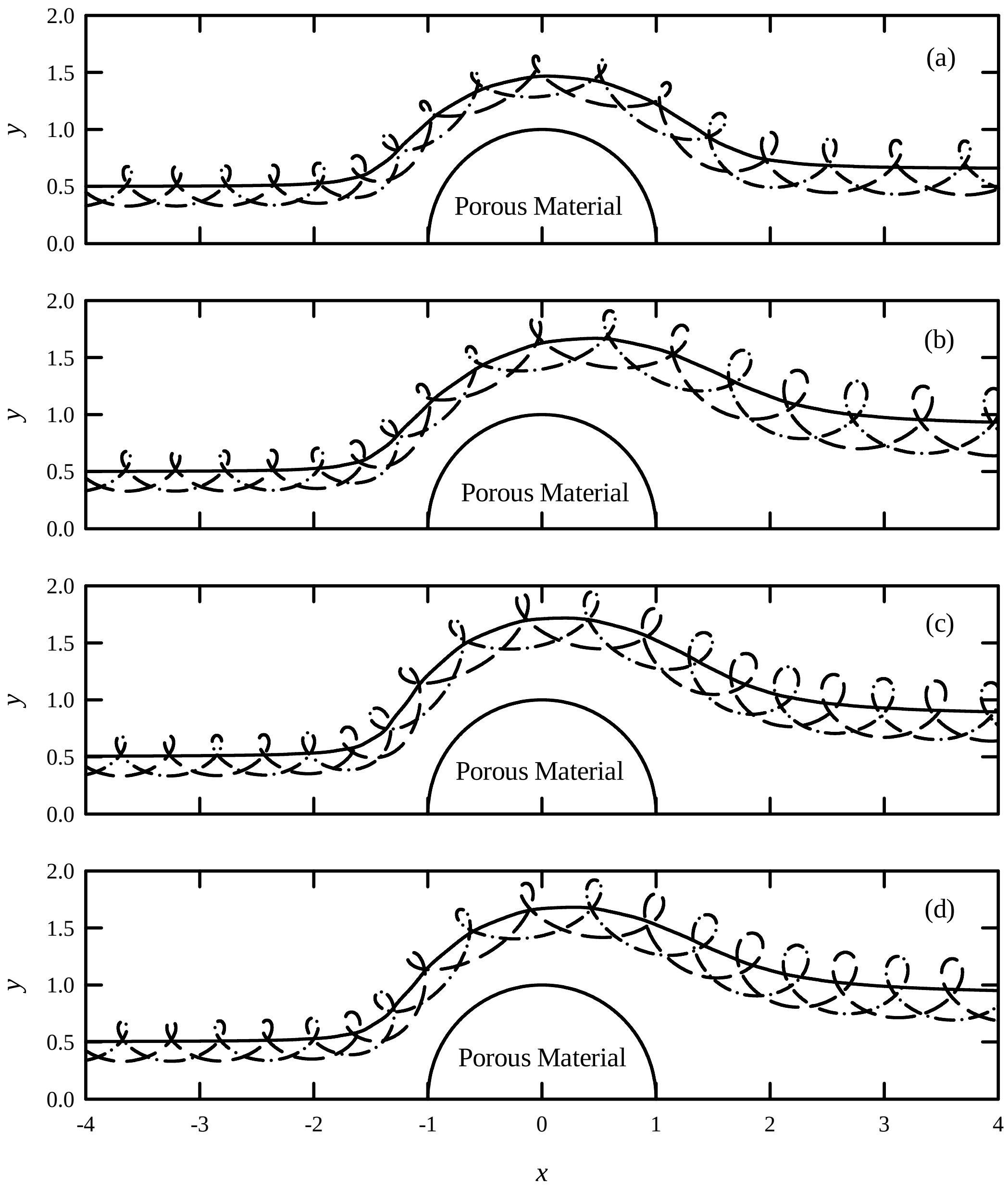

Figure 3.17 Combined effects of effective fluid density and flow resistance on the vortex paths. (a) η = 5, R_f = 10; (b) η = 5, R_f = 1; (c) η = 5, R_f = 0.1;(d) η = 3, R_f = 0.1. ——— z_1; — · — z_2; ——— z_c. Initial z_{1i} = (–10.2, 0.5), initial z_{2i} = (–9.8, 0.5), $\Gamma_1 = \Gamma_2$ = 0.5, ε = 0.4.

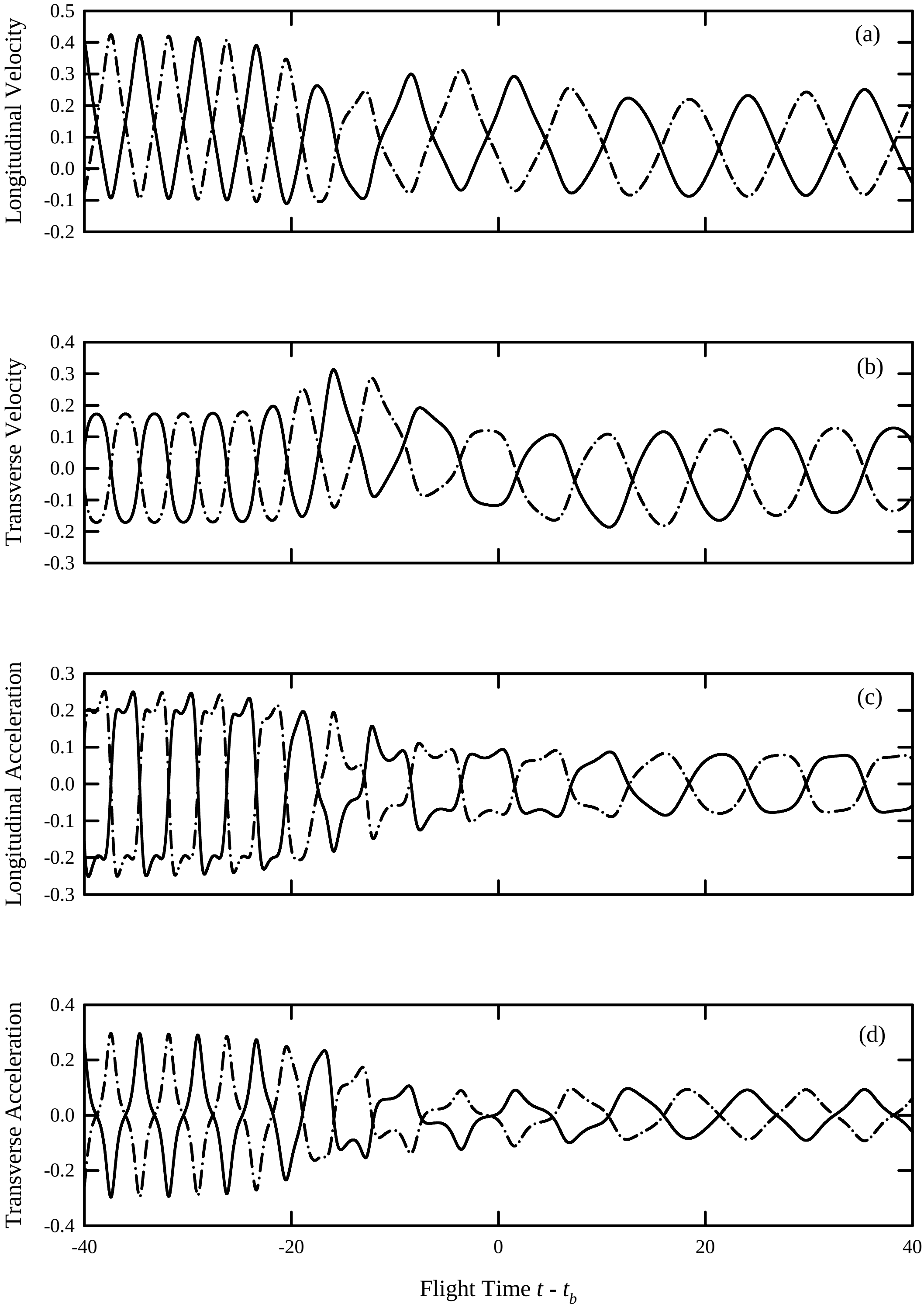

Figure 3.18 Time variation of vortex velocity and acceleration at η = 5 and R_f = 0.1. (a) Longitudinal velocity; (b) Transverse velocity; (c) Longitudinal acceleration; (d) Transverse acceleration. ——— z_1; — · — z_2. z_{ci} initially located at (–10, 0.5), $\Gamma_1 = \Gamma_2 = 0.5$, $\varepsilon = 0.4$.

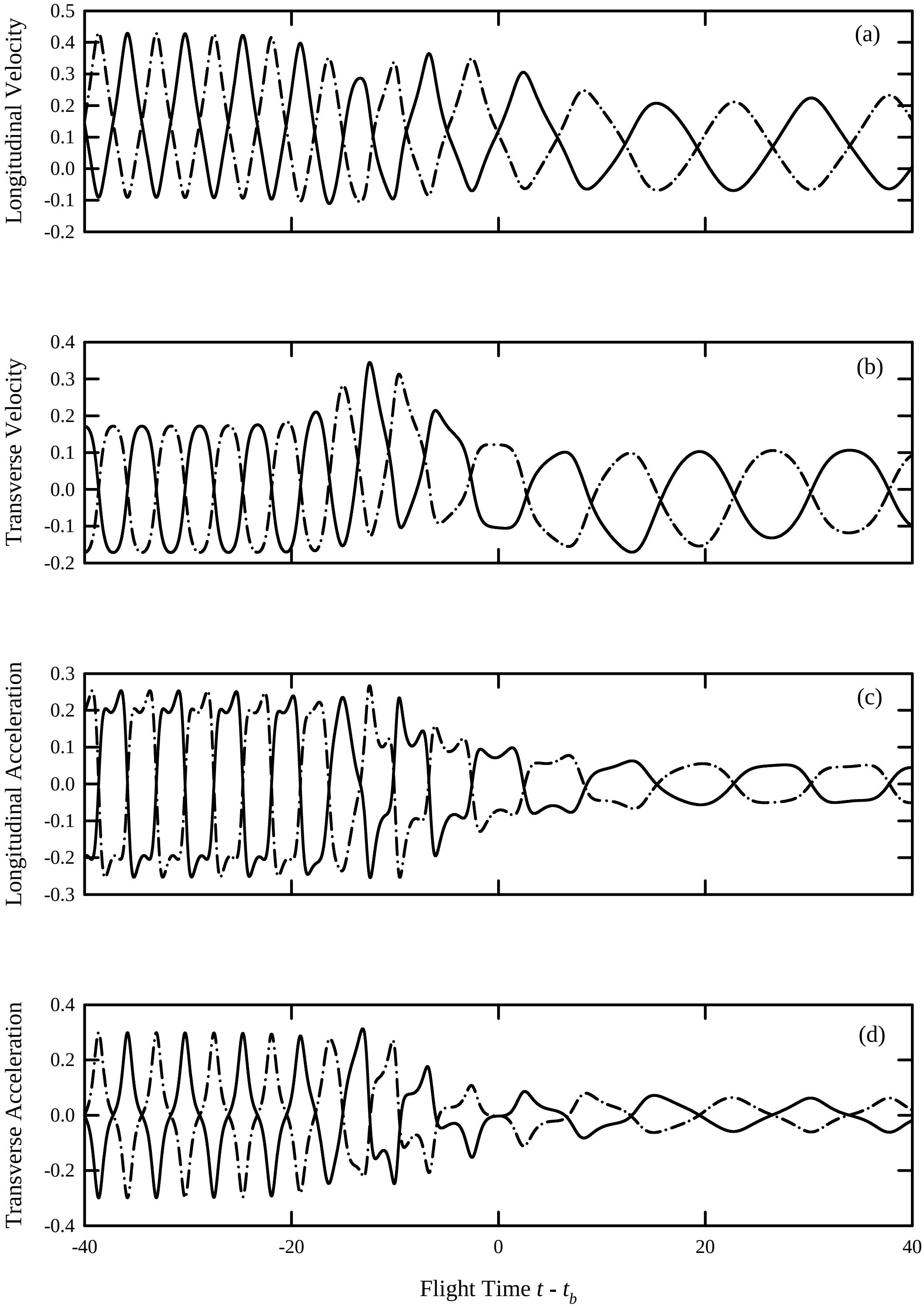

Figure 3.19 Time variation of vortex velocity and acceleration at η = 5 and R_f = 1. (a) Longitudinal velocity; (b) Transverse velocity; (c) Longitudinal acceleration; (d) Transverse acceleration. ——— z_1; — · — z_2. z_{ci} initially located at (–10, 0.5), $\Gamma_1 = \Gamma_2 = 0.5$, $\varepsilon = 0.4$.

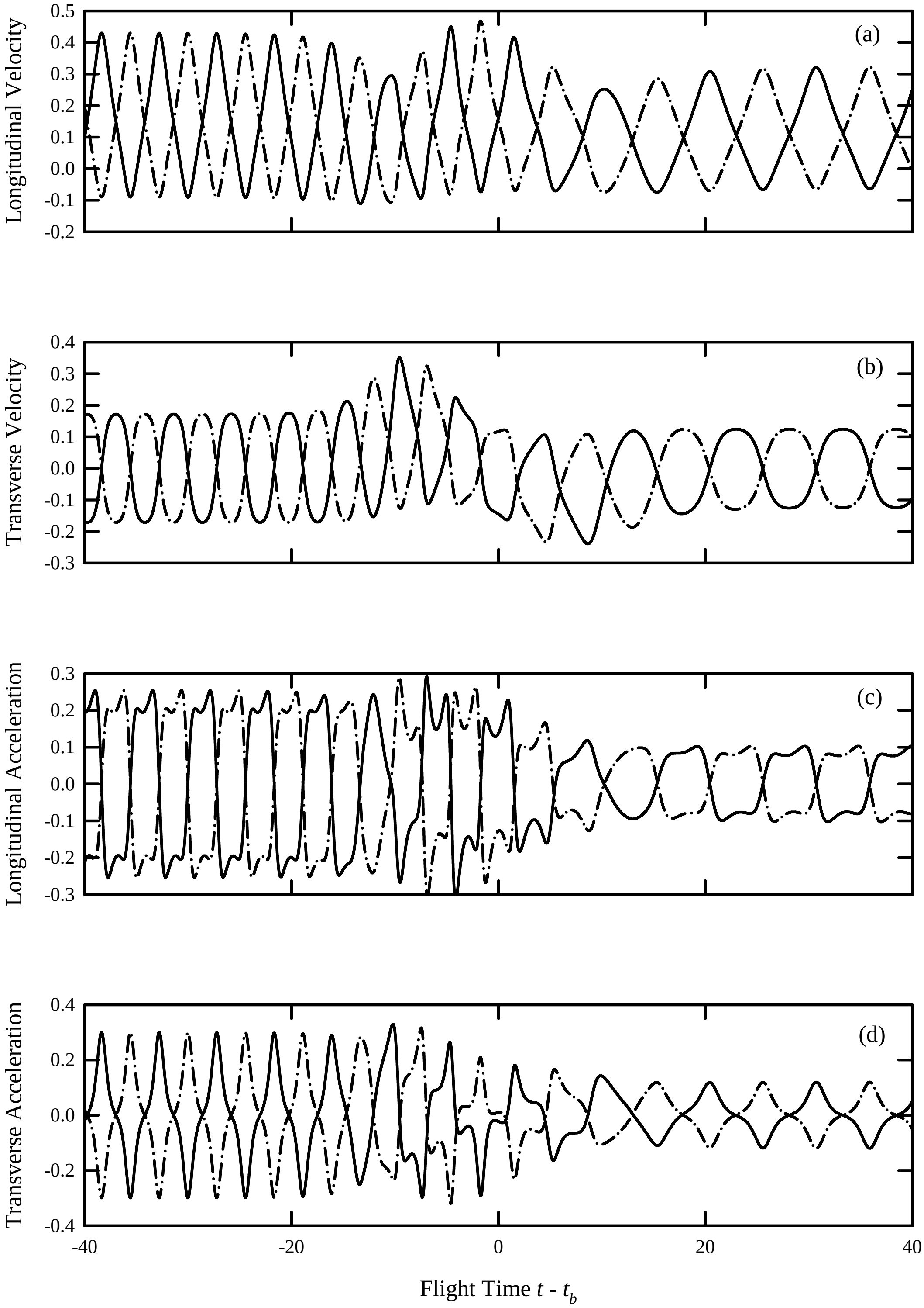

Figure 3.20 Time variation of vortex velocity and acceleration at η = 5 and R_f = 10. (a) Longitudinal velocity; (b) Transverse velocity; (c) Longitudinal acceleration; (d) Transverse acceleration. ——— z_1; — · — z_2. z_{ci} initially located at (–10, 0.5), $\Gamma_1 = \Gamma_2 = 0.5$, $\varepsilon = 0.4$.

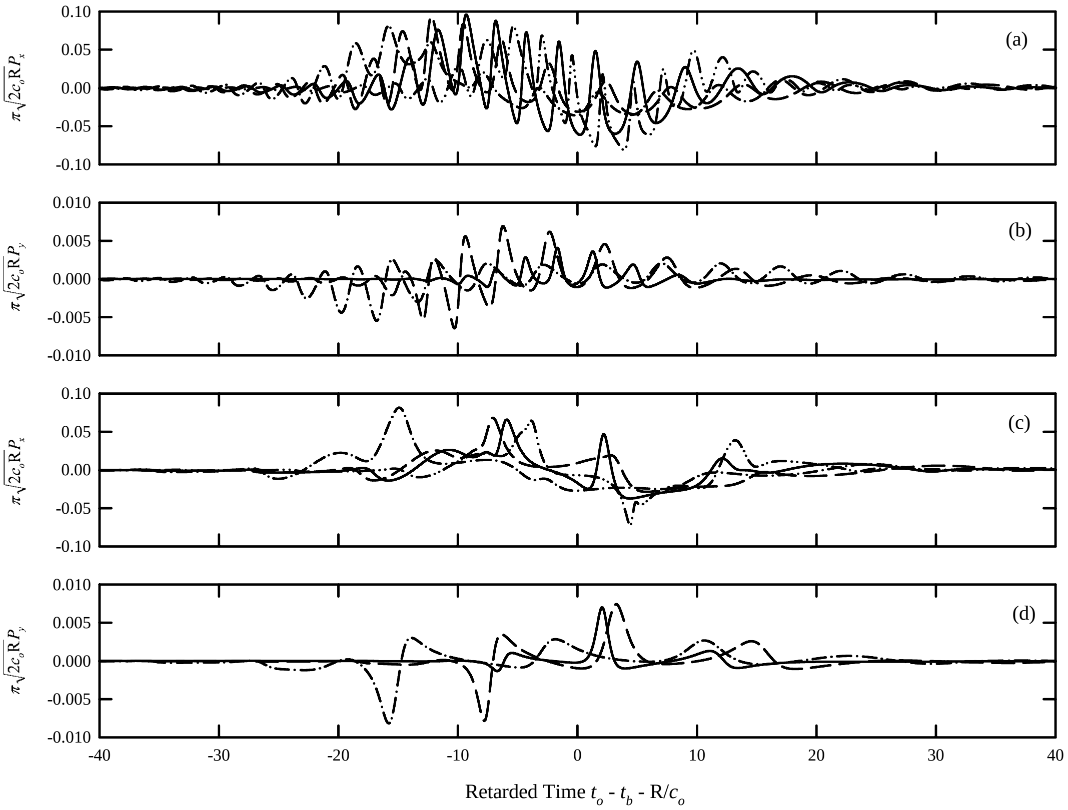

Figure 3.21 Examples of time variation of dipole magnitudes at finite effective fluid density and flow resistance. (a) P_x, ε = 0.4; (b) P_y, ε = 0.4; (c) P_x, ε = 0.8; (d) P_y, ε = 0.8. —— · —— R_f = 0.1; — — — R_f = 1; ——— R_f = 10; —— ·· —— rigid half cylinder. Initial z_{ci} = (–10, 0.5), Γ_1 = Γ_2 = 0.5.

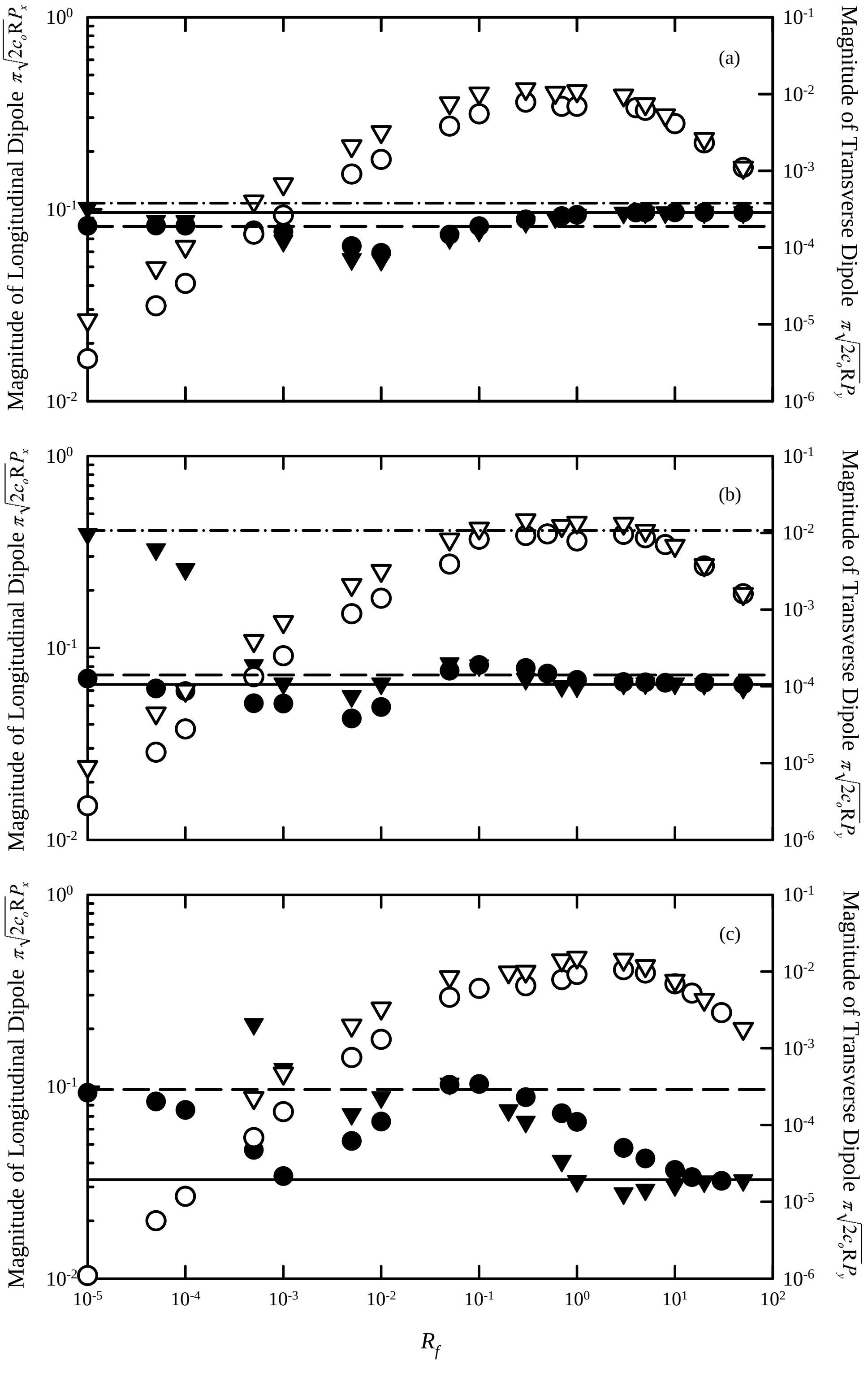

Figure 3.22 Amplitudes of the dipoles produced by two interacting identical vortices. (a) $\varepsilon = 0.4$; (b) $\varepsilon = 0.8$; (c) $\varepsilon = 1.6$. — · — P_x for $\eta = 3$, $R_f = 0$; — — — P_x for $\eta = 5$, $R_f = 0$; ——— rigid half cylinder. ▽ $\eta = 3$; ○ $\eta = 5$. Closed Symbols for P_x, open symbols for P_y. Initial $z_{ci} = (-10, 0.5)$, $\Gamma_1 = \Gamma_2 = 0.5$.

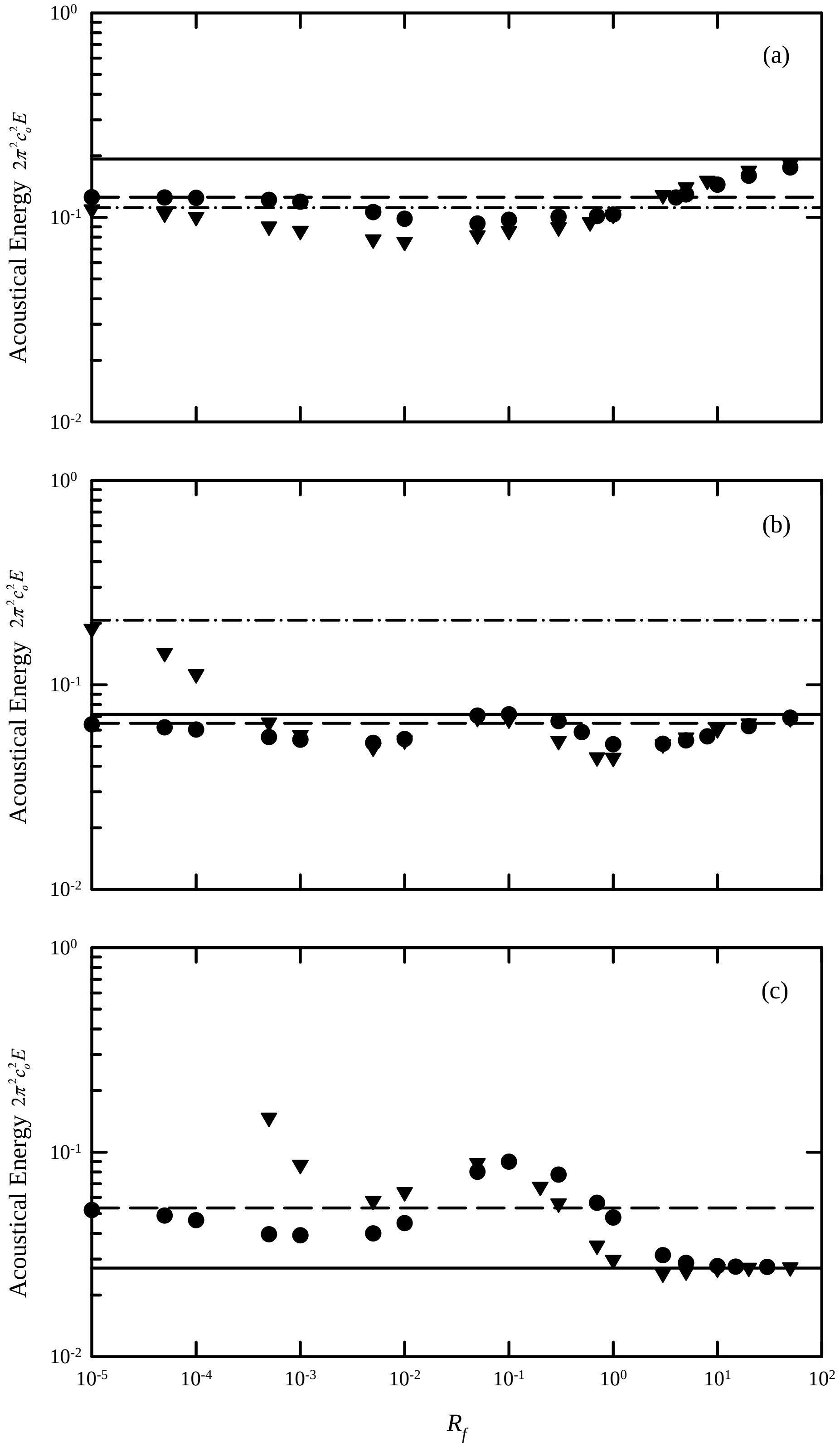

Figure 3.23 Acoustical energy radiated by two interacting identical vortices. (a) ε = 0.4; (b) ε = 0.8; (c) ε = 1.6. —·— P_x for $\eta = 3$, $R_f = 0$; — — — P_x for $\eta = 5$, $R_f = 0$; ——— rigid half cylinder. ▼ $\eta = 3$; ● $\eta = 5$. Initial z_{ci} = (–10, 0.5), $\Gamma_1 = \Gamma_2 = 0.5$.

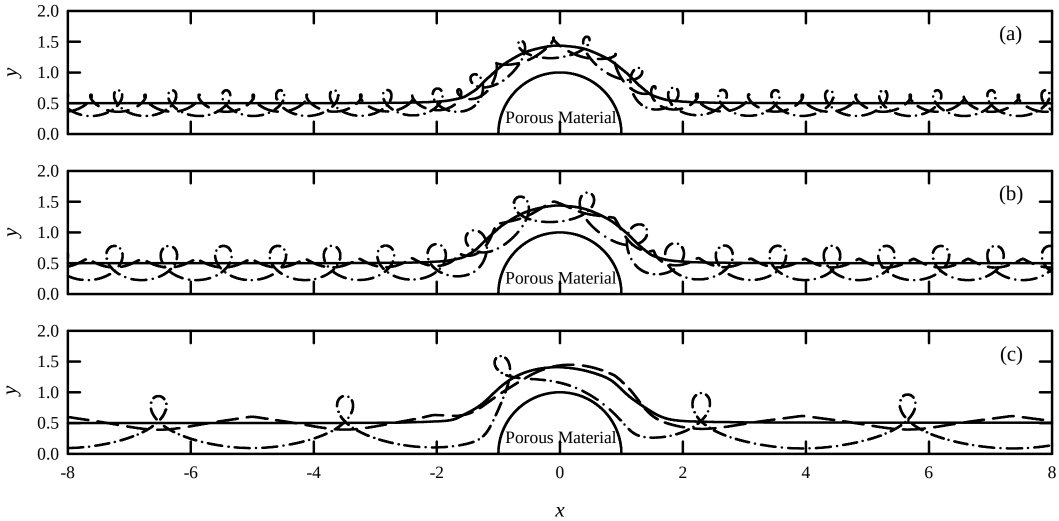

Figure 3.24 Paths of two interacting vortices with different vortex strengths near a rigid half cylinder. (a) $\varepsilon = 0.4$, $\Gamma_1 = 0.6$, $\Gamma_2 = 0.4$; (b) $\varepsilon = 0.4$, $\Gamma_1 = 0.8$, $\Gamma_2 = 0.2$; (c) $\varepsilon = 0.8$, $\Gamma_1 = 0.6$, $\Gamma_2 = 0.4$. ———— z_1; — · — z_2; ——— z_c.

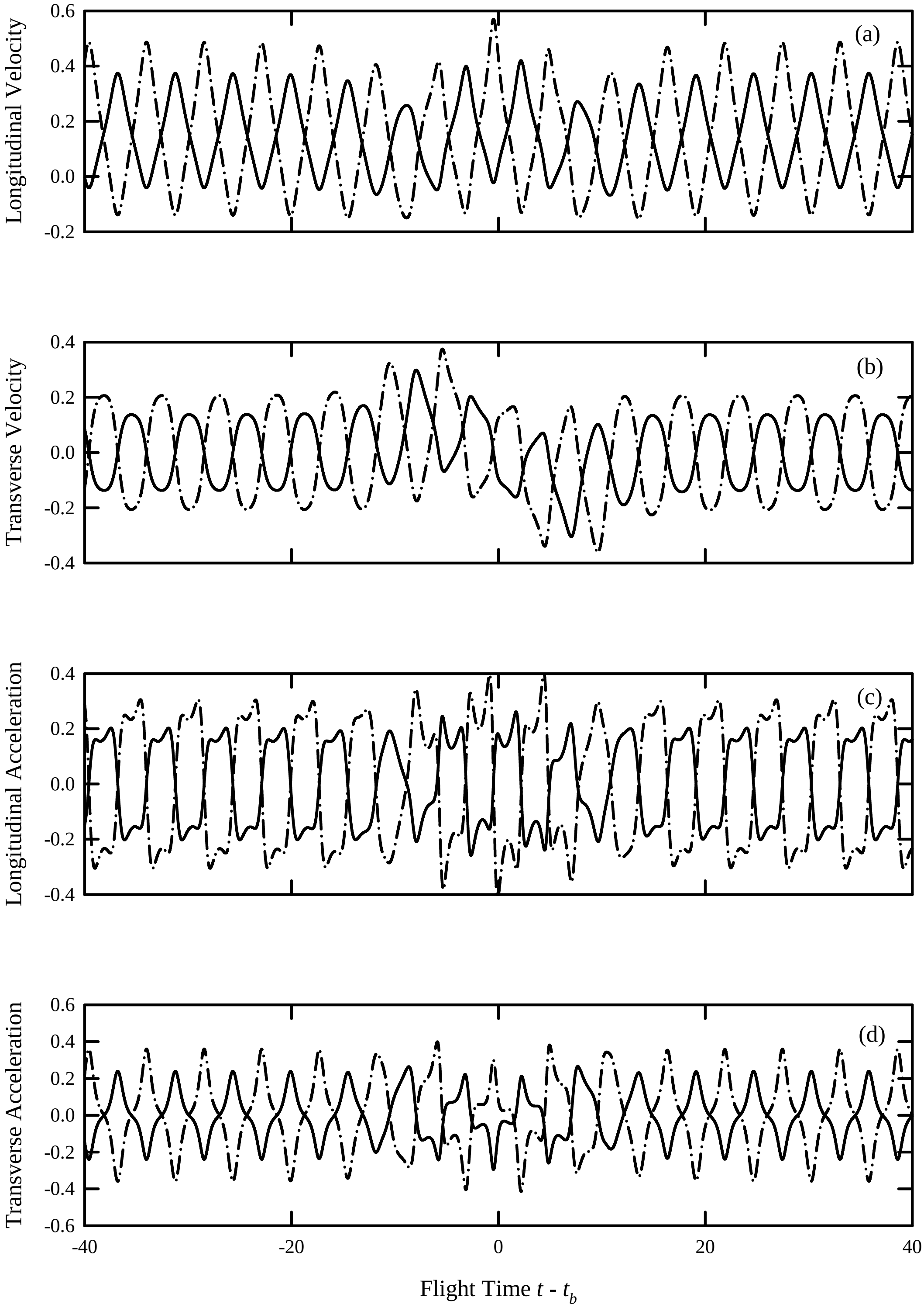

Figure 3.25 Time variation of vortex velocity and acceleration at ε = 0.4 with different vortex strengths in the presence of a rigid half cylinder. (a) Longitudinal velocity; (b) Transverse velocity; (c) Longitudinal acceleration; (d) Transverse acceleration. ———z_1; —·—z_2. $\Gamma_1 = 0.6$, $\Gamma_2 = 0.4$, $\varepsilon = 0.4$.

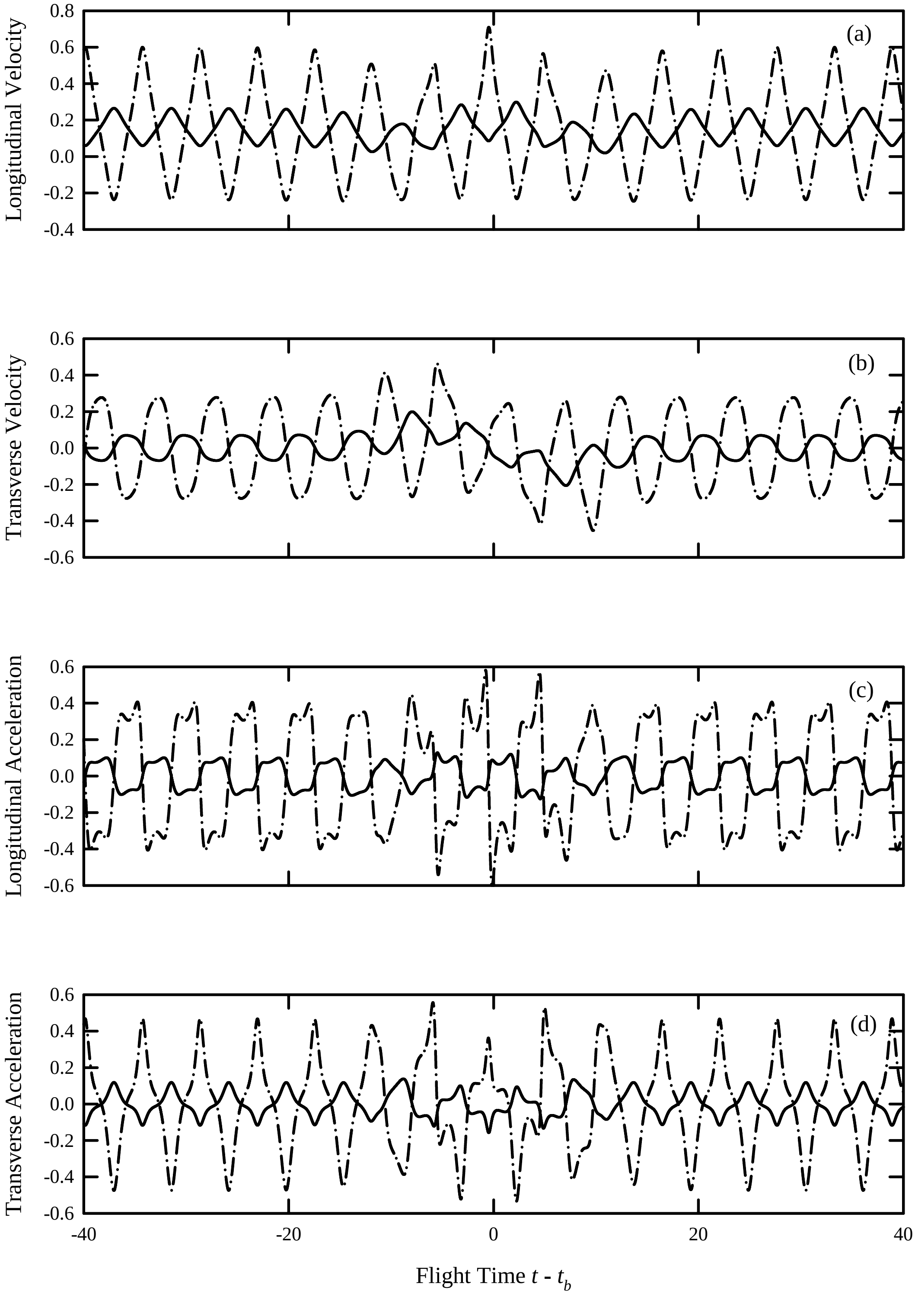

Figure 3.26 Time variation of vortex velocity and acceleration at ε = 0.4 with different vortex strengths in the presence of a rigid half cylinder. (a) Longitudinal velocity; (b) Transverse velocity; (c) Longitudinal acceleration; (d) Transverse acceleration. ———z_1; — · —z_2. Γ_1 = 0.8, Γ_2 = 0.2, ε = 0.4.

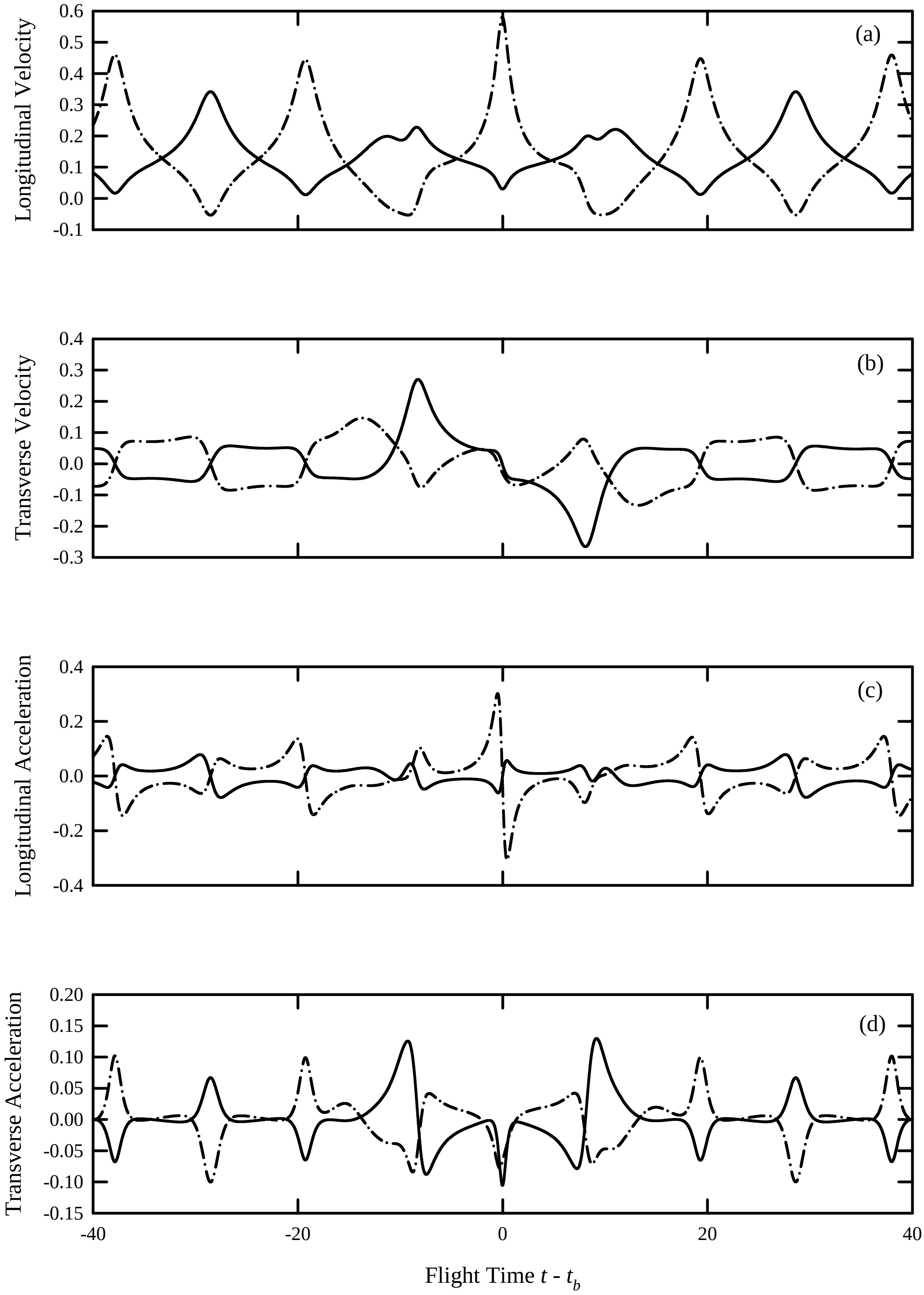

Figure 3.27 Time variation of vortex velocity and acceleration at ε = 0.8 with different vortex strengths in the presence of a rigid half cylinder. (a) Longitudinal velocity; (b) Transverse velocity; (c) Longitudinal acceleration; (d) Transverse acceleration. ——— z_1; — · — z_2. $\Gamma_1 = 0.6$, $\Gamma_2 = 0.4$, $\varepsilon = 0.8$.

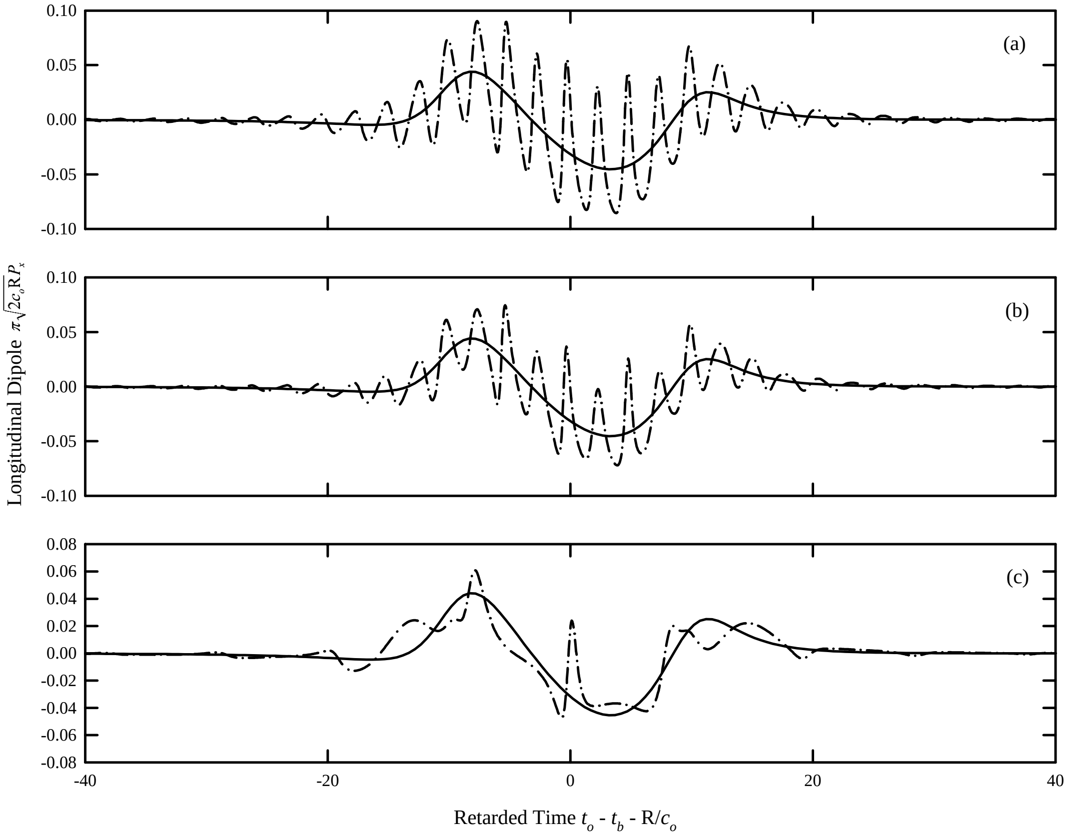

Figure 3.28 Time variation of longitudinal dipole magnitude at different separation distance and vortex strengths in the presence of a rigid half cylinder. (a) $\varepsilon = 0.4$, $\Gamma_1 = 0.6$, $\Gamma_2 = 0.4$; (b) $\varepsilon = 0.4$, $\Gamma_1 = 0.8$, $\Gamma_2 = 0.2$; (c) $\varepsilon = 0.8$, $\Gamma_1 = 0.6$, $\Gamma_2 = 0.4$. ——— Equivalent single vortex results; — · — two interacting vortices results.

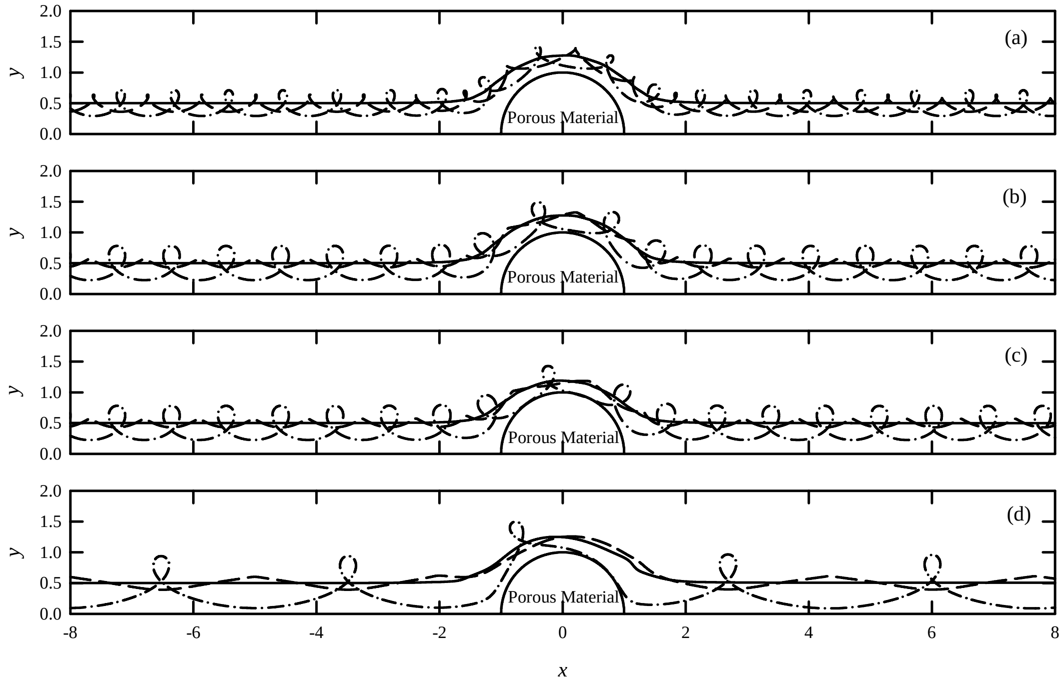

Fgiure 3.29 Paths of two interacting vortices with different vortex strengths for perfectly inviscid fluid. (a) ε = 0.4, Γ_1 = 0.6, Γ_2 = 0.4, η = 5; (b) ε = 0.4, Γ_1 = 0.8, Γ_2 = 0.2, η = 5; (c) ε = 0.4, Γ_1 = 0.8, Γ_2 = 0.2, η = 3; (d) ε = 0.8, Γ_1 = 0.8, Γ_2 = 0.2, η = 5. ——— z_1; —·— z_2; ——— z_c.

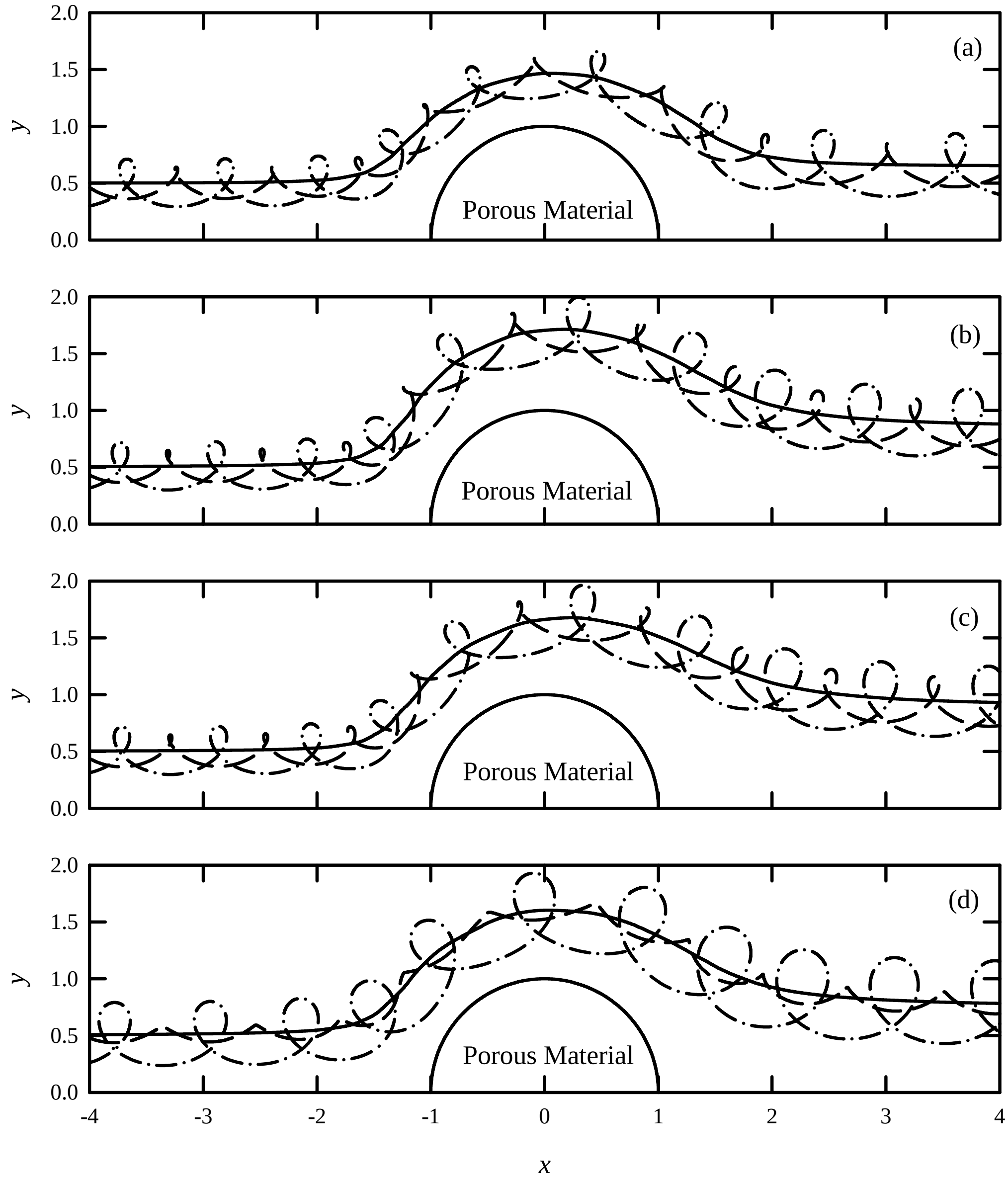

Figure 3.30 Combined effects of effective fluid density and flow resistance on the vortex paths. (a) ε = 0.4, Γ_1 = 0.6, Γ_2 = 0.4, η = 5, R_f = 10; (b) ε = 0.4, Γ_1 = 0.6, Γ_2 = 0.4, η = 5, R_f = 0.1; (c) ε = 0.4, Γ_1 = 0.6, Γ_2 = 0.4, η = 3, R_f = 0.1; (d) ε = 0.4, Γ_1 = 0.8, Γ_2 = 0.2, η = 3, R_f = 0.1.——— z_1; —·— z_2; ——— z_c.

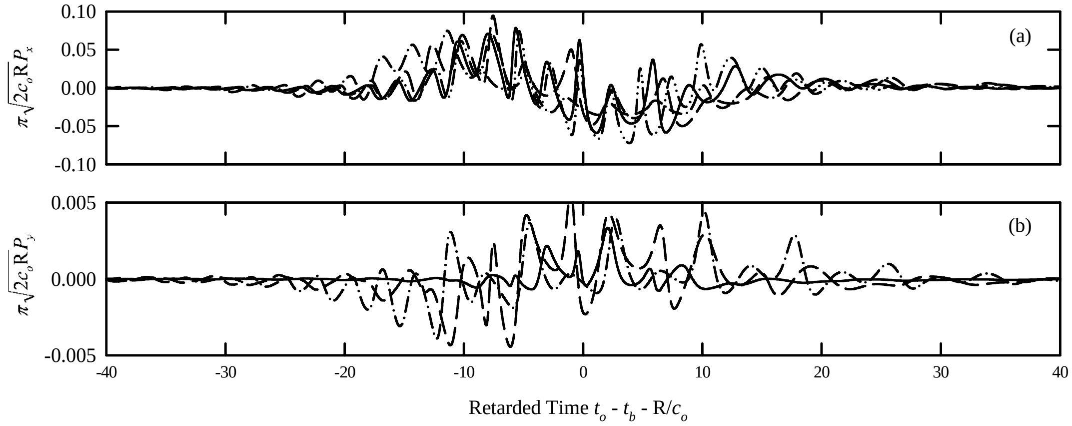

Figure 3.31 Examples of time variation of dipole magnitudes at finite effective fluid density, flow resistance and different vortex strengths. (a) P_x; (b) P_y. —·— R_f = 0.01; ——— R_f = 1; —— R_f = 10; —··— rigid half cylinder. ε = 0.4, Γ_1 = 0.8, Γ_2 = 0.2 η = 5.

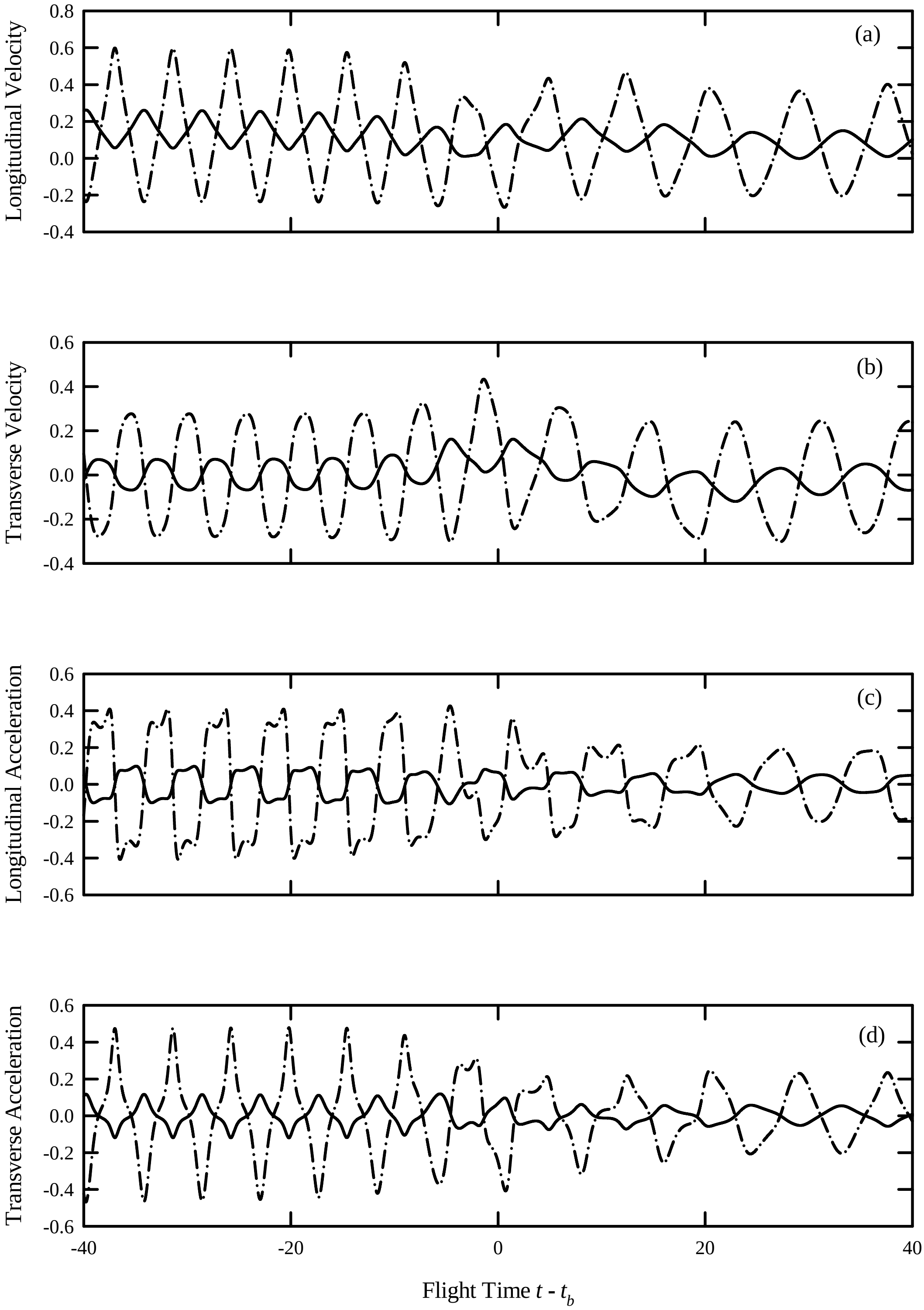

Figure 3.32 Combined effects of η and R_f on the time variation of vortex velocity and acceleration at η = 5 and R_f = 0.1 with different vortex strengths. (a) Longitudinal velocity; (b) Transverse velocity; (c) Longitudinal acceleration; (d) Transverse acceleration. ———z_1; —·—z_2. $\Gamma_1 = 0.8$, $\Gamma_2 = 0.2$, $\varepsilon = 0.4$.

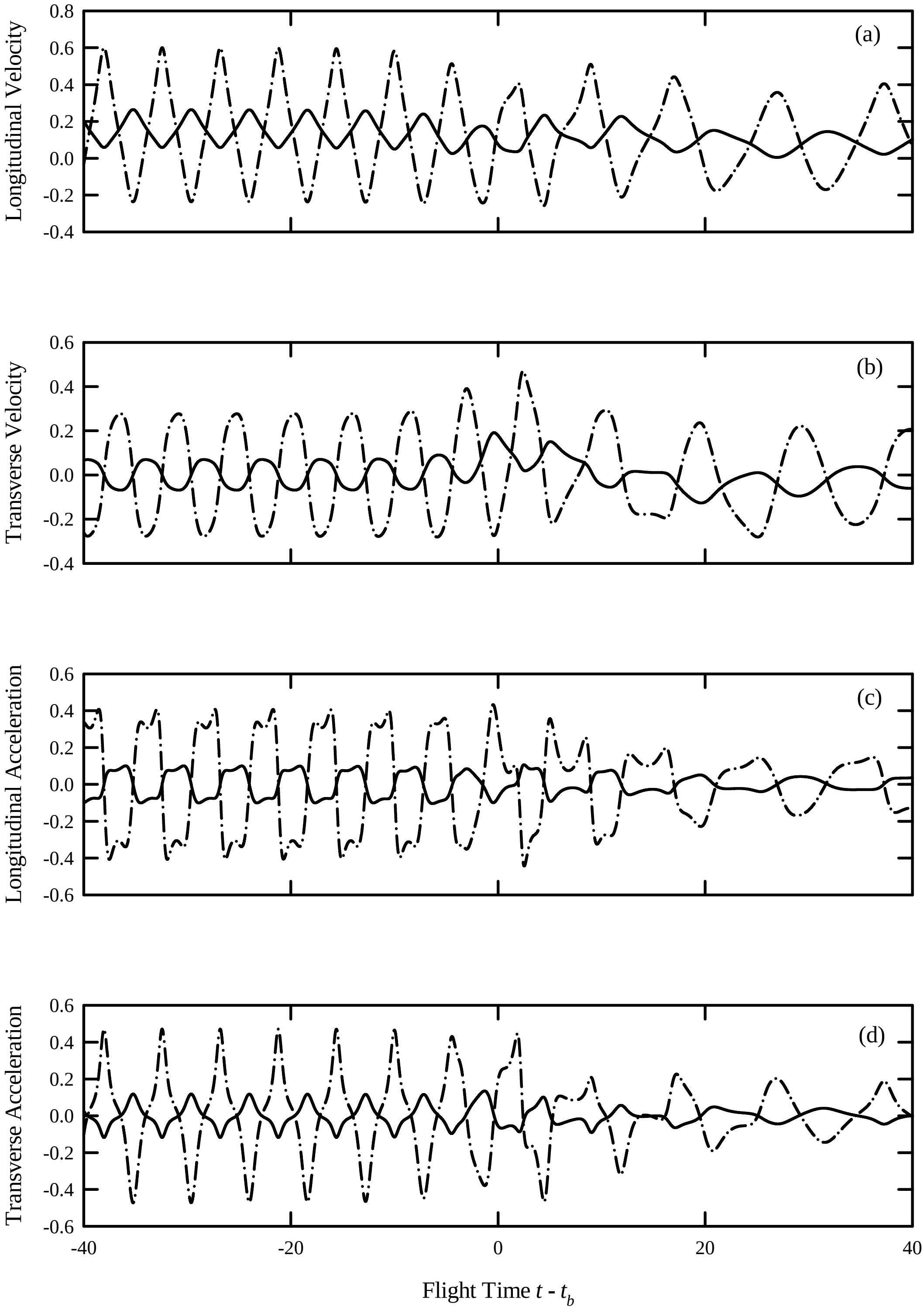

Figure 3.33 Combined effects of η and R_f on the time variation of vortex velocity and acceleration at η = 5 and R_f = 1 with different vortex strengths. (a) Longitudinal velocity; (b) Transverse velocity; (c) Longitudinal acceleration; (d) Transverse acceleration. ———z_1; — · —z_2. Γ_1 = 0.8, Γ_2 = 0.2, ε = 0.4.

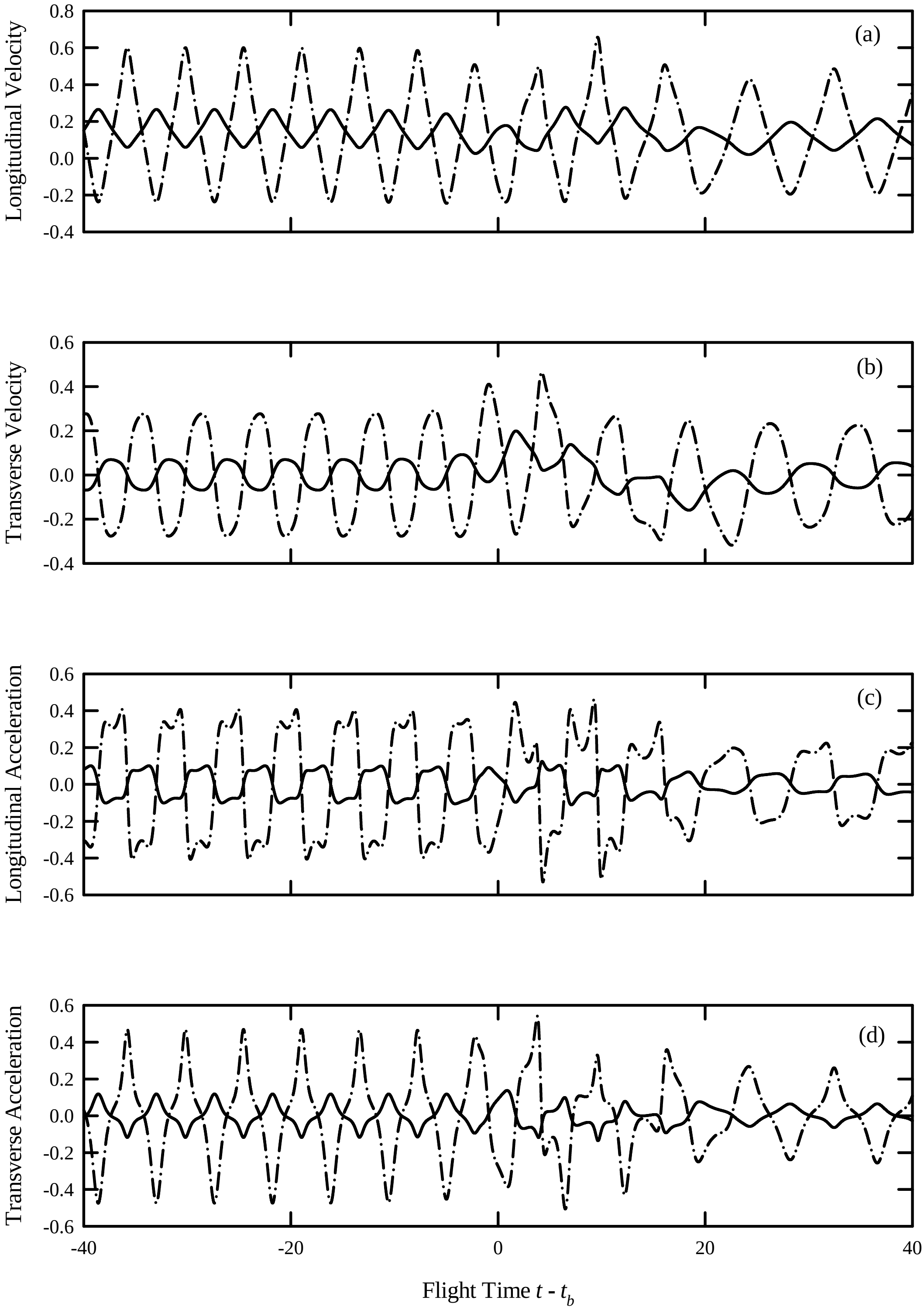

Figure 3.34 Combined effects of η and R_f on the time variation of vortex velocity and acceleration at η = 5 and R_f = 10 with different vortex strengths. (a) Longitudinal velocity; (b) Transverse velocity; (c) Longitudinal acceleration; (d) Transverse acceleration. ——— z_1; — · — z_2. Γ_1 = 0.8, Γ_2 = 0.2, ε = 0.4.

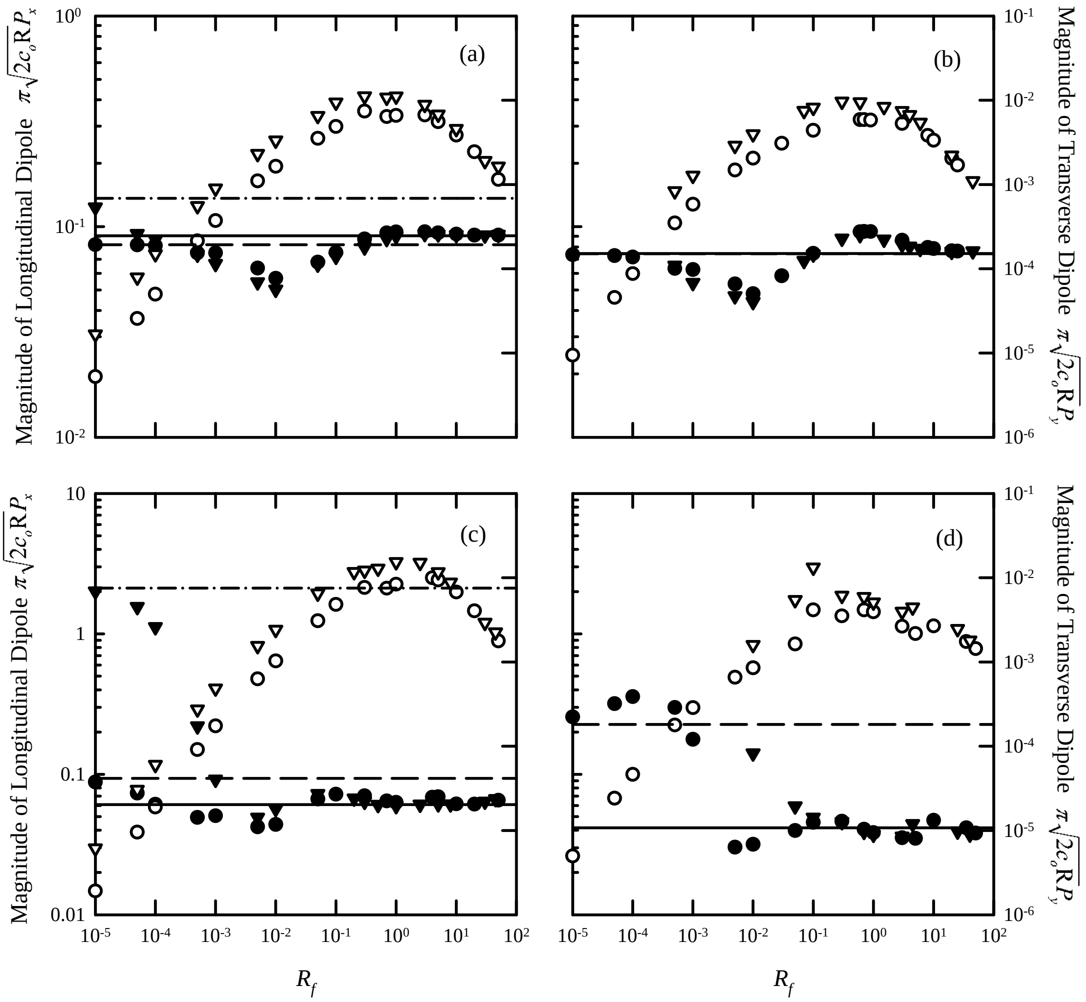

Figure 3.35 Amplitudes of the dipoles produced by two vortices with different strengths. (a) ε = 0.4, Γ_1 = 0.6, Γ_2 = 0.4; (b) ε = 0.4, Γ_1 = 0.8, Γ_2 = 0.2; (c) ε = 0.8, Γ_1 = 0.6, Γ_2 = 0.4; (d) ε = 0.8, Γ_1 = 0.8, Γ_2 = 0.2. — · — P_x for η = 3, R_f = 0; — — — P_x for η = 5, R_f = 0; ——— rigid half cylinder. ▽ η = 3; ○ η = 5. Closed Symbols for P_x, open symbols for P_y.

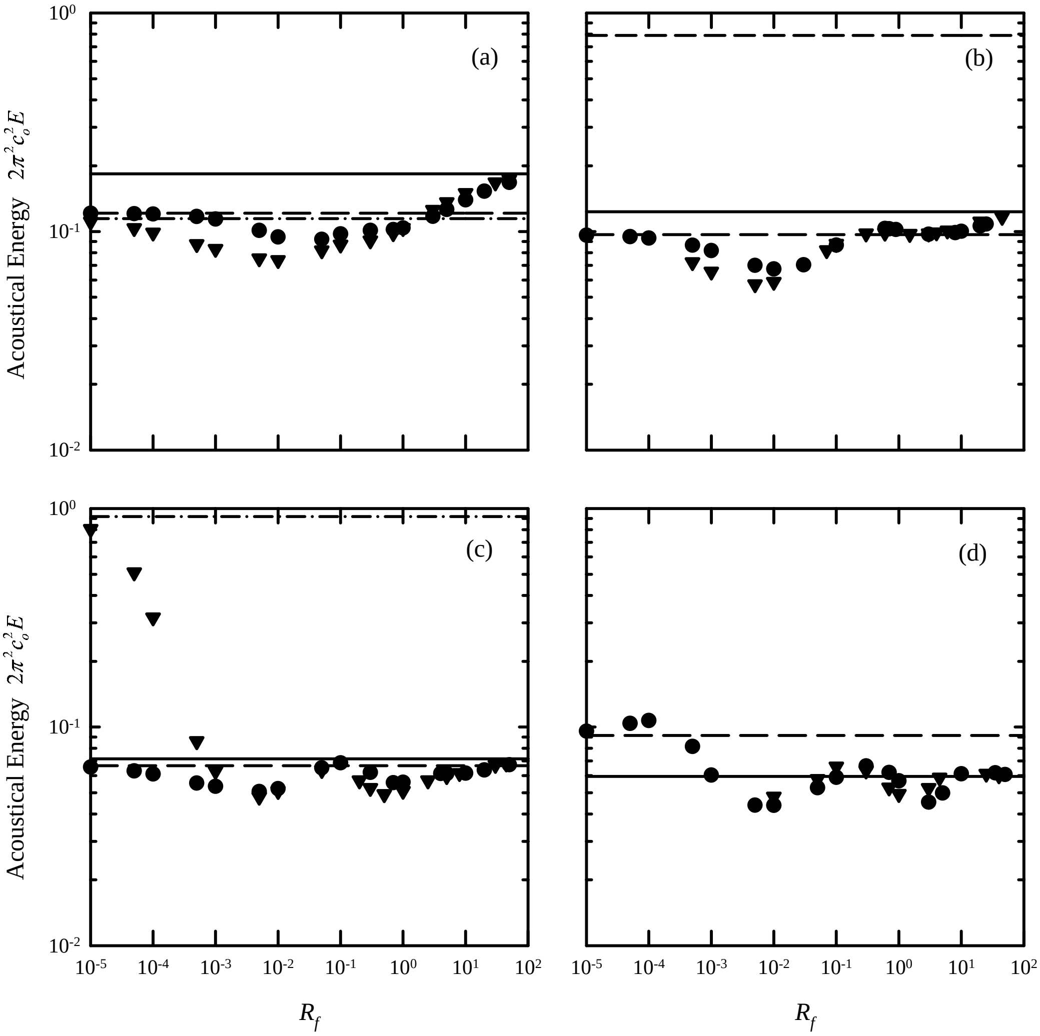

Figure 3.36 Acoustical energy radiated by two vortices with different strengths. (a) ε = 0.4, Γ_1 = 0.6, Γ_2 = 0.4; (b) ε = 0.4, Γ_1 = 0.8, Γ_2 = 0.2; (c) ε = 0.8, Γ_1 = 0.6, Γ_2 = 0.4; (d) ε = 0.8, Γ_1 = 0.8, Γ_2 = 0.2. — · — P_x for η = 3, R_f = 0; — — — P_x for η = 5, R_f = 0; ——— rigid half cylinder. ▼ η = 3; ● η = 5.

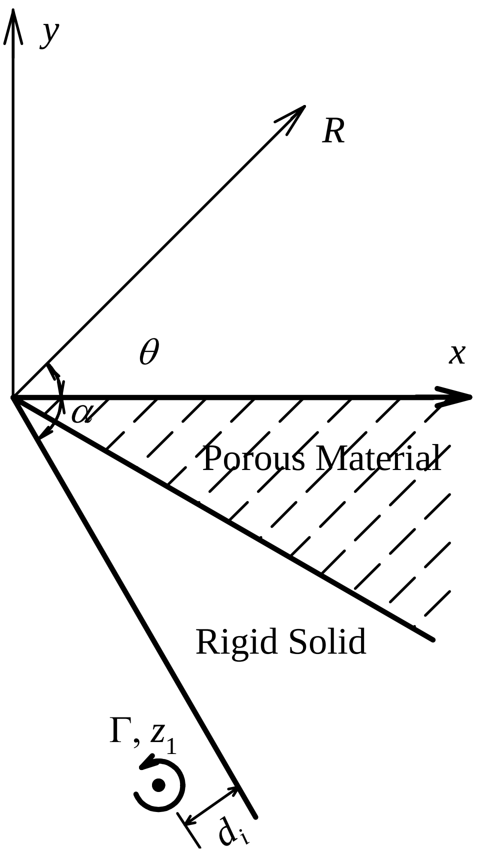

Figure 4.1 Schematic diagram for the present vortex-wedge system (z-plane).

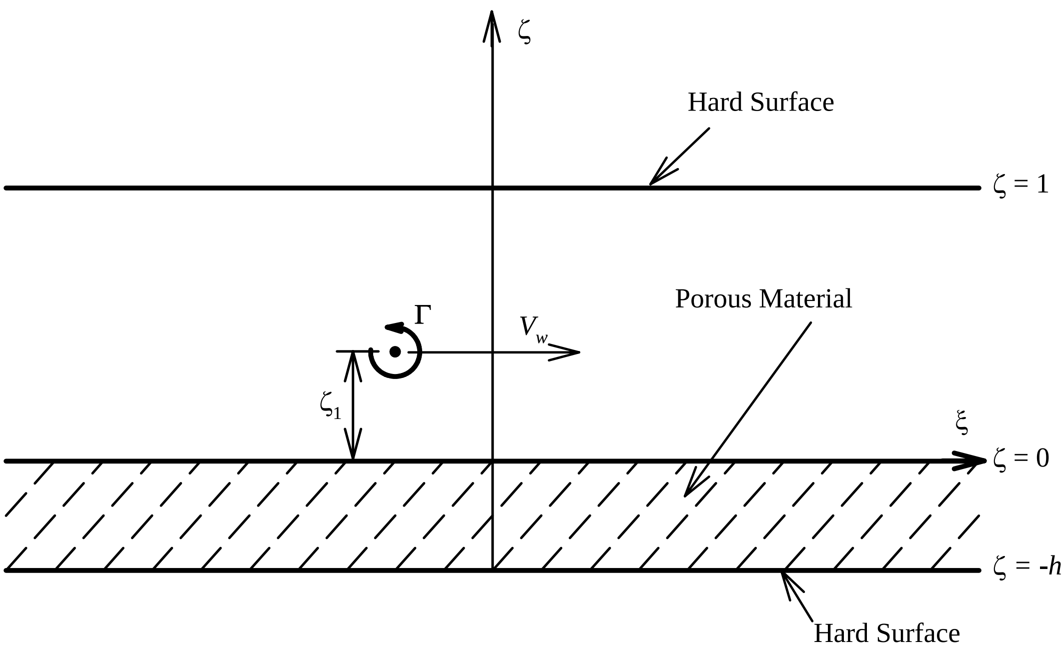

Figure 4.2 The w-plane.

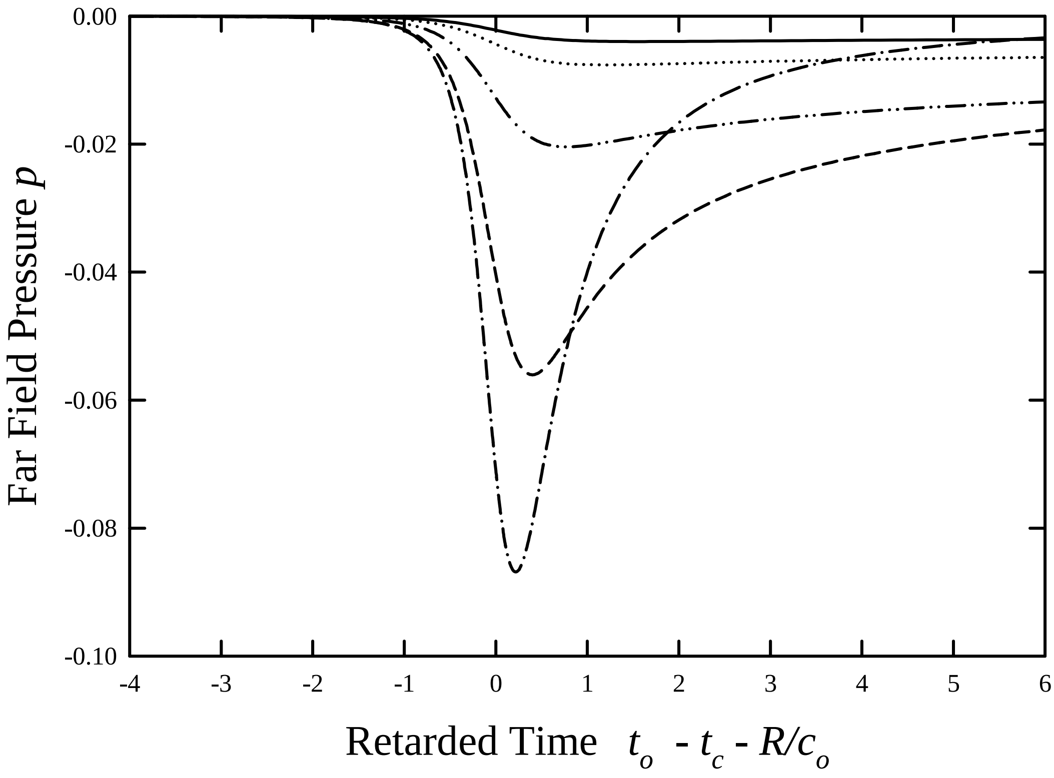

Figure 4.3 Time variation of the sound pulse for rigid wedge. —·— $\alpha = 0$; — — $\alpha = \pi/3$; —··— $\alpha = 2\pi/3$; ········ $\alpha = 5\pi/6$; —— $\alpha = 9\pi/10$.

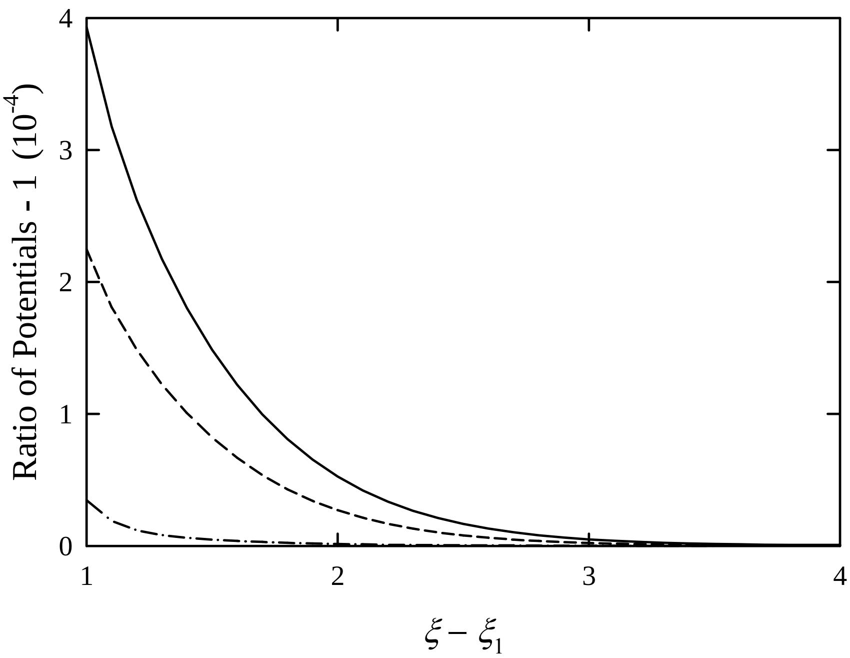

Figure 4.4 Accuracy of the approximation of Equation (4.19). —— $\eta = 2$; — — $\eta = 5$; —·— $\eta = 100$.

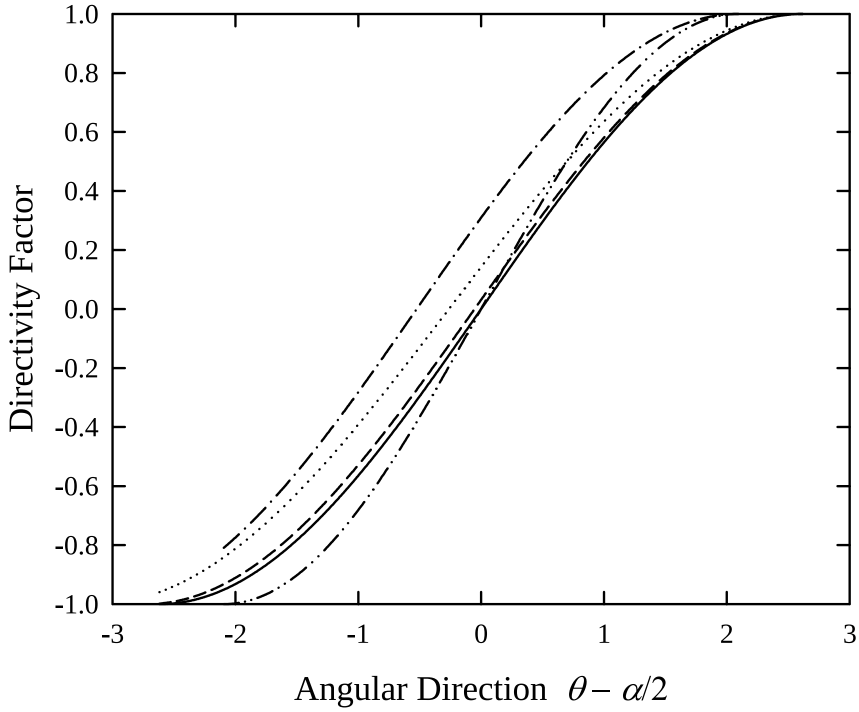

Figure 4.5 Effect of effective fluid density on the radiation directivity for a perfectly inviscid medium. ········ *η = 1, α = π/3;* — — *η = 5, α = π/3;* —— *rigid wedge, α = π/3;* — · — *η = 1, α = 2π/3;* — ·· — *rigid wedge, α = 2π/3.*

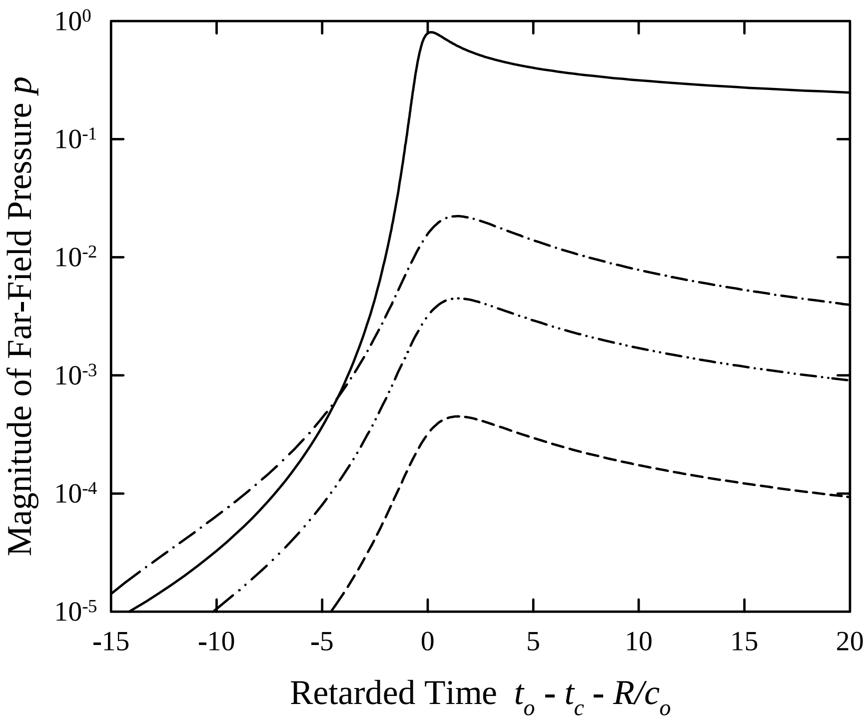

Figure 4.6 Effect of effective fluid density on sound pressure fluctuations for perfectly inviscid medium. —— *η = 1;* — · — *η = 20;* — ·· — *η = 100;* — — *η = 1000. α = π.*

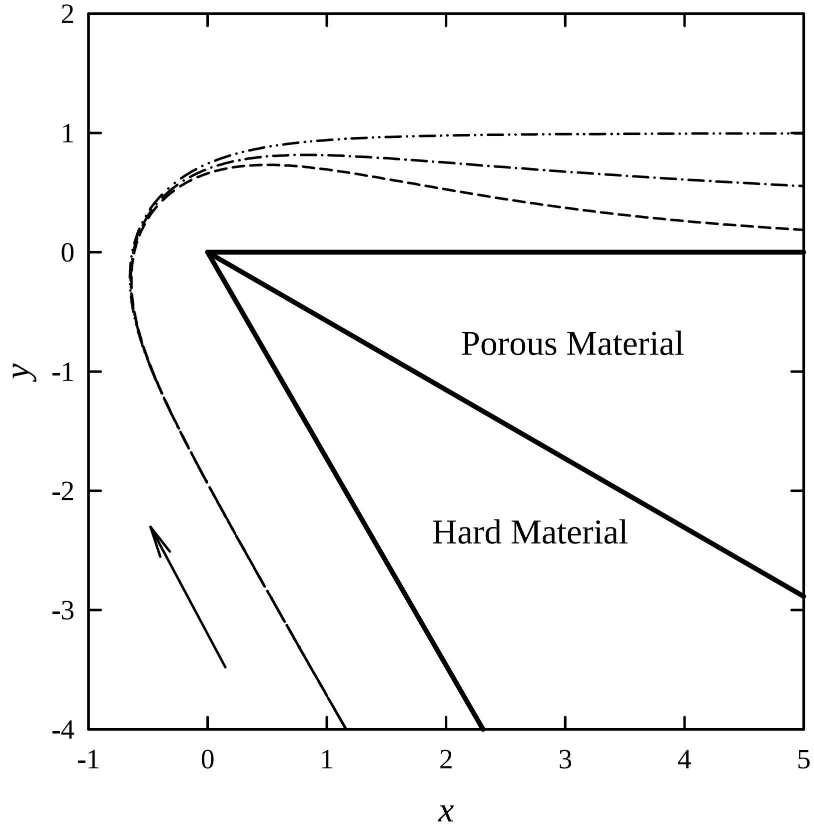

Figure 4.7 Vortex flight path in a perfectly inviscid medium. —— —— η = 2; —— · —— η = 4; —— ·· —— rigid wedge. $\alpha = \pi/3$.

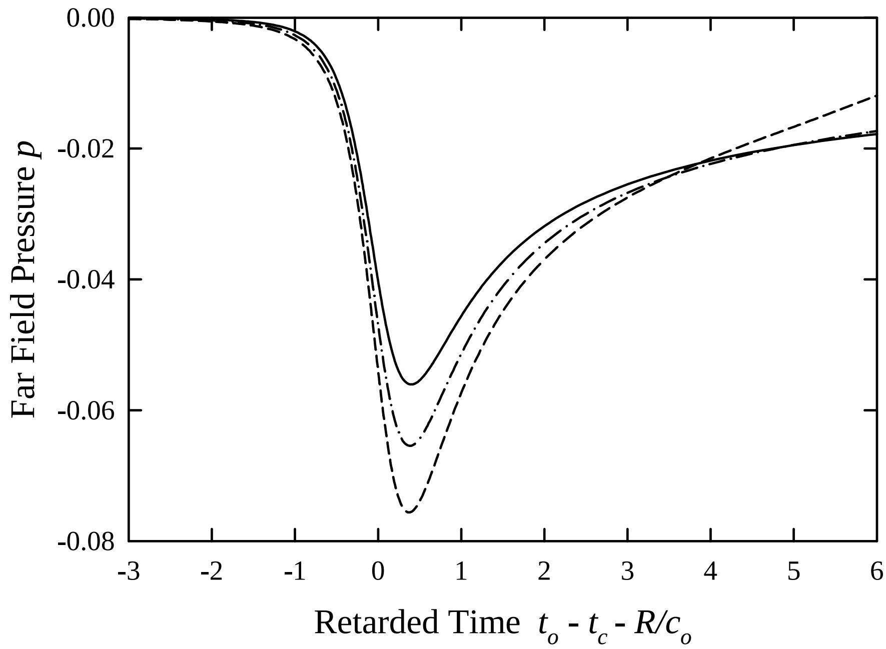

Figure 4.8 Sound pressure time variation for finite η at r = 100, $\alpha = \pi/3$. —— —— η = 2; —— · —— η = 4; ———— rigid wedge.

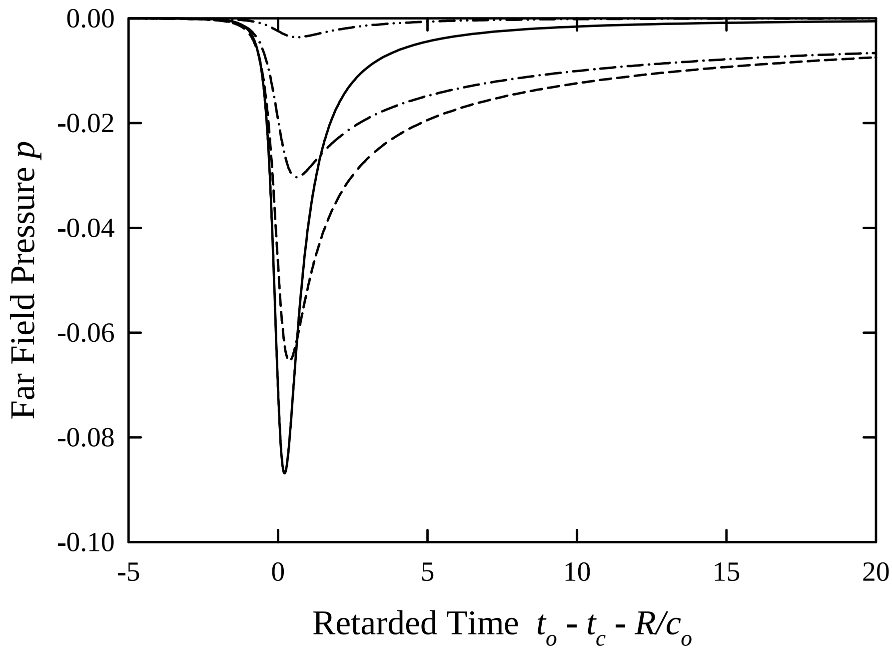

Figure 4.9 Effect of wedge angle on the sound pulse magnitude. —— $\alpha = 0$; — — $\alpha = \pi/3$; — · — $\alpha = 2\pi/3$; — · — $\alpha = \pi$. $\eta = 4$.

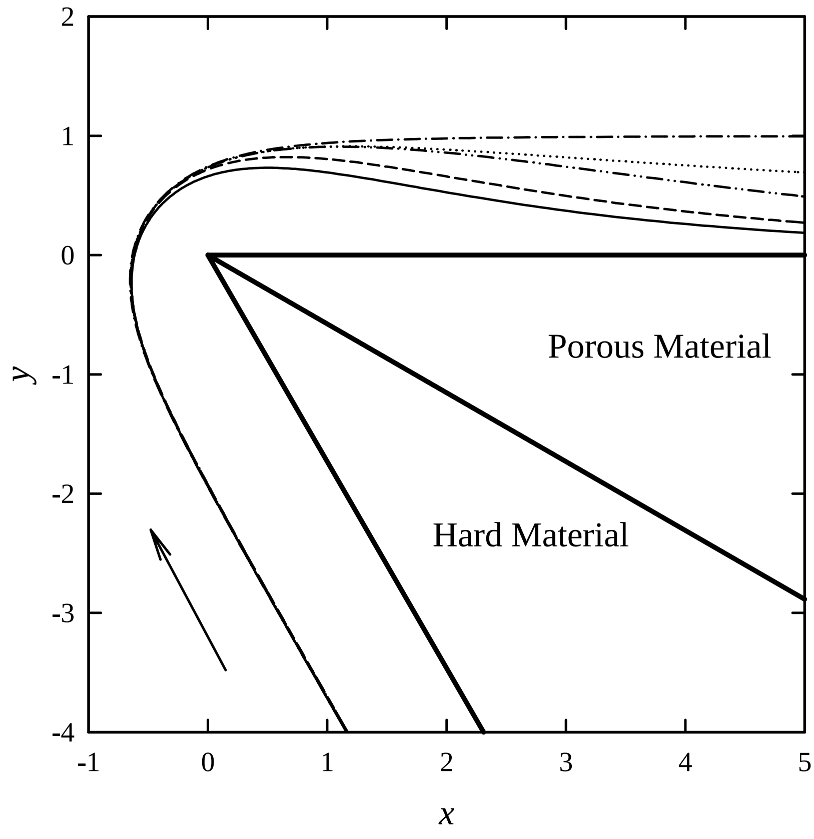

Figure 4.10 Combined effects of effective fluid density and flow resistance on the vortex path. —— $\eta = 2$, $4\pi R_f = 0$; — — $\eta = 2$, $4\pi R_f = 10$; — ·· — $\eta = 2$, $4\pi R_f = 100$; ········ $\eta = 4$, $4\pi R_f = 100$; — · — rigid wedge. $\alpha = \pi/3$.

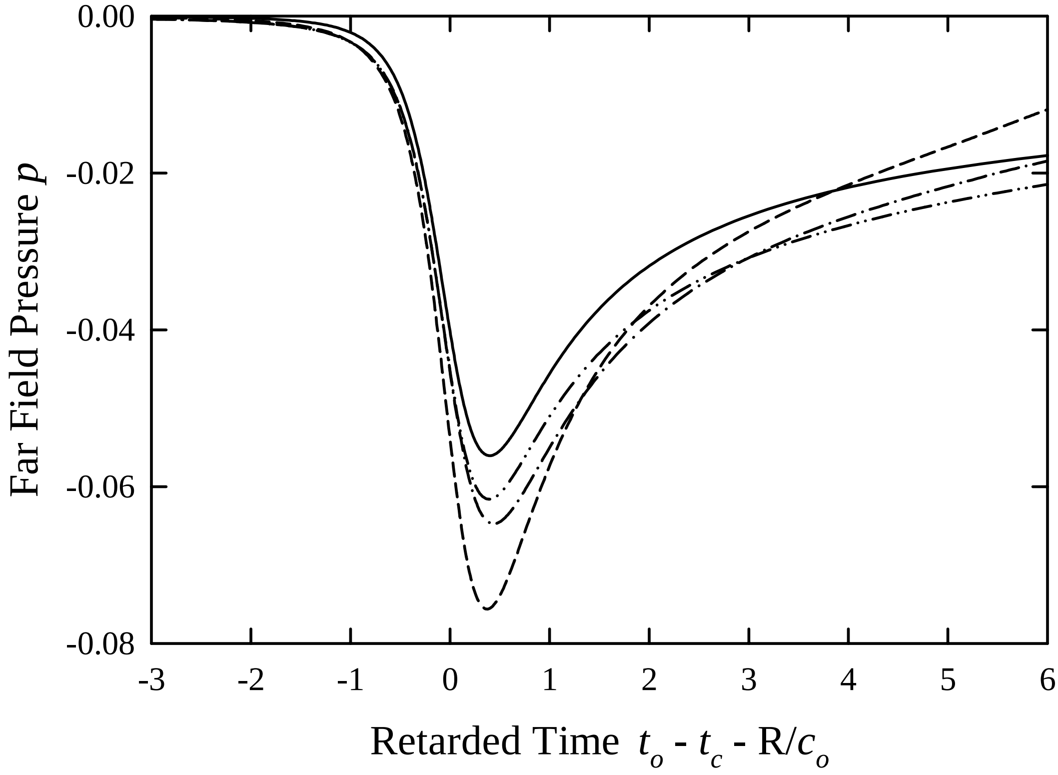

Figure 4.11 Effect of flow resistance on the far-field sound radiation. —— $4\pi R_f = 0$; —·— $4\pi R_f = 10$; —··— $4\pi R_f = 100$; —— rigid wedge. $\eta = 2$, $\alpha = \pi/3$.

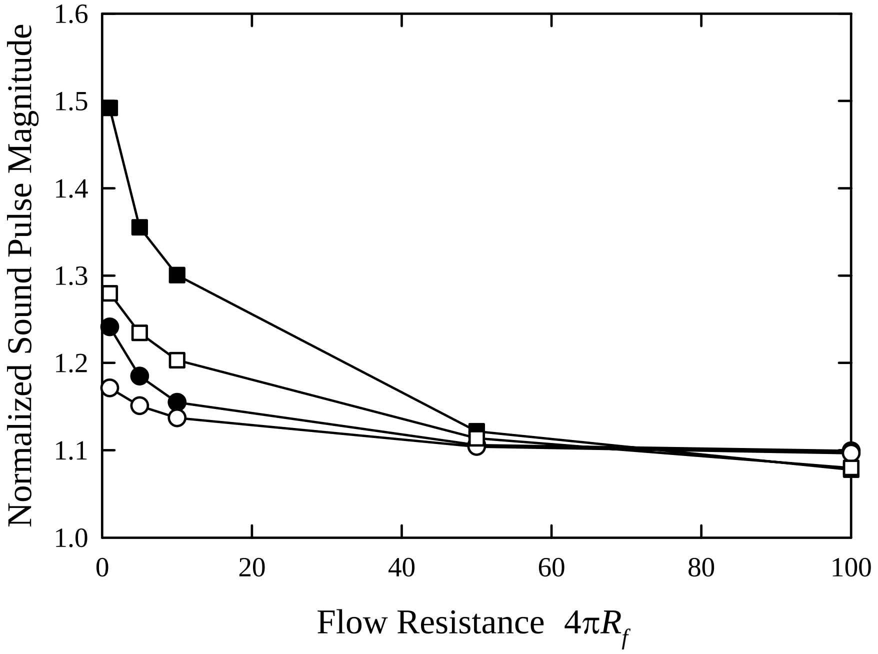

Figure 4.12 Combined effects of effective fluid density, flow resistance and wedge angle on sound radiation. ● $\eta = 2$, $\alpha = \pi/3$; ○ $\eta = 2$, $\alpha = 2\pi/3$; ■ $\eta = 4$, $\alpha = \pi/3$; □ $\eta = 4$, $\alpha = 2\pi/3$.

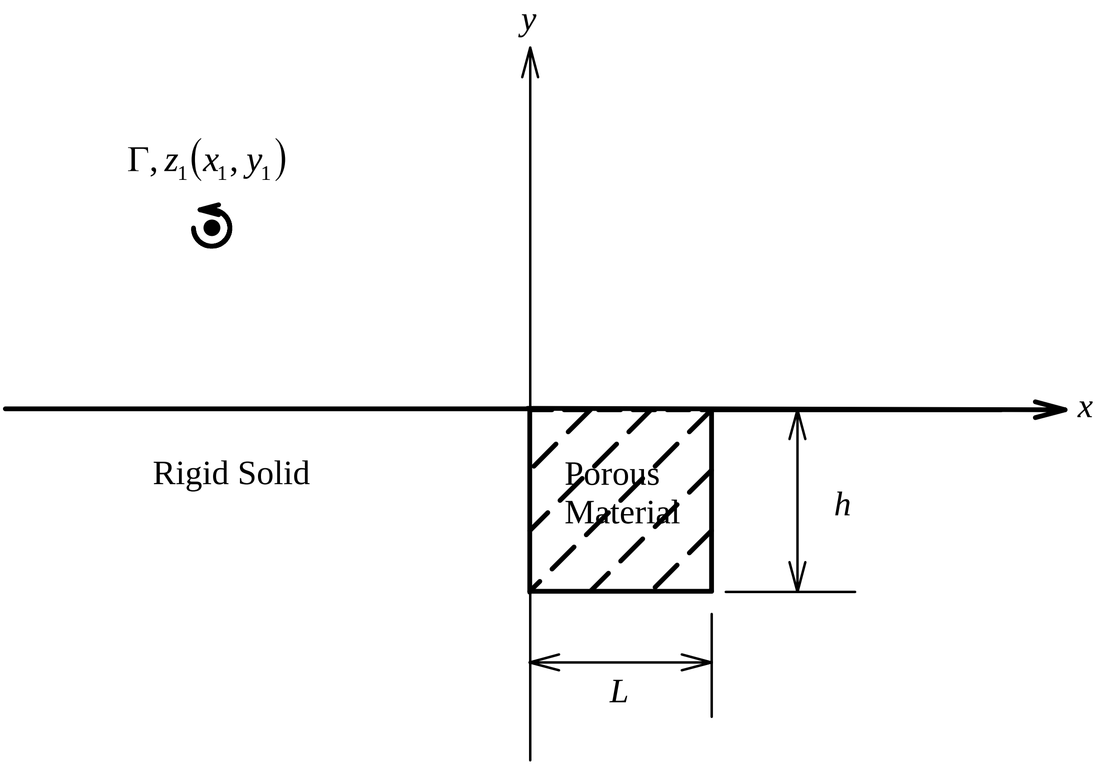

Figure 5.1 Schematic diagram of vortex model in the present study.

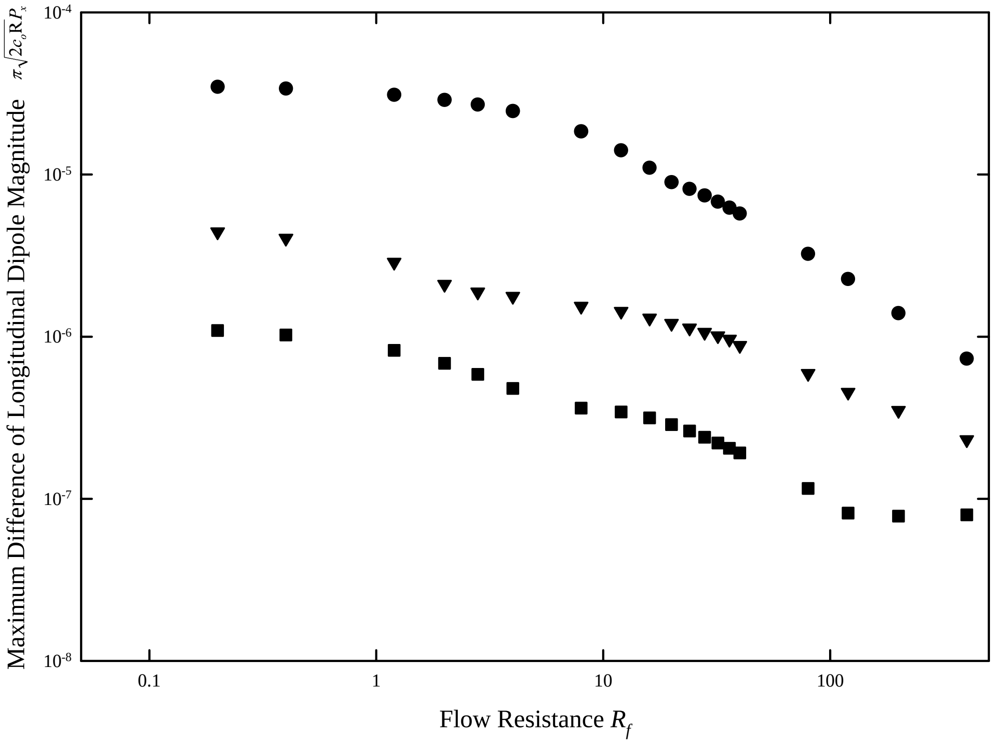

Figure 5.2 Maximum difference of the longitudinal dipole magnitude P_x for 5, 10, 15 and 20 terms truncation. ● $|P_5 - P_{20}|$; ▼ $|P_{10} - P_{20}|$; ■ $|P_{15} - P_{20}|$ *. $L = 2$, $h = 2$ and $\eta = 5$.*

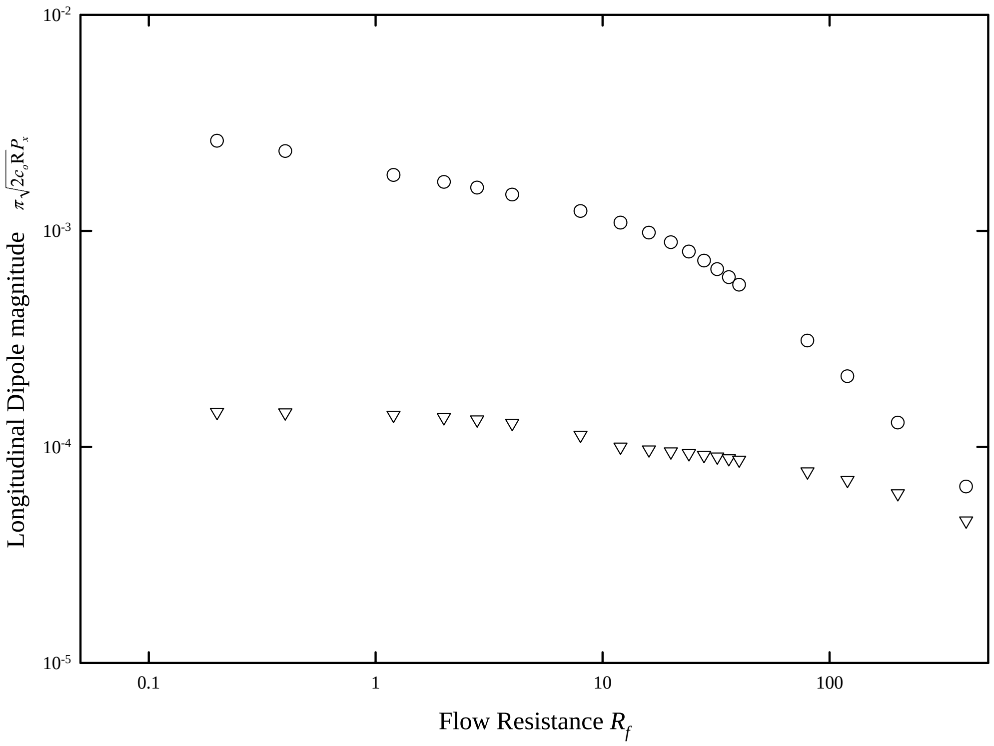

Figure 5.3 Validation of longitudinal dipole magnitude for the present vortex model. ○ *P_{20} for $\eta = 5$;* ▽ *P_{10} for $\eta = 100$. $L = 2$, $h = 2$.*

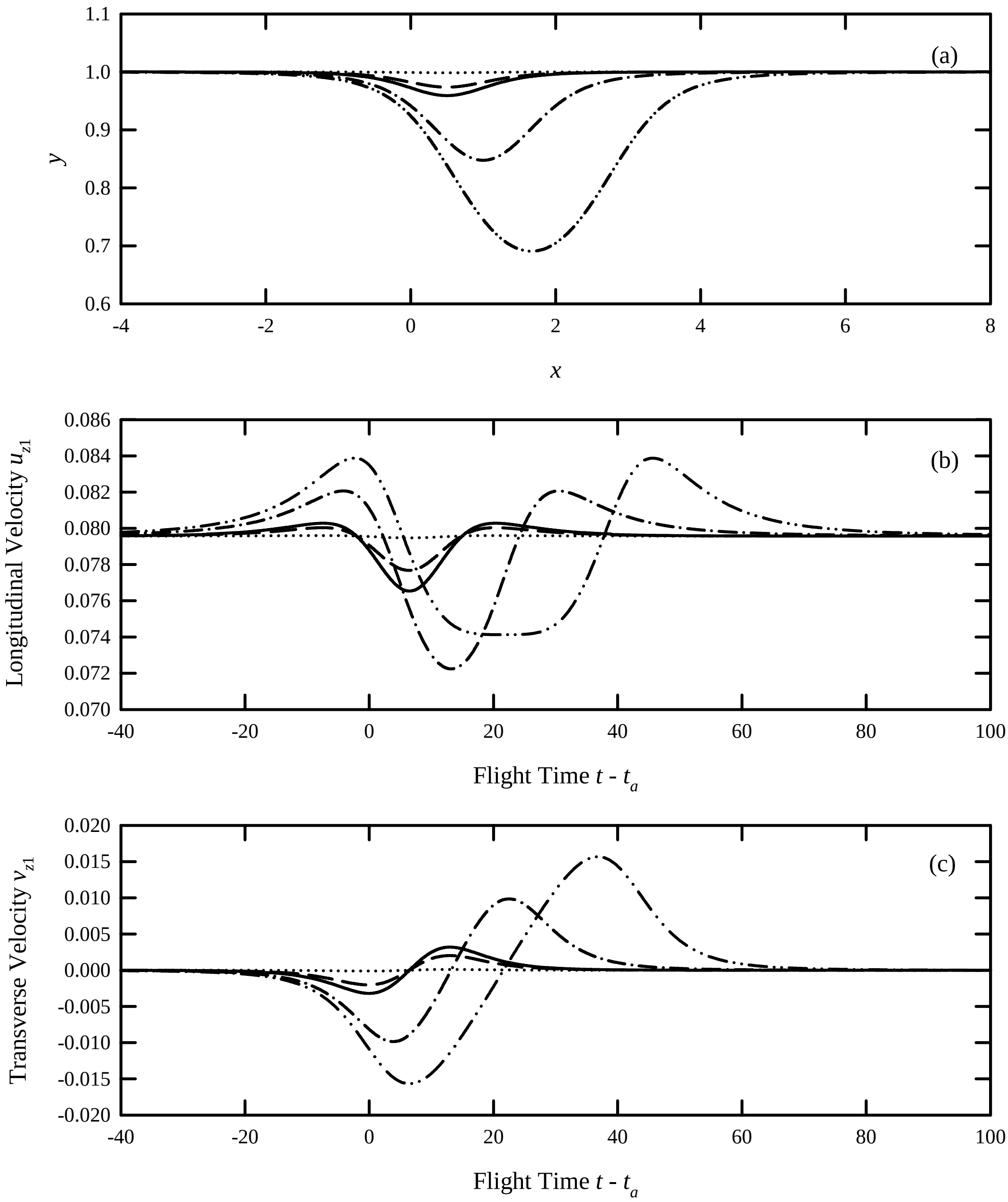

Figure 5.4 Effect of pressure-releasing surface on the vortex motion, velocity, acceleration and the sound generation at a fixed h. (a) Vortex path; (b) Longitudinal velocity; (c) Transverse velocity; (d) Longitudinal acceleration; (e) Transverse acceleration; (f) Sound pressure. ———L = 1, η = 3; — — —L = 1, η = 5; ·············L = 1, η = 100; — · —L = 2, η = 3; — ·· —L = 10/3, η = 3. h = 2.

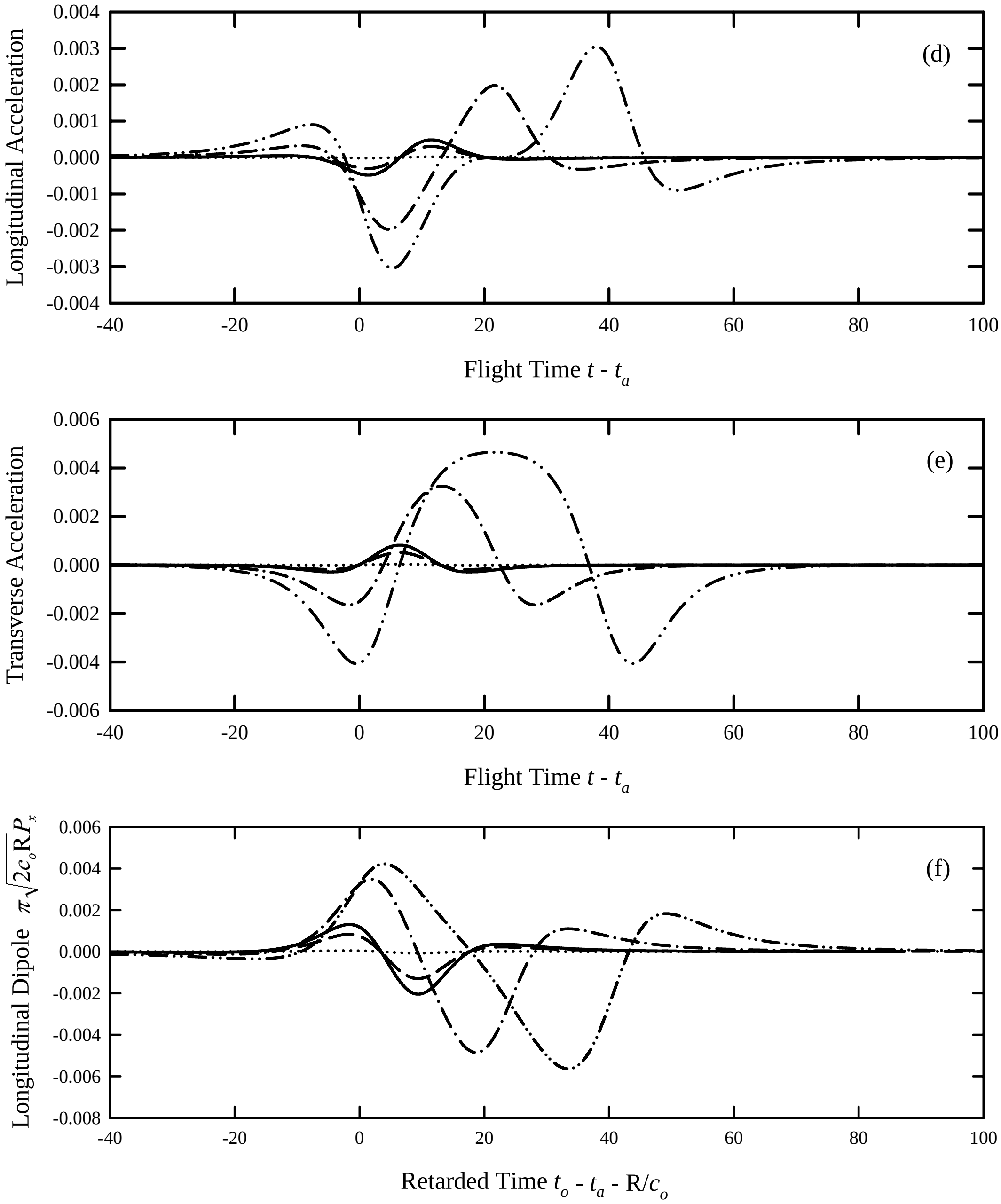

Figure 5.4 Continued

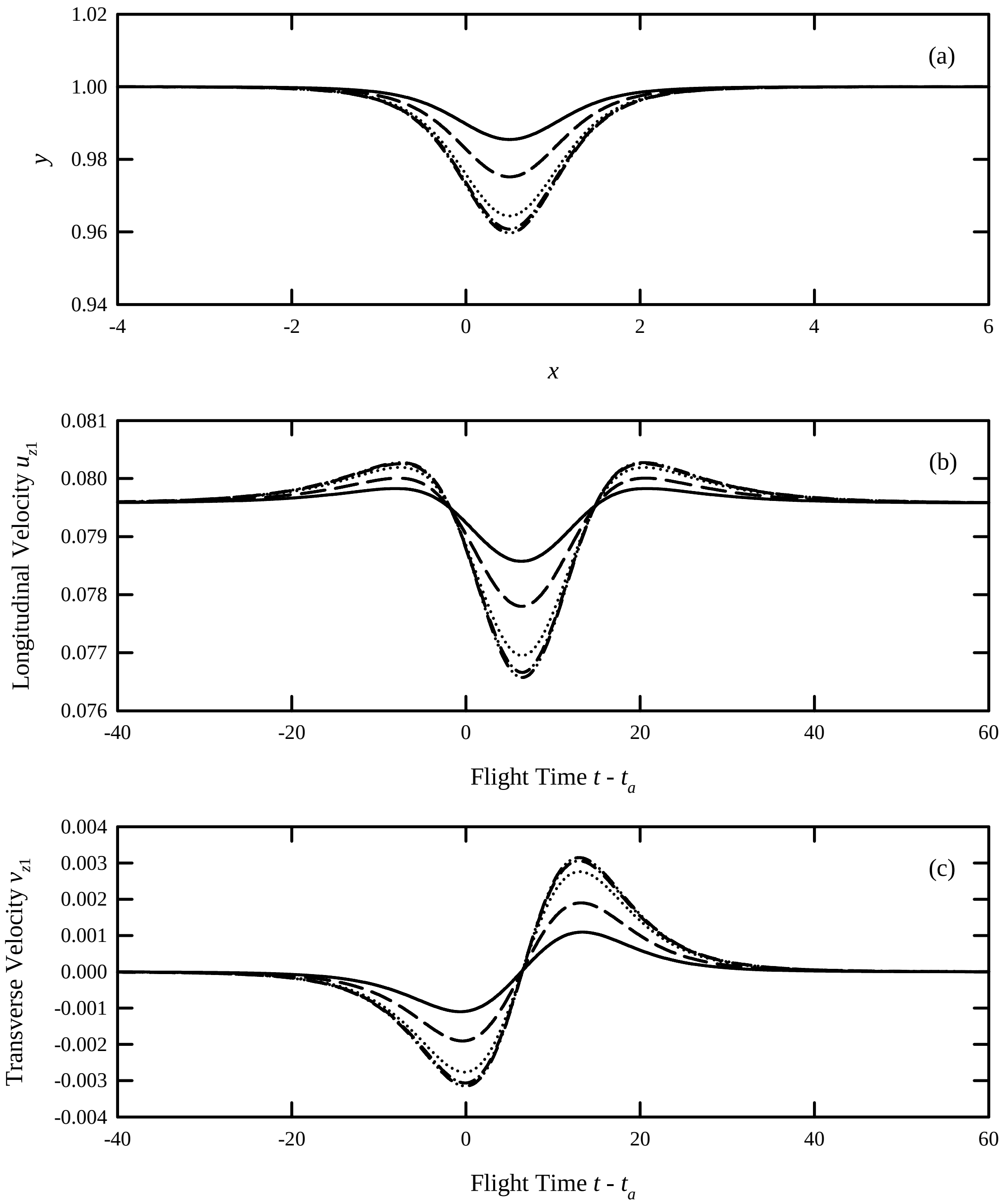

Figure 5.5 Effect of pressure releasing surface on the vortex motion, velocity, acceleration and the sound generation at a fixed L = 1 and η = 3. (a) Vortex path; (b) Longitudinal velocity; (c) Transverse velocity; (d) Longitudinal acceleration; (e) Transverse acceleration; (f) Sound pressure. ——— h = 0.1; — — — h = 0.2; ············ h = 0.4; — · — h = 0.6; — ·· — h = 0.8.

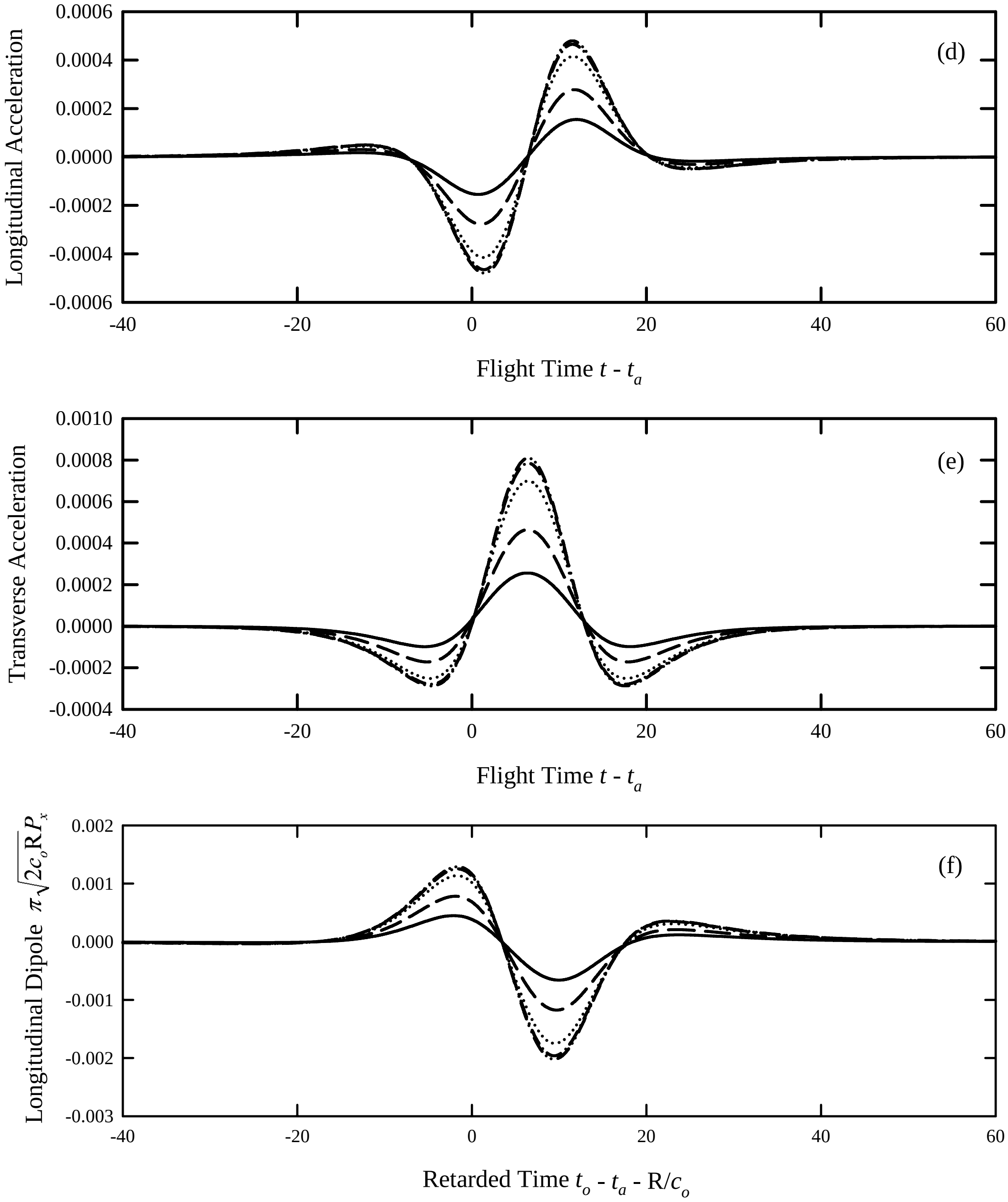

Figure 5.5 Continued

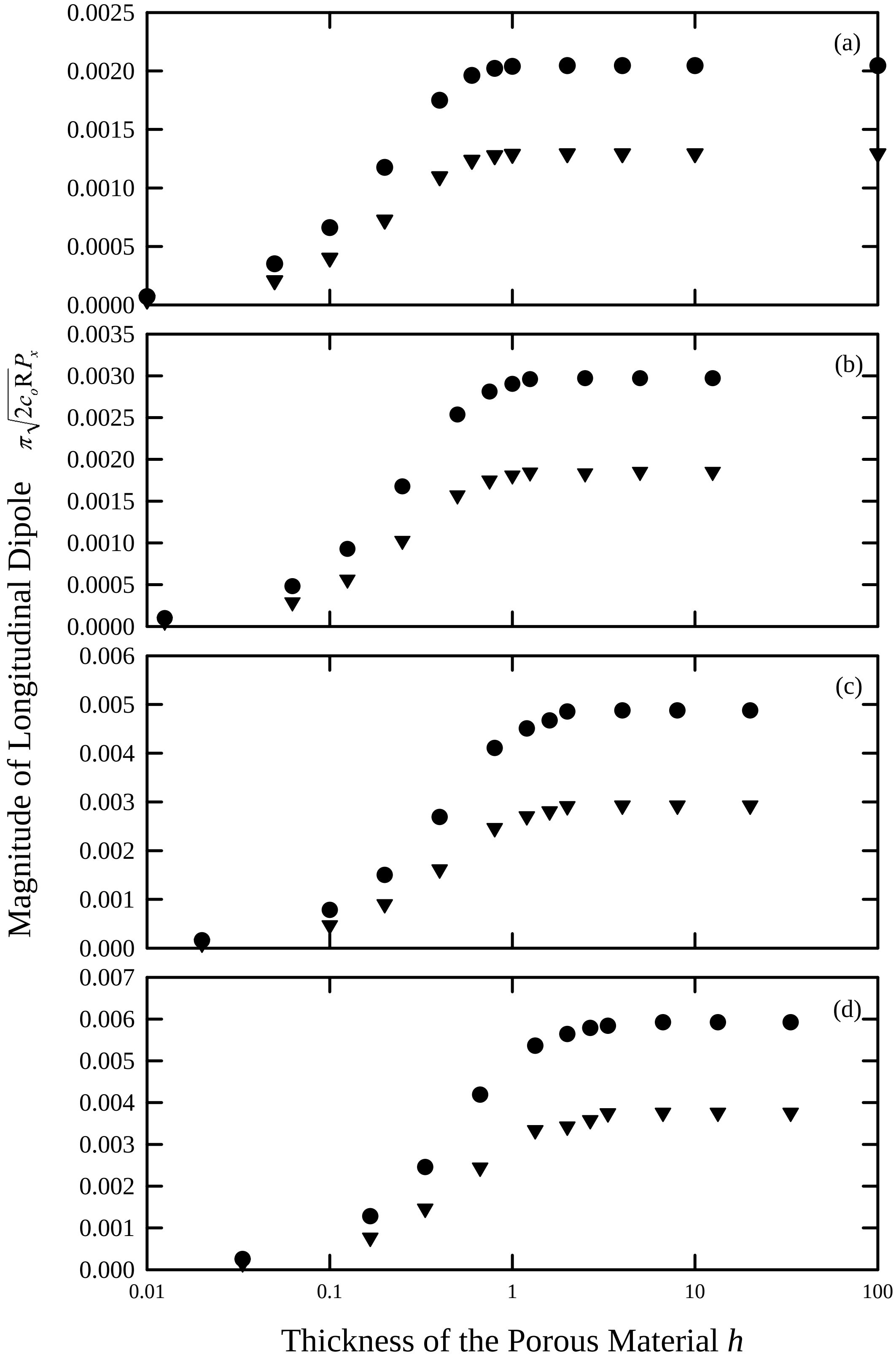

Figure 5.6 Combined effects of L and h on the radiated longitudinal dipole amplitude in perfectly inviscid fluid. (a) L = 1; (b) L = 1.25; (c) L = 2; (d) L = 10/3.● *η = 3 ;* ▼ *η = 5.*

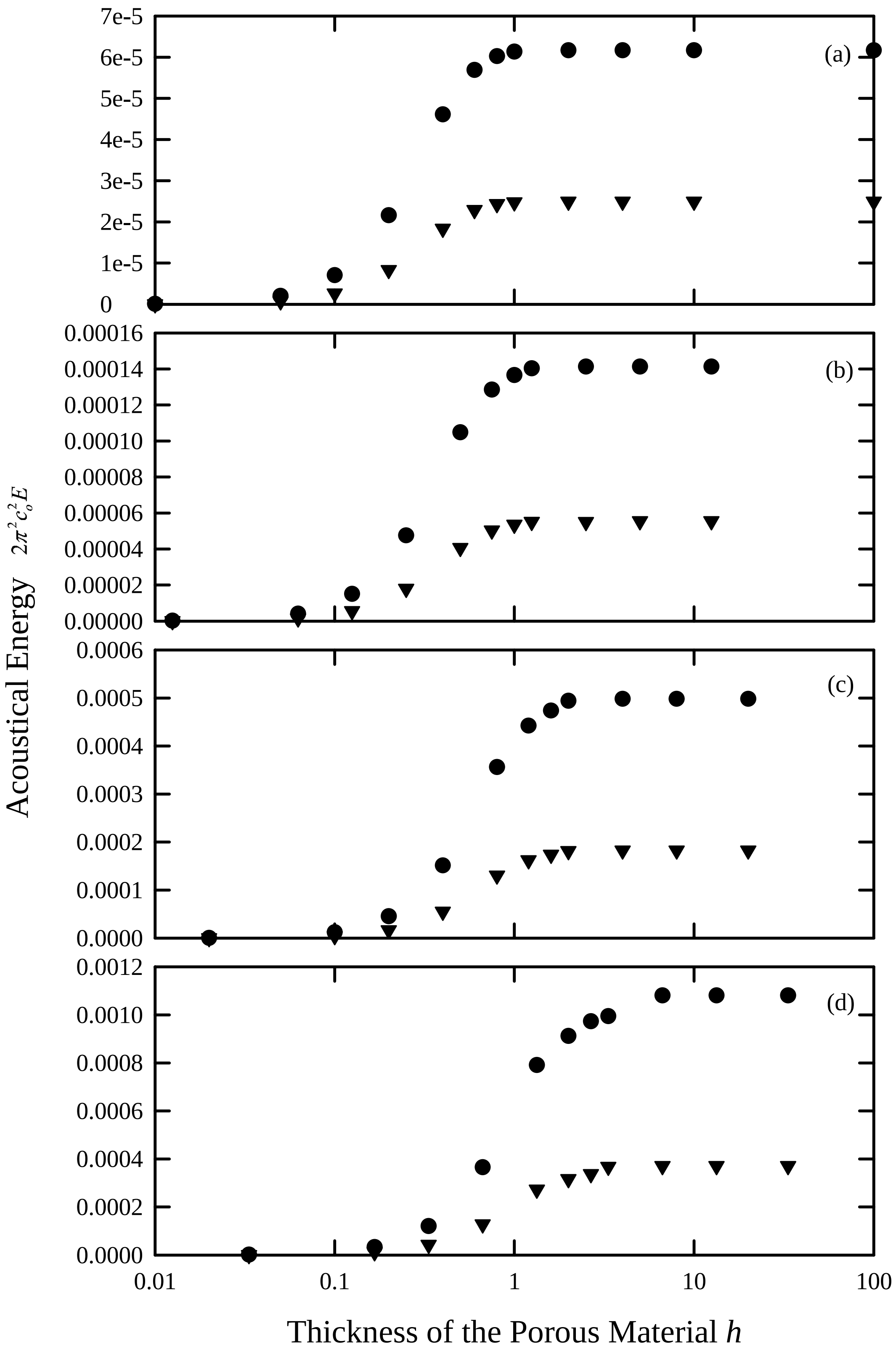

Figure 5.7 Combined effects of L and h on acoustical energy radiation in perfectly inviscid fluid. (a) L = 1; (b) L = 1.25; (c) L = 2; (d) L = 10/3. ● *η = 3 ;* ▼ *η = 5.*

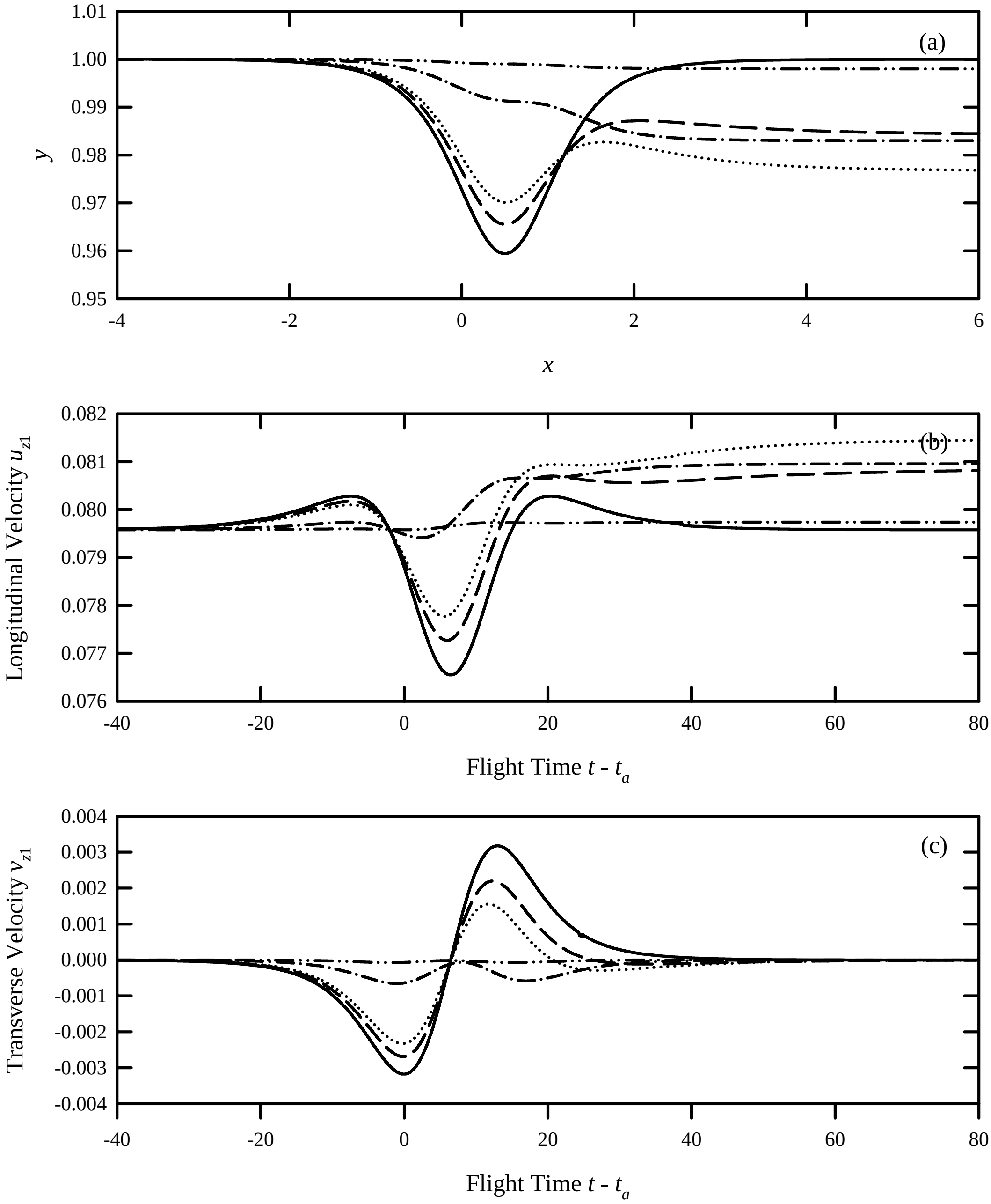

Figure 5.8 Combined effects of effective fluid density and flow resistance on the vortex motion, velocity, acceleration and the sound generation at a fixed L = 1, h = 1 and η = 3. (a) Vortex path; (b) Longitudinal velocity; (c) Transverse velocity; (d) Longitudinal acceleration; (e) Transverse acceleration; (f) Sound pressure. ——— R_f = 0; — — — R_f = 0.05; ············· R_f = 0.1; — · — R_f = 1; — ·· — R_f = 10.

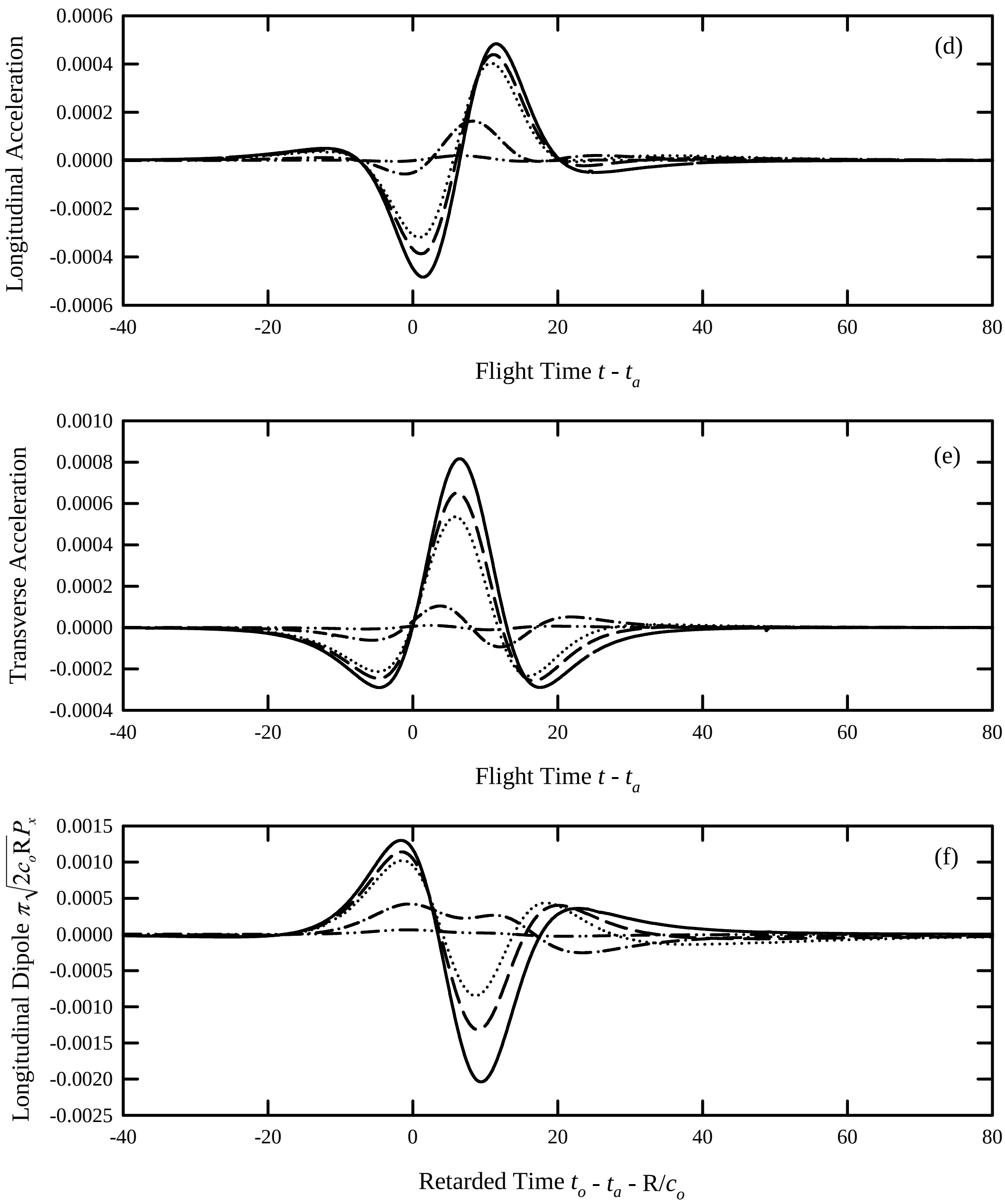

Figure 5.8 Continued

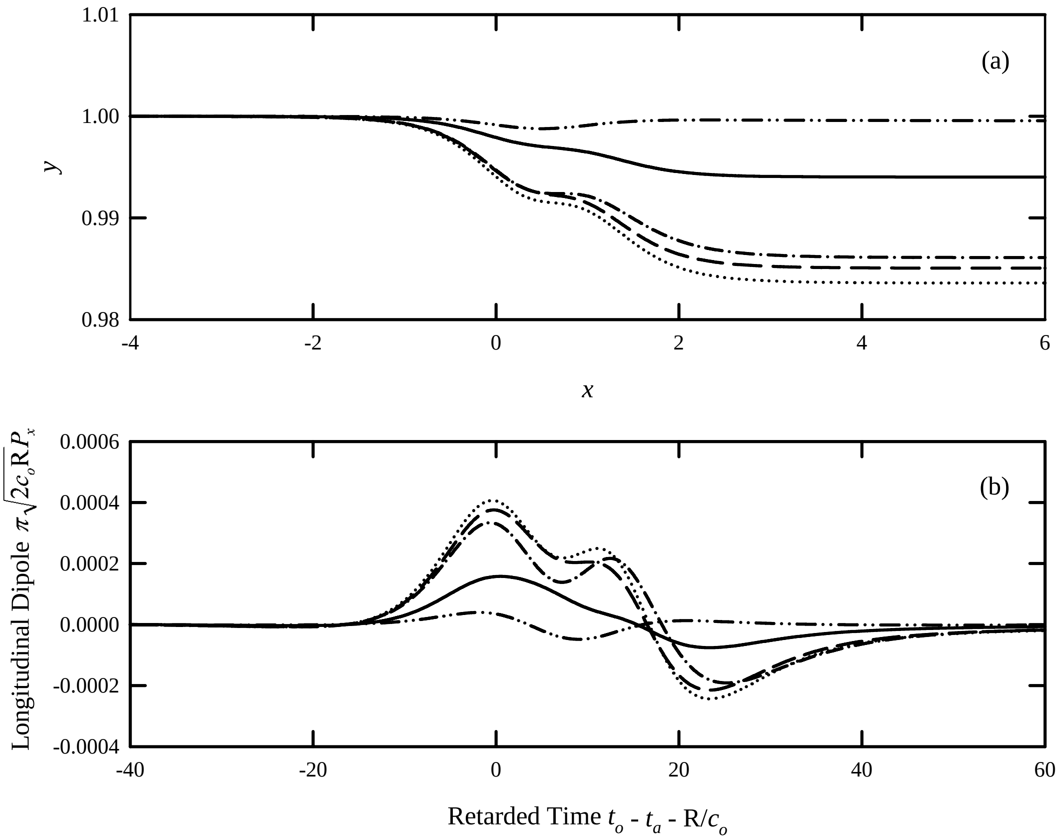

Figure 5.9 Effects of h and η on the vortex path and the sound generation for non-vanishing R_f. (a) Vortex motion; (b) Sound pressure. ——— h = 0.1, η = 3; — — — h = 0.4, η = 3; ············ h = 0.6, η = 3; — · — h = 0.6, η = 5; — ·· — h = 0.6, η = 100. L = 1 and R_f = 1.

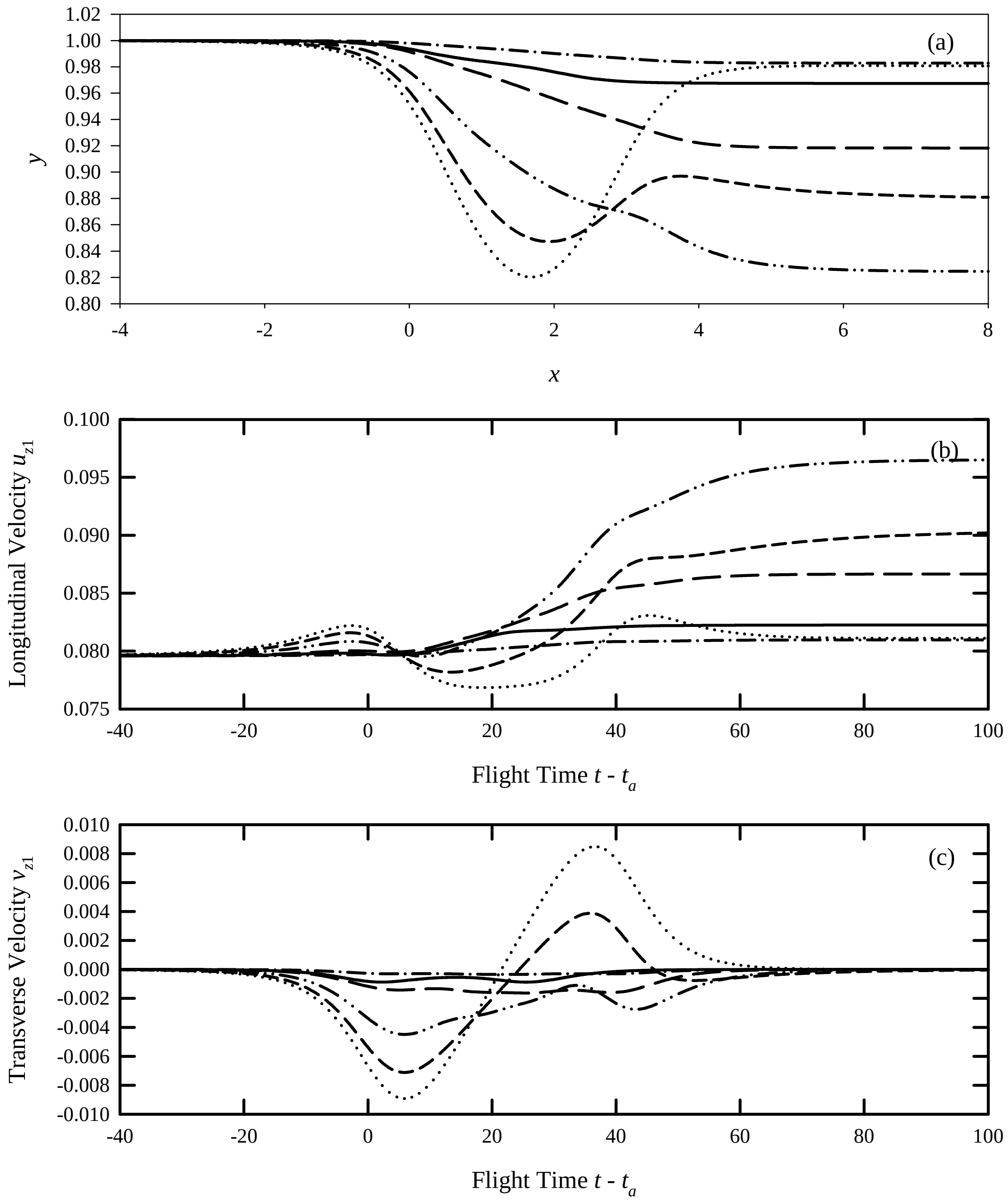

Figure 5.10 Vortex motion and time variation of vortex velocity, acceleration and sound generation of the inviscid vortex at a fixed h and η. (a) Vortex path; (b) Longitudinal velocity; (c) Transverse velocity; (d) Longitudinal acceleration; (e) Transverse acceleration; (f) Sound pressure. ———$L = 2$, $R_f = 2$; ············ $L = 10/3$, $R_f = 0.01$; – – – – $L = 10/3$, $R_f = 0.09$; — ·· —$L = 10/3$, $R_f = 0.36$; ————$L = 10/3$, $R_f = 2$; — · —$L = 10/3$, $R_f = 9$. $h = 2$ and $\eta = 5$.

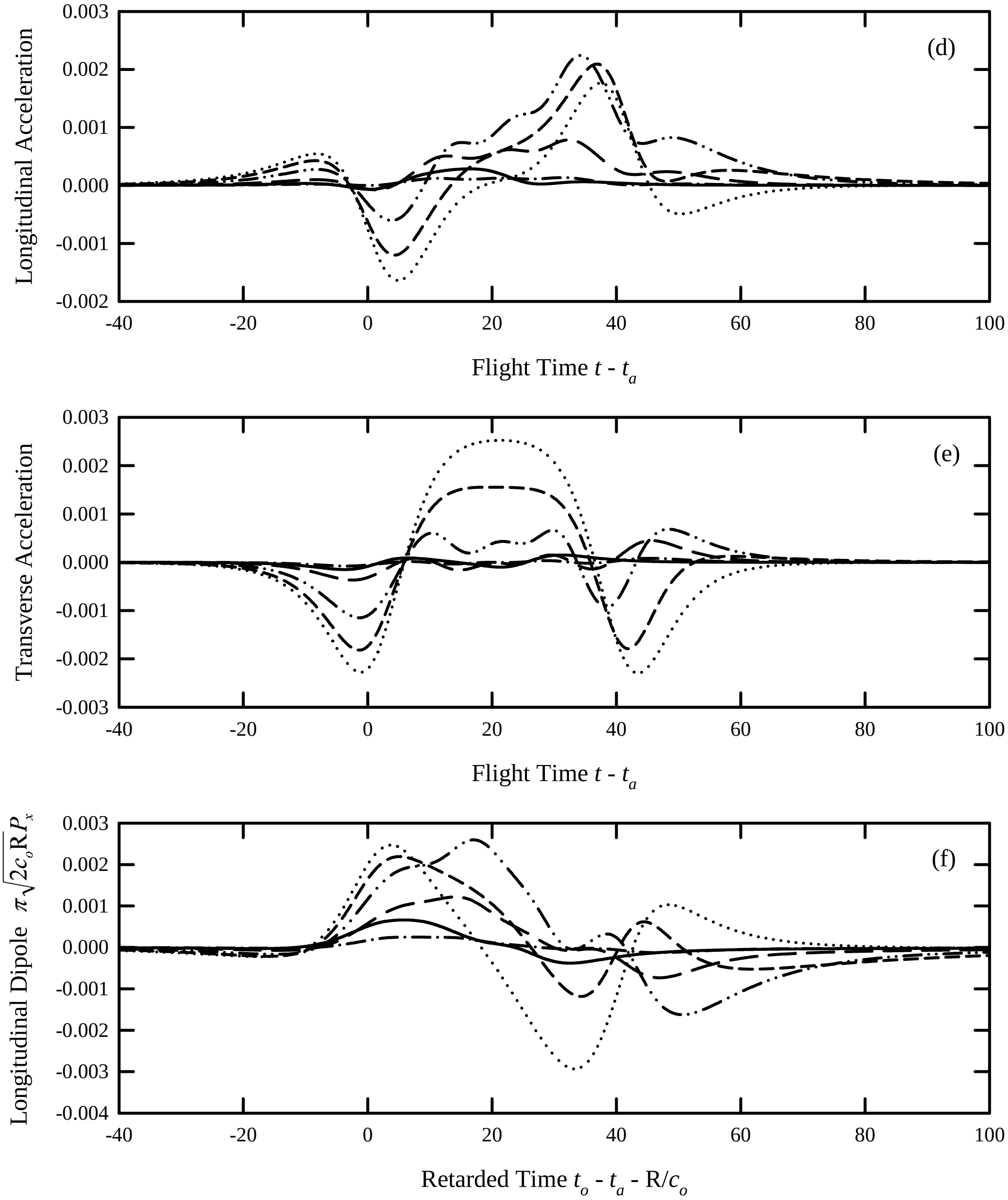

Figure 5.10 Continued

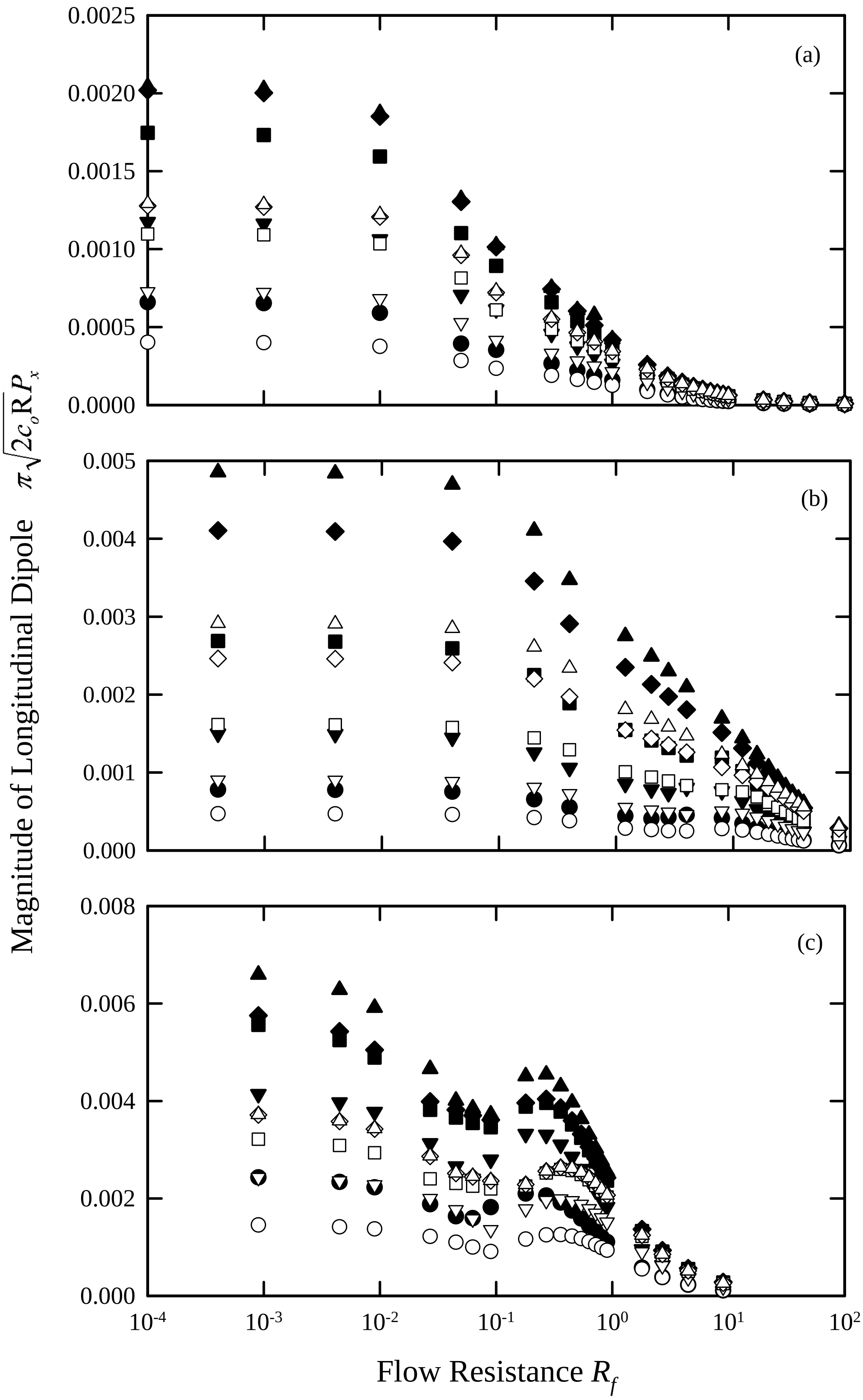

Figure 5.11 Amplitudes of the longitudinal dipole P_x with different L, h, η and R_f. (a) L = 1; (b) L = 2; ● h = 0.1; ▼ h = 0.2; ■ h = 0.4; ◆ h = 0.8; ▲ h = 2. (c) L = 10/3. ● h = 1/3; ▼ h = 2/3; ■ h = 2; ◆ h = 10/3; ▲ h = 20/3. Closed symbols for η = 3, open symbols for η = 5.

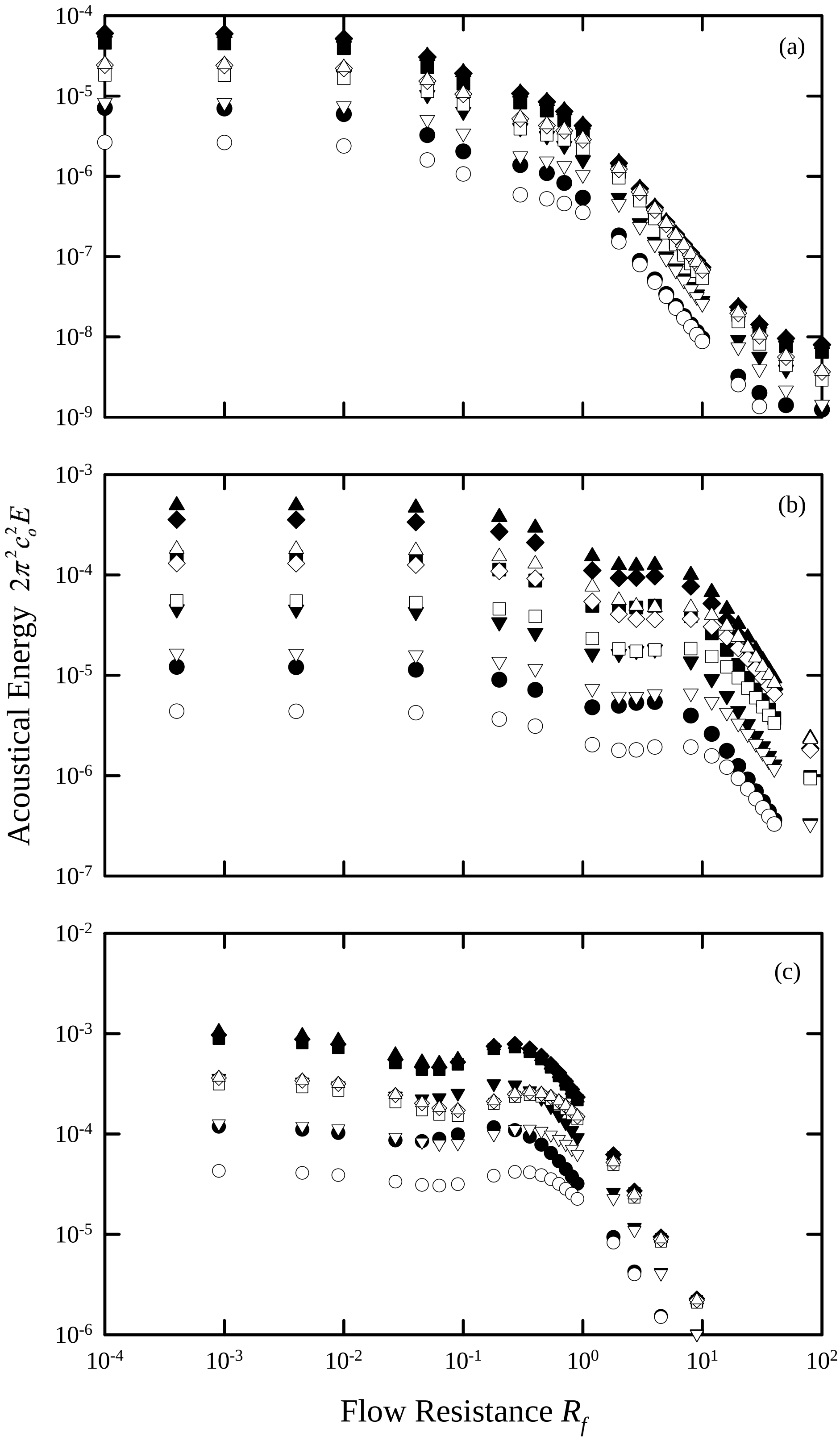

Figure 5.12 Acoustical energy radiated with different L, h, η and R_f. (a) L = 1; (b) L = 2; ● h = 0.1; ▼ h = 0.2; ■ h = 0.4; ◆ h = 0.8; ▲ h = 2. (c) L = 10/3. ● h = 1/3; ▼ h = 2/3; ■ h = 2; ◆ h = 10/3; ▲ h = 20/3. Closed symbols for η = 3, open symbols for η = 5.

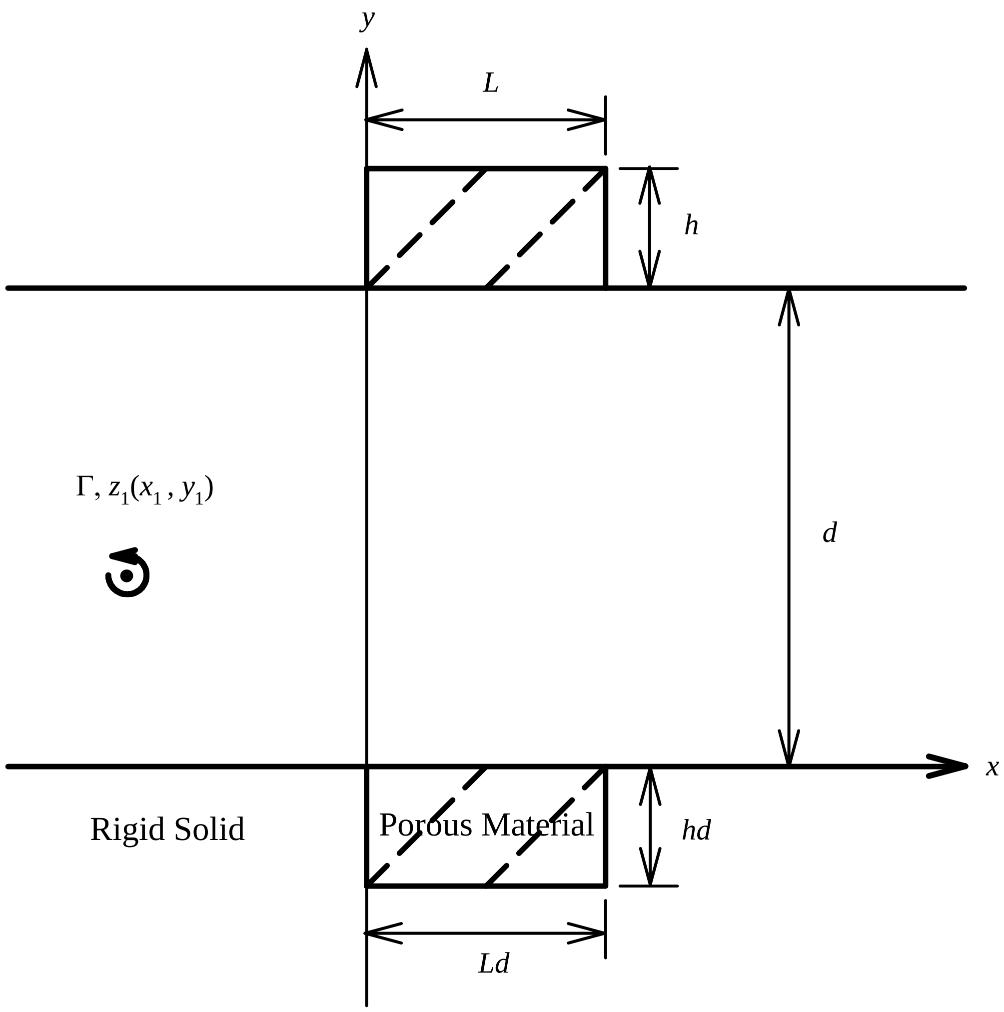

Figure 6.1 Schematics diagram of an inviscid vortex in a lined duct.

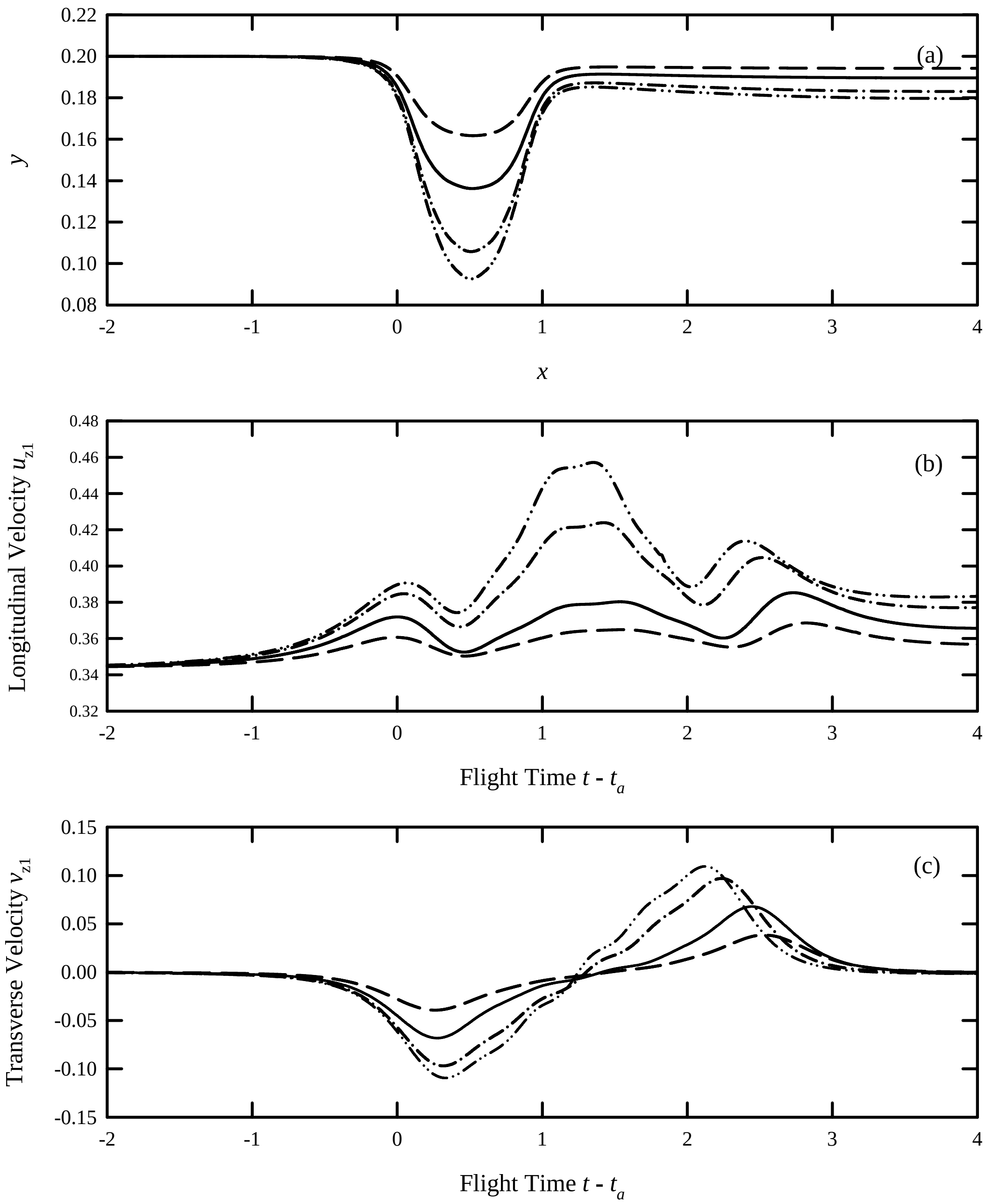

Figure 6.2 Effects of h and η on the vortex motion, velocity, acceleration and sound pressure at a fixed y_{1i} = 0.2 and L = 1.(a) Vortex path; (b) Longitudinal velocity; (c) Transverse velocity; (d) Longitudinal acceleration; (e) Transverse acceleration. ——— *h = 0.2, η = 3;* — — — *h = 0.2, η = 5;* — · — *h = 0.4, η = 3;* — ·· — *h = 0.8, η = 3.*

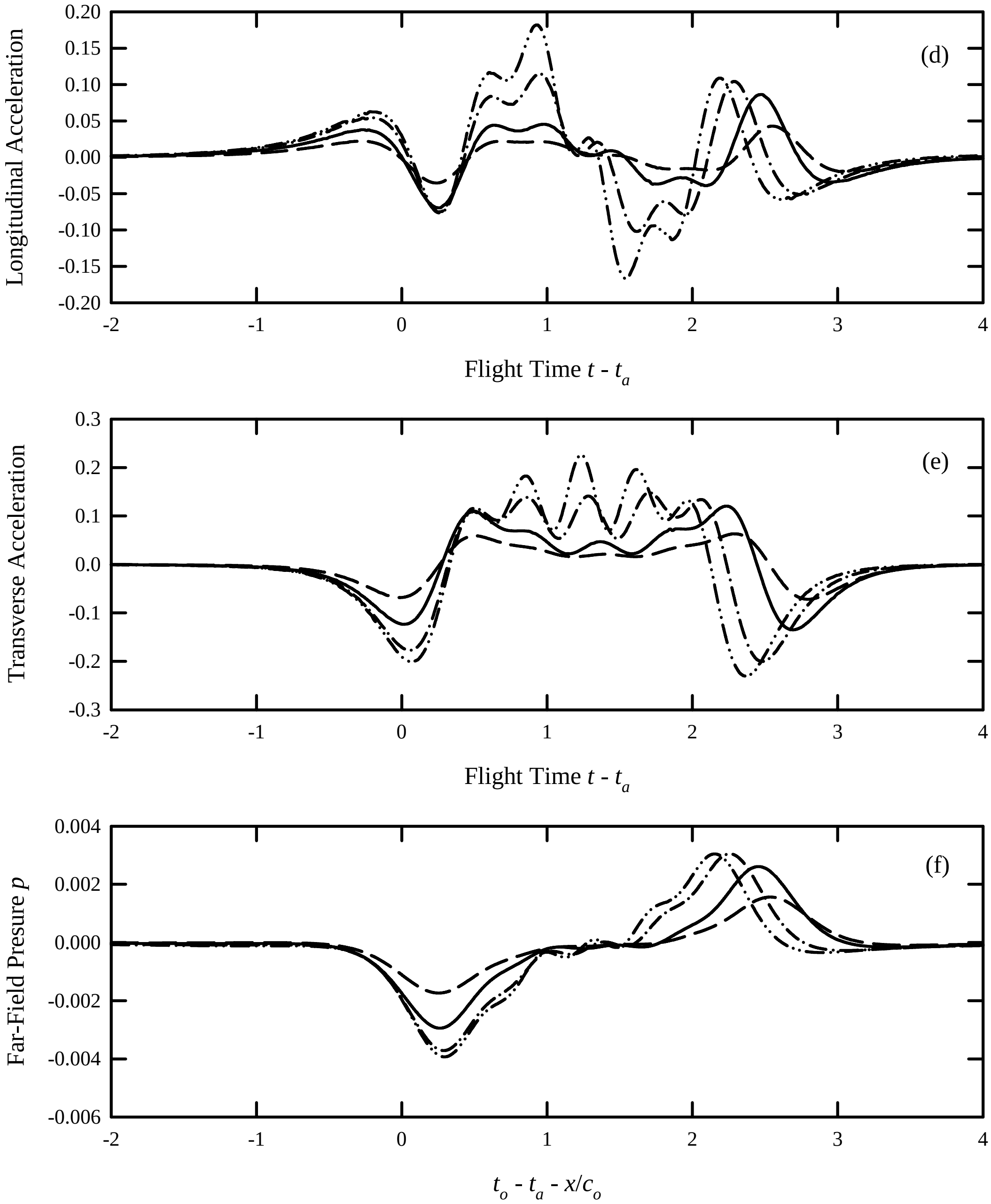

Figure 6.2 Continued

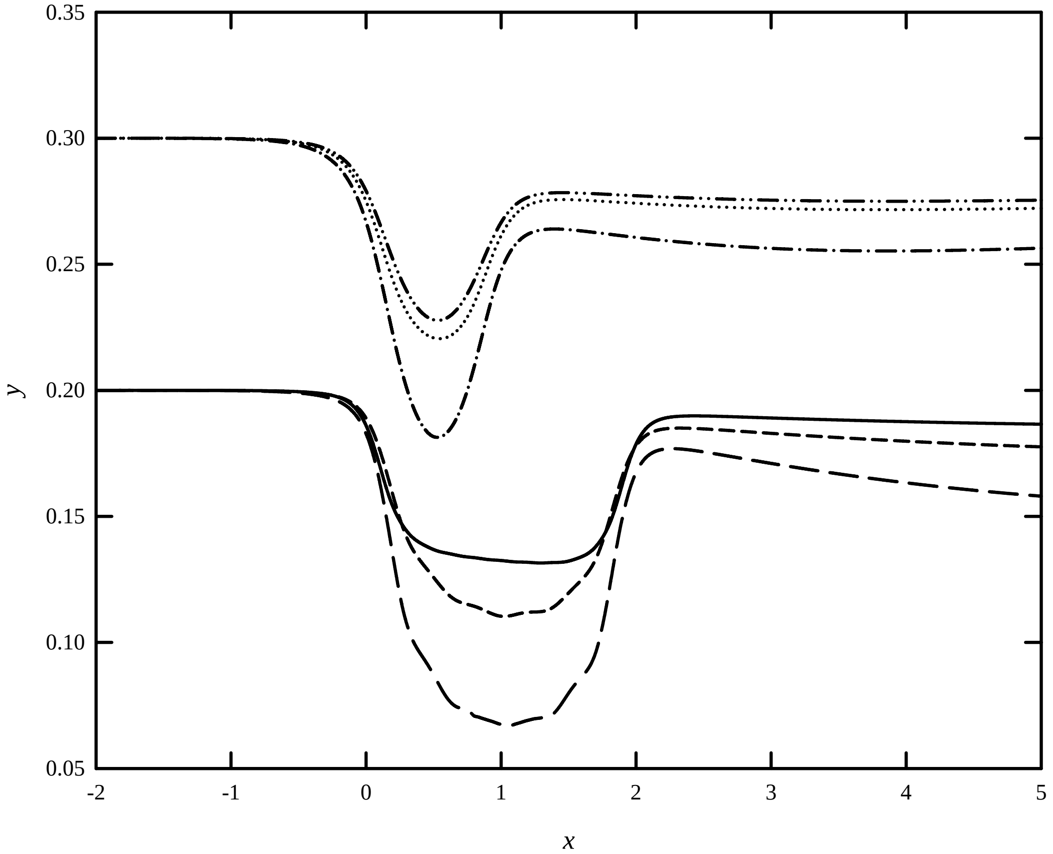

Figure 6.3 Effect of pressure-releasing surface on the vortex motion. ——— $y_{1i} = 0.2$, $h = 0.2$, $\eta = 3$, $L = 2$; — — — $y_{1i} = 0.2$, $h = 0.8$, $\eta = 3$, $L = 2$; - - - - $y_{1i} = 0.2$, $h = 0.8$, $\eta = 5$, $L = 2$; ············ $y_{1i} = 0.3$, $h = 0.2$, $\eta = 3$, $L = 1$; — · — $y_{1i} = 0.3$, $h = 0.4$, $\eta = 3$, $L = 1$; — ·· — $y_{1i} = 0.3$, $h = 0.4$, $\eta = 5$, $L = 1$.

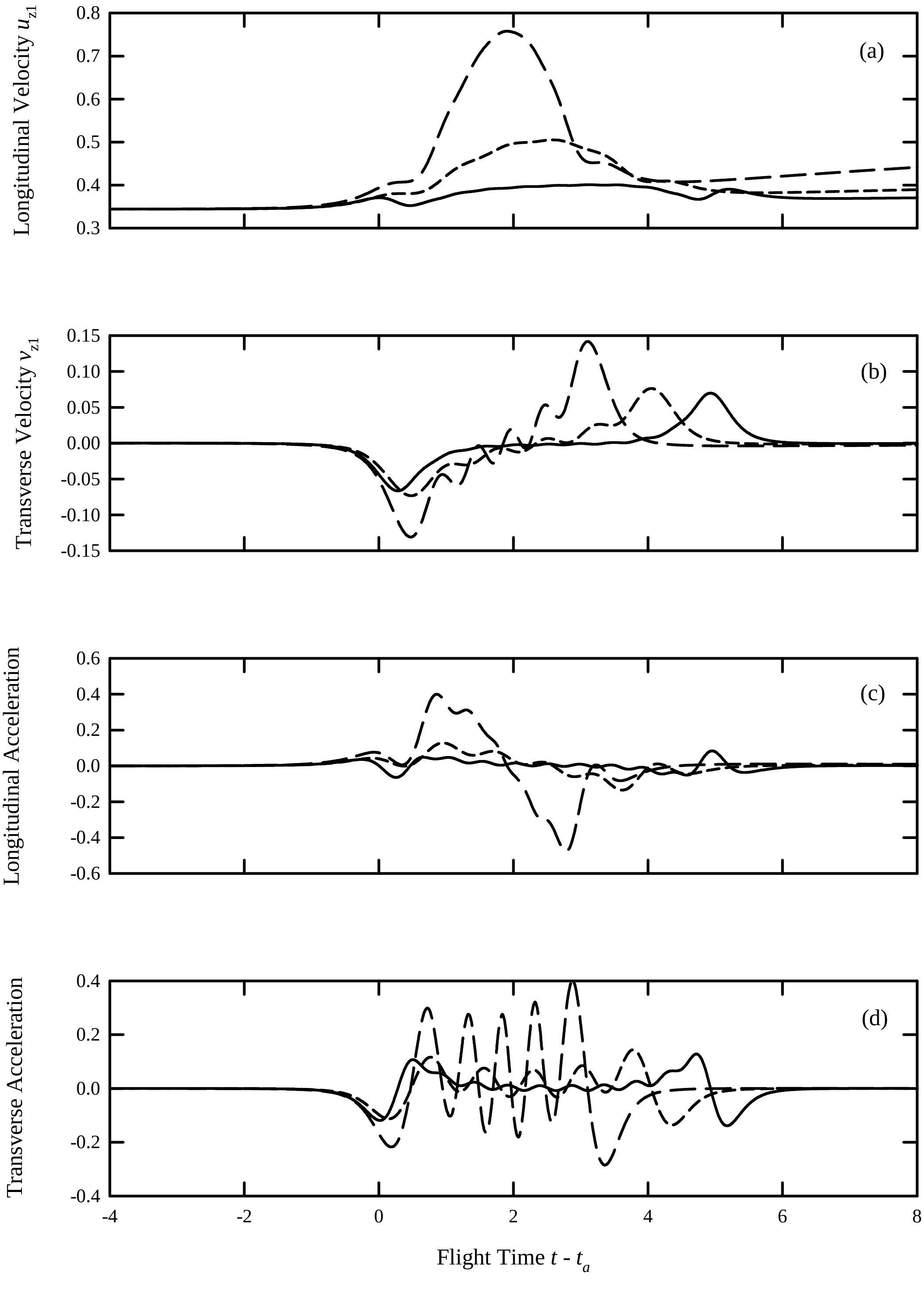

Figure 6.4 Time variations of vortex velocity and acceleration at a fixed y_{1i} = 0.2 and L = 2. ——— h = 0.2, η = 3; — — — h = 0.8, η = 3; - - - - h = 0.8, η = 5.

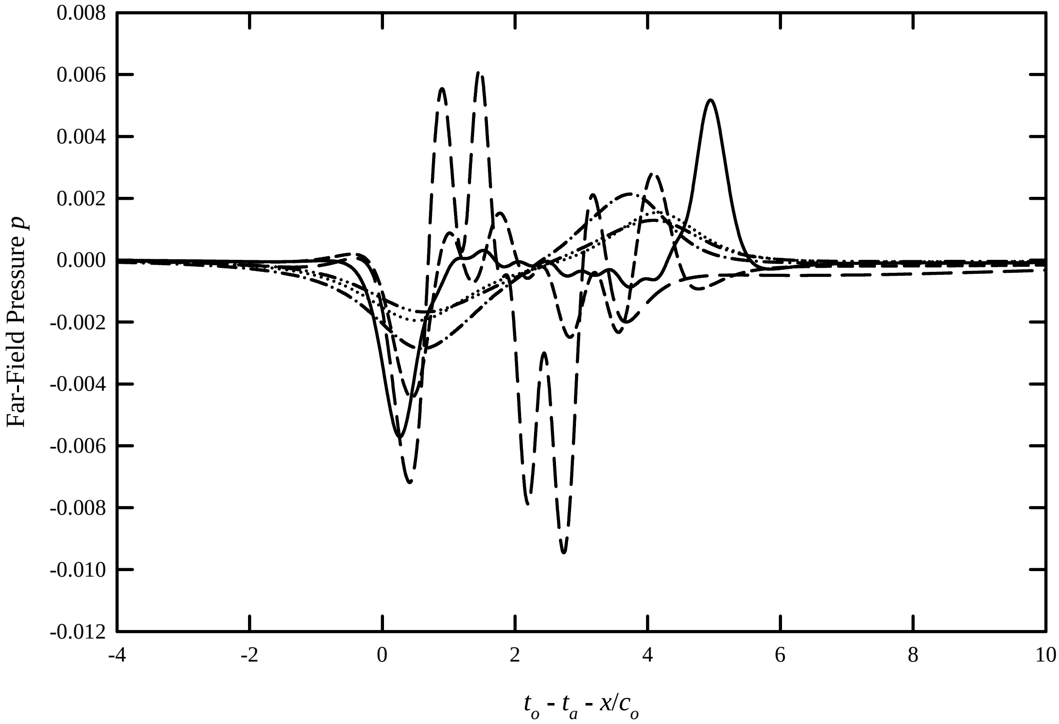

Figure 6.5 Effect of pressure-releasing surface on the sound pressure fluctuations. ——— $y_{1i} = 0.2$, $h = 0.2$, $\eta = 3$, $L = 2$; — — — $y_{1i} = 0.2$, $h = 0.8$, $\eta = 3$, $L = 2$; - - - - $y_{1i} = 0.2$, $h = 0.8$, $\eta = 5$, $L = 2$; ············ $y_{1i} = 0.3$, $h = 0.2$, $\eta = 3$, $L = 1$; — · — $y_{1i} = 0.3$, $h = 0.4$, $\eta = 3$, $L = 1$; — ·· — $y_{1i} = 0.3$, $h = 0.4$, $\eta = 5$, $L = 1$.

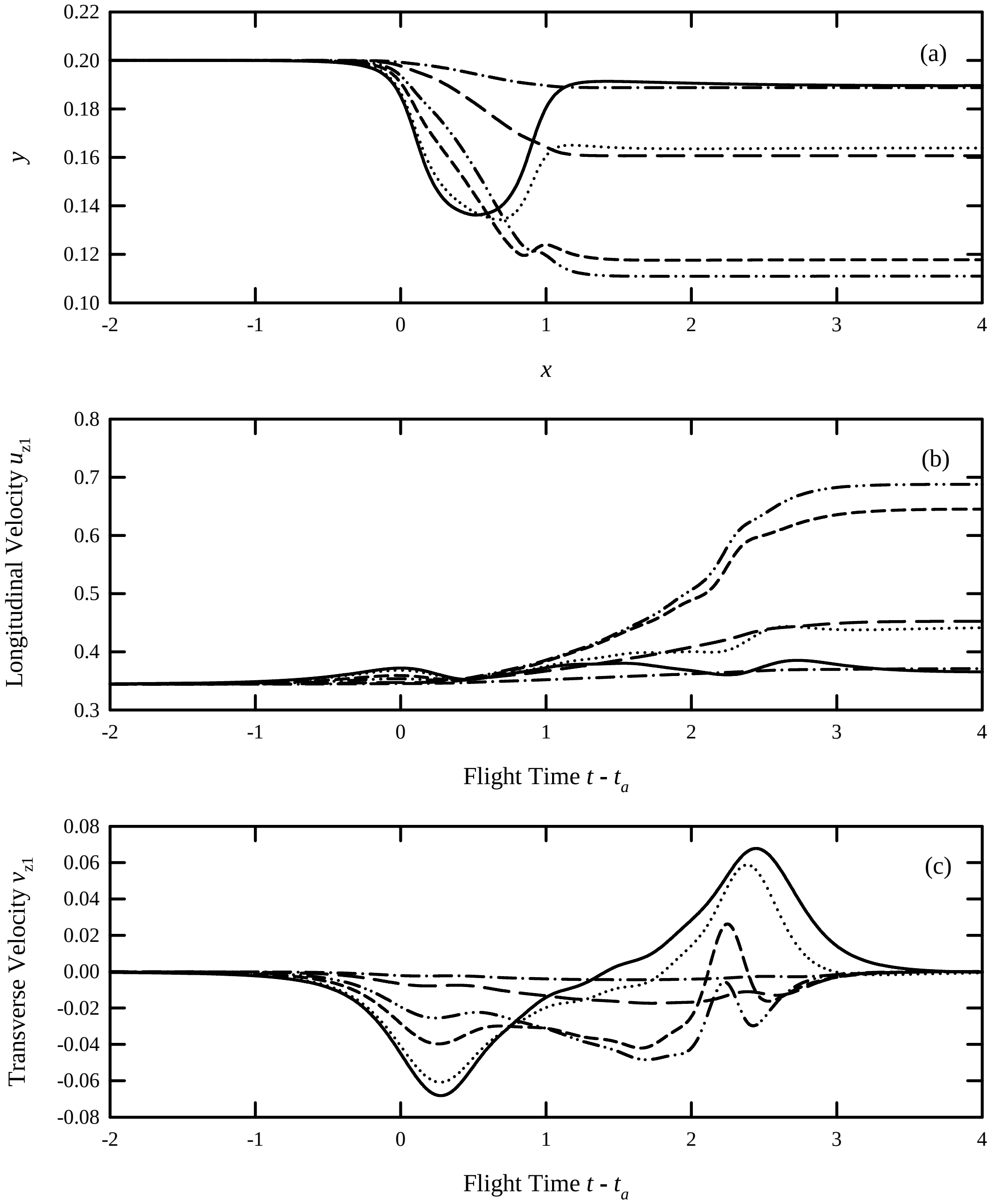

Figure 6.6 Effects of flow resistance on the vortex dynamic, velocity, acceleration and sound pressure. (a) Vortex path; (b) Longitudinal velocity; (c) Transverse velocity; (d) Longitudinal acceleration; (e) Transverse acceleration; (f) Sound pressure. ——— $R_f = 0$; ············ $R_f = 0.5$; - - - - $R_f = 3$; — ·· — $R_f = 7$; — — — $R_f = 30$; — · — $R_f = 100$. $y_{1i} = 0.2$, $h = 0.2$, $\eta = 3$, $L = 1$.

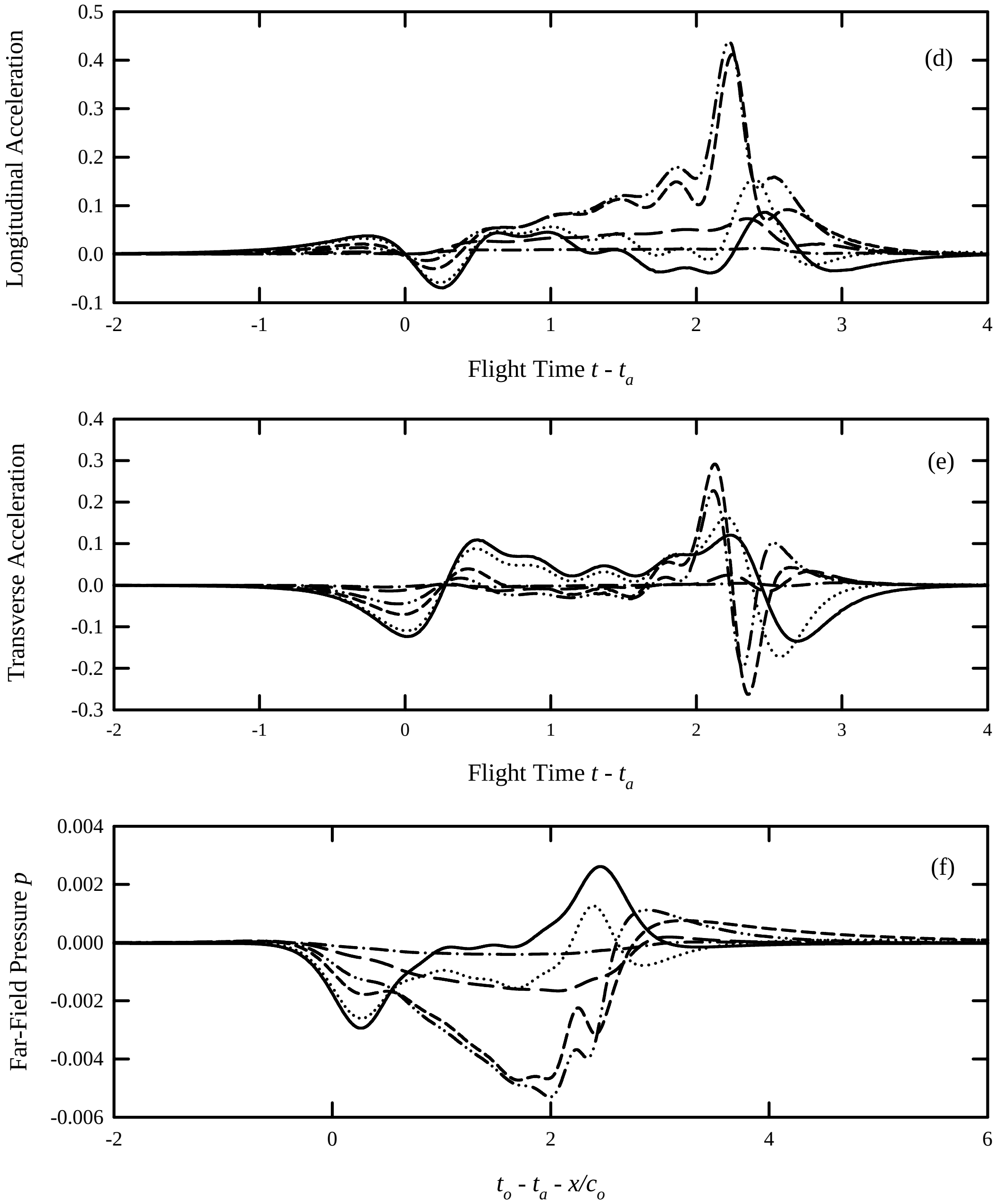

Figure 6.6 Continued

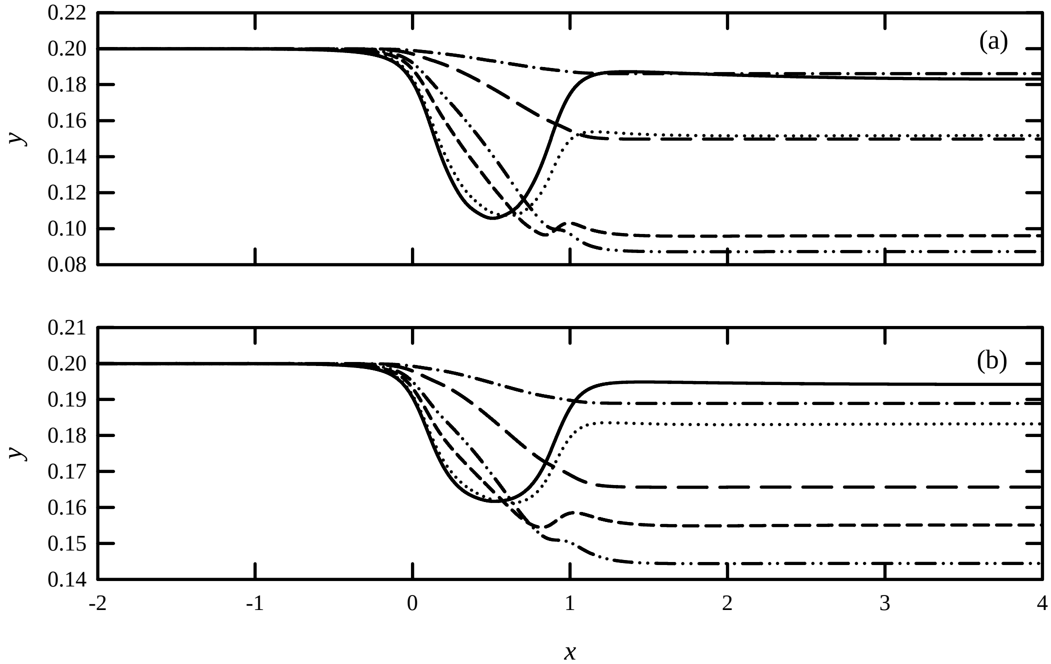

Figure 6.7 Effects of flow resistance on the vortex dynamic. (a) $y_{1i} = 0.2$, $h = 0.4$, $\eta = 3$; (b) $y_{1i} = 0.2$, $h = 0.2$, $\eta = 5$. ——— $R_f = 0$; ············ $R_f = 0.5$; - - - - $R_f = 3$; —··— $R_f = 7$; ——— $R_f = 30$; —·— $R_f = 100$. $L = 1$.

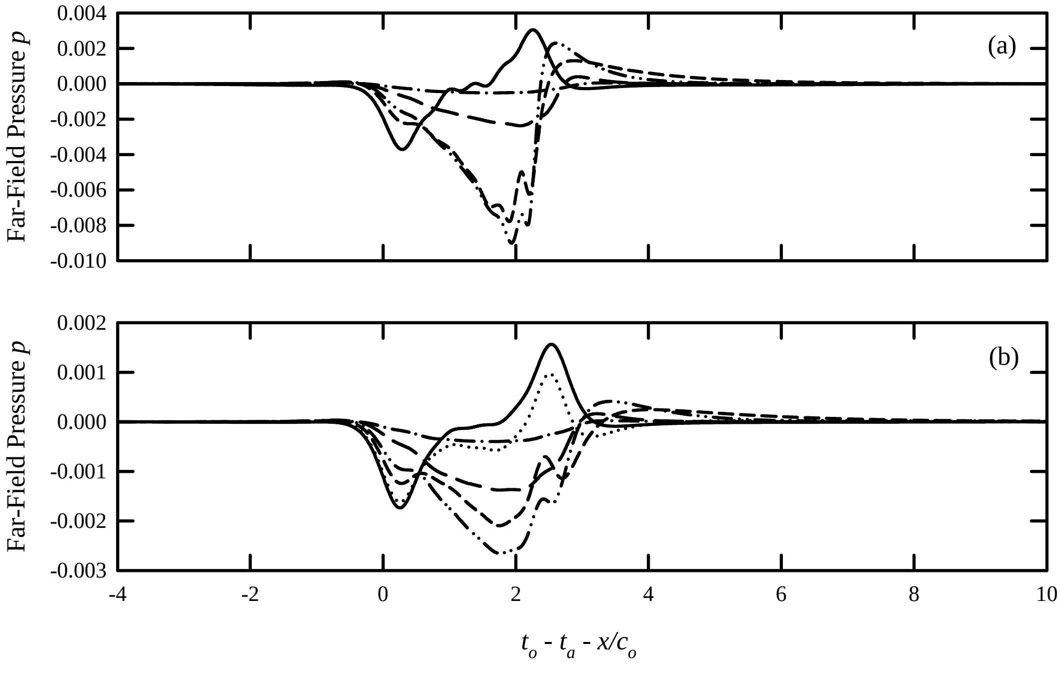

Figure 6.8 Effects of flow resistance on the sound pressure generation. (a) $y_{1i} = 0.2$, $h = 0.4$, $\eta = 3$; (b) $y_{1i} = 0.2$, $h = 0.2$, $\eta = 5$. ——— $R_f = 0$; ············ $R_f = 0.5$; - - - - $R_f = 3$; —··— $R_f = 7$; ——— $R_f = 30$; —·— $R_f = 100$. $L = 1$.

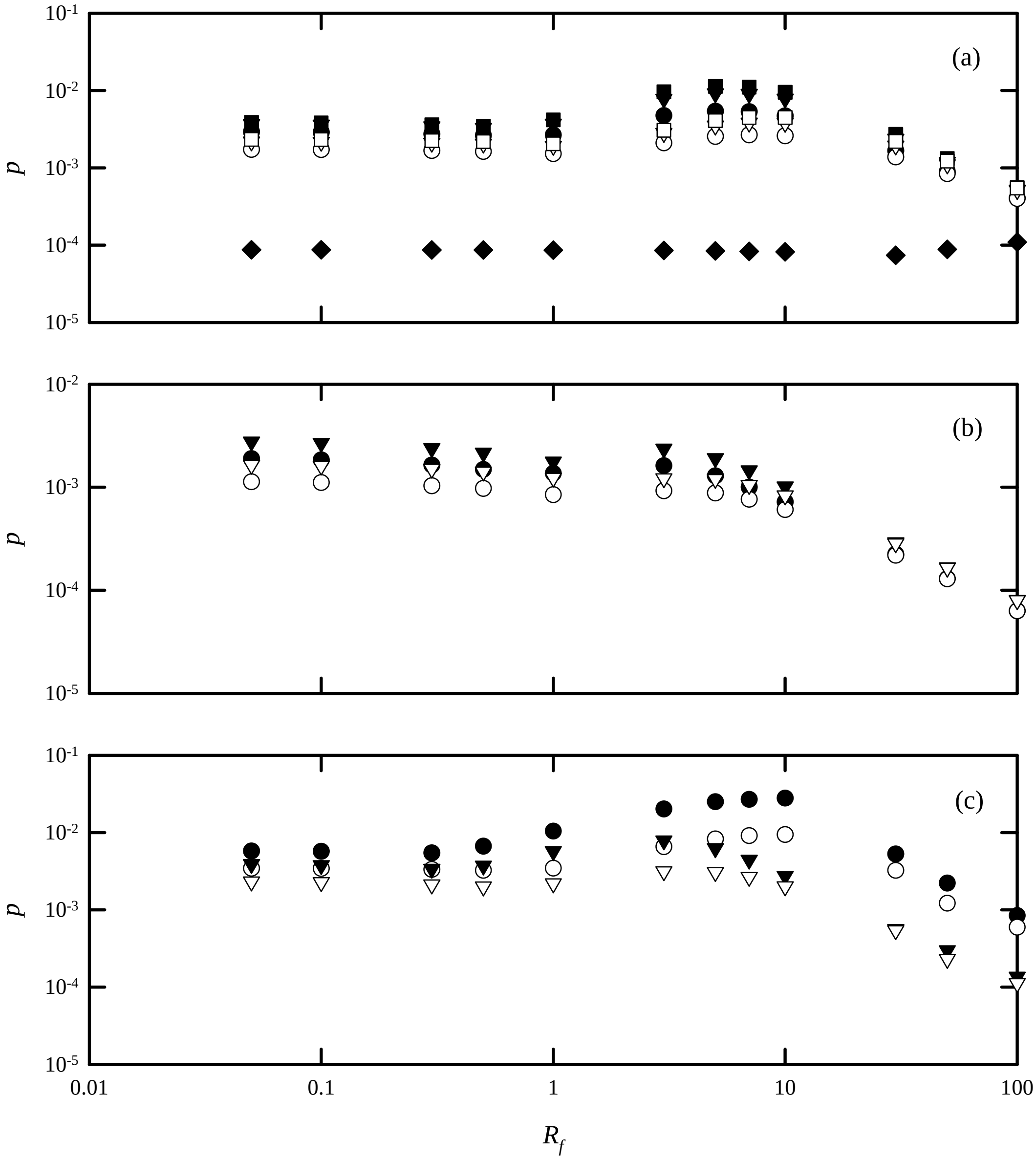

Figure 6.9 Summary of the sound pressure magnitude with various y_{1i}, h, η and L against R_f. (a) y_{1i} = 0.2, L = 1; ● h = 0.2, η = 3; ▼ h = 0.4, η = 3; ■ h = 0.8, η = 3; ◆ h = 0.2, η = 100. (b) y_{1i} = 0.3, L = 1; ● h = 0.2, η = 3; ▼ h = 0.4, η = 3; (c) L = 2. ● y_{1i} = 0.2, h = 0.2, η = 3; ▼ y_{1i} = 0.3, h = 0.2, η = 3. Closed symbols for η = 3, open symbols for η = 5.

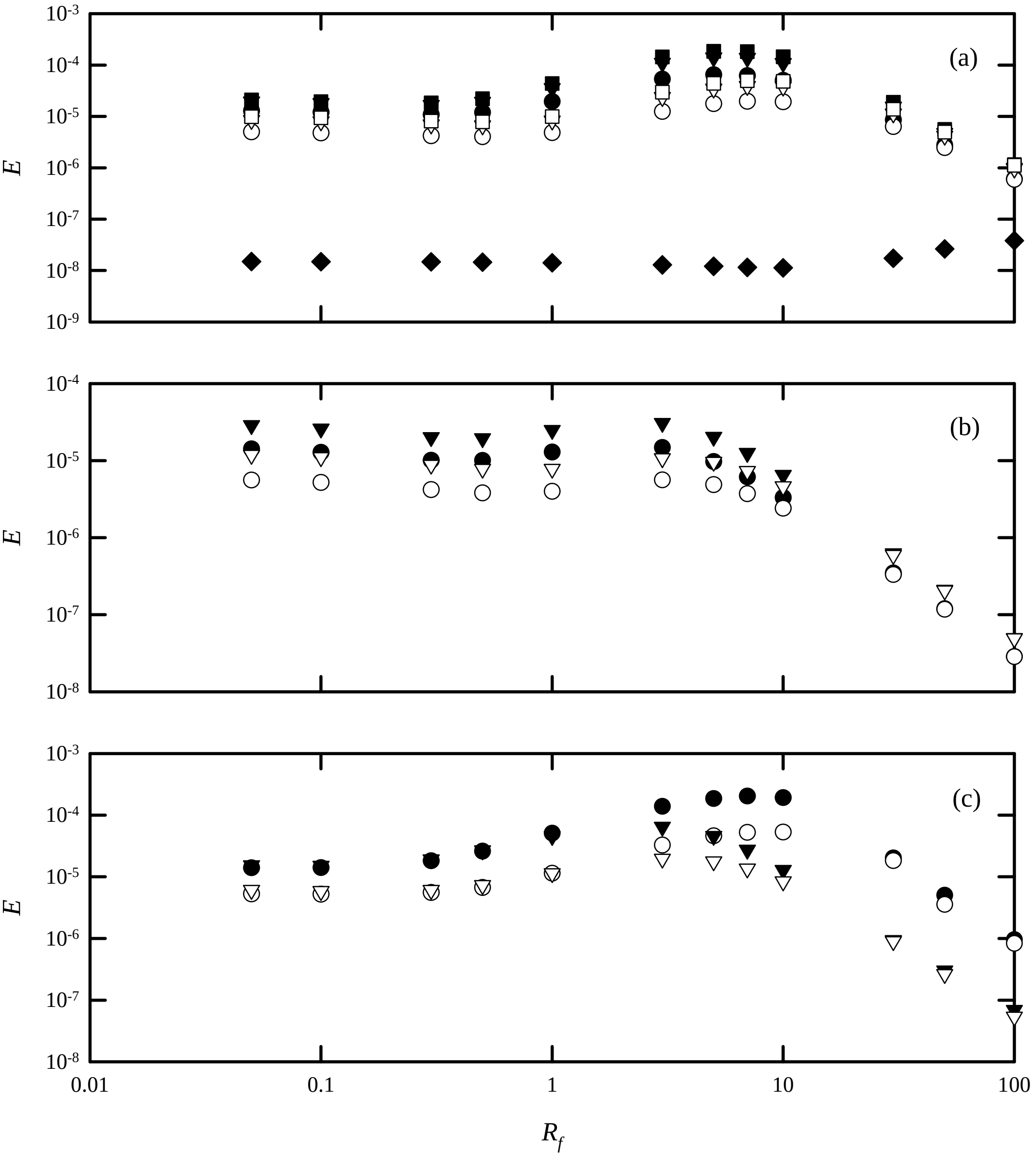

Figure 6.10 Summary of the acoustical energy radiated with various y_{1i}, h, η and L against R_f. (a) y_{1i} = 0.2, L = 1; ● h = 0.2, η = 3; ▼ h = 0.4, η = 3; ■ h = 0.8, η = 3; ◆ h = 0.2, η = 100. (b) y_{1i} = 0.3, L = 1; ● h = 0.2, η = 3; ▼ h = 0.4, η = 3; (c) L = 2. ● y_{1i} = 0.2, h = 0.2, η = 3; ▼ y_{1i} = 0.3, h = 0.2, η = 3. Closed symbols for η = 3, open symbols for η = 5.